The low-energy extension of the Surface Detector Array of the Pierre Auger Observatory

For the attainment of the academic degree of

Doctorate in Science

from the
Karlsruher Institut für Technologie (KIT)
and the
Universidad Nacional de San Martín (UNSAM)

accepted

Dissertation

of

M.Sc. Gaia Silli
from Rome, Lazio, Italy

Day of the oral examination: 26th of November 2021
Referee: Dr. Alberto Etchegoyen
Co-referee: Prof. Dr. Dr. h.c. Johannes Blümer
Advisor: Dr. Diego Melo
Advisor: Dr. Diego Ravignani
Advisor: Dr. Markus Roth

The low-energy extension of the Surface Detector Array of the Pierre Auger Observatory

Zur Erlangung des akademischen Grades eines

Doktors der Naturwissenschaften (Dr. rer. nat.)

von der KIT-Fakultät für Physik des
Karlsruher Instituts für Technologie (KIT)
und der
Universidad Nacional de San Martín (UNSAM)

genehmigte

Dissertation

von

M.Sc. Gaia Silli
aus Rom, Lazio, Italien

Tag der mündlichen Prüfung: 26. November 2021
Referent: Dr. Alberto Etchegoyen
Korreferent: Prof. Dr. Dr. h.c. Johannes Blümer
Betreuer: Dr. Diego Melo
Betreuer: Dr. Diego Ravignani
Betreuer: Dr. Markus Roth

The low-energy extension of the Surface Detector Array of the Pierre Auger Observatory

Tesis presentada para optar por el título de

Doctor en astrofìsica

del Instituto de Tecnología "Prof. Jorge A. Sábato" de la
Universidad Nacional de San Martín (UNSAM)
y del
Karlsruher Instituts für Technologie (KIT)

aprobado

Tesis doctoral

de

M.Sc. Gaia Silli

desde Roma

Fecha de la defensa oral:

Director; Dr. A. Etchegoyen

Co-Director: Prof. Dr. Dr. h.c. J. Blümer

Colaborador: Dr. Diego Melo

Colaborador: Dr. Diego Ravignani

Colaborador: Dr. Markus Roth

Abstract

The detection of the cosmic-ray energy spectrum with surface detectors spans over six orders of magnitude in energy, from 10^{15} eV up to more than 10^{20} eV. The energy spectrum follows a power-law with a spectral index $\gamma \simeq 3$ exhibiting five features identified by small deviations in the spectral index: the knee, the second knee, the ankle, the "instep", and a suppression at the highest energies. Particularly, the second knee has been observed at $\sim 10^{17}$ eV by several observatories as a steepening of the spectrum. Its interpretation may be connected to the maximal energy of the accelerators in the Galaxy, considering that a gradually heavier composition has been observed at these energies, which is along the lines of the so-called Peters cycles. The astrophysical interpretation of the acquired data is still delicate, mainly because the nature of the sources, the propagation effects, and the cosmic rays composition are strongly entwined.

The Pierre Auger Observatory, located in western Argentina, is the world's largest cosmic-ray observatory. While it was originally built to study the cosmic-ray flux above $10^{18.5}$ eV, several enhancements have reduced this energy threshold. One of such enhancements is going to be presented in this thesis work. A more accurate understanding of the origin of the second knee may be possible if one observatory is capable of measuring all spectral features and the cosmic rays mass composition with a unique energy scale. In this sense, the Pierre Auger Observatory extended its Surface Detector with the deployment of a 433 m spaced triangular array of water-Cherenkov detectors to unveil the spectral region below 10^{17} eV. Our Collaboration already reported some preliminary evidence of the second knee from the 750-metre surface detector data and from measurements of the Cherenkov light with the fluorescence detector. Therefore, the 433-metre array will allow for the first time to measure the three UHE spectrum features not only by a single observatory but with the same detection technique.

The main objective of this thesis is to extend the energy spectrum measured with the Surface detector of the Pierre Auger Observatory down to energies of $10^{16.5}$ eV. Towards this goal, a variety of analysis steps were carried out. To characterize the array's abilities to detect and sample air showers, studies of simulated showers were performed to obtain trigger efficiency curves that are a vital ingredient in defining the effective exposure of the array and the essential step heading for a final energy spectrum. The deployment of the denser array has required the optimization, extension, and improvement of the event-reconstruction process, based on a previous basic reconstruction already existing in the $\overline{\text{Off}}\underline{\text{line}}$ framework. Therefore, this thesis includes an extensive update to the reconstruction methods used to estimate the trajectory and energy of a cosmic ray using the new surface detector array. The update was motivated by the inclusion of a new set of detectors and by the production of

a whole new data set. The standard reconstruction of air showers is based on an empirical description of the overall lateral distribution of secondary particles on the ground. For each event, the expected size at a certain distance to the shower core is a robust estimator of the primary energy. The nominated optimal distance is the distance to the core at which the lack of knowledge of the lateral distribution of showers has the smallest impact on the estimation of the shower size, which means that at this reference distance the bias of the reconstructed signal is minimal. The lateral fall-off of the deposited signal, with increasing distance to the shower axis in the shower plane is modeled with a lateral distribution function which has a slope that is parametrised as functions of the shower observables, notably the zenith angle and the estimation of the primary energy measurement at the optimal distance. Both the lateral distribution function used to fit the observed signals as a function of distance from an air shower's central axis and the optimal distance strongly depend on the spacing between stations. Therefore, for 433-metre dense array we updated the reference distance and the set of parameters for an optimized fitting procedure, also benefiting from the new available data set.

The lateral distribution is particularly important as it is used to find the expected signal at the fixed reference distance from the axis to estimate the primary energy. The energy estimation strongly dependent on the shower inclination, is corrected using the the Constant Intensity Cut method to produce a zenith angle independent energy estimator. We found that the 433-metre array, completed in May 2019, observes cosmic rays with full efficiency from 3×10^{16} eV, thus bringing within detection range the energy at which the second knee has been observed in the spectrum. As a result of the increased sensitivity to lower energy showers, it was possible to measure the cosmic ray flux down to energies half an order of magnitude lower than what was previously possible by the surface array.

We built an energy energy spectrum of cosmic rays using the 433-metre surface detector array of the Pierre Auger Observatory. The presented spectrum shows an inflection around $\sim 10^{17}$ eV, where the spectral index of the otherwise monotonous power law spectrum changes value, confirming the presence of the second knee spectral feature. This feature is important as a signature of the change in origin and/or types of arriving cosmic rays. We compared the resulting energy spectrum with results of other experiments. This study lays the ground mark for future measurements in the energy range as low as 10^{16} eV with a surface detector thus expanding the scientific output of the Auger Observatory.

Zusammenfassung

Der Nachweis des Energiespektrums der kosmischen Strahlung mit Oberflächendetektoren erstreckt sich über sechs Größenordnungen der Energie, von 10^{15} eV bis zu mehr als 10^{20} eV. Es folgt einem Potenzgesetz mit einem Spektralindex $\gamma \simeq 3$ und weist fünf Merkmale auf, die durch kleine Abweichungen im Spektralindex gekennzeichnet sind: das Knie, das zweite Knie oder Eisenknie, der Knöchel, der "Instep" und eine Unterdrückung bei den höchsten Energien. Insbesondere das zweite Knie wurde bei $\sim 10^{17}$ eV von mehreren Observatorien als Versteilerung des Spektrums beobachtet. Seine Deutung könnte mit der maximalen Energie der Beschleunigungsorte in der Galaxie zusammenhängen, da bei diesen Energien eine allmähliche schwerere Zusammensetzung beobachtet wurde, die den sogenannten Peters-Zyklen entspricht. Die astrophysikalische Interpretation der gewonnenen Daten ist immer noch heikel, vor allem weil die Art der Quellen, die Ausbreitungseffekte und die Zusammensetzung der kosmischen Strahlung stark miteinander verwoben sind. Ein genaueres Verständnis des Ursprungs des zweiten Knies könnte möglich sein, wenn ein Observatorium in der Lage ist, alle spektralen Merkmale und die Massenzusammensetzung der kosmischen Strahlung mit einer gemeinsamen Energieskala zu messen.

Das Pierre-Auger-Observatorium im Westen Argentiniens ist das weltweit größte Observatorium für kosmische Strahlung. Ursprünglich wurde es gebaut, um den kosmischen Strahlungsfluss oberhalb von $10^{18.5}$ eV zu untersuchen, doch mehrere Erweiterungen haben diese Energieschwelle gesenkt. Eine dieser Erweiterungen wird in dieser Arbeit vorgestellt.

Um eine wirkliche Interpretation des zweiten Knies zu erreichen, hat das Pierre-Auger-Observatorium seinen Oberflächendetektor um eine dreieckige Anordnung von Wasser-Cherenkov-Detektoren mit einem Abstand von 433 m erweitert, um den Spektralbereich unterhalb von 10^{17} eV zu enthüllen. Unsere Kollaboration hat bereits erste Hinweise auf das zweite Knie aus den Daten des 750-Meter-Oberflächendetektors und aus Messungen des Cherenkov-Lichts mit dem Fluoreszenzdetektor gemeldet. Daher wird diese Erweiterung zum ersten Mal die Messung der drei Spektrumsmerkmale im höchsten Energiebereich nicht nur durch ein einziges Observatorium, sondern mit der gleichen Detektionstechnik ermöglichen.

Das Hauptziel dieser Arbeit ist die Erweiterung des mit dem Oberflächendetektor des Pierre-Auger-Observatoriums gemessenen Energiespektrums bis hinunter zu Energien von $10^{16,5}$ eV. Um dieses Ziel zu erreichen, wurde eine Reihe von Analyseschritten durchgeführt. Zur Charakterisierung der Fähigkeiten des Arrays, Luftschauer aufzuspüren und zu beproben, wurden Studien mit simulierten Schauern durchgeführt, um Trigger-Effizienz-Kurven zu erhalten. Diese Kurven sind ein wesentlicher Bestandteil der Definition der effektiven Exposition des Arrays und der entscheidende Schritt auf dem Weg zu einem endgültigen

Energiespektrum. Der Einsatz des dichteren Arrays erforderte die Optimierung, Erweiterung und Verbesserung des Prozesses zur Ereignisrekonstruktion, der auf einer bereits im Rahmen von Offline existierenden Grundrekonstruktion basiert. Daher beinhaltet diese Arbeit eine umfassende Aktualisierung der Rekonstruktionsmethoden, die zur Abschätzung der Flugbahn und Energie eines kosmischen Strahls unter Verwendung des neuen Oberflächendetektor-Arrays. Die Aktualisierung wurde motiviert durch die Einbeziehung eines neuen Satzes von Detektoren und durch die Produktion eines völlig neuen Datensatzes. Die Standardrekonstruktion von Luftschauern basiert auf einer empirischen Beschreibung der der gesamten lateralen Verteilung von Sekundärteilchen am Boden. Für jedes Ereignis wird die die erwartete Schauergröße in einem bestimmten Abstand zum Schauerkern ein robuster Estimator für die Primärenergie. Der nominell optimale Abstand ist der Abstand zum Kern, bei dem die fehlende Kenntnis der seitlichen Verteilung der Schauer den geringsten Einfluss auf die Schätzung der Schauergröße hat, was bedeutet, dass bei diesem Referenzabstand die Verzerrung des rekonstruierten Signals minimal ist. Der seitliche Abfall des deponierten Signals mit zunehmendem Abstand zur Schauerachse in der Schauer-Ebene wird mit einer lateralen Verteilungsfunktion modelliert, deren Steigung als Funktion der Schauerbeobachtungsgrößen parametrisiert wird, insbesondere der Zenitwinkel und die Schätzung der Primärenergiemessung im optimalen Abstand. Sowohl die laterale Verteilungsfunktion, die zur Anpassung der beobachteten Signale als Funktion der Entfernung von der zentralen Achse eines Luftschauers verwendet wird, als auch der optimale Abstand hängen stark vom Abstand zwischen den Stationen ab. Daher haben wir für das 433 Meter dichte Array den Referenzabstand und den Parametersatz für ein optimiertes Anpassungsverfahren aktualisiert, wobei wir auch von dem neuen verfügbaren Datensatz profitierten.

Die seitliche Verteilung ist besonders wichtig, da sie verwendet wird, um das erwartete Signal in einem festen Referenzabstand von der Achse zu finden, um die Primärenergie zu schätzen. Die stark von der Schauerneigung abhängige Energieschätzung Neigung abhängt, wird mit der Constant Intensity Cut-Methode korrigiert, um einen vom Zenitwinkel unabhängigen Energieschätzer zu erhalten. Wir haben festgestellt, dass das 433-Meter-Array, das im Mai 2019 fertiggestellt wurde, kosmische Strahlung mit voller Effizienz ab 3×10^{16} eV beobachtet und damit die Energie, bei der das zweite Knie im Spektrum beobachtet wurde, in den Erfassungsbereich bringt. Infolge der erhöhten Empfindlichkeit für Schauer niedrigerer Energie war es möglich, den kosmischen Strahlungsfluss bis hinunter zu Energien zu messen, die eine halbe Größenordnung niedriger sind als dies zuvor mit dem Oberflächenarray möglich war.

Wir haben ein Energiespektrum der kosmischen Strahlung mit Hilfe des 433 Meter langen Oberflächendetektor-Arrays des Pierre-Auger-Observatoriums erstellt. Das dargestellte Spektrum zeigt einen Knick um $\sim 10^{17}$ eV, wo der Spektralindex des ansonsten monotonen Potenzspektrums seinen Wert ändert, was das Vorhandensein des zweiten Kniespektrums bestätigt. Dieses Merkmal ist wichtig als Signatur für die Änderung des Ursprungs und/oder der Arten der ankommenden kosmischen Strahlung.

Wir haben das resultierende Energiespektrum mit den Ergebnissen anderer Experimente verglichen. Die hier vorgelegte Studie legt den Grundstein für zukünftige Messungen im Energiebereich bis hinunter zu 10^{16} eV mit einem Oberflächendetektor und erweitert damit den wissenschaftlichen Output des Auger Observatoriums.

Resumen

La detección del espectro de energía de los rayos cósmicos con detectores de superficie abarca más de seis órdenes de magnitud en energía, desde 10^{15} eV hasta más de 10^{20} eV. El espectro de energía sigue una ley de potencia con un índice espectral $\gamma \simeq 3$ que presenta cinco características identificadas por pequeñas desviaciones en el índice espectral: la rodilla, la segunda rodilla, el tobillo, el "instep" y una supresión en las energías más altas. En particular, la segunda rodilla ha sido observada a $\sim 10^{17}$ eV por varios observatorios como un empinamiento del espectro. Su interpretación puede estar relacionada con la energía máxima de los aceleradores en la Galaxia, teniendo en cuenta que se ha observado una composición gradualmente más pesada a estas energías, lo que está en la línea de los llamados ciclos de Peters. La interpretación astrofísica de los datos adquiridos sigue siendo delicada, principalmente porque la naturaleza de las fuentes, los efectos de propagación y la composición de los rayos cósmicos están fuertemente entrelazados.

El Observatorio Pierre Auger, situado en el oeste de Argentina, es el mayor observatorio de rayos cósmicos del mundo. Aunque originalmente se construyó para estudiar el flujo de rayos cósmicos por encima de $10^{18,5}$ eV, varias mejoras han reducido este umbral de energía. En este trabajo de tesis se va a presentar una de esas mejoras. Una comprensión más precisa del origen de la segunda rodilla puede ser posible si un observatorio es capaz de medir todas las características espectrales y la composición de la masa de los rayos cósmicos con una única escala de energía. En este sentido, el Observatorio Pierre Auger amplió su Detector de Superficie con el despliegue de un arreglo triangular de detectores Cherenkov en agua espaciados a 433 m para desvelar la región espectral por debajo de 10^{17} eV. Nuestra Colaboración ya informó de algunas pruebas preliminares de la segunda rodilla a partir de los datos del detector de superficie de 750 metros y de las mediciones de la luz Cherenkov con el detector de fluorescencia. Por lo tanto, el arreglo de 433 metros permitirá por primera vez medir las tres características del espectro UHE no sólo con un único observatorio sino con la misma técnica de detección.

El objetivo principal de esta tesis es ampliar el espectro energético medido con el detector de superficie del Observatorio Pierre Auger hasta energías de $10^{16,5}$ eV. Para lograr este objetivo, se han llevado a cabo varios pasos de análisis. Para caracterizar las capacidades del arreglo para detectar y muestrear lluvias de rayos cosmicos, se realizaron estudios de simulaciones para obtener curvas de eficiencia de trigger que son un ingrediente vital para definir la exposición efectiva del arreglo y el paso esencial que dirige un espectro de energía final. El despliegue del arreglo más denso ha requerido la optimización, ampliación y mejora del proceso de reconstrucción de eventos, partiendo de una reconstrucción básica previa ya existente en el marco de $\overline{\text{Off}}\underline{\text{line}}$. Por lo tanto, esta tesis incluye una amplia actualización

de los métodos de reconstrucción utilizados para estimar la trayectoria y la energía de un rayo cósmico utilizando el nuevo arreglo de detectores de superficie. La actualización fue motivada por la inclusión de un nuevo arreglo de detectores y por la producción de un conjunto de datos completamente nuevo. La reconstrucción estándar de las lluvias se basa en una descripción empírica de la distribución lateral global de las partículas secundarias en el suelo. Para cada evento, el tamaño esperado a una determinada distancia del centro de la lluvia es un estimador robusto de la energía primaria. La distancia óptima nominada es la distancia del centro en la que el desconocimiento de la distribución lateral de las lluvia tiene el menor impacto en la estimación del tamaño de la misma, lo que significa que a esta distancia de referencia el sesgo de la señal reconstruida es mínimo. La caída lateral de la señal depositada, con el aumento de la distancia del eje de la lluvia en el plano de la misma se modela con una función de distribución lateral cuya pendiente se parametriza en función de los observables de la lluvia, especialmente el ángulo cenital y la estimación de la medición de la energía primaria a la distancia óptima. Tanto la función de distribución lateral utilizada para ajustar las señales observadas en función de la distancia al eje central de la lluvia como la distancia óptima dependen en gran medida de la separación entre estaciones. Por lo tanto, para el arreglo de 433 metros actualizamos la distancia de referencia y el conjunto de parámetros para un procedimiento de ajuste optimizado, beneficiándonos también del nuevo grupo de datos disponibles.

La distribución lateral es especialmente importante, ya que se utiliza para encontrar la señal esperada a la distancia de referencia fija para estimar la energía primaria. La estimación de la energía fuertemente dependiente de la lluvia, se corrige utilizando el método de corte de intensidad constante para producir un estimador de energía independiente del ángulo cenital. Descubrimos que el arreglo de 433 metros, completado en mayo de 2019, observa los rayos cósmicos con plena eficiencia a partir de 3×10^{16} eV, poniendo así dentro del rango de detección la energía a la que se ha observado la segunda rodilla en el espectro. Como resultado de la mayor sensibilidad a las lluvias de menor energía, fue posible medir el flujo de rayos cósmicos hasta energías medio orden de magnitud inferiores de lo que era posible anteriormente con el arreglo de superficie.

Construimos un espectro de energía de los rayos cósmicos utilizando el arreglo de detectores de superficie de 433 metros del Observatorio Pierre Auger. El espectro presentado muestra una inflexión alrededor de $\sim 10^{17}$ eV, donde el índice espectral del espectro de ley de potencia, por lo demás monótono, cambia de valor, confirmando la presencia de la segunda característica espectral de rodilla. de ley de potencia cambia de valor, confirmando la presencia de la segunda característica espectral de rodilla. Este rasgo es importante como firma del cambio de origen y/o tipos de rayos cósmicos que llegan. Comparamos el espectro energético resultante con los resultados de otros experimentos. Este estudio sienta las bases para futuras mediciones en el rango de energía tan bajo como 10^{16} eV con un detector de superficie, ampliando así la producción científica del Observatorio Auger.

Contents

---

[1] ultra-high energy cosmic rays

---

[2] 750 m SD vertical
[3] 433 m SD infill
[4] Auger Muon Detectors for the Infill Ground Array

CHAPTER 1

Cosmic rays

1.1 Historical overview

After the discovery of radioactivity at the end of the 19th century by Becquerel, the general opinion was that the ionization of air is mainly caused by radiation of radioactive elements in the ground. After some similar, but not as widely known, attempts by scientists like Pacini in the years before, in 1912, Victor Hess measured the ionization of air up to a height of 5300 m using enhanced electrometers carried into the atmosphere with balloons [1, 2].

Figure 1.1: Victor F. Hess, center, departing from Vienna about 1911, was awarded the Nobel Prize in Physics in 1936. Between 1911 and 1912, Victor Franz Hess made ten balloon trips carrying electroscopes to determine the source of the atmospheric radiation. This photograph shows him in the ascent to nearly 4900 m realized in August of 1912. Credits to 'Victor Franz Hess Society', Schloss Pöllau, Austria.

The Fig. 1.1 shows Hess in one of these ascents. In contrast to the leading opinion, he found a rising ionization with increasing atmospheric height. He assumed that there might be an extraterrestrial source of high energy radiation that ionizes particles in earth's atmosphere. By performing his measurement during a near-total eclipse, he also found out that the sun is not the unknown source. Hess's discovery started the era of cosmic ray (CR[1]) physics and in 1936 he received the Nobel Prize in Physics for his work.

Since their discovery, CRs have never ceased to arouse interest [1]. The mysteries related to their existence always led to significant experimental efforts in building new detectors. Many of the great discoveries in particle physics came from the observation of cosmic rays. Indeed, positrons, muons and pions, were discovered measuring this "radiation coming from above" [3–5]. It was shown that the primary cosmic rays are mainly protons and always particles with positive charge [6] and that, at ground level, most of the observed particles are photons and electrons (the electromagnetic component) or muons.

In 1938 Pierre Auger made his great discovery: positioning particle counters at roughly the same height above sea level with a certain distance between them, would trigger sometimes simultaneously. This experiment demonstrated that some particles were arriving in groups at the surface of the Earth, and that the observed particles were secondaries from a common source. Pierre Auger was the first to conclude that particles, detected in time coincidence, were secondary particles produced from a single (primary) particle, interacting with the air molecules creating cascades of secondary particles further interacting with the atmosphere until they reach the surface of the Earth. Such cascades, with billions of particles, are distributed over areas of 10-100 square kilometres, hence the name Extensive Air Showers (EASs[2]) [7].

Auger and his colleagues realized that particles exist in Nature with very high energies, above 10^{15} eV and beyond at a time when the highest observed energies were of a few MeV in radioactive phenomena. In 1949, Enrico Fermi proposed a mechanism of acceleration based on the interaction with the interstellar magnetic fields to explain how these particles acquired such energy [8] According to this mechanism, particles would gain energy by colliding with a moving magnetized plasma cloud. The original Fermi theory was modified in 1954 [9], proposing a more efficient acceleration process in which particles would be accelerated in successive encounters with large astrophysical shock waves, reaching energies up to 10^{15} eV. In Sec. 1.2.3 and 1.2.3 both models are described.

After the discovery of high energy particles, large arrays of detectors were developed to study extensive air showers. The first measurements of energy and arrival direction of cosmic rays above 10^{15} eV were carried out in 1954 by the Rossi Cosmic Ray Group of the University of Massachusetts using an array of 11 scintillation detectors arranged in a circle of 230 m radius. Between 1954 and 1957, the cosmic-ray energy spectrum was extended to 10^{18} eV with data provided by the Agassiz Station at Harvard [10].

In the sixties, the largest detector array had been installed by the MIT group at Volcano Ranch (New Mexico). It was covering an area of 12 km^2 with 20 stations in a triangular grid, and it showed the existence of UHECRs by observing an incredibly large air shower generated by a 10^{20} eV particle in February 1962. The particle energy was twice as high as the energy of the most energetic particle measured before [11]. From these and similar works, it was concluded that the energy spectrum of the primary cosmic rays extended beyond 10^{20} eV. The energy spectrum and its features are described in Sec. 1.4.

In 1966, Greisen [12], Zatsepin and Kuz'min [13] calculated that there should be a significant suppression of the ultra-high energy cosmic ray flux at the highest energies (see also Sec. 1.4.1). The reason is the interaction at energies above 5×10^{19} eV protons traveling through outer space begin to interact with the cosmic microwave background, the photonic remainder of the big bang, producing secondary pions. This interaction degrades the proton energy, preventing particles with energies greater than $\sim 5 \times 10^{19}$ eV to be observed at

---

[1] cosmic ray

[2] extensive air showers

distances greater than $\sim$ 100 Mpc[3]. The suppression of cosmic rays with higher energies is known as the GZK[4] cut-off and it will be discussed in Sec. 1.4.1.

Since the mid 1940s, counters were primarily made exploiting scintillator materials. Alternative instruments were constructed using a medium, such as water, in which particles generate light through the Cherenkov effect. Such detectors, were developed in the fifties and some years after, physicists have turned also to the possibility of observing the light generated by the fast secondary particles in the atmosphere itself. Atmospheric fluorescence light, was observed by W. Galbraith and J.V. Jelley in 1953 [14], and subsequent studies brought important advances in cosmic-ray research. As this fluorescence light signal is very weak, it can only be observed during dark nights, limiting the uptime for this detection technique. Then, to avoid this problem, Jelley himself started to consider the option to change the frequency of observation from the optical to the radio band. The conclusion he reached by considering this option was not encouraging at all, but the theoretical results of G.A. Askaryan in 1962/1963 led him to make a great discovery in 1964: the first observation of radio pulses from extensive air showers [15]. Despite the initial success, the radio-detection technique of cosmic rays was abandoned because of technical difficulties and because interest moved to cm radiation. For this reason, in the subsequent years, all experiments aiming to observe UHECRs were exploiting mainly two approaches: detection of secondary particles at the ground level, and detection of the atmospheric-fluorescence light. In the first category fall big air-shower arrays such as Haverah Park [16], and AGASA [17]. Whilst, in the second one, it is worth to mention the Fly's Eye experiment [18], famous for having observed a cosmic-ray event with an energy of 3×10^{20} eV, also known as the "Oh-My-God" particle [19]. On the one hand, more events with energies higher than the GZK cut-off were detected by various experiments and on the other hand experiments like HiRes found evidence of this suppression around 6×10^{19} eV, leaving the situation unresolved. The inconclusive experimental proof about the existence of the GZK cut-off was a main reason for the design of a new Observatory. In 1995 an international group of researches started designing the Pierre Auger Observatory, a hybrid cosmic-ray observatory based on both detection techniques mentioned above to measure particles at highest energies with increased precision and exposure, allowing us to solve contradictions related to the measured energy spectra. Its construction began in 2000 and after the successfully detected radio signals from EAs by the LOPES [20] and CODALEMA [21] radio-antenna arrays, in 2010 started the installation of the Auger Engineering Radio Array(AERA[5])of the Observatory. Further suiting the hybrid conception of the Observatory, other enhancements have been installed at the Observatory site as the Auger Muon and Infill for the Ground Array (AMIGA) detector, the High-Elevation Auger Telescopes (HEAT[6]) and the addition of scintillator detectors as the upgrade of the already existing surface detectors. Thanks to these additional detection techniques, measuring the cascades generated by CRs, it is possible to maximize the amount of information about the primary particles. Nowadays, cosmic rays remains a subject of study and debate because the astrophysical mechanisms that accelerate particles at energies 10^{20} eV have not been fully explained, nor the details of the observed spectrum that would be generated in its propagation, nor the mass composition and the he Pierre Auger Collaboration will push towards a breakthrough in UHECR research; for the first time in history we shall be able to simultaneously measure most of the observables of the primary particle, such as its energy, incoming direction, and muon content.

---

[3] One parsec (pc) is equivalent to 3.2616 light years or 3.0857×10^{16} m.

[4] Greisen–Zatsepin–Kuzmin

[5] Auger Engineering Radio Array

[6] High Elevation Auger Telescopes

1.2 Cosmic ray acceleration

Since the detection of two cosmic-ray showers with energies above 10^{20} eV [22], the origin and the nature of the highest energies known in nature have been the subject of strong interest and intense discussion. It seems reasonable to take the most energetic astrophysical objects in the Universe, characterized by surrounding matter in the state of plasma and by the presence of intense magnetic fields, as perfect candidate to explain these high observed energies. The origin of UHECRs continues to be an unsolved problem. Generally, two scenarios have the attention of the scientific community: the so called top-down and *bottom-up* scenarios. In the first case, Ultra-High Energy Cosmic Rays (UHECRs) are produced by the decay of super-massive exotic particles released e. g. from topological defects (possibly created in cosmological phase transitions) or dark-matter candidates while, in the second case, UHECRs are nothing but ordinary particles accelerated by astrophysical sources to extreme energies. In the first scenario, photons are expected as primaries, which data hacve indicated to be unlikely [23]. On the one hand, the motivation for some of the more exotic scenarios may have diminished by newest data while on the other hand conventional shock have been favored by the large-scale anisotropy in the cosmic-ray arrival directions above 8×10^{18} eV reported by the Pierre Auger Collaboration [24], although such acceleration mechanisms in astrophysical objects pushes the present theoretical ideas to their extreme. A brief review of the mechanisms that could accelerate particles up to high energies (10^{20} eV) at galactic and extragalactic astrophysical sites is presented. These mechanisms must fulfil a series of general requirements, which include geometric and energetic constraints. Among these, the Hillas criterion, a geometrical constraint on the size of the acceleration region, is most useful in selecting potential sources of cosmic rays.

1.2.1 General constraints on acceleration sites

The purpose of this subsection is to give a brief description of the general constraints on acceleration sites. In order to be considered as a possible source of ultra-high-energy cosmic rays (UHECRs), an astrophysical object has to fulfil several conditions [25]:

- **geometry** the accelerated particle should be maintained within the object during the acceleration process;
- **power:** the source should be able to provide the necessary energy for the accelerated particles;
- **radiation losses:** within the accelerating field the energy gained by a particle should be no less than its radiation energy loss;
- **interaction losses:** the energy lost by a particle due to its interaction with other particles should not be greater than its energy gain;
- **emissivity:** the density and power of sources must be enough to account for the observed UHECR flux;
- **coexisting radiation:** the accompanying photon and neutrino flux, and the low-energy cosmic-ray flux, should not be greater than the observed fluxes (this constraint must be satisfied by the flux from a single source and by the diffuse flux)

1.2.2 The Hillas criterion

If a particle escapes from the region where it was being accelerated, it will be unable to gain more energy.

This situation imposes a limit on its maximum energy ϵ_{max} acquired by a particle passing in a medium with magnetic field B that can be expressed as follows:

$$\epsilon_{\mathrm{max}} = ZqBR \tag{1.1}$$

where q is the electric charge of the accelerated particle, B is the magnetic field, R is the size of the accelerator and Z the atomic number of the particle. Eq. 1.1 is obtained by demanding that the Larmor radius of the particle not exceed the size of the acceleration region $R_L = \epsilon_{\mathrm{max}}/(ZqB) \leq R$. This is a general geometrical criterion known as the *Hillas criterion* for all types of cosmic ray sources.

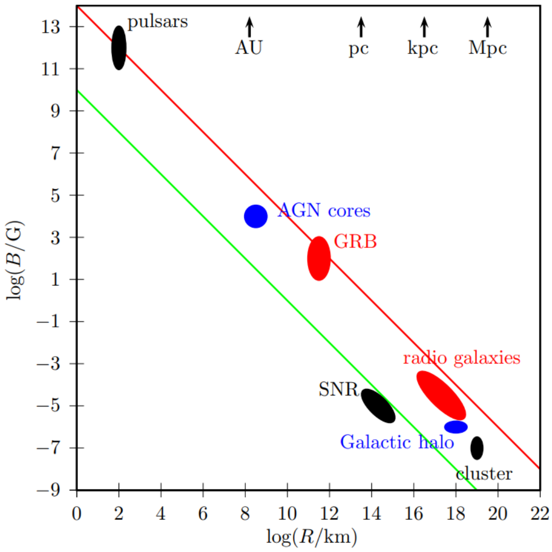

Figure 1.2: Hillas plot. Magnetic field strength versus size of various suggested cosmic ray sources. Sources above the top (red) line are able to accelerate protons up to 10^{21} eV, while sources above the bottom (green) line are able to accelerate iron up to 10^{20} eV. Figure reproduced from [26]

Neglecting energy losses, i.e., the accelerator is 100% efficient, we see that for a given maximum energy ϵ_{max} of the accelerated particle only the parameters R and B can describe the source, showing a relationship between the strength of the magnetic field and the size of the sources as displayed in Fig. 1.2. Sources above the top line are able to accelerate protons up to 10^{21} eV, while sources above the bottom line are able to accelerate iron up to 10^{20} eV. A more realistic description of particle acceleration takes into account the energy lost during the process. The maximal energy that a particle can get in an accelerator of infinite size if energy losses are accounted for is determined by the condition

$$\frac{d\epsilon^{(+)}}{dt} = -\frac{d\epsilon^{(-)}}{dt}, \tag{1.2}$$

i.e., the situation where energy lost and gained is equal. Depending on particular conditions in the accelerator the maximum energy ϵ_{max} of the particle is limited either by geometrical or by energy-loss arguments, hence it is given by the minimum between the value obtained from this equality and the one obtained from the Hillas criterion:

$$\epsilon_{\mathrm{max}} = min\left\{\epsilon_{\mathrm{H}}, \epsilon_{\mathrm{loss}}\right\} . \tag{1.3}$$

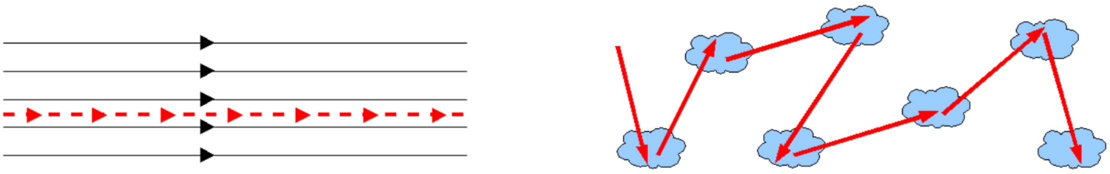

(a) One-shot (b) Diffusive shock

Figure 1.3: Inductive acceleration mechanisms.

1.2.3 Main acceleration processes: bottom-up models

The *bottom-up* scenarios are the conventional astrophysical models which focus the explanation on the existence of active objects to accelerate particles and thus, generating the cosmic rays. Depending on the scenario of acceleration, we will consider inductive (one-shot, or direct) and diffusive (stochastic) mechanisms (see e.g. Ref. [27] for a general discussion of these two approaches to UHECR acceleration). In the first case, the process takes place in intense electric fields, such as those found in compact objects like neutron stars or black hole accretion discs. In the second case, nuclei are accelerated in magnetized plasma, such as shock wave systems in supernova remnants (SNRs[7]).

Inductive acceleration Back in 1930s, Willam F. G. Swann pointed out that particle acceleration may take place in the increasing magnetic field of a sunspot [28]. The extension of this accelerating mechanism to astrophysical objects, such as the rapidly-rotating highly-magnetized neutron stars (pulsars), active Galactic nuclei (AGNs[8]) or radio-active galaxies, is the so called "one-shot" acceleration and occurs when a particle is accelerated in a continuous way by an ordered field [see Fig.1.3(a)]. Radiation losses from accelerated charged particles moving at relativistic velocities are composed of two terms [25], attributed to synchrotron and curvature radiation. In the synchrotron-dominated losses regime, the maximum energy is given by

$$\epsilon_{\rm s} = \sqrt{\frac{3}{2}\frac{m^2}{q^{3/2}}}B^{-1/2}\,, \tag{1.4}$$

where B is the strength of the magnetic field, and m, q are the mass and charge of the particle, respectively.

In the special case when $\vec{v} \parallel \vec{E} \parallel \vec{B}$, curvature losses dominate. This might be the situation in the vicinity of neutron stars and black holes. The corresponding maximum energy is

$$\epsilon_{\rm c} = \frac{3^{1/4}}{2}\frac{m^2}{q^{1/4}}B^{1/4}R^{1/2}\,. \tag{1.5}$$

Pulsars are formed when the core of a massive star collapses to a neutron star during a supernova. Young pulsars, such as the Crab or the Vela [29], with surface magnetic field in the $10^{12} - 10^{14}$ G range can accelerate iron cosmic rays through relativistic hydro-dynamical winds to greater than $\sim$ 1020 eV [30]. The electric fields are located in regions of high energy densities, and thus the cross section for synchrotron radiation is high. Therefore, the accelerated particles would interact and subsequent formation of cascades of electron-positron pairs would reduce the efficiency of such acceleration processes. The maximum attainable energy for charged particles in this environment is in the order of 10^{15} eV [31]. It

---

[7] supernova remnants

[8] active galactic nuclei

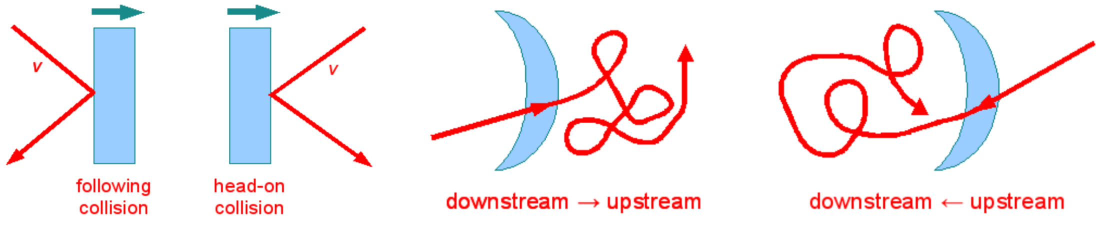

(a) Second-order Fermi acceleration (b) First-order Fermi acceleration

Figure 1.4: Fermi acceleration mechanisms. On the left: particles would acquire energy due to collisionless scatterings with randomly moving inhomogeneity of the turbulent magnetic field, a process which resembles the acceleration of a ball bouncing elastically between two rigid walls that approach each other. On the right: In this model particles can be accelerated by a shock wave front propagating through interstellar space .

has also been proposed the conjecture that the central engines of AGNs, the supermassive black holes (BHs[9]) with mass $\sim 10^8 10^{10} \mathrm{M}_\odot$, where $\mathrm{M}_\odot = 1.98 \times 10^{30}$ kg is the mass of the Sun) with magnetic fields $\mathrm{B} \sim 10^4 - 10^6$ G , could operate as powerful particle accelerators up to $\sim 10^{20}$ eV [32]. The direct acceleration mechanisms are, however, not widely favored these days as the cosmic-ray acceleration mechanism. A major disadvantage of the mechanism is that it is difficult to obtain the characteristic power-law spectrum of the cosmic rays in any natural way [33].

Diffusive acceleration In this mechanism the particle is accelerated in bursts, as a result of its interaction with regions of high magnetic field intensity, as shown in Fig. 1.3(b). The maximum energy, considering synchrotron-dominated losses, is

$$\epsilon_{\mathrm{d}} = \frac{3^{3/4}}{2} \frac{m}{q^{1/4}} B^{1/4} R^{1/2} , \tag{1.6}$$

Diffusive acceleration, and in particular Fermi acceleration is the preferred acceleration mechanism in bottom-up scenarios of cosmic-ray production.

Second-order Fermi acceleration The most plausible theories on cosmic-ray acceleration are based on the Fermi mechanisms, which have firstly been introduced in 1949 by Enrico Fermi [34]. This first version of the Fermi acceleration mechanism (later dubbed second-order acceleration) explains the acceleration of relativistic particles by means of their collision with interstellar clouds. These clouds move randomly and act as 'magnetic mirrors', so that the particles are reflected off them, as shown in Fig. 1.4(a).

After many encounters, although in each individual encounter the particle may either gain or lose energy, it can be shown [35] that the average energy gain ΔE per collision is

$$\left\langle \frac{\Delta E}{E} \right\rangle = \frac{8}{3} \beta^2 , \tag{1.7}$$

where $\beta = V/c$ is the ratio between the speed of the cloud and the speed of light. Due to the quadratic dependence of the average energy gain on β, the process is known as "second-order" Fermi acceleration mechanism. Then, the acceleration timescale of this process can be calculated as:

$$t_{\mathrm{acc}} := \frac{E}{\langle dE/dt \rangle} \simeq \left\langle \frac{E}{\Delta E} \right\rangle \cdot \tau_{\mathrm{col}} \simeq \frac{3}{4\beta^2} \frac{\lambda}{c} = \frac{3\lambda}{4c} \left(\frac{c}{V} \right)^2 , \tag{1.8}$$

---

[9] Black holes

with $\tau_{\text{col}} = c/\lambda$ the mean time two collisions and λ the average distance between two interactions (mean free path) [36]. From above an acceleration rate can be derived:

$$\frac{1}{t_{\text{acc}}} = \frac{1}{E}\left\langle\frac{dE}{dt}\right\rangle\frac{4}{3}\frac{c}{\lambda}\beta^2 , \tag{1.9}$$

leading to an energy rate of:

$$\left\langle\frac{dE}{dt}\right\rangle = \frac{E}{t_{\text{acc}}} = \frac{4c}{3\lambda}\beta^2 E = \alpha E , \tag{1.10}$$

It is possible to find the energy spectrum $N(E)$ considering this energy rate plus the assumption that τ_{esc} is the characteristic time for a particle to remain in the accelerating region as:

$$N(E)dE = const. \times E^{1+\frac{1}{\alpha\tau_{\text{esc}}}} dE \implies N(E) \propto E^{-\alpha} \quad \text{with} \quad \alpha = 1 + \frac{t_{\text{acc}}}{\tau_{\text{esc}}} , \tag{1.11}$$

thus succeeding in deriving a power-law energy spectrum.

Even though second-order acceleration succeeds in generating a power-law spectrum, it is not a completely satisfactory mechanism and it has at least two disadvantages. First, the energy gain is too slow. Even around supernovae, we have $V/c \sim 10^4$, and second-order processes are simply too inefficient to account for the presence of high energy cosmic-rays. In fact, the acceleration is too slow even to compete with ionization losses if one were to begin from low energies. Second, this process can in fact produce a power-law energy spectrum. However, the power-law index is unconstrained (determined by the uncertain value of the combination $\alpha\tau_{\text{esc}}$) and can presumably be any value, in contrast with observations that typically indicate a power law index between 2 3. On the other hand, second-order Fermi process may be responsible for the re-acceleration of existing population of non-thermal particles. For instance, radio halos in some galaxy clusters are likely produced by turbulent re-acceleration of mildly-relativistic electrons via the second-order Fermi process.

First-order Fermi acceleration For many years, the second-order Fermi mechanism was considered the only possible way to accelerate particles, despite the difficulties associated with it. In the late 1970s [37], Blandford & Ostriker (1978) and Bell (1978) realized that Fermi acceleration can achieve first order around shock waves.

Before we discuss first-order Fermi acceleration it is convenient to formulate the Fermi mechanism in a more general and simple way, valid for both the second- and first-order versions. For that purpose, we suppose that initially, there are N_0 particles with initial energy E_0. Let $E = AE_0$ be the average energy of the particle after one collision, and P be the probability that the particle remains in the acceleration region after one collision. After n collisions, we have $N = N_0 P^n$ particles with energies $E = E_0 A^n$. In other words, after sufficient number of collisions, the cumulative particle energy distribution (number of particles with energy larger than E) becomes

$$N(\geq E) = N_0 P^{\ln(E/E_0)/\ln A} = N_0 \exp\left[\ln\frac{E}{E_0}\cdot\frac{\ln P}{\ln A}\right] = N_0\left(\frac{E}{E_0}\right)^{\ln P/\ln A} . \tag{1.12}$$

Hence the energy spectrum results in a power-law distribution

$$N(E)d(E) = \text{const.} \times E^{-1+\ln P/\ln A} , \tag{1.13}$$

with power law index

$$s = 1 - \frac{\ln P}{\ln A} . \tag{1.14}$$

Our previous analysis shows that $A = 1 + (4/3)V/c$. The parameters P and A can be translated into the ones that were found for the Fermi second-order mechanism, and are also going to be applied to the first-order one. The goal of the first-order acceleration mechanism is to obtain an energy gain that is linear in (V/c), a condition that would make the acceleration process more effective, especially at relatively high values of V. This set-up will occur when the relativistic particles collide with strong shock waves (e.g., like those produced in supernova explosions, active galactic nuclei, etc.), which can reach supersonic velocities (10^3 times the velocity of an interstellar cloud). Let us consider a shock propagating in the x direction. We first work in the shock frame, where the plasmas enter the shock from upstream with velocity V_u from right to left, and are adverted downstream with velocity V_d. Let r be the shock compression ratio. By mass conservation, we have

$$V_d = \frac{1}{r} V_u \,. \tag{1.15}$$

The velocity difference between the upstream and downstream flow is given by

$$V = V_u - V_d = (r-1)V_d = \frac{r-1}{r} V_u \,. \tag{1.16}$$

Since $r > 1$, this means the plasma flow is converging across the shock front. Consider CR particles in the vicinity of the shock front. These particles are largely collisionless and travel at velocities much larger than the shock velocity. Correspondingly, they barely feel (directly) the existence of the shock, but mainly respond to electromagnetic fluctuations in the plasma. We assume that both the shock upstream and downstream plasmas are sufficiently turbulent, so that the CR particles experience efficient scattering by such turbulence and get isotropized with respect to the upstream/downstream fluid that they reside. Consequently, there is a complete symmetry when a high-energy particle crosses the shock from downstream to upstream or from upstream to downstream; this is illustrated in Fig. 1.4(b). In both types of crossing, the particle gains energy. It is possible to show [35] that the mean energy gain at every shock crossing is

$$\left\langle \frac{\Delta E}{E} \right\rangle = \frac{2}{3}\frac{V}{c} \,. \tag{1.17}$$

Since particles are reflected twice per cycle (from upstream to downstream and then back to upstream), the mean energy gain per cycle is

$$\left\langle \frac{\Delta E}{E} \right\rangle_{cycle} = \frac{4}{3}\frac{V}{c} \,. \tag{1.18}$$

The mechanism is more efficient for greater confinements of the particles, which can be easily achieved if the magnetic fields are increasingly intense. In particular, this situation is favored when the direction of the magnetic field is parallel to the front of the shock wave. The complementary situation, where the magnetic field is perpendicular to the front of the collision, allows the particles to diffuse away from the region thus reducing confinement and decreasing the efficiency of the acceleration mechanism. Assuming a typical value for the shock wave speed of 0.1 and particles with energies $\sim 10^{18}$ eV, the acceleration time is $\sim 10^6$ yr. Consequently, this process of acceleration by shock waves is several orders of magnitude faster than the second-order model.

Another quantity that must be considered is the particle escape probability P. To estimate P, let us again work in the frame of the shock. Let J_+ be the flux of CR particles entering the shock from downstream, J be the flux of CR particles returning to the shock upstream from downstream, and J_∞ be the CR particle flux that escapes into the far downstream (towards infinity). Note that no particle escapes from the shock upstream because the upstream plasma is always advected towards the shock. In steady state, conservation of CR flux requires $J_+ = J_- + J_\infty$. The escape probability is thus given by

$$P = \frac{J_-}{J_+} = \frac{J_-}{J_- + J_\infty} \,. \tag{1.19}$$

Considering $J_- = \frac{nc}{4}$ the flux of particles crossing the shock surface from downstream and assuming an isotropic particle distribution, the escaping CR particle flux is simply given by

$$J_\infty = n_0 V_d \,, \tag{1.20}$$

where n_0 is the CR particle number density in the vicinity of the shock front.

Therefore, we obtain

$$P = \frac{c}{c + 4V_d} \approx 1 - \frac{4V_d}{c} \,. \tag{1.21}$$

Note that we assumed $V \ll c$, hence P is only slightly smaller than 1. In other words, only a tiny fraction of particles escape from the diffusive shock acceleration (DSA) process per cycle.

Jointly, the power law index of the CR energy spectrum is given by

$$s = 1 - \frac{\ln P}{\ln A} \approx 1 + \frac{3V_d}{V} = 1 + \frac{3}{r-1} \,. \tag{1.22}$$

We see that in the DSA theory, a universal power-law index can be obtained which depends only on the shock compression ratio. For a strong non-relativistic shock, the compression ratio $r = 4$ and then, we arrive at s = 2. Replacing these two parameters in Eq. 1.13, we get

$$N(E)d(E) = \text{const.} \times E^{-2} dE \,, \tag{1.23}$$

close to the cosmic-ray energy spectrum (where $s \sim 2.7$). In spite of not having obtained the observed exponent of 2.7 yet, the first-order mechanism is very promising, being the most effective and probable one, since shock waves are expected to be present in different astrophysical environments. In addition, in contrast to the second-order mechanism, here we find a fixed numerical value for the exponent.

Possible regions of acceleration The cosmic rays must be accelerated to ultra-high energies by electromagnetic processes at extragalactic sites, both because there are no known sites in our Galaxy which can accelerate and magnetically contain them and also because most of the observed cosmic rays arrive from directions outside of the Galactic plane. So far, no astrophysical object has been unambiguously identified as a source for ultra-high energy cosmic rays. Despite the exact acceleration mechanism, there is an argument proposed by Anthony M. Hillas 1.2.2 that limits the source candidates. Hillas noted that any object that accelerates charged particles must have a magnetic field intense enough to confine them for a minimum amount of time, similar to the situation in man-made accelerators such as at CERN. Sometimes the acceleration region itself only exists for a limited period of time; for example, supernovae shock waves dissipate after about 10^4 yr [38]. According to the Fermi model, particles gain an amount of energy that is proportional to their current energy per acceleration cycle, where a cycle is the passage of the particle from the non-shocked part to the shocked part of the medium and back. At each cycle, there is a finite probability for the particle to leave the acceleration region, and start its interstellar journey. Therefore, such an acceleration process is gradual, and particles performing as many as possible (irregular) loops in the accelerating region would gain the highest energies. The maximum achievable per-particle energy $\epsilon_{\max}$ is governed by the condition that the size L of the accelerating region containing the field must be greater than twice the Larmor radius r_L [39]. The Larmor radius of a relativistic particle of charge Ze in a magnetic field B is $r_L = 1.08E/ZB$ pc, where E is the energy of the particle in PeV (= 10^{15} eV) units and B in μG. Taking into account the velocity of the shock front βc, it turns out that L has to be larger than $2r_L/\beta$ [39], and therefore:

$$L \geq \frac{2E}{Z\beta cB} \quad \Longrightarrow \quad \epsilon_{\max} = \beta cZqBL \tag{1.24}$$

This relation, already introduced before (see Eq. 1.1) provides an upper limit of the energy to which particles of a certain charge can be accelerated, given the size of a source and its magnetic field.

For cosmic rays of the highest energies, exceedingly vast sources or extremely powerful magnetic fields are required to accelerate them. Particles with higher charge are easier to confine in the magnetic fields, so they can be accelerated to higher energies. The dimensional argument expressed by Eq. 1.24 is often presented in the form of the famous "Hillas diagram" in Fig. 1.2 which shows candidates for possible accelerator objects depending on the strength of their magnetic field and their characteristic size. It can be seen in the diagram that there are few astrophysical objects capable of transferring an energy of the order of 10^{20} eV to a charged particle, such as pulsars ($B \sim 10^{13}$ G, $R \sim 10$ km),AGNs ($B \sim 10^4$ G, $R \sim 10$ au) and giant radiogalactic lobes ($B \sim 0.1$ μG, $R \sim 10$ kpc). Below the knee ($\simeq 10^{15}$ eV) possible source candidates are the Supernovae. In fact, considering a magnetic field of intensity $B \sim 0.1$ μG and a Larmor radius of ~ 0.1pc, the maximal reachable energy as function of Z is $\epsilon_{\max} \simeq Z \cdot 10^{15}$ eV. Another argument supporting the galactic origin for cosmic rays below the knee, is the comparison between the luminosity of the Supernovae in our Galaxy and the luminosity of low energy cosmic rays, as emphasized long ago by Ginzburg and Syrovatskii [40]. They have shown that only $\sim 1\%$ of the energy emitted by Supernovae is needed to accelerate all the cosmic rays produced inside the Milky Way, supporting the hypothesis that low energy cosmic rays (below the ankle) can be produced in our Galaxy. Following a list of the astrophysical candidate sources, that have been proposed for the acceleration of the highest energy cosmic rays, is provided. The first two candidates are both related to Active Galactic Nuclei (AGNs), Galaxies with a nuclear super-massive black hole with accretion processes running.

Active Galactic Nuclei (AGN) The compact region at the centre of a galaxy whose luminosity exceeds the standard one which have been considered as appealing candidate sources of cosmic rays for the last 50 years [41]. ForAGNs, the engine of the acceleration is the accretion disk of matter orbiting around a super-massive black hole ($10^6 - 10^{10}$ solar masses) in the nucleus of the Galaxy, as shown in Fig. 1.6. Those accretion disks are known to have magnetic fields of the order of few Gauss (~ 5 G) along linear dimensions of 0.02 pc. Those accretion disks are known to have magnetic fields of the order of few Gauss. These parameters are marginally consistent with acceleration up to 100 EeV. The high radiation field around the central engine of an AGNs is likely to interact with the accelerated protons while energy losses, due to synchrotron radiation, Compton processes, and adiabatic losses, will also take place. The situation is worse for nuclei that will photo-disintegrate even faster. For this reason, it is now believed that the inner part of AGNs galaxies could only contribute to accelerating particles up to small fractions of EeV [42].

FR radio Galaxy lobes In Fanaroff-Riley (FR) radio-loud active galaxies, extended lobes of magnetized plasma originate from the central black hole. The lobes are observed mainly in radio through synchrotron emission, and may slowly vanish with distance from

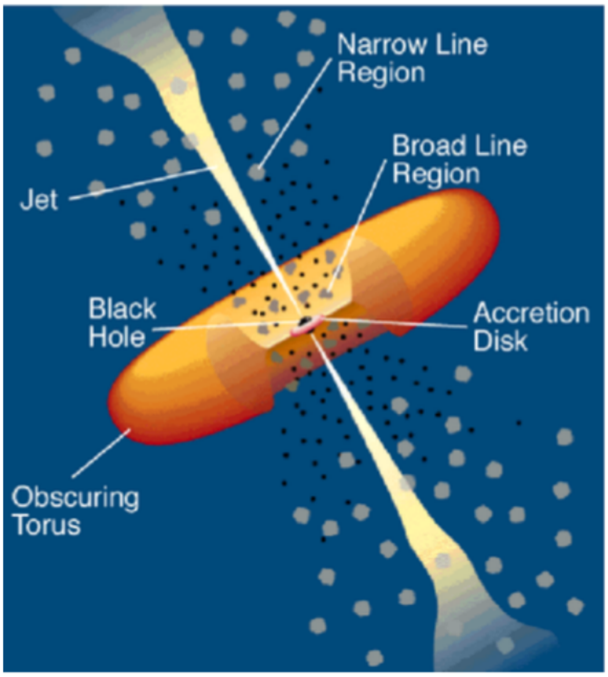

Figure 1.5: Active Galactic Nuclei scheme. It is possible to see the supermassive black hole surrounded by its accretion disk. The jets here represented are typical of Radio Loud AGNs and Blazars, and are not present in every active Galaxy. Figure from [43].

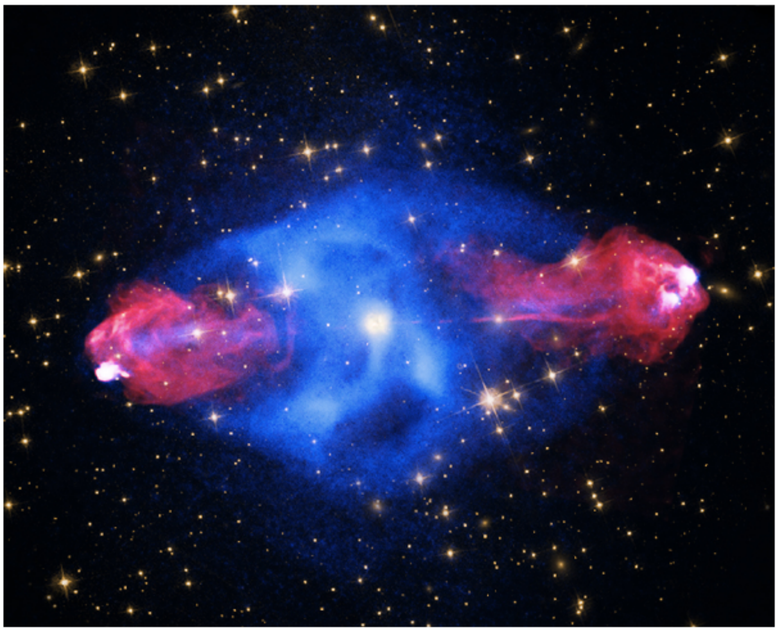

Figure 1.6: The Cygnus A radio-active AGNs. Each color represents a frequency band in the electromagnetic spectrum: X-ray in blue, radio in red and visible in yellow. Radio emission extends to either side along the same axis for nearly $\sim 3 \times 10^5$ light-years powered by jets of relativistic particles emanating from the AGNs. Hot spots likely mark the ends of the jets impacting surrounding cool, dense material [44]

the nucleus or show high density areas called hot-spots at the lobe edges [41]. Lobes usually exceed in size the Galaxy itself with dimensions up to hundreds of kpc. In the lobes, magnetic fields are usually of less than a μG. On the other hand, hot spots are usually of the order of few kpc and show magnetic fields of the order of hundreds of μG. Both the lobes and the hot spots are candidates to accelerate protons up to hundreds of EeV. If the jets are oriented towards the Earth, these objects are usually called ”blazars”. Blazars are much brighter and can be detected at higher distances than radiogalaxies; but, since the jet is collimated, they are much rarer than radiogalaxies. Nevertheless, blazars and radiogalaxies are the same objects and can be equally considered as candidates for UHECR acceleration. The Cygnus A radio Galaxy (3C 405), situated at 232 Mpc with a supermassive black hole of $\sim 25 \times 10^8 M_\odot$ at its center [45], is shown in Fig. 1.6. In contrast to particles accelerated in the inner region of an AGNs, particles accelerated at the end of the jets can leave the acceleration region without large energy losses, since the radiation field is much less dense than in the inner region of the AGNs. However, there is considerable debate as to what values have to be considered for B and L. The magnetic field within the hot spots of the lobes varies from source to source. Additionally, the observed energy spectrum of the cosmic rays (discussed in Sec. 1.4) can be obtained assuming a magnetic field intensity in the local supercluster of about 0.1 μG [46]. Whereas Galactic magnetic fields are reasonably well studied, extragalactic fields are still poorly understood [47]. In general, when these sites are considered more carefully, great difficulties are found due to either energy losses in the acceleration region or the great distances of known sources from our Galaxy (discussed in Sec. 1.3). The mechanisms of energy loss and gain compete in any acceleration site. With Fermi shock acceleration, the acceleration time is proportional to the mean free path for scattering in the shock wave (see Eq. 1.8), which is itself approximately inversely proportional to the magnetic field strength. Therefore, a certain magnitude of B is required, not only to confine the particles within the site, but also to accelerate them quickly. However, if the magnetic field is too strong it can cause charged particles to lose their energy via synchrotron radiation. Other strong energy losses are caused by collisions with photons and/or matter at the acceleration site. This leads to the additional requirement that the site must have sufficiently low densities of radiation and matter. For example, the core regions ofAGNs are ruled out because of this reason. On the other hand, in the regions of space where the magnetic fields are weak the main mechanism that produces energy loss is the interaction with the CMB[10]. This last process is manifested essentially through the photoproduction of pions and pair-production, which are feasible due to the high energy of the protons. As a consequence, a fraction of the energy gained by the acceleration is lost through synchrotron emission and CMB interactions, further limiting the possible candidates for ultra-high energy cosmic-ray sources.

Clusters of galaxies Huge objects originating from the clustering of several galaxies by gravitational interactions. Magnetic fields of the order of μG have been observed and their size can extend up to 500 kpc. This should allow acceleration of UHECRs up to 100 EeV [48].

Compact objects: pulsars and magnetars They are formed when the core of a massive star collapses to a neutron star during a supernova. Those highly magnetized rotating neutron stars emitting beams of electromagnetic radiation are very compact objects in size and their magnetic field are of the order of 10^{12} G. In this case the maximum achievable energy should be $E_{\max} = \omega \cdot Z \cdot B \cdot R^2$ where ω is the spinning velocity of the object, Z the charge of the accelerated particle, B the magnetic field at the surface and R the radius of the object. For example, using values from the Crab Nebula Pulsar shown in Fig. 1.7: $B \sim 10^{12}$G, $R \sim 10$ km, $\omega \sim 200$ Hz, we obtain a maximum energy of about 10^{18} eV for a proton. Objects such as magnetars, characterized by having even stronger magnetic fields (up to 10^{16} G) in comparison to pulsars, are then necessary to explain UHECRs [49].

---

[10] cosmic microwave background radiation

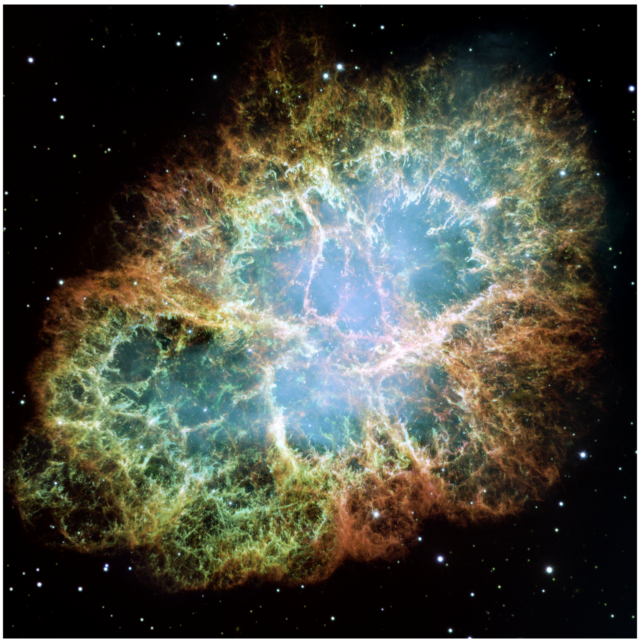

Figure 1.7:]
This is one of the largest ever taken by NASA's Hubble Space Telescope, of the Crab Nebula, a six-light-year-wide expanding remnant of a star's supernova explosion. The orange filaments are the tattered remains of the star and consist mostly of hydrogen. The blue light comes from electrons whirling at nearly the speed of light around magnetic field lines from the neutron star. The Crab Nebula derived its name from its appearance in a drawing made by Irish astronomer Lord Rosse in 1844, using a 36-inch telescope. credits to: NASA, ESA, J. Hester and A. Loll (Arizona State University)

Gamma-Ray Bursts (GRBs) Flashes of gamma rays associated with extremely energetic events that have been observed in the Universe originating in jets. Given the GRBs[11] duration distributions, we can distinguish between two different origins: short (< 1 s) GRBs are possibly the result of the merge of two neutron stars of a binary system into a black hole, while long ($> 1-2$ s) ones have been associated collapsing massive stars. Some GRBs may be also single Soft Gamma-ray Repeaters (SGR[12]), a class of γ-emitting neutron stars. In particular, the accretion disk around the neutron star binary system could be a good site for particles acceleration. The main model used to describe the radiation of the GRBs is the fireball model [50][51] for which the GRBs observable effects are due to the dissipation of the kinetic energy of a relativistic expanding plasma wind whose primal cause is not yet known. According to this model, GRBs should be able to accelerate proton up to the highest energies although they are disfavored as primary UHECR source since the major fraction of them were observed at high redshifts (up to $z = 5$) and the few GRBs observed within the GZK horizon would not explain the observed flux [52].

1.2.4 Non-acceleration processes: Top-down models

The basic idea of a top-down origin of cosmic rays can be found in the precursor to the Big Bang model hipotized by Georges Lemaître [53], who first noted in 1927 that an expanding universe could be traced back in time to an originating single point, which he called the *Primeval Atom*. The entire material content of the Universe and its expansion, according to

---

[11] gamma-ray bursts

[12] Soft Gamma-ray Repeaters

Lemaître, originated from the "super radioactive disintegration" of a single atom of extremely large atomic weight, the Primeval Atom. The cosmic rays were envisaged as the energetic particles produced in intermediate stages of its decay. They were thus "glimpses of the primeval fireworks" *Primeval Atom*. Indeed, Lemaître regarded cosmic rays as the main evident relics of the Primeval Atom in the present Universe. In modern versions of the Primeval Atom, some cosmologists have related the origin of ultra- high energy cosmic rays to other basic ideas beyond the Standard Model.

Top-down models have been proposed to explain the energies of UHECRs, but most of them have been disfavored by experimental results. These models were mainly introduced to explain the spectrum published by the AGASA experiment in 1998, which did not observe the expected GZK cut-off, the energy loss of cosmic rays due to the interaction with the CM ((see Sec. 1.4.1)), at the highest energies [54]. If no GZK cutoff is found to be present in the UHECR spectrum, then either local (within 10 to 50 Mpc) sources of UHECRs must exist [55], or some kind of exotic physics must be invoked to evade the GZK effect. Among exotic possibilities, proposals have included UHECRs composed of exotic hadrons [56], or strongly-interacting neutrinos [57], or that protons can travel super-GZK distances due to a violation of Lorentz invariance [58]. Here the main types of top-down models are introduced.

Z-burst The Z-burst models [59], is based on the idea that ultra-high energy neutrino (ν_{UHE}), generated somewhere in the universe, interact with a background relic neutrino (ν_r) into a Z-resonance which decays into a fermion/anti-fermion pair:

$$\nu_{\mathrm{UHE}} + \nu_r \longrightarrow Z \longrightarrow f\bar{f}\,. \tag{1.25}$$

To generate a Z-resonance with a sizeable cross-section, the energy available in the interaction must be:

$$E_\nu = \frac{M_Z^2}{2m_\nu} = 4.2 \times 10^{21}\mathrm{eV}\frac{1\mathrm{eV}}{m_\nu}\,, \tag{1.26}$$

where M_ZZ is the mass of the boson Z and m_ν is the mass of the neutrino. The fermion/antifermion pair originating from this interaction could thus have a large amount of energy available, in the order of the UHECRs.

Decay of heavy particles In these scenarios γ-rays, leptons and nucleons are expected to be produced at ultra-high energies by the decays of supermassive (mass $\gtrsim 10^{21}$ eV) particles generically called X-particles. The super heavy dark matter (SHDM) models [60][61][62] assume X to be metastable heavy dark matter particles, formed during the inflation stage of the Universe, that are part of the cold dark matter component of DM. As DM density is expected to be higher in the halo of our galaxy compared to the extragalactic medium, the produced flux of UHECRs would originate from close enough to avoid the GZK cut-off on its way to Earth.

Topological defects have also been proposed to generate these heavy particles X [63][64]. Most top-down models have been disfavored by UHE-photons and UHE-neutrinos searches performed on observational data (after the AGASA result) [65][66][67], usually because the observed flux are too low compared to the ones expected by these models.

1.3 Propagation of UHECRs and energy loss

The task of understanding the origin of UHECRs is further made difficult by their propagation through the interstellar medium. During the travel from the source to the Earth, UHECRs suffer interactions with background radiation fields that may affects their characteristics as the kind of particle, the energy that will be detected at Earth and the propagation direction. The study of UHECR propagation across the interstellar space, continuously challenges our understanding of the processes involved, and in general of the Universe as a whole.

Here, only an overview of the processes happening during UHECRs propagation is presented. A detailed description of the interaction processes encountered by the CRs as they propagate through the Universe can be found in [68] and the GZK process, source of cosmogenic photons is discussed in the next subsection. It is important to underline here that pair-production, pion photoproduction and photodisintegration processes all produce high energy photons. The main sources of energy losses for UHECRs are listed below.

1.3.1 Adiabatic energy loss

The adiabatic energy loss due to the expansion of the universe is given by $E = \frac{E_0}{1+z}$, where z is the redshift parameter defined as

$$z = \frac{\Delta\lambda}{\lambda} = \frac{\lambda_1}{\lambda_0} - 1\,. \tag{1.27}$$

The observed photon wavelength λ_1 is increased with respect to the emitted one λ_0; this effect is called cosmological redshift and expresses the fact that the Universe was smaller when the photon was emitted.

1.3.2 Photo-interaction with background photons

Hereafter the interaction with background photons are discussed. In fact, during the travel from the source to the Earth, UHECRs could interact changing their energy and mass. The background photons usually taken into account are the Cosmic Microwave Background radiation (CMB) and the radiations in the infrared, optical and ultraviolet bands, called Extra-galactic Background Light (EBL). The spectral energy distribution of the two photon fields are sketched in Fig. 1.8.

1.3.3 Pair-production loss

The interaction of a charged particle with a background photon can create an electron/-positron pair:

$$N + \gamma \longrightarrow N + e^- + e^+ \tag{1.28}$$

This interaction has a very short mean free path, but it leads to a very small fractional energy loss with inelasticity $\simeq 0.1\%$ which make it not dominant at higher energies.

To obtain the energy threshold for this interaction, we must work in the Lorentz geometry, where the line segment is defined by $ds^2 = c^2dt - dx^2 - dy^2 - dz^2$. We define the four-momentum of a particle to be $P = (E/c, \vec{p})$, where $P^2 = m^2c^2$ is an invariant quantity. In general, the energy threshold for particle production occurs when the initial energy of all particles in the center-of-mass frame is equal to the rest mass of all particles following the interaction. The total energy before the interaction in the center-of-mass frame is given by

$$(E^{\mathrm{CM}}_{\mathrm{total}})^2 = (E^{\mathrm{CM}}_a + E^{\mathrm{CM}}_b)^2 = c^2(P^{\mathrm{CM}}_a + P^{\mathrm{CM}}_b)^2 = c^2(P_a + P_b)^2 \tag{1.29}$$

by virtue of the invariance of P^2 and using $P^2 = m^2c^2$ and $P_aP_b = \frac{E_a}{c}\frac{E_b}{c} - \vec{p_a} \cdot \vec{p_b}$, we obtain

$$(E^{\mathrm{CM}}_{\mathrm{total}})^2 = m_a^2c^4 + m_b^2c^4 + 2E_aE_b - 2(\vec{p_a} \cdot \vec{p_b})c^2\,. \tag{1.30}$$

The energy threshold of this interaction is

$$E_{\text{th}} = m_a c^2 + m_b c^2 + \Delta m c^2 \,, \tag{1.31}$$

where Δm is the difference in rest mass between the incoming and outgoing particles. Setting $E^{\text{CM}}_{\text{total}} = E_{\text{th}}$, we have

$$E_a E_b - (\overrightarrow{p_a} \cdot \overrightarrow{p_b}) c^2 = m_a c^2 m_b c^2 + \Delta m c^4 \left(m_a + m_b + \frac{\Delta m}{2} \right) \,. \tag{1.32}$$

Then, simplifying the Eq. 1.32, we have

$$\frac{E_a E_b - (\overrightarrow{p_a} \cdot \overrightarrow{p_b}) c^2}{m_a m_b c^4} = 1 + \Delta m \left(\frac{1}{m_a} + \frac{1}{m_b} \frac{\Delta m}{2 m_a m_b} \right) \,. \tag{1.33}$$

We can now rewrite the left-hand side of Eq. 1.33 in terms of the Lorentz factor $\gamma = E/mc^2$ and also use $\overrightarrow{p_a} \cdot \overrightarrow{p_b} = |p_a|\,|p_b|\, \cos\theta$ and $p = \sqrt{\gamma^2 - 1} mc$. This leads to

$$\gamma_a \gamma_b - \sqrt{(\gamma_a^2 - 1)(\gamma_b^2 - 1)\cos\theta} = 1 + \Delta m \left(\frac{1}{m_a} + \frac{1}{m_b} \frac{\Delta m}{2 m_a m_b} \right) \,. \tag{1.34}$$

In the case of a proton-photon interaction, where particle b is massless, Eq. 1.32 becomes

$$E_b \left(\gamma_a - \sqrt{(\gamma_b^2 - 1)\cos\theta} \right) = \Delta m c^2 \left(1 + \frac{\Delta m}{2 m_a} \right) \,. \tag{1.35}$$

For relativistic cosmic rays we have $\gamma \gg 1$, thus the Eq. 1.35 produces

$$\gamma_a = \frac{\Delta m c^2}{(1 - \cos\theta) E_b} \left(1 + \frac{\Delta m}{2 m_a} \right) \,. \tag{1.36}$$

The energy required for the interaction is therefore

$$E = \gamma_a m_a c^2 = \frac{[(\Delta m + m_a)^2 - m_a^2] c^4}{2 E_b (1 - \cos\theta)} \,. \tag{1.37}$$

The minimum energy for the interaction occurs in a head-on collision which means that $\theta = 180^\circ$ and then $\cos\theta = -1$. For this case, the Eq. 1.37 reduces to

$$E_{\text{min}} = \frac{[(\Delta m + m_a)^2 - m_a^2] c^4}{4 E_b} \,. \tag{1.38}$$

Using $E_b = \langle E \rangle$ as the average energy of CMB photons, the minimum energy required for electron pair production with a CMB photon to occur is

$$E_{\text{min}} = \frac{[(2 m_e + 2 m_p)^2 - m_p^2] c^4}{4 \langle E \rangle} \,. \tag{1.39}$$

Given the electron mass of 0.511 MeV, $\langle E \rangle = 7 \times 10^{-4}$ eV, and $m_p = 938.272$ MeV$/c^2$, the threshold energy for this process is

$$E_{\text{min}} = 6.9 \times 10^{17}\,\text{eV} \,. \tag{1.40}$$

The mean energy loss for this process is only 0.1% per encounter, compared to 20% for photo-pion production (See Sec. 1.4.1), making photo-pair production a less efficient mechanism

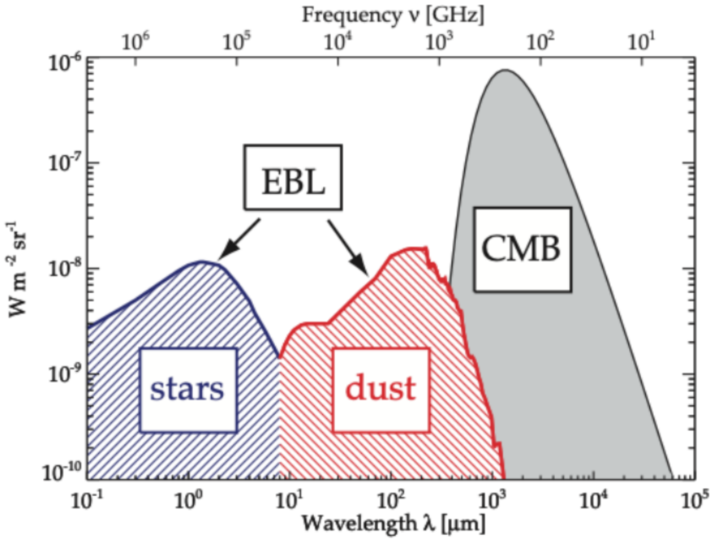

Figure 1.8: Schematic Spectral Energy Distributions of the most important backgrounds in the Universe. From right to left: the cosmic microwave background (CMB), the cosmic infrared background (CIB) and the cosmic optical background (COB). The last two components together are called EBL.

for energy loss [69]. The attenuation length for pair production reaches a minimum of approximately 1000 Mpc at 2×10^{19} eV [64]. In the case of nuclei, since the photon energies in the extra-galactic space are much smaller than nuclear binding energies, the nucleus behaves as a point particle; the cross section is proportional to Z^2 and the inelasticity to $1/A$, so the fractional energy loss rate is Z^2/A times that for a single proton with the same Lorentz factor. This process can happen both on a CMB or a EBL photon. However, the density of EBL photons is considerably lower compared to the CMB, as shown in Fig. 1.8. In addition, at higher energies, the pair production on CMB photons is strongly dominant, hence the EBL contribution to pair production can usually be neglected [70]. Energy loss by pair production begins to dominate below about 3×10^{19} eV [71].

1.3.4 Photo-disintegration of nuclei

Heavier nuclei are affected by the same processes as protons but also by photo-disintegration mechanisms, in which the CR nucleus loses some of its nucleons. These processes include, giant dipole resonance and quasi-deuterium mechanisms. Photodisintegration processes have threshold energies which varies with the mass of the nucleus. The evolution of the contribution to the energy loss of photodisintegration and pair production is shown in Fig. 1.9. For primary cosmic rays with mass number A > 1, the photo-disintegration processes come into play, both with the CMB and CIB, according to the following relation:

$$A + \gamma \longrightarrow (A - nN) + nN\,, \tag{1.41}$$

where a CR nucleus is excited by photons, triggering the emission of one or several nucleons. Given that the energy of the primary nuclei is shared between nucleons, the threshold energy for these processes is typically higher than for proton. The photo-disintegration process leads to the ejection of one or several nucleons N from the nucleus.

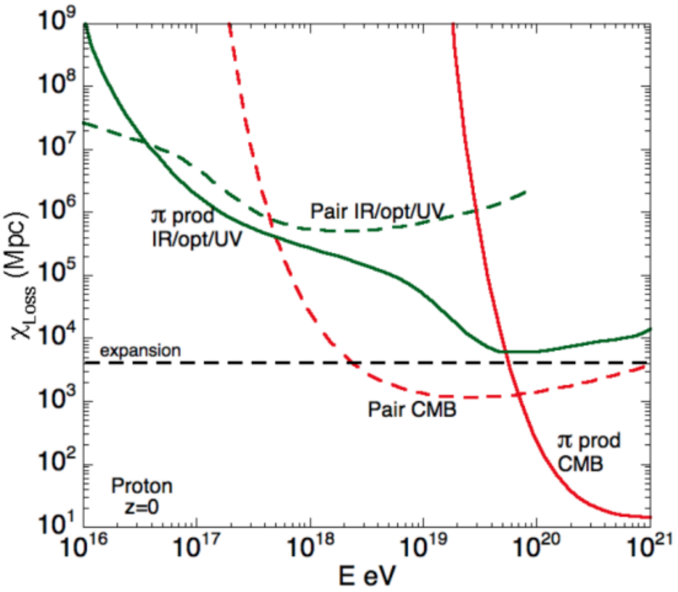

Figure 1.9: Evolution of the energy loss length for an UHE proton at redshift $z = 0$ as a function of its energy. Three processes are represented, the adiabatic expansion of the universe (black dashed horizontal line), the pair production mechanism (dashed curves) and the pion photo-production mechanism (continuous curves). The pair production and pion photo-production mechanism are drawn for interactions of the proton with CMB photons (in red) and for other sources of background photons (IR/opt/UV) (in green). From [72].

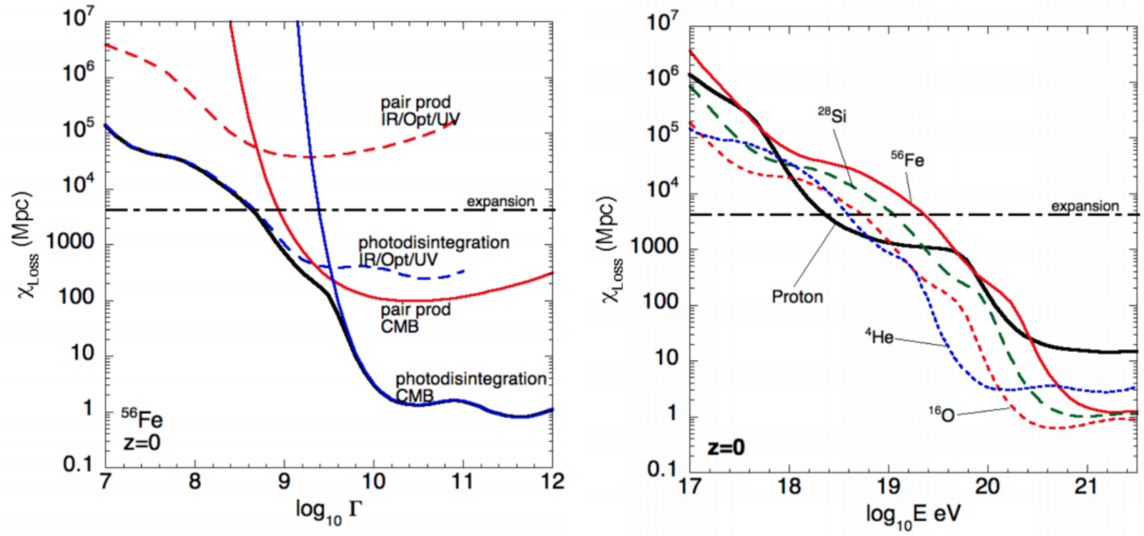

Figure 1.10: Left: Evolution of the attenuation length of iron as a function of the energy at $z = 0$. The contribution of pair production and photodisintegration processes off the CMB and IR/Opt/UV photons are separated. Right: Comparison of the attenuation length of different nuclei at $z = 0$. From [72]

1.3.5 Photo-pion production

Photons with energy in the nucleus rest frame above ~ 145 MeV can interact with nucleons producing pions

$$N + \gamma \longrightarrow N + \pi\,. \tag{1.42}$$

Photo-pion production mechanism is the dominant source of energy loss for the high energy protons and will be discuss further in Sec. 1.4.1.

1.3.6 Magnetic deflection

Another very important phenomenon that affects the UHECRs in their propagation to Earth is their deflections in magnetic fields. It is widely accepted that UHECRs, at least at the highest energies, are of extragalactic origin. Thus, UHECRs will encounter different fields depending on whether they are accelerated in our Galaxy or if they have an extragalactic origin. Extragalactic magnetic fields are still poorly known. They are expected to be rather low, since no convincing mechanism able to generate strong magnetic fields over a wide scale has been discovered. The processes that could generate extragalactic magnetic fields (EGMF) are still being discussed [73][74]. But the lack of observational data prevents a precise modeling of the EGMF and the uncertainties on the deflections of extragalactic UHECRs are high. Galactic magnetic fields are comparatively well known and have been modeled against observational data [75][76]. For galactic magnetic fields, the deflections highly depend on the rigidity of the UHECR. In [77], using the model introduced in [75], the authors have found that the average deflection for UHECRs with rigidity[13] below 10 EV can be beyond 90°. for almost all sources. However, the deflections quickly become less important with higher rigidity, with the deflections thought to behave as $\sim 3^\circ \times Z(E/10^{20}4\mathrm{eV})^{-1}$ [78]. If the deflections are weak enough, the arrival directions of UHECRs should mirror the distribution of the sources.

1.4 Energy spectrum of Cosmic Rays

Cosmic rays are ionized atomic nuclei that travel through the Universe and can be detected on Earth. They span a range of energy from a few 10^8 eV to at least a few 10^{20} eV. Around 1000 CRs $m^2 s^1$ hit the top of atmosphere, of which around ∼90% are protons. The CR flux intensity decreases with increasing energies , following an approximate power law on 12 orders of magnitude in energies and 30 in flux and is well described by a steeply falling power law. The spectrum of high energy cosmic rays has been measured by different experiments focusing on different energy ranges for many years. At low energies (compared to UHECRs), CRs can be observed directly thanks to experiments like BESS [79] and CREAM [80] using air baloons, like PAMELA [81] which uses satellites and on the International Space Station like AMS [82]. At high energies however, CRs have to be detected indirectly, through the observation of the cascades that are produced as they go through the atmosphere . The reason for such a limitation precisely dwells on the cosmic-ray arrival rate, which depends on their energy. If, for instance, one particle with energy of about 10^2 GeV is expected to arrive per square meter per second, then only one particle with energy of $\approx 10^{10}$ GeV will arrive per square kilometer per year.

The differential energy spectrum of CRs follows approximately the power law with increasing energies:

$$\frac{dN}{dE} \propto E^{-\gamma} \tag{1.43}$$

with N the observed number of CRs with energy between E, and $E + dE$ per unit area, solid angle, and time and a nearly constant spectral index $\gamma \sim 3$, meaning that for an increase of energy of one order of magnitude, the flux decreases by approximately 3 orders of magnitude. The value of the spectral index indicates the steepness of the decrease in the spectrum.

---

[13] The rigidity R of a CR represent the effect a magnetic field has on it. For ultra-relativistic particle $R = pc/Ze$, where pc is the relativistic kinetic energy of the particle and Ze its electric charge.

The combined cosmic-ray flux above 10^{13} eV from different experiments is shown in Fig. 1.11 versus the energy. Beware that the flux is scaled by $E^{2.6}$ in order to display the features of the steep spectrum that are otherwise difficult to discern. Three spectral features immediately stand out. The first one occurring at (3 - 5)$\times 10^{15}$ eV with a steepening of the spectrum. The second feature is visible at around 5×10^{18} eV eV with a flattening of the spectrum. The features are known by the name of knee and ankle in the astrophysics community, as the spectrum resembles the shape of a leg. Finally, in Fig.1.11 are shown two additional spectral features: the so-called second knee which appears as a steepening of the spectrum around 10^{17} eV and above energies of $\times 10^{19}$ eV a strong suppression of the flux is visible.

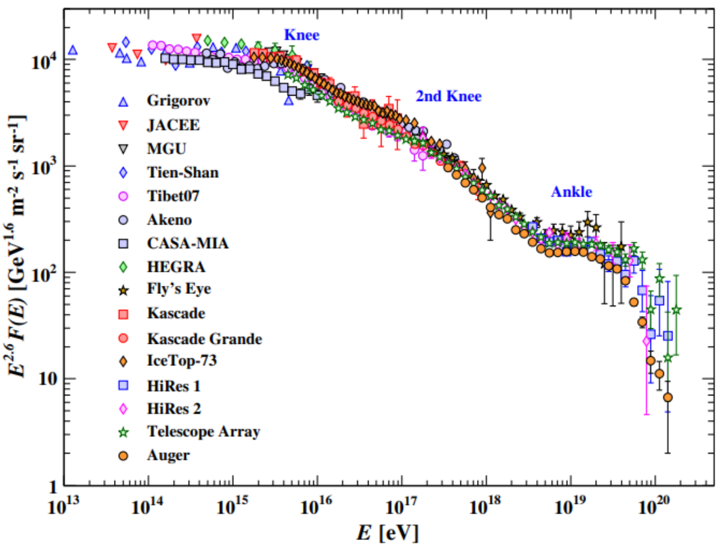

Figure 1.11: Cosmic ray energy spectrum measured from 10^{13} eV to few 10^{20} eV observed with different experiments. The spectral features knee, second knee and ankle are annotated. The features are discussed in the text. The flux has been multiplied by $E^{2.6}$ to get a clear look at the features. The spectrum features corresponding to inflection points around 4×10^{15} eV, 10^{17} eV and 4×10^{18} eV are highlighted with the "Knee", "2nd Knee" and the "Ankle". Taken from [83], see also [84].

1.4.1 Features of the energy spectrum

In Fig. 1.11 the following features are indicated:

- the knee: a steepening of the spectrum at $\approx 5 \times 10^{15}$ eV after which the spectral index γ increases to ~ 3.0;

- the 2nd knee: another steepening of the spectrum at $\approx 10^{15}$ eV, where γ further increases to ~ 3.2;

- the ankle: a flattening of the spectrum at $\approx 3 \times 10^{18}$ eV, here the spectral index γ decreases to ~ 2.7;

- the cutoff at the end of the spectrum: an abrupt suppression of the flux of UHECRs at $\approx 6 \times 10^{19}$ eV, predicted by Greisen [12], and independently by Zatsepin and Kuzmin [13], in 1966.

Certainly, these features are manifestations of significant changes in one or more char- acteristics of UHECRs, such a possible change of the composition, propagation-related effects from the source to the Earth, or the suggested different nature of the sources. In the next Sections, some of the most accredited explanations for such changes of the spectral slope will be summarized.

The knee around 5×10^{15} eV

The first steepening of the spectrum, known as the *knee*, occurs at $\sim 10^{15.5}$ eV, after which the spectral index γ increases from 2.7 to 3.0 [85]. Several scenarios have been proposed to explain the knee-like structure in the all-particle spectrum. A popular explanation of this phenomenon is that for a cosmic ray to get accelerated, the particle must still be confined (at least partially) in the region of acceleration. This means that the gyroradius of the particle may not be larger then the region of acceleration. Above the knee, the light particles are not confined in the regions of acceleration since their Larmor radius is similar to the characteristic length of the shock waves and, therefore, they escape before being accelerated. Accordingly, the composition would tend to become heavier. At energies around the knee, the results of the KASCADE[14] Collaboration show that there is a gradual change in the composition from light to heavy elements [86]. The cosmic rays flux in this region could also be explained by a superposition of power laws (corresponding to the different types of primaries) with dedicated breaks (knees) at different energies[15].

The Second knee around $\times 10^{17}$ eV

Another steepening, less clear than the first and still under discussion, has been observed at $\sim 10^{17.6}$ eV by detectors like HiRes [91], Akeno [92] and KASCADE-Grande around 8×10^{18} eV attributed to a decrease of the flux in the heavy component, just as the knee is supposed to coincide with the extinction of the light component [93]. The break would correspond to a further softening to an index of~ 3.3. It receives the name of *second knee*. If confirmed, the second knee could represent a limit for the acceleration of Galactic heavy elements since between 10^{17} eV and 10^{18} eV eV the Galactic SNRs would cease to be effective accelerators.

The second knee is believed to be caused by the maximum acceleration energy available at the Galactic sources, and by the maximum energies of the magnetic confinement of protons and high$-Z$ nuclei in the Galaxy. The gyro-radii of CRs with energies beyond the second knee in the galactic magnetic field become larger than the size of the Galaxy, and therefore the magnetic confinement of CRs in the Galaxy is no longer effective. Consequently, the CRs of energies above 10^{18} eV, the so-called ultra-high energy cosmic rays (UHECRs), must be of extragalactic origin. Thus, the second knee would correspond to the acceleration limit for the heaviest CRs indicating the energy above which the extragalactic cosmic-ray component becomes dominant. In any case, the mass composition of the primary cosmic rays is the key to describe this transition and rule out acceleration and propagation models.

The ankle around 4×10^{18} eV

Around $\sim 4 \times 10^{18}$ eV, the spectrum retreats by retaking the exponent 2.7 leading to a flattening in the spectrum that the community baptized as *the ankle* of the spectrum. The

---

[14] Karlsruhe Shower Core and Array Detector

[15] The energy spectrum manifests a flattening at about 10^{16} eV, a feature often called low energy ankle, firstly reported by the KASCADE-Grande Collaboration [87], and recently confirmed independently by the Yakutsk [88], IceCube [89] and Telescope Array [90] Collaborations. Its interpretation is still unclear.

ankle can be interpreted as an extragalactic component starting to take over the galactic one at sufficiently high energies [94]. This transition from galactic to extragalactic is located in the range 10^{16} eV-10^{18} eV somewhere in the spectrum between the second knee and the ankle. All theories explaining the knees agree on the galactic origin of the particles measured in this energy range. With increasing energy, the gyroradius of the particles approaches the galactic scale height ($\sim$1 kpc), and the probability that they escape the Galaxy increases. In return, particles originating from outside the Milky Way are likely to enter the Galaxy and reach Earth. Actually, it is still unclear where the Galactic Cosmic Ray (GCR) component ends and the Extra-Galactic Cosmic Ray (EGCR) begins, if one accepts the presence of such a transition. In this case, different interpretations of the ankle are compatible with the observations. To properly describe the GCR–EGCR transition, it is necessary to precisely measure the flux and the composition, also in view of the fact that composition measurements are still model dependent. The presence of the ankle can be interpreted differently. In the following we explain three commonly used models: the dip model [95], the mixed composition model [96], and the ankle model [97]. Fig. 1.12 shows a comparison between the prediction from each of these three models and the measured cosmic-ray spectrum.

The first model we are going to discuss is the dip model (Fig. 1.12(a) which assumes a pure-proton extragalactic component, with the GCR–EGCR transition occurring at the second knee or at least to be completed before the ankle, at an energy of about 1×10^{18} eV. The ankle is then a consequence of propagation effects of a proton-dominated extragalactic flux which interacting with CMB photons produces e^+e^- pairs during. their propagation from the source to the Earth . Thus, the ankle feature is reproduced as a signature of the proton energy losses through the interaction with the CMB photons, during their propagation from the source to the Earth, leading to a flattening of the spectrum.

The mixed composition model, displayed in Fig. 1.12(b), assumes protons with a fraction $\geq$15% of heavy nuclei with mass number A$\leq$56. Here, the galactic component is dominant before the ankle and the transition transition to extragalactic particles takes place at energies above 10^{18} eV. with the ankle appearing as a signature of the transition end, whilst the galactic component requires a higher maximum acceleration energy than the previous model. Finally, the traditional way to reproduce the ankle-feature is to model it as the intersection of a flat extra-galactic component with a steep galactic component. Stated otherwise, the ankle would be the natural signature of the transition to the extra-galactic component of a pure proton spectrum, with the galactic cosmic-ray component extending well several EeV (Fig. 1.12(c)).

A more recent model proposes a mechanism whereby photo-disintegration of ultrahigh energy nuclei in the region surrounding a UHECR accelerator to explain the ankle feature [99]. In this model, extragalactic cosmic rays below the ankle are predominantly protons from nucleons knocked off higher energy nuclei in the region surrounding the accelerator, and the spectrum and composition above the ankle are predominantly dictated by the accelerator and propagation to Earth. The insight underlying the mechanism at the basis of the model, is that photo-disintegration outside the accelerator generally acts as a highpass filter on the energy spectrum of the injected nuclei, permitting the highest energy cosmic rays to escape unscathed while the lower energy ones are disintegrated inside the source region, generating nucleons with energy $1/A$ of the original nucleus of mass A. As we shall see, these spallated nucleons naturally produce the ankle feature giving a natural explanation to a lighter composition below the ankle evolving into a heavy composition above.

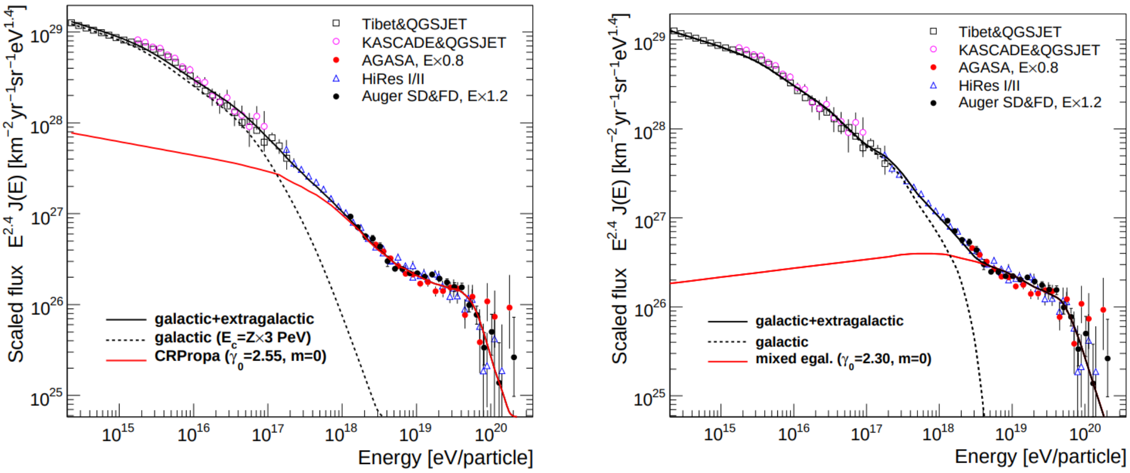

(a) Dip Model (b) Mixed Composition Model

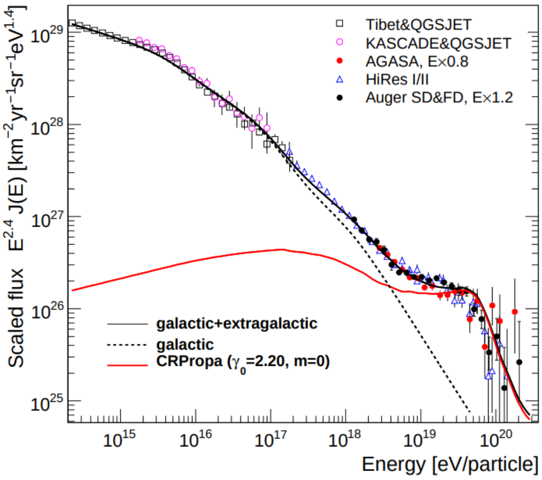

(c) Ankle Model

Figure 1.12: Three scenarios to describe the ankle feature. In the dip scenario 1.12(a) the ankle is a signature caused by the interaction of an extragalactic proton component with the CMB photons producing electron-positron pairs. The mixed composition scenario 1.12(b) assumes a composition similar to the one of galactic CRs and the ankle is associated with the emergence of extragalactic particles. The ankle scenario 1.12(c) is the traditional way to reproduce the ankle-feature modeling it as the intersection of a flat extra-galactic component with a steep galactic component. Image adapted from [98]

The GZK cutoff

After the discovery of the cosmic microwave background (CMB) in 1964, Greisen in the US and Zatsepin and Kuz´min in the USSR investigated the propagation of UHECRs in extragalactic space (Greisen, 1966; Zatsepin & Kuz'min, 1966) and independently realized that high energy protons could interact with CMB photons resulting in energy loss and flux suppression. Photo-pion production is the dominant source of energy loss for the high energy protons. When UHECR protons with sufficient energy propagate through the Universe and interact with the CMB radiation, they produce a Delta resonance. In the decay of the Delta

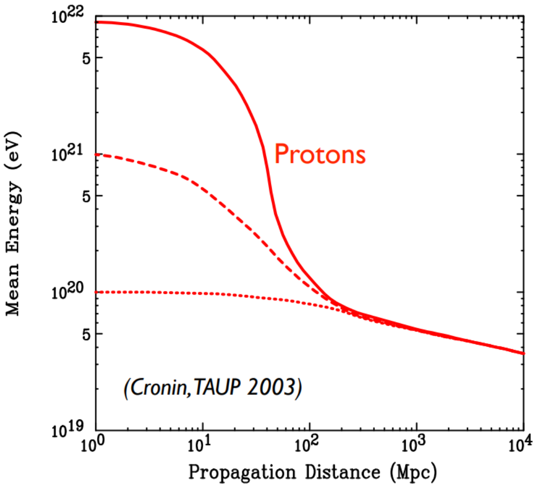

Figure 1.13: Energy losses of nuclei during the propagation due to interactions with the photons of the CMB. The energy loss for proton primaries is shown (reference as stated in the plot)

baryon, a pion is produced, thus taking energy from the primary particle. This resonant process in the case can be expressed as:

$$\begin{aligned} p + \gamma_{\mathrm{CMB}} \quad &\longrightarrow \Delta^{+} \quad \longrightarrow \quad p + \pi^{0} \\ &\longrightarrow \Delta^{+} \quad \longrightarrow \quad n + \pi^{0} \end{aligned} \tag{1.44}$$

From Eq. 1.38, in the case of the photo-pion production mechanism, we have then $m_a = m_p$ and $\Delta m = \Sigma m_\pi$ as the total mass of pions produced. Then, the minimum energy needed for the proton to initiate pion production is given by

$$E_{\mathrm{min}} = \frac{[(\Sigma m_\pi + 2m_p)^2 - m_p^2]c^4}{4\langle E \rangle}\,. \tag{1.45}$$

Using $m_\pi^{\pm} = 139.570\ \mathrm{MeV}/c^2 (m_\pi^0 = 134.977\ \mathrm{MeV}/c^2)$ and $m_p = 938.272\ \mathrm{MeV}/c^2$, we have for the case of single pion production

$$E_{\mathrm{min}} = 1.0 \times 10^{20}\,\mathrm{eV}\,. \tag{1.46}$$

The net effect of these photo-pion production processes is that the proton loses about 20% of its energy with each interaction. Energy loss continues until the proton reaches the so-called " GZK cutoff", which is the name for the expected drop in the UHECR spectrum at the highest energies due to the energy loss in pion photoproduction.

The GZK effect results in a comparable suppression energy due to interactions of protons and iron nuclei with photons of the CMB during the propagation, as in Fig 1.13 and in Fig. 1.10 where the energy loss for proton primaries and the attenuation length of different nuclei depicted over the energy are shown. Around 10^{20} eV the attenuation length for the heaviest nuclei are compatible with those of proton primaries leading to a similar suppression energy.

As UHECR protons propagate through the interstellar medium and continuously experience the above processes, a theoretical upper limit on the energy of cosmic rays from sources can be estimated as $5-6 \times 10^{19}$ eV eV for a distance range of the order of 100 Mpc under the assumption of almost uniformly distributed sources across the Universe [16]. The

---

[16] Apart from the energy loss, a consequence of the GZK effect is a constraint on the maximum propagation distance of extragalactic nuclei.

measured flux of cosmic ray particles supports this theoretical expectation [100]. Moreover, when cosmic rays travel over a distance larger than 50 Mpc and with energies greater than this threshold, they have a small probability of being observed on Earth. This is referred to as the " GZK horizon" as the mean distance beyond which UHECRs cannot arrive on Earth without losing energy. The horizon distance decreases with increasing energy, passing approximately from 200 Mpc at $\approx 5 \times 10^{19}$ eV to 50 Mpc at energies of about 10^{20} eV for UHECR protons.

1.5 Extensive Air Shower Physics

UHECRs induce a cascade of secondary particles when they collide with air molecules high in the atmosphere. The secondary particles, which are products of the first nuclear interaction of a primary CR with the atmosphere, continue to travel down through the atmosphere at nearly the speed of light. These secondary particles produce more particles as they interact with more air molecules, causing the extent of the shower to cover many kilometers across the ground. This phenomenon is referred to as an air shower, and, if such air showers are large enough, they are known as Extensive Air Showers (EASs). With a starting energy of 10 EeV, in EASs about 10^{10} secondary particles are created by interaction or by decay processes at ground level that are spread over an area of order 20 km^2. At the same time, because the energy of the primary CR gets distributed among a swarm of secondaries, this cascade-generating process does not continue indefinitely, and once the available energy per produced particle drops below a certain critical value, ionisation energy-loss processes take over and the number of particles in the shower start to decrease. The minimal energy for an incident primary particle to produce a cascade that reaches ground is about 10^{14} eV With increasing energy of the primary cosmic ray, the number of secondary particles taking part in the shower will increase as well; but, the type of secondary particles that can be created depends on the nature of the primary CR, i. e. on its chemical composition. Most primary CRs are familiar stable subatomic particles that normally occur on Earth, such as protons, atomic nuclei, photons (gamma rays), electrons and neutrinos. The main difference between air showers initiated by different primaries, is the difference in the density of the various secondary particles, which means how many particles of a given type are present in the shower. Within the showers, photons, electrons, and positrons carry about 85% of the total energy; muons carry about 10% of the total energy; pions carry about 4%; and neutrinos carry the remainder. It is possible to identify three major components interplaying in an EAS and based on the Heitler model, they will be discussed in short below.

A Heitler model for the hadronic cascade in air showers has been constructed by Matthews [101]. The Heitler-Matthews model is useful for the explanation of hadronic cascades as well as for the analytical derivation of relations between quantities as primary energy, muon number, electron number and depth of maximum shower size.

1.5.1 Electromagnetic component

In 1954, Heitler presented a very simple model for the development of electromagnetic (EM) cascades. The pure EM showers are composed of only electrons, positrons, and photons, as depicted in Fig. 1.14. Electrons and positrons may radiate one photon by bremsstrahlung after travelling one interaction step length, X, defined as

$$X = X_0^{\mathrm{em}} \ln 2 \,. \tag{1.47}$$

where X_0^{em} is the radiation length in the medium (e.g. in air, $X_0^{\mathrm{em}} \approx 37\mathrm{g/cm}^2$ ([102]), defined as the quantity of atmospheric depth in which an electron gets its energy reduced of a factor

1/e≃0.37 and it is proportional to the interaction step length. It is defined this way so that, on average, the particle loses half of its energy, E, by radiation, as described by

$$\frac{1}{2}E = E^{-X/X_0^{\mathrm{em}}}\,. \tag{1.48}$$

Meanwhile, photons produce an electron and positron through pair production. In general, after one interaction step length, the number of particles is doubled with the energy equally divided between the two outgoing particles. After n interaction step lengths in the atmosphere, the distance travelled is then

$$X_n = nX_0^{\mathrm{em}} \ln 2\,, \tag{1.49}$$

the size of the shower is

$$N_n = 2^n = e^{X_n/X_0^{\mathrm{em}}}\,, \tag{1.50}$$

and the average energy per particle is

$$\langle E\rangle = \frac{E}{2^n}\,. \tag{1.51}$$

The shower development continues until the individual energy of the particles drops below a critical energy, ϵ_{em} (e.g. in air, ϵ_{em} =85 MeV, which means in other words that the average energy at which the shower reaches its maximum is given by $\langle E\rangle = \epsilon_{\mathrm{em}}$. ϵ_{em} is called critical energy and is defined as the value when energy the rate of energy loss of electrons via bremsstrahlung is equal to the rate of energy loss via ionization. Above ϵ_{em}, bremsstrahlung and pair production are more likely to occur than ionization. Below ϵ_{em}, the probability of energy loss by bremsstrahlung or pair production is less than that of ionization, thus ionization is the dominant mode of energy loss. When the average secondary particles are at the ϵ_{em}, the shower reaches its maximum size at a depth, $X_{\max}^{\mathrm{em}}$, in the atmosphere. The depth of the electromagnetic shower maximum, after n_{c} interaction step lengths is given by

$$X_{\max}^{\mathrm{em}} = n_{\mathrm{c}} X_0^{\mathrm{em}} \ln 2\,. \tag{1.52}$$

By definition, at the shower maximum depth, all particle have energy ϵ_{em} leading to a total energy E_0 of

$$E_0 = \epsilon_{\mathrm{em}} N_{\max}\,. \tag{1.53}$$

Follows that the number of partricle at the maximum depth is

$$N_{\max} = \frac{E_0}{\epsilon_{\mathrm{em}}} = 2^{n_{\mathrm{c}}}\,, \tag{1.54}$$

which is proportional to primary cosmic ray energy. From Eq.1.54 we can determine n_{c} as follows

$$n_{\mathrm{c}} = \frac{\ln\left(\frac{E_0}{\epsilon_{\mathrm{em}}}\right)}{\ln 2}\,. \tag{1.55}$$

We can then rewrite the $X_{\max}^{\mathrm{em}}$ in Eq. 1.52 with the total energy E_0 as

$$X_{\max}^{\mathrm{em}} = X_0^{\mathrm{em}} \ln\left(\frac{E_0}{\epsilon_{\mathrm{em}}}\right)\,. \tag{1.56}$$

The Eq. 1.56 and 1.54 suggest that in electromagnetic EAS, the maximum number of particles is proportional to the initial energy ($N_{\max} \propto E_0$) and the depth of shower maximum is proportional to the logarithm of the primary energy ($X_{\max}^{\mathrm{em}} \propto \ln(E_0)$). The logarithmic relation between $X_{\text{max}}^{\text{em}}$ and E_0 has a critical role in identifying the composition of incoming primary cosmic ray particles. From this expression we can also obtain the evolution rate of the depth of the maximum as function of primary energy. This quantity is called elongation rate Λ and is defined as the rate of increase of the mean $X_{\text{max}}^{\text{em}}$ per decade in energy as in

$$\Lambda \equiv \frac{dX_{\text{max}}^{\text{em}}}{d\log_{10} E_0}, \tag{1.57}$$

finding that, after applying Eq. 1.56, the elongation rate of the EM shower in air is

$$\Lambda^{\text{em}} = 2.3X_0^{\text{em}}. \tag{1.58}$$

We can see that the elongation rate is dependent upon the radiation length of the medium. For a pure EM shower in air, the elongation rate is about 85 g/cm^2. The Heitler model for the electromagnetic shower is just a first approach in the EAS analysis. It makes multiple assumptions as that all the cross-sections of the processes are treated as independent of the energy of particles, while in reality, the cross-section depends on the energy of particles, collision energy losses are neglected, and the energy distribution of particles, it is assumed to be equally divided over the secondary particles, which in reality is highly inhomogeneous. Nonetheless, it correctly reproduces the proportionality between the shower size, defined as the maximum number of particle N_{max} during the shower propagation, and the primary energy E_0. Furthermore, it provides a logarithmic relation between $X_{\text{max}}^{\text{em}}$ and E_0, suggesting that the nuclear species of the primary particle initiating an EAS can be determined by observing the longitudinal development of the shower.

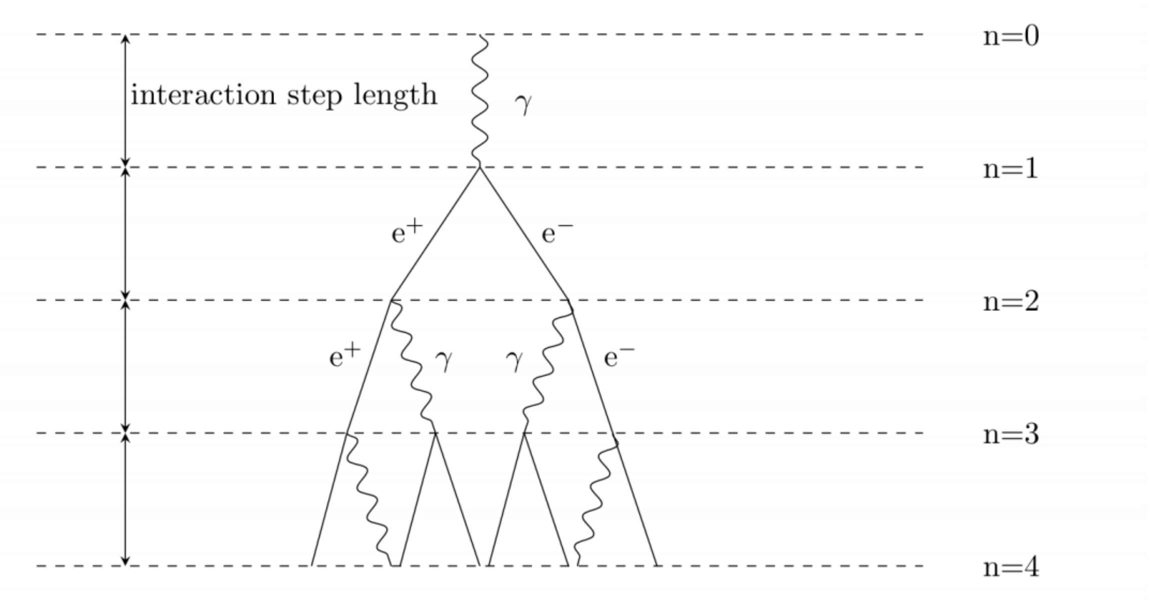

Figure 1.14: Schematic view of an electromagnetic cascade induced by a cosmic ray photon. A high energy photon initiates the cascade by pair production of an electron and a positron. Each lepton then creates a gamma ray via bremsstrahlung; the gamma rays then pair produce, which creates another electron/positron pair; and so forth.

1.5.2 Hadronic component

The hadronic EAS can be induced by either a proton or heavier nucleus. In both cases, the first interaction happens when the primary particle hits an atmospheric nucleus, such as nitrogen or oxygen and produces pions ($\pi^{\pm}, \pi^{0}$), kaons ($K^{\pm}$), and secondary nuclei with significant fractions of the primary particle energy. The secondary particles continue interacting in the atmosphere as long as they have sufficient energies and small interaction lengths. Neutral pions immediately decay into two photons $\pi^0 \to \gamma\gamma$, feeding the electromagnetic component of the air shower. The $\pi^{\pm}$ decay into muons and neutrinos $\pi^{\pm} \to \mu^{\pm}\nu$. The produced neutrinos have essentially no interactions while carrying away a significant amount of the primary energy. Charged kaons also produce muons and neutrinos $K^{\pm} \to \mu^{\pm} + \nu$ or charged and neutral pions $K^{\pm} \to \pi^{\pm} + \pi^{0}$. These two interactions have a branching ratio of 63.5% to 21.2% ([103]). The pion and kaon interactions produce the most important observable part of the EAS, the muon. Muons have a relatively large interaction length and lifetime of $\sim 2.2 \times 10^{-6}$s.

In a Heitler-like model, the development of hadronic showers is similar to the development of electromagnetic showers, which is based on a very approximate model which divides the atmosphere into layers of fixed thickness X as depicted in Fig. 1.15. The interaction mean free path of the incoming primary cosmic ray is described as

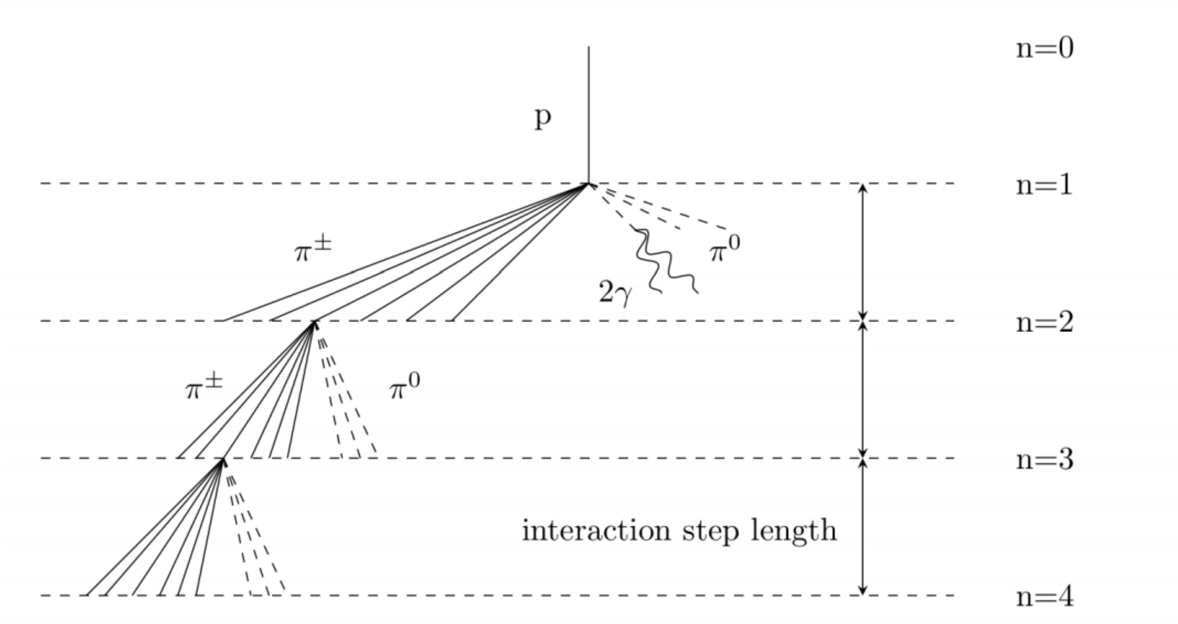

Figure 1.15: Schematic view of a hadronic cascade induced by a cosmic ray proton. At each interaction step length, charged pions are created and keep interacting until their energy is equal to the critical energy and neutral pions are produced and quickly decayed to photons, producing electromagnetic sub-showers. The dashed line indicates neutral pions and the solid line indicates charged pions

$$\lambda = \frac{A}{N_A \rho \sigma}, \tag{1.59}$$

where λ is the mean free path of the cosmic ray through the atmosphere, A is the mass number of the nucleus, N_A is Avogadro's number, ρ is the density of the atmosphere, and σ is the cross-sectional area for the collision. When the primary particle travels an interaction step length, it many secondary particles, mostly pions. The interaction step length, X, previously introduced as the thickness of each layer of atmosphere, can be defined as

$$X = X_0^{\text{had}} \ln 2 \,. \tag{1.60}$$

where X_0^{had} is the nuclear interaction length in the medium, given by 35 $\text{g/cm}^2 A^{1/}3$ (one interaction length in air $X_0^{\text{had}} \approx 90\text{g/cm}^2$ ([102]) and $X_0^{\text{had}} \approx 120\text{g/cm}^2$ for pions in the atmosphere ([104])). The model assumes X_0^{had} is constant, which is a fairly good approximation for interactions between 10 and 1000 GeV. The secondary particles are all created with an equal amount of energy, regardless of the number of interaction step lengths traversed. As discussed previously, π^0 decays to photons and initiates electromagnetic showers immediately. On the other hand, the $\pi^\pm$ will travel through another layer and interact. This process will continue until $\pi^\pm$ reach a critical energy ϵ_π and decay to muons and neutrinos. In other words, when the energy of the charged pions is below the critical energy, it is difficult for them to travel another atmospheric layer. This critical energy, ϵ_π, and the number of interactions depend on the initial energy of the incoming primary cosmic ray particle. Therefore, the hadronic showers are a combination of electromagnetic cascades induced by the neutral pions and hadronic cascades induced by the charged pions. The electromagnetic portion continues to grow via the neutral pions feeding it and the reminder is due to the charged component. Here, ϵ_π is considered to be 20 GeV and N_{ch} = 10 appropriate in the range from 1 GeV to 10 TeV. We assume a proton with an initial energy E_0 hits the atmosphere. After n_{c} interaction step lengths, there will be $N_\pi = (N_{\text{ch}})^n$ charged pions. In this model, if the energy is divided equally in all pions, every hadron produces N_{ch} charged pions and $N_{\text{ch}}/2$ neutral pions in each interaction per layer. The charged pions carry an energy of $2/3E_0$ and the neutral pions carry the remainder of the total energy, $1/3E_0$. After the n^{th} interaction step lengths the energy of the charged pion is the critical energy, therefore

$$E_{n_{\text{c}}} = \frac{E_0}{\left(\frac{3}{2}N_{\text{ch}}\right)^{n_{\text{c}}}} = \epsilon_\pi \,. \tag{1.61}$$

The number of interactions n_{c} before $E_{n_{\text{c}}}$ falls below the critical energy ϵ_π may be determined rearranging Eq. 1.61 as

$$\begin{aligned}
\frac{E_0}{\epsilon_\pi} &= \left(\frac{3}{2}N_{\text{ch}}\right) \\
\ln\left(\frac{E_0}{\epsilon_\pi}\right) &= n_{\text{c}} \ln\left(\frac{3}{2}N_{\text{ch}}\right) \\
n_{\text{c}} &= \frac{\ln\left(\frac{E_0}{\epsilon_\pi}\right)}{\ln\left(\frac{3}{2}N_{\text{ch}}\right)} \\
&= 0.85 \ln[E_0/\epsilon_\pi] \,.
\end{aligned} \tag{1.62}$$

Since the number of produced muons in the $\pi^\pm$ decay is the same as the charged pions, the primary energy can be estimated by the energy carried by pions and electromagnetic particles. Then, the relation between the total energy and the number of electrons or the number of muons is linear and in air has the form

$$E_0 = \epsilon_{\text{em}} N_{e^\pm} + \epsilon_\pi N_\mu \approx 0.85(N_{e^\pm} + 24N_\mu)\ \text{GeV} \,. \tag{1.63}$$

Here, Eq. 1.63 points out that understanding the relation between the number of muons and primary cosmic ray energy is important in order to predict the missing energy that is carried by muons. So, the primary energy can be calculated by measuring the $N_{e^\pm}$ and N_μ regardless of the primary particle type and fluctuation. We can estimate the number of muons by considering the number of charged pions. Remembering that at each interaction, $N_{\rm ch}$ charged pions are created and when they fall below the critical energy, ϵ_π, the charged pion decays into one muon and one neutrino as $\pi^+ \to \mu^+ + \nu$ or $\pi^- \to \mu^- + \bar{\nu}$ and considering Eq. 1.62, the number of muons created in the shower can be expressed as

$$N_\mu = N_{\pi^\pm} = (N_{\rm ch})^{n_{\rm c}} = (N_{\rm ch})^{\ln\left(\frac{E_0}{\epsilon_\pi}\right)/\ln\left(\frac{3}{2}N_{\rm ch}\right)} \Rightarrow \ln N_\mu = \ln\left(\frac{E_0}{\epsilon_\pi}\right)^\beta . \tag{1.64}$$

In the above, β is defined as $\ln N_{\rm ch}/\ln\left(\frac{3}{2}N_{\rm ch}\right)$ telling us that the number of muons is proportional to a power law of the primary energy with a spectral index $\beta : N_\mu \approx (E_0)^\beta$. Eq. 1.64 can be rewritten as

$$N_\mu = (N_{\rm ch})^{0.85\ln[E_0/\epsilon_\pi]} = (E_0/\epsilon_\pi)^{0.85} \approx 10^4\left(\frac{E_0}{\rm PeV}\right)^{0.85} . \tag{1.65}$$

The number of electrons can be obtained as a function of primary energy as

$$N_{e^\pm} \approx 10^6\left(\frac{E_0}{\rm PeV}\right)^{1.03} . \tag{1.66}$$

We can use this to estimate the fraction of energy in the hadronic cascade. The fraction of energy that goes into a hadronic cascade is related to the missing energy that muons and neutrinos take from the shower and is not observable. The energy of a hadronic cascade $E_{\rm h}$ is

$$E_{\rm h} = N_\mu \epsilon_\pi = (N_{\rm ch})^{n_{\rm c}}\epsilon_\pi . \tag{1.67}$$

We can then write the total energy as

$$E_{\rm h} = \left(\frac{3}{2}N_{\rm ch}\right)^{n_{\rm c}} \epsilon_\pi , \tag{1.68}$$

which gives us the energy fraction of the hadronic cascade as

$$\frac{E_{\rm h}}{E_0} = \frac{(N_{\rm ch})^{n_{\rm c}}\epsilon_\pi}{\left(\frac{3}{2}N_{\rm ch}\right)^{n_{\rm c}}\epsilon_\pi} = \left(\frac{2}{3}\right)^{n_{\rm c}} . \tag{1.69}$$

Eq. 1.69 tells us that showers with higher primary energies, which travel through a greater number of atmospheric layers, have smaller hadronic components. In order to determine the depth at which the maximum size of the hadronic cascade occurs, $X_{\rm max}$, we have to take into considerations the depth of the maximum shower development of the EM sub-shower of a hadronic cascade, knowing that after the first interaction length $\frac{1}{2}N_{\rm ch}$ neutral pion are produced and decay in $N_{\rm ch}$ photons as $\pi^0 \to 2\gamma$. The energy of the EM shower initiated by each photon is

$$E_{\rm em} = \frac{\frac{1}{3}E_0}{N_{\rm ch}} = \frac{E_0}{3N_{\rm ch}} . \tag{1.70}$$

Then, the maximum size of the electromagnetic component of the shower generated by the interaction of cosmic ray protons with the atmosphere, $X^{\rm p}_{\rm max}$, can be calculated as follows

$$\begin{aligned} X^{\rm p}_{\rm max} &= X^{\rm p}_0 + X^{\rm em}_0 \ln\left(\frac{E_0}{3N_{\rm ch}\epsilon_{\rm em}}\right) \\ &= X^{\rm p}_0 + X^{\rm em}_0 \ln\left(\frac{E_0}{\epsilon_{\rm em}}\right) - X^{\rm em}_0 \ln\left(3N_{\rm ch}\right) . \end{aligned} \tag{1.71}$$

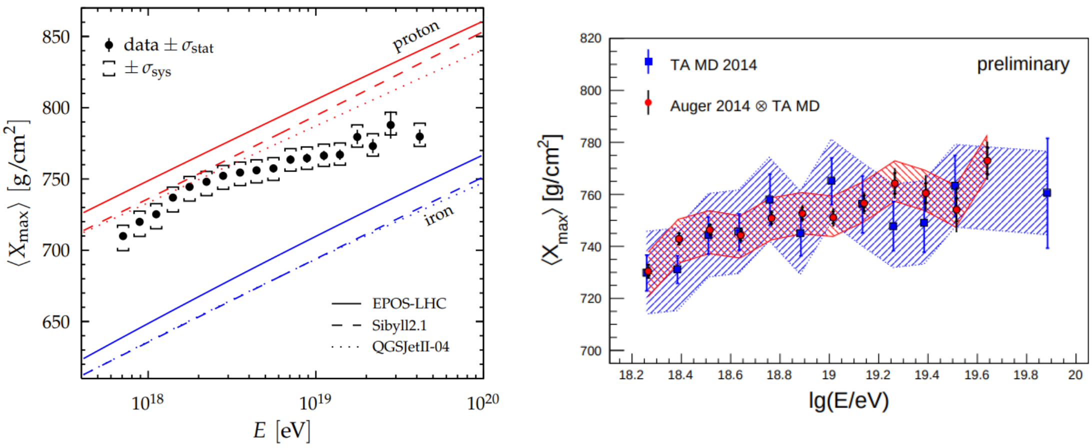

(a) (b)

Figure 1.16: Energy evolution of the average depth of the shower maximum. In 1.16(a) The Auger data is compared with predictions from air-shower simulations for proton- and iron-initiated showers to air-shower simulations using current hadronic interaction models [105]. In 1.16(b) The comparison of $\langle X_{\text{max}} \rangle$ as measured with the Middle Drum detector of TA[17] (blue squares) and the $\langle X_{\text{max}} \rangle$ of the Auger data folded with the MD acceptance (red circles). The measurements agree within their uncertainties [106].

Using Eq. 1.56 we obtain

$$X^{\text{p}}_{\text{max}} = X^{\text{p}}_0 + X^{\text{em}}_{\text{max}} - X^{\text{em}}_0 \ln\left(3N_{\text{ch}}\right) . \tag{1.72}$$

Eq. 1.72 tells us that $X^{\text{p}}_{\text{max}}$ is composed of the first interaction length of the primary proton, the depth of maximum development of the EM sub-shower, and the number of charged pions produced ater the first interaction in the hadronic cascade, providing a clue on the primary particle composition.

The elongation rate Λ^{p} of an hadronic shower may be determined by means of the E. 1.57 as

$$\begin{aligned} \Lambda^{\text{p}} &= \frac{dX^{\text{p}}_{\text{max}}}{d\log_{10} E_0} \\ &= \frac{dX^{\text{p}}_0}{d\log_{10} E_0} + \Lambda^{\text{em}} - \frac{d\left(X^{\text{em}}_0 \ln(3N_{\text{ch}})\right)}{d\log_{10} E_0} . \end{aligned} \tag{1.73}$$

By employing the inelastic proton-air cross-section and proton-proton multiplicity data, we can find that $\Lambda^{\text{p}} \sim 58\ \text{g/cm}^2$ in air per decade in energy [101]. Nevertheless, the proton-air cross-section that affects the full air shower development depends on the energy of the incoming primary cosmic ray particle. The cross-section rises with energy and results in different shower maximums, constraining the composition of primary particle. Until now, we have only considered protons as primary particles but if the primary particle is a heavier nucleus than proton, then superposition approximation can be used. In a simple model, heavier nuclei can be considered as the superposition of many nucleons, meaning a nucleus with mass number A and total energy E_0 can be represented by A individual showers in which each nucleon has energy E_0/A. The A showers are all starting at the same point and superposed. The number of muons, N^A_μ, can be estimated using Eq. 1.64 as below

$$N^A_\mu = A\left(\frac{E_0/A}{\epsilon_\pi}\right)^\beta = \left(\frac{E_0}{\epsilon_\pi}\right)^\beta A^{1-\beta} = N^{\text{p}}_\mu A^{1-\beta} = A^{0.15} N^{\text{p}}_\mu , \tag{1.74}$$

where the A exponent of 0.15 results mainly from the fraction of pions that are charged ($\approx 2/3$) [101]. The depth where it reaches the maximum size in the atmosphere, $X^A_{\rm max}$ can be obtained from Eq. 1.72 as

$$\begin{aligned} X^A_{\rm max} &= X_0^{\rm p} + X_0^{\rm em} \ln\left(\frac{E_0/A}{3N_{\rm ch}\epsilon_{\rm em}}\right) \\ &= X_0^{\rm p} + X_0^{\rm em} \ln\left(\frac{E_0}{3N_{\rm ch}\epsilon_{\rm em}}\right) - X_0^{\rm em}\ln A \\ &= X^{\rm p}_{\rm max} - X_0^{\rm em}\ln A\,. \end{aligned} \tag{1.75}$$

Eq. 1.75 indicates that air showers starting by heavy nuclei will reach maximum development higher in the atmosphere than a proton-initiated air shower. In the case of iron nuclei, the shower contain about 40% more muons than a proton showers at the same total energy. More over the depth of maximum size for iron-initiated showers becomes about 80-100 g/cm^2 shallower, which means that it is reached earlier and and higher in the atmosphere. In other words, protons are expected to have the longer interaction mean free path, resulting in wider distributions, while heavier nuclei, e.g. iron nuclei, have a shorter interaction mean free path, resulting in a more reliable and narrow distribution. Thus, the depth when the showers reach the maximum size is a critical estimator of the composition of incoming cosmic rays. The mass composition is a key observable used to understand the features present in the energy spectrum. As the depth of the shower maximum, $X_{\rm max}$, differs for different primary species,it is well-suited to discriminate particles by their primary mass. The evolution of $X_{\rm max}$ with energy as measured by Auger is depicted in Fig. 1.16.

1.5.3 Development of Air-Showers

First of all, we are going to introduce the quantities that will be used all along this work which define the dynamics of Air-Shower development in order to simplify the following discussion. The general structure of an EAS is schematically shown in Fig. 1.17.

- ***zenith angle θ:*** is the incidence angle of the primary particle with respect to the vertical ($\theta = 0$) and it can be determined from measurements of the arrival time of the particles on the plane of observation;

- ***shower axis:*** the direction of motion of the primary CR initiating the air shower or in other words, the extension of the initial momentum vector of the incident primary in the direction of cascade propagation. Experimentally its interception with the plane of observation is reconstructed from the measured lateral density distribution of the shower particles.

- ***shower core:*** the central region of an air shower around the shower axis, where the particle density is highest;

- ***shower front:*** the particle disk of finite thickness that can show a slight curvature depending on the primary energy and direction of incidence. The particle disk is where all the produced secondaries lie and becomes wider at greater radial distances from the shower axis because of larger fluctuations in the path length due to increased scattering at lower energies and because of lower Lorentz factors of the parent nucleons, responsible for the local sub-cascades. The bulk of particles arrives in a narrow time interval, from only a few nanoseconds in the vicinity of the shower axis to some ~ 10 ns at larger distances from the shower core.

- ***atmospheric depth X [g/cm^2]:*** has been already introduced before in Sec. 1.5.1 It is a measure of the amount of traversed atmospheric matter per unit area in the vertical column of air, by an air shower from its top ($X = 0$). For inclined trajectories, one uses the expression slant depth $X_s \approx X \sec\theta$ g/cm^2.

Longitudinal Profile As mentioned before an air shower is a cascade of particles generated by the interaction of a single high energy primary cosmic ray particle with the atmosphere. The secondary particles produced in each collision in case of a primary hadron mostly charged and neutral pions, may either decay or interact with another nucleus, thereby multiplying the particles within an extensive air shower. Thus, various types of particles can be created and each type of particle interacts differently during their travel to the ground through the atmosphere. More over, on the kinetic energy of each particle depends whether this particle will continue to generate new particles, or rather will be absorbed. The shape of the extensive air shower longitudinal profile contains information about the nature of the primary cosmic ray. However, with the current detection capabilities, the assessment of this quantity in an event-by-event basis is still very challenging. The longitudinal profile of EAS mainly depends on the energy, E_0, of the incident primary particle, the angle on incidence, θ, and the height of the first interaction h_1 above sea level. Instead of the height h in the atmosphere, it is usually more convenient to use, as a characteristic unit of the amount of matter traversed by a particle, the atmospheric depth X from the top of the atmosphere downwards, related to the height h through a formula that in turns depends on the atmospheric density ρ as below:

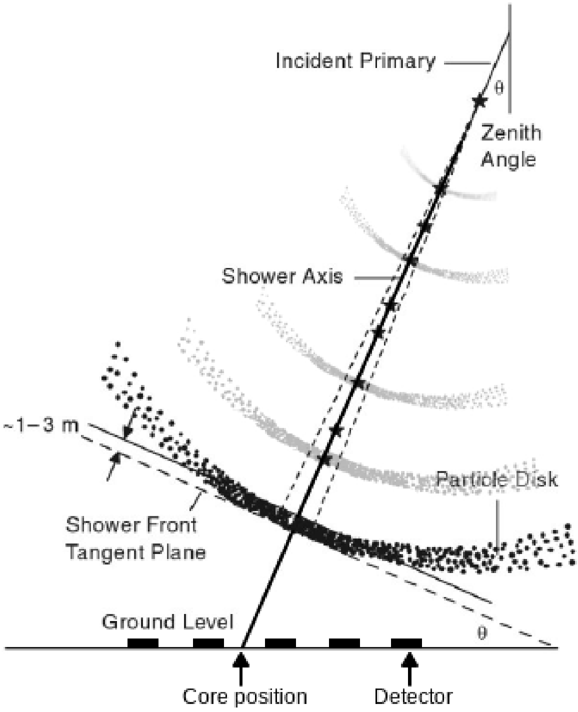

Figure 1.17: Schematic representation of a developing air shower in the atmosphere, and the corresponding shower-related quantities. Image adapted from [107].

$$X(h,\theta) = \frac{\int_h^\infty \rho(h')dh'}{\cos\theta}, \tag{1.76}$$

where θ is the zenith angle of the impingin particle. The features of the different components of the EAS change with the altitude. One of them is the number, $N(X)$, of produced particles as a function of atmospheric depth, which is intimately related to the type and energy of the primary particle. The location of its maximum, $N_{\max}$, is widely known as atmospheric depth of shower maximum, $X_{\max}$,and it is often used to reconstruct the elemental composition of primary cosmic rays. The depth of the first interaction X_1 decreases with increasing primary mass A at a given energy, because the chance of interacting increases with the atomic mass of the projectile[19]. Fig. 1.18, shows the trajectories across the atmosphere of the secondary particles of energy $\geq$3 GeV, down to the sea level produced by three different types of primary particles (γ, proton, and iron nucleus) at a given energy of 10^{17} eV. The three vertical ($\theta = 0$) EASs have been simulated by means of COsmic Ray SImulations for KAscade (CORSIKA) [108], using SIBYLL as the high-energy hadronic interaction code [109]. There are certain phenomena affecting the longitudinal development that are unique to EAS initiated by photons. As it can be seen, the shower initiated by primary photons develop, on average, deeper in the atmosphere. This is due to the small multiplicity of the EM interactions, in contrast to the large number of secondaries produced in inelastic interactions of high-energy hadrons. More over, proton primary starts to interact deeper compared to the iron nucleus, though not so much.

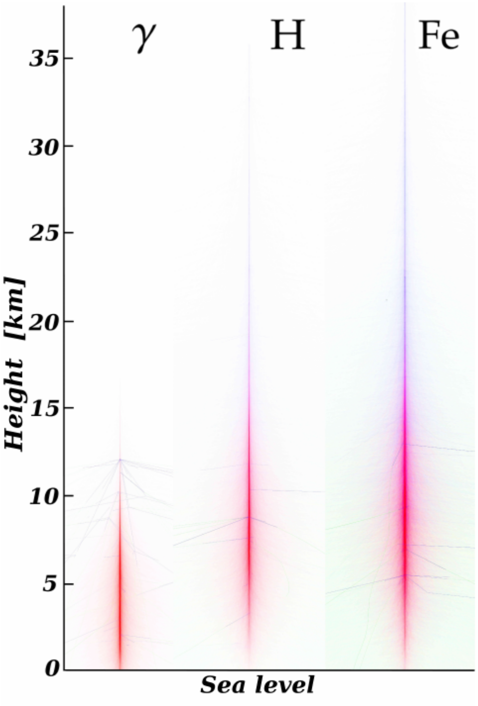

Figure 1.18: Schematic two-dimensional representation of three vertical ($\theta = 0$) EASs respectively generated by a photon (left), a proton (center), and a iron nucleus (right), all having a primary energy of 10^{17} eV by means of the CORSIKA[18] simulation tool.

In Fig. 1.19 the longitudinal profiles for the three considered air showers are depicted, where the same behaviour can be observed for $X_{\max}$ as well. However, since the primary-mass dependency of $X_{\max}$ is ultimately related to the interaction cross-section, even with identical particles having the same energy and zenith angle will have different longitudinal profiles, and consequently, different $X_{\max}$. This means that showers induced by two

---

[19] We have higher interaction cross-section for higher mass number A

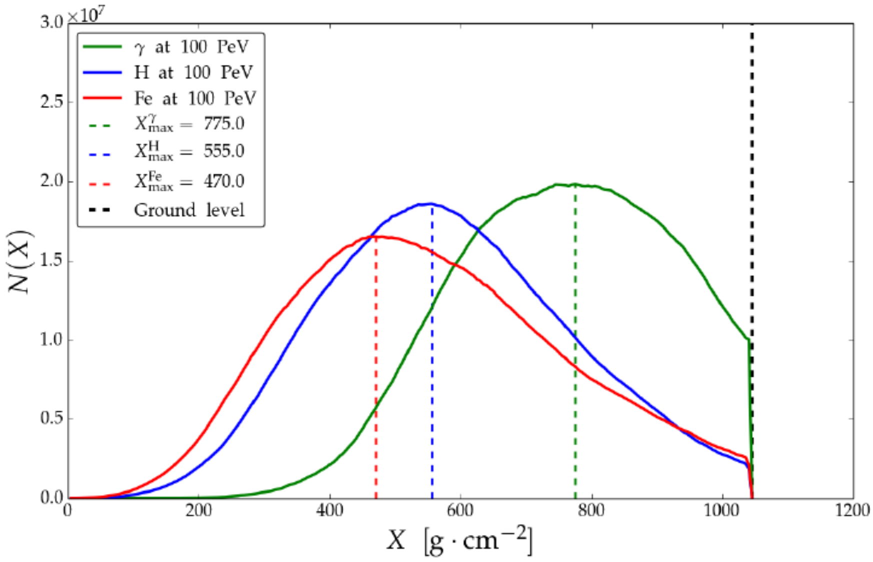

Figure 1.19: The longitudinal profiles of the three vertical air showers respectively generated by a photon (solid-green line), a proton (solid-blue), and a iron nucleus (solid red), with the same primary energy of 10^{17} eV. Dashed lines indicate the position of each $X_{\max}$.

primary particles with the exact same energy, mass and arrival direction will differ even though they were initiated with the same primary quantities and propagate through the very same atmosphere. These statistical fluctuations of the shower development are jointly called *shower-to-shower* fluctuations. In Fig. 1.20, the fluctuations on the longitudinal profile are illustrated for the three simulated air showers showed above. These fluctuations are also due to the several stochastic processes that compete in the development of air showers, as a consequence of the low density nature of the atmosphere. As the chance of interacting is directly proportional to the projectile mass, in Fig. 1.20 we can observe how heavy nuclei produce smaller fluctuations than light ones. In addition, hadronic processes are the main contributors to air-shower fluctuations, and purely electromagnetic showers are in general less subject to fluctuations.

Fluorescence telescopes are used in a number of UHECR experiments to measure the longitudinal profile of an EAS generated by UHECR. These telescopes make use of the fact that as an EAS develops, it produces fluorescence light through interactions with the nitrogen in the atmosphere. Because this light is generated isotropically, a small fraction of it will be in the direction of the telescope. Because the light is detected as the shower propagates, the longitudinal development of the shower can be measured. The fluorescence technique will therefore be discussed in detail in Chapter 2. At the same time, electromagnetic pulses are caused by the changing number of secondaries charge carriers, which makes the radio-detection technique sensitive to the derivative of $N(X)$. On the contrary, surface arrays measure the last stage of the longitudinal profile which means they detect the particle density at ground level, where the air shower is characterized by the lateral displacement of the particles in the shower front with respect to the shower core.

Lateral Distribution Together with the longitudinal profile, the lateral structure of the shower front, i. e. the Lateral (density) Distribution Function (LDF) of the particles, characterizes air showers and is used to compute the particle content N, required in turn to estimate the primary energy. The lateral distribution, as the longitudinal profile, is an important fea-

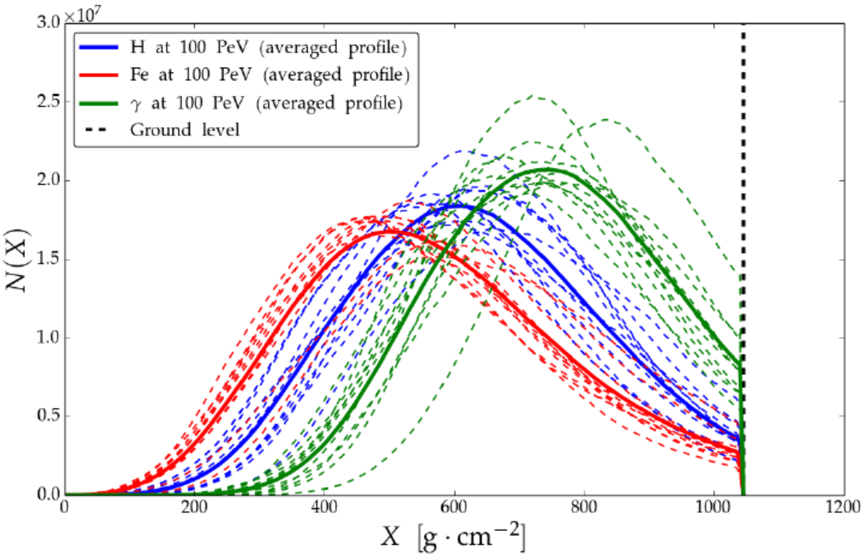

Figure 1.20: An illustrative example of shower-to-shower fluctuations in the longitudinal pro files of the three vertical air showers already shown in Fig. 1.18 respectively generated by a photon (green lines), a proton (blue), and a iron nucleus (red), with the same primary energy of 10^{17} eV. Each dashed line corresponds to a simulated air-shower longitudinal profile, whereas the solid lines represent the average longitudinal profile for each primary [110].

ture of the particle dynamics responsible of the EAS spread. After few hadronic interactions, the produced secondary particles inherit a transverse momentum component for the momentum conservation. In the case of muons produced by hadron decays, the resulting momentum partly gains this transverse component, further enhancing the lateral development. On the contrary, EM sub-cascades produced by primary photons, since their development is governed by the bremsstrahlung and pair production mechanisms, they leads to an increased lateral displacement of electromagnetic particles. Therefore, the shower-front lateral structure of an EAS is well dependent on whether the EAS is of EM or hadronic nature: the photon-initiated showers almost lack of hadronic and muonic components, as opposed to the proton- and nucleus-initiated EAS. For this reason, the lateral distribution function of a purely electromagnetic cascade is essentially different from a hadronic one. Fig. 1.21 shows the lateral (i.e., transverse to the shower axis) and longitudinal particle profiles of the different shower components, simulated with CORSIKA [112] for proton-induced showers of 10^{19} eV. The hadronic EAS have a prominent muonic component arriving at ground and for this reason, the LDF of Proton- and nucleus-initiated EAS extends to larger distances than in the case of photon EAS, where the muonic components dominates over the EM component at sufficiently large distances from the shower axis. This effect can be noticed in Fig. 1.21 as a flatter lateral development of muons than the one of EM particles because at large lateral distances the latter component is more attenuated than the former one.

On the contrary, because of the delayed longitudinal development of photon EAS compared to the hadronic ones, the photon-initiated shower presents an LDF spatially very compact with the bulk of secondary particles arriving at the ground distributed close to the shower core, since less atmospheric mass is traversed by a photon-initiated compared to hadronic-initiated shower. More over, since the muonic component is almost absent in photon-initiated EAS, the lateral profile of particles on ground is expected to be steeper in the case of photon primaries than in their hadronic counterparts.

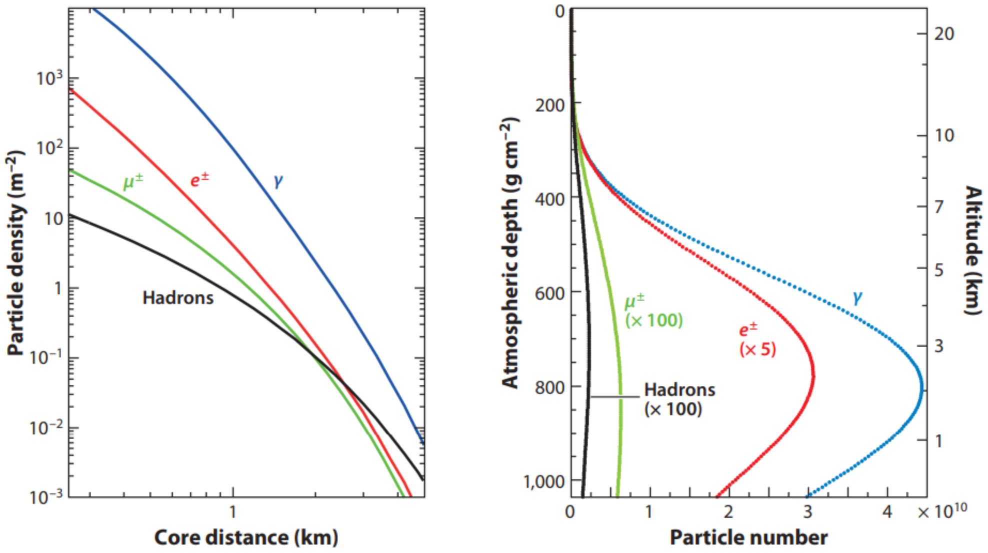

Figure 1.21: Average (left) lateral and (right) longitudinal shower profiles for vertical, proton-induced showers at 10^{19} eV. The lateral distribution of the particles at ground is calculated for 870 g/cm^2, the depth of the Pierre Auger Observatory [111].

The all-particle density $\rho(r)$ is in first approximation axially symmetric, and for this reason usually is only a function of the radial (lateral) distance r from the shower axis. For strongly inclined showers, asymmetries in the particle density arise from zenith-angle and geomagnetic effects, and act differently on the muonic and electromagnetic components. The zenith-angle effect is correlated to the increasing amount of traversed atmosphere by the EAS. As the zenith angle increases, the number of particles arriving to the ground decreases due to the strong *atmospheric attenuation*. When a primary particle impinges the atmosphere with an inclined incidence, the subsequent EAS would arrive at the observation level in a more mature stage of development. This is translated in a flatter lateral distribution of particles, as in Fig. 1.21, and does not necessarily indicate that more particles would arrive to the ground. We shall consider the zenith-angle effect, better known as *atmospheric attenuation*, which is correlated to the increasing amount of traversed atmosphere by the EAS. As the zenith angle increases, the shower crosses more atmosphere, more particles will be absorbed resulting in a decreased number of particles arriving to the ground due to the strong *atmospheric attenuation*. More over, the rate of absorption depends on the particle type, with the final effect that the particle mix changes as well with increasing zenith angle: at sea level the EM component of inclined showers will be mostly absorbed, while the muonic component is hardly affected. If the atmospheric attenuation effect is not taken into account, two showers differing only for their zenith angles θ will appear with different energies, since the particle content $N(X)$ ($\propto E_0$[20]) is estimated by the particle-density distribution. This means that the density and distribution of secondary particles on ground are affected by varying atmospheric conditions and the geomagnetic field and that the difference in the total number of particle has to be associated to the particle absorption rather than to a different primary energy. These effects need to be taken into consideration in order to obtain an unbiased angular dependence of the flux of CR. The Constant Intensity Cut (CIC) method provides an empirical way to correct for the atmospheric attenuation of the shower particles. We assume an isotropic primary

---

[20] E_0 is the primary CR energy

CR flux, and therefore the arrival rate of air showers generated by primaries with the same energy and composition is constant as a function of the zenith angle at a given energy. The application of this method is necessary in order to find the corrected energy estimator from which one can determine the primary CR energy.

1.6 Final Remarks

The physics of Ultra high energy cosmic rays is basically associated to our understanding of EASs, as only with indirect measurements of EASs we are able to uncover the valuable data carried by these cosmic couriers. In recent times, our understanding of physical phenomena is has vastly improved using simulations as the principal tool in order to reproduce the physical phenomena. As said before (see Sec. 1.5.3), some shower may originate from from hadronic interactions and the highest energetic cosmic rays, with energies of 10^{20} eV are still past those energies reachable with the Large Hadron Collider[21]. As a matter of truth the highest-energy measurement of the proton-air cross-section has been measured by the Auger collaboration [113]. In addition the condition and the characteristics of the atmosphere have been deeply investigated [114] and, to account for the influence of a varying atmosphere on the shower development, atmospheric models are used within any reliable simulation of air showers. In the context of simulations, hadronic interaction models are a key element to study the physics of EASs. Unfortunately, the number of muons in simulations is underestimated by an amount of 30% to 60%, depending on which hadronic interaction model is used, especially for energies above 10^{19} eV [115, 116]. More over, although the data have been compared to predictions from the contemporary interaction models which were tuned with data measured at the LHC, none of them is able to predict an amount of muons as seen in data and to deliver a consistent prediction of both the electromagnetic and muonic components as observed by Auger.

---

[21] corresponds to a center-of-mass energy that is a factor of 100 larger than accessible at the Large Hadron Collider (LHC[22]).

CHAPTER 2

The Pierre Auger Observatory

The Pierre Auger Observatory is the world's largest observatory to measure ultra high energy cosmic rays and it was originally designed to detect extensive air showers produced by primary cosmic rays above 0.1 EeV. It is located on the vast plain of the Pampa Amarilla at an altitude of 1400 m, close to Malargüe in the Mendoza Province, Argentina. Several aspects were taken into account in the choice of the Auger location, both related to the scientific goals and the construction feasibility [117]. The suited place has been the result of a site survey all around the globe, including Australia, South Africa, Spain, Russia, and the United States. The location at 1400 m above the sea level or 875 g/cm^2 in atmospheric overburden has been chosen to optimize the detection of cosmic rays at 10^{19} eV since it resides close to the maximum of air-shower development within the atmosphere. From the map in Fig 2.1, where the layout of the observatory is shown, in visible that the region is generally flat with scarce vegetation, with a maximum deviation of 270 m in altitude, making it possible to measure air showers at the same shower age over the whole array and matching with the communications and deployment requirements. In the decision, physics considerations have mainly motivated the selection criteria, in particular, the need to detect the faint fluorescence signals produced by the EAS required a location with optical characteristics close to those sought by astronomical telescopes. Then, in addiction to the flatness, the accessibility of the surface-detector-dedicated area, and the altitude, the good visibility for the fluorescence-light observation at the site was one of the important considerations in the selection of the deployment place. The appropriate atmospheric conditions such as hardly no rain, a clear atmosphere, and minimal light pollution due to the sparse population, make the Argentinean region of the Pampa Amarilla to be an excellent emplacement for the observatory. It comprises a surface detector (SD[1]) array of 1660 water-Cherenkov stations deployed over a triangular grid of 1.5 km spacing and a system of 27 telescopes grouped in four sites forming the fluorescence detector (FD[2]). The telescopes are erected at the periphery of the Observatory to observe the atmosphere over the full area of 3000 km^2 covered by the SD array. The SD stations sample the density of the secondary particles of the air shower at the ground and are sensitive to the electromagnetic, muonic and hadronic components. The FD observes the longitudinal development of the air shower by detecting the fluorescence and Cherenkov light (see Sec. 2.2) emitted during the passage of the secondary particles of the shower in the atmosphere. The uniqueness of the PAO[3] derives from having

---

[1] Surface detector

[2] Fluorescence detector

[3] Pierre Auger Observatory

brought together, for the first time, these two complementary detection techniques to form a hybrid detector. The PAO is the first experiment that has combined both ground detectors and fluorescence detectors at the same site in a hybrid detection technique. The combination of information from the two detection systems enhances the reconstruction capability with respect to the individual detector reconstruction and it is used for cross-calibration and as such enables the reconstruction of cosmic ray properties without a heavy use of simulations, making the analyses robust against changes of hadronic interaction models. A hybrid event is an EAS that is simultaneously detected by the FD and the SD and if an EAS independently triggers and has been successfully reconstructed by both detectors independently, the event is tagged as a golden hybrid.

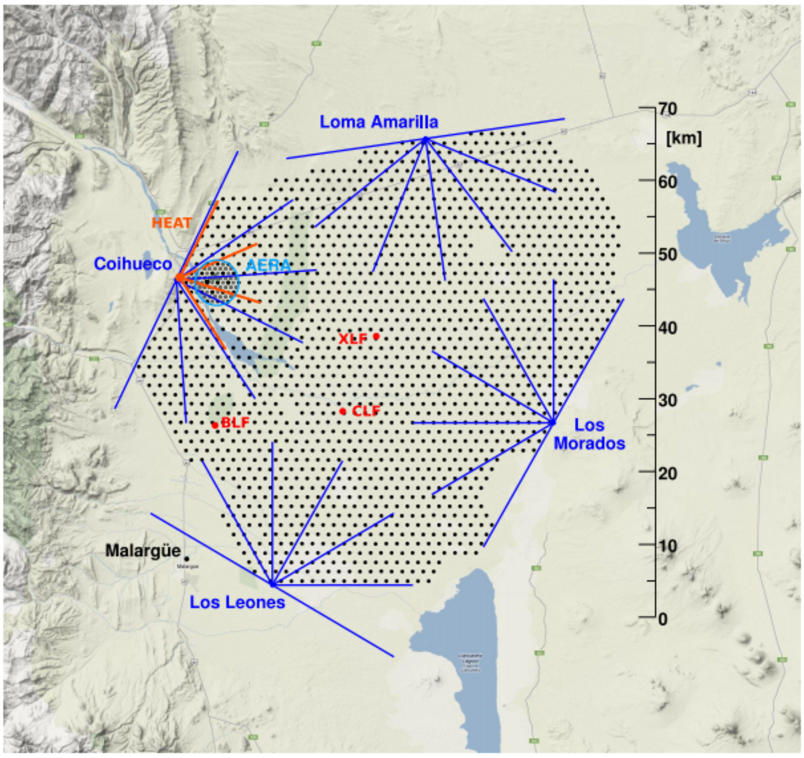

Figure 2.1: Schematic layout of the Pierre Auger Observatory overimposed on a satellite image of the actual site close to Malargüe, in the province of Mendoza, Argentina. Black dots indicate the Auger SD stations, whilst the FD sites, located at Los Leones, Coihueco, Los Morados and Loma Amarilla are shown in blue. The blue lines give an idea of the field of view associated with the FD telescopes at the perimeter of the surface array. The Infill (the more dense area of black dots) and SD-433[4] (the most dense in the middle of the Infill) arrays are located close to Coihueco (to the west), where the AERA[5] antennas are placed as well. Additionally, essential facilities for atmospheric monitoring as well as detector extensions are depicted (adapted from [118]). Details on the various facilities of the observatory are given in the text.

The construction of The Observatory began in 2001 with an Engineering Array (EA) consisting of two fluorescence telescopes and 40 water Cherenkov detectors (WCDs[6]) deployed within the fields of view of the two telescopes. The construction and operation of the EA allowed to optimize the techniques related to the production and deployment of the detector components, the trigger algorithms, the data acquisition, monitoring software and telecommunications for both detection systems [119]. In 2004, the project entered into the

---

[6] water-Cherenkov detector s

production phase and in 2008 the construction of the base design was concluded. Subsequently, two significant enhancements have been incorporated into the baseline detectors that significantly extended the Observatory science capability: The Auger Muons and Infill for the Ground Array (AMIGA[7]) enhancement and The High Elevation Auger Telescopes (HEAT[8])(described in Sec. 2.3.1). The AMIGA enhancement also included the deployment of an additional SD array of 61 WCDs separated by 750 m (SD-750[9]) (See Sec. 2.3.1) to lower the energy threshold of the main array (SD-1500[10]) to $\sim 10^{17.5}$ eV and encompassed the installation of a denser triangular grid of WCDs spaced 433 m (SD-433) among several positions of the SD-750, which is the milestone of this thesis and it has been extensively described in Sec. 2.3.2.

2.1 Fluorescence Detector

The detection of UHECRs relies on the EAS generated by the high energy particles as they reach the atmosphere. One of the major methods for study these showers is by mean of the fluorescence detection. As an EAS develops in the atmosphere, charged particles excite the nitrogen molecules which then de-excite by the emission of fluorescence light in the wavelength range between ∼300 and 430 nm in dry air [120]. Because this UV light is generated isotropically, a small fraction of it will be in the direction of the telescope. The number of emitted photons is proportional to the energy deposited by the charged particles through electromagnetic energy losses [121]. Because the light is detected as the shower propagates[11], the longitudinal development profile $dE(X)/dX$ of the shower can be measured, thus its integral which is nothing but a calorimetric measure of the total electromagnetic shower energy, which is ≈90% of the primary energy of the CR.

2.1.1 Telescope Design

The standard Fluorescence Detector (FD) consists of twenty-four specialized telescopes that overlook the atmosphere above the SD and detect the nitrogen fluorescence light due to the passage of particles in the atmosphere. The twenty-four telescopes are located at four different sites at the periphery of the observatory: Los Leones, Los Morados, Loma Amarilla, and Coihueco. An additional three telescopes combine to form HEAT, the low energy extension of the FD (Section 2.3). At each site there is an FD building, like the one shown in Fig. 2.2(b), that houses six fluorescence telescopes. Each telescope has a field of view of $30^\circ \times 30^\circ$ in azimuth and elevation with a minimum elevation of 1.5° above horizon, providing each site an azimuthal field of view of 180°. Fig. 2.2(a) shows a schematic representation of an eye together with its six telescopes. The FD cameras are highly sensitive so that under standard operation the FD requires clear nights with minimal moonlight contamination. Another limitation is given by the weather. The operation of the telescopes is put on hold in case of rain, snow or high wind speeds to avoid damages to the detector, giving an average duty cycle of approximately 15%. The FD buildings have retractable shutters that cover the windows at each telescope bay, providing protection from the elements and only open when the FD is being operated. The internal temperature of each building is carefully controlled to minimise the effects of temperature variations on the system. All telescopes are built with a Schmidt optics with an optical filter placed at the entrance window, designed to only transmit UV

---

[7] Auger Muon Detectors for the Infill Ground Array

[8] High Elevation Auger Telescopes

[9] 750 m SD vertical

[10] 1500 m SD vertical

[11] The UV light is measured by the telescope at many atmospheric depths.

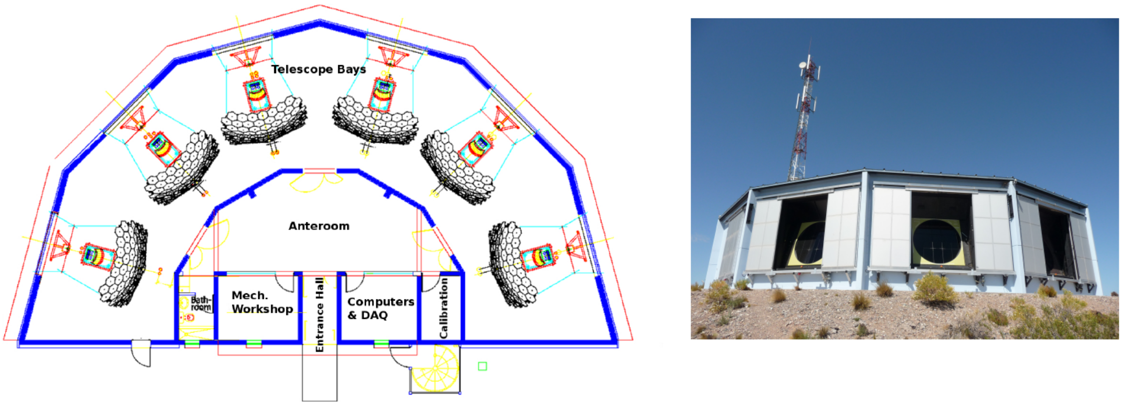

(a) (b)

Figure 2.2: Fig. 2.2(a): illustration of an FD building, called eye, with its six telescopes. Fig. 2.2(b): Los Leones, one of the FD sites with its communication tower.

photons of wavelengths between 290 nm and 410 nm. The presence of the filter allows for the transmission of nitrogen fluorescence photons which would otherwise be lost amongst the noise of visible photons and also helps to prevent dust going into the camera system. An annular corrector ring with a diameter of 1.1 m is used to provide a larger effective aperture for the telescopes, while correcting spherical aberration and largely eliminating coma aberration. The air-fluorescence light, entering through a UV-passing filter, is focused by a 10 m^2 spherical mirror into a camera composed by 440 hexagonal Photo-Multiplier Tubes (PMTs) sensors (pixels), each viewing a 1.5° diameter region of sky arranged on a 20×22 grid. We have two different mirror designs due to the use of two different manufacturers: at the sites of Los Leones and Los Morados, the mirrors are made of 36 rectangular anodised aluminium mirror segments, while the ones at the Coihueco and Loma Amarilla are comprised of 60 hexagonal glass segments layered with a reflective aluminium coating. Lasers are used to to achieve a correct spherical shape with the centre of curvature aligned with the optical axis of the camera. Surrounding each PMT[12]are 6 light collectors referred to as *Mercedes stars* designed to complement the light collection of the PMTs, maximising the light collection efficiency across the camera which is. when averaged over the entire camera, 94%, compared to a value of 70% when the Mercedes stars are not in place. Each PMTgives a signal that is digitised with a 100 MHz Flash Analog to Digital Converter (FADC). All the main component of the FD telescope are shown in Fig. 2.3.

2.1.2 Atmospheric monitoring

The atmosphere above the SD array serves as calorimeter and monitoring its state is a crucial ingredient for the FD measurements. Atmospheric parameters such as temperature, humidity and air pressure influence the longitudinal development of the EAS and the amount of emitted fluorescence light. The atmospheric aerosols may scatter and attenuate the fluorescence light during its propagation as well as clouds layers may block the line of sight creating a bias in the shower observation towards deeper penetrating events. Hence, monitoring the atmospheric conditions is of great importance, and for this reason, to continuously monitor and study the atmospheric properties an extensive array of instruments were designed and are deployed at the Observatory [122]. In Fig. 2.4 the locations of the various monitoring instruments across the Observatory are represented. The abundance of atmospheric aerosols

---

[12] photo-multiplier tube

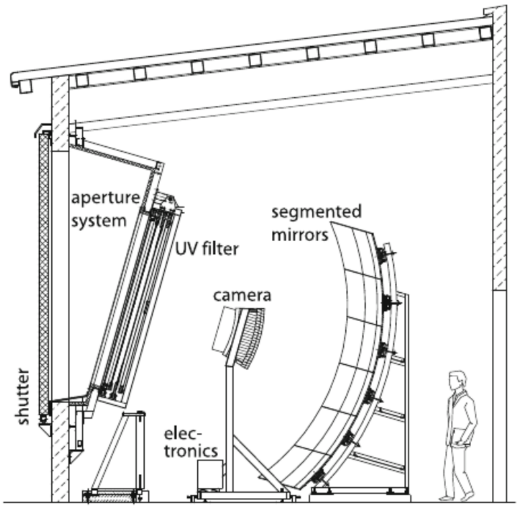

Figure 2.3: Schematic side view of the fluorescence telescope optical system. Image adapted from [121].

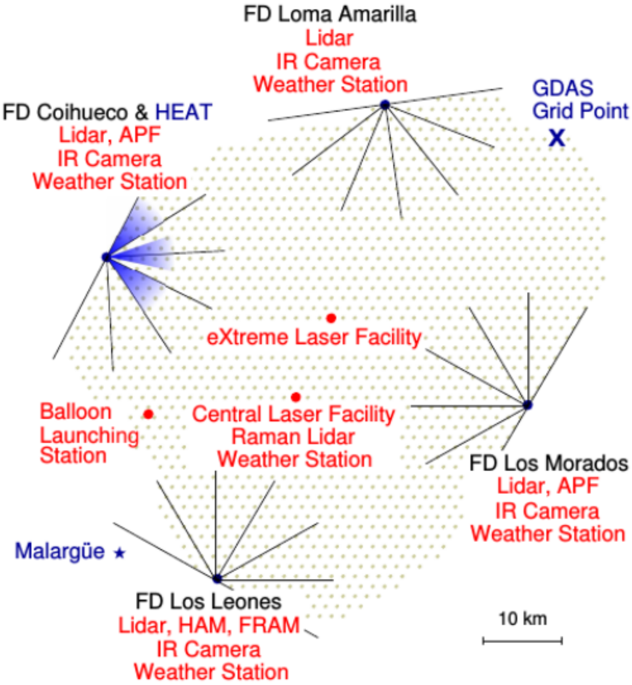

Figure 2.4: Schematic map of the instruments used to monitor atmospheric conditions.

is characterised using measurements from regular laser shots observed from the various FD locations along the Observatory's perimeter. Aerosols are able to affect the transmission of fluorescence light from the shower to the FD telescopes, and the scattering of Cherenkov light into the fields of view of the telescopes. The aerosol concentration and distribution are monitored using the *Central* and *eXtreme Laser Facilities* (CLF/XLF) and four elastic scattering Lidar systems at each FD site, among other smaller facilities. The concentration of aerosols is highly variable even on time scales of approximately one hour and it can vary over the area of the Observatory. For this reason, during FD data taking, hourly vertical aerosol optical depth (VAOD) profiles[13] are measured for each of the four FD sites by the CLF and the XLF, located towards the centre of the Observatory. Both laser facilities use a frequency tripled Nd:YAG laser which provide pulsed laser shots at a wavelength of 355 nm and the mean energy per pulse is around 7 mJ, similar to the amount of fluorescence light produced by an EAS with an energy of 10^{20} eV. The CLF and XLF fire 50 vertical shots at a frequency of 50 Hz every 15 minutes. Then, laser light is scattered out of the beam and propagates through the atmosphere reaching the telescopes and its propagation depends on the atmospheric conditions between the laser and the detector. The aerosol transmission and the presence of clouds within the laser site and FD can then be estimated. The telescope collects back scattered laser light, and the analysis of the return signal can be used to infer the presence of aerosols and clouds along the light path. Because the laser wavelength is in the center of the UV acceptance window of the FD telescopes, the operation of the lidar must be carefully controlled to avoid triggering the FD telescopes with scattered laser light. For this reason, close to each FD building four elastic back-scatter lidar stations have been equipped with a UV laser and 3 PMTs for the detection of the elastic back-scattered light.

Although these atmospheric monitors are sensitive to the presence of clouds, they do not provide a detailed all-sky map of cloud distributions. Information regarding the day-to-day fluctuations of the pressure, temperature, humidity and density[14] across the Observatory are provided by a network of weather stations, balloon launches and satellite measurements. In addition The presence of clouds can alter the observed optical signatures of an EAS and reduce the aperture of the FD. Clouds can attenuate or block light from an air shower, producing a dip in the longitudinal profile observed by the FD. Conversely, if a shower passes through a cloud layer, the cloud can enhance the scattering of the intense Cherenkov light beam, producing a bump. A cloud is warmer than the surrounding atmosphere and produces an infrared signal that depends on the cloud temperature and emissivity. Thus, the Observatory uses measurements from infrared cameras to detect clouds. Those cameras are installed on the roof of each FD site providing detailed information about cloud coverage across the fields of view of individual fluorescence telescopes. They are sensitive in the $7\ \mu m$ to $14\ \mu m$ wavelength range, appropriate for the peak of the blackbody radiation from thick clouds. Fig. 2.6 shows a panorama taken at night-time with the Los Leones infrared camera when clouds were present. In Fig. 2.5(a) is shown the cloud camera viewing different regions of the sky while Fig. 2.5(b) shows an example of a full-sky mosaic which provide information for the FD shifters on-site on the general cloud cover at the site, but are also useful for calibrating the cameras. Every 5 minutes each camera scans the field of view (FOV) of the telescopes, and every 15 minutes the entire hemisphere is imaged. Information from the CLF, Lidars and clouds cameras are store in a database for crossing all the available information.

2.1.3 FD trigger

The FD uses a hierarchical trigger chain to select real air-shower events. The trigger logic is split in two hardware levels and one software level and it is optimized to have maximum efficiency at energies above 10^{19} eV. The trigger levels are called: first level trigger (FLT), second level trigger (SLT) and third level trigger (TLT). The FLT is on the single PMTlevel decides the pixel status. The pixel response is a current pulse of 100 ns to about 2.5 μs width [124], which is digitized at 40 MHz. A pixel trigger is generated if the running sum over

---

[13] for the calculation of hourly VAOD profiles it is assumed that scattered laser light attenuates through the atmosphere in the same way as fluorescence light.

[14] In particular, the density profiles of the atmosphere are estimated using the Global Data Assimilation System (GDAS) [114].

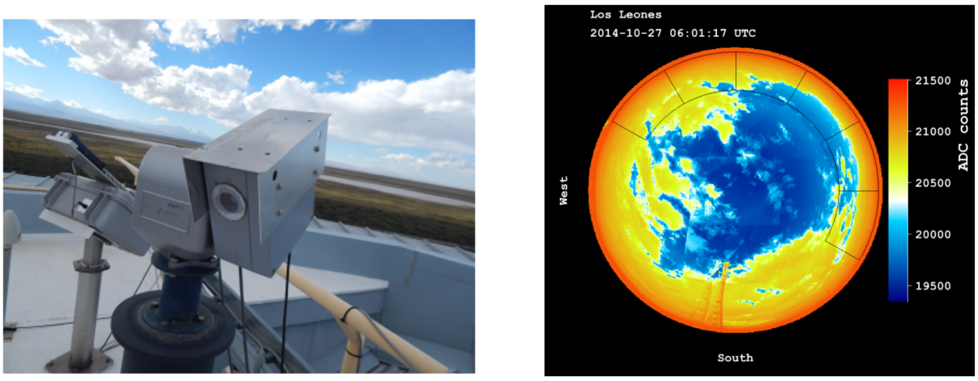

(a) (b)

Figure 2.5: Fig. 2.5(a): the infrared cloud camera system at the Los Leones fluorescence detector site. Fig. 2.5(b): an example of a full-sky mosaic at Los Leones, consisting of 19 individual images. The ADC counts relate to the infrared brightness in the camera's field of view. The black lines indicate the fields of view of the fluorescence telescopes.[123]).

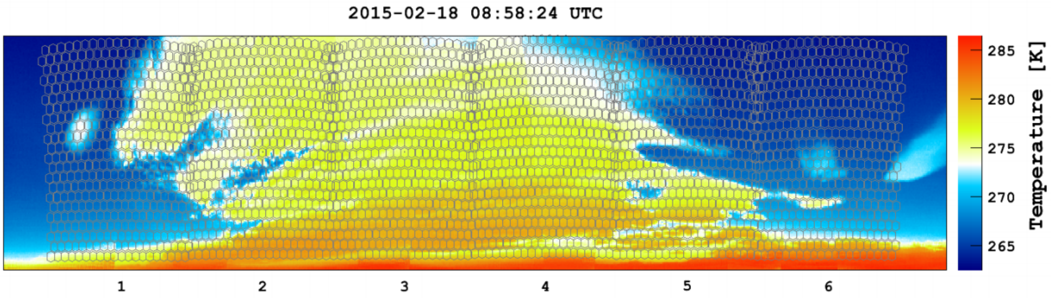

(a) Raw image

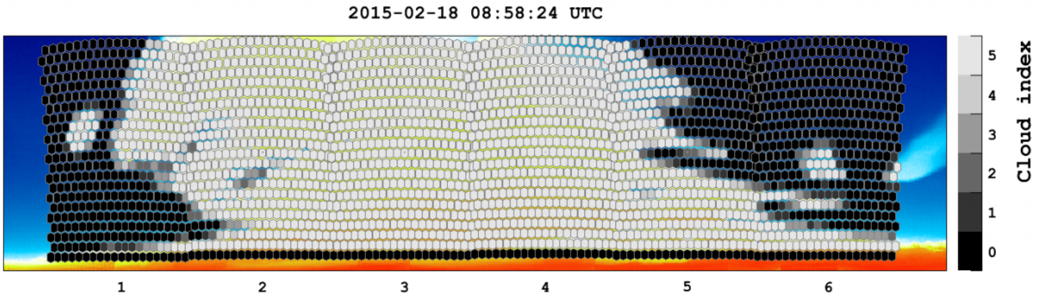

(b) Pixel cloud mask

Figure 2.6: A panorama captured during a full-sky scan performed with the Los Leones infrared camera at night-time. Clouds stand out in the thermal images because they have warmer effective temperatures than the clear sky. The panorama has been cropped to show the approximate field of view of the fluorescence detector. The grey hexagons are the pointing directions of the 2640 FD pixels for the site. Each FD pixel has been assigned a cloud index that represents the fraction of cloud contained within its field of view. Lighter colours (a higher cloud index) correspond to greater amounts of cloud cover. A cloud mask can be created by determining the fraction of cloud cloud cover contained within each FD pixel (Fig. 2.6(b)[123]).

the last n ADC bins (each one of 25 ns), with $5n \leq 16$ exceeds the threshold. When the running sum is smaller than the threshold, the pixel trigger is extended for 5 to 30 μs, which increases the probability of coincident pixel triggers The threshold is adjusted such, that the single-pixel trigger rate is 100 Hz. This results in on average four randomly triggered pixels per event.

The SLT checks for geometrical patterns, as air showers are expected to leave a track in the camera. The five pixel pattern types that are used are shown in Fig. 2.7. If four out of five pixels in a pattern can be matched to the FLTs, the second level is passed. Finally, the TLT then checks the timing structure inside the pattern, rejecting those track formed by pixels with a wrong time ordering and merges track segments by software. This catches 99% of all lightning and random triggers. FLT to TLT are performed on the telescope level. Once the event has passed the TLT, it is sent to the *Central Data Acquisition System* (CDAS[15]) where data from all triggered telescopes of a site is collected and combined, checking for coincidences between telescopes triggers and the SD triggers to search for hybrid events. On the combined data a hybrid trigger, called T3, is run, which performs a preliminary reconstruction of the event. The T3 is then used as an external trigger to the SD, to read out the SD stations closest to the building, allowing to record events below the SD full efficiency threshold. For low energies, not many SD stations survive the trigger selection (one or two), but together with the information coming from the FD measurements it is possible to achieve a high-quality hybrid reconstruction. The hybrid approach improves the FD-only detection method which suffers from a high uncertainty in the determination of geometrical properties of the shower, mainly because it is hard to determine the distance to the shower with a single-telescope. Measurements coming from SD stations provide essential information about the core location and the arrival time of the shower at the ground, removes a degeneracy in the traditional FD monocular approach that uses pixel timing to reconstruct the shower axis. With the hybrid technique the resolution of the arrival direction and of the core position are respectively better than 0.6° and 50 m [125] [126].

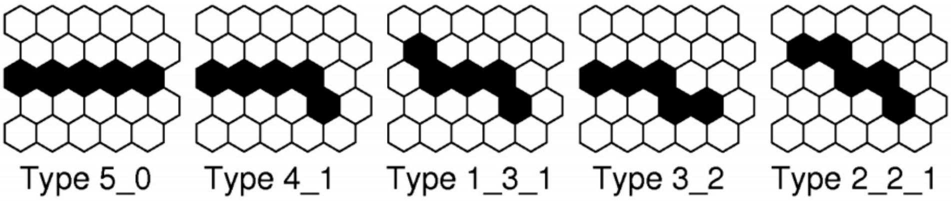

Figure 2.7: Fundamental track patterns used by the the SLT.

2.1.4 FD Reconstruction

An EAS, in the FD field of view is seen by many camera pixels and can also be seen by multiple telescopes depending on the trajectory. The air shower detection with the FD begins with establishing the shower geometry using the sequence of triggered pixels' timing and signal (see Fig. 2.9(a)). The standard method for the FD reconstruction begins with the calculation of the *shower-detector plane* (SDP[16]), defined as the plane that contains the location of the telescope observing the event and the axis of shower propagation, shown schematically in Fig. 2.8. The SDP can be determined by fitting the pointing directions of each triggered pixel, weighted by the size of that signal. Once the SDP has been established, timing information provided by individual pixels is used to define the orientation of the shower axis within the SDP. Some trajectories may have different possible orientations within the plane. It is possible to break this degeneracy using the timing information provided from the triggered

---

[15] central data acquisition system

[16] Shower detector plane

SD stations, which one of the benefits of the hybrid reconstruction. The shower axis can be characterised by two parameters χ_0 and R_{p}: the former defines the angle between the shower axis and the ground plane while the latter is the closest distance[17] between the telescope and the shower axis. The arrival time of light at the i^{th} pixel, t_{i}, is given by:

$$t_{\mathrm{i}} = t_0 + \frac{R_{\mathrm{p}}}{c} \tan\left(\frac{\chi_0 - \chi_{\mathrm{i}}}{2}\right) , \tag{2.1}$$

where c is the speed of light and χ_{i} is the pointing elevation of the i^{th} pixel within the SDP with respect to the ground. t_0 is the time at which the shower axis crosses the point R_{p} of closest approach to the telescope and $\chi_0 - \chi_{\mathrm{i}}$ is the angle between the shower axis and the camera within the SDP. The shower parameters R_{p} and χ_0 are obtained by a χ^2 minimization, in which the predicted values of t_{i} are compared to the data timing information. For a shower detected by a single Fluorescence detector, named *monocular reconstruction*, the values of the fit parameters depend on the measured angular speed ($d\chi/dt$) over the length of the track, which can change very little for shorter tracks, leading to a fit degeneracy between R_{p} and χ_0. As mentioned before, this degeneracy can be removed performing a hybrid reconstruction, combining the timing information coming from the SD stations with the FD [127].

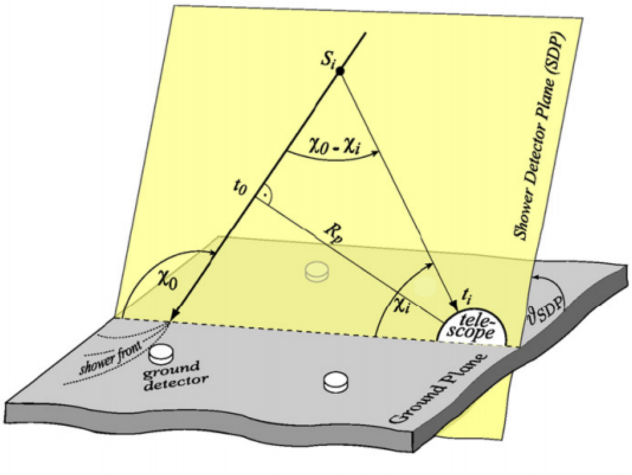

Figure 2.8: Illustration of the position of the SDP (yellow) and shower axis relative to the fluorescence telescope that observed the shower.

Following the geometry reconstruction, the shower energy can be determined. This procedure requires the conversion of the signal recorded by the detector's PMTs to a longitudinal energy deposit profile (dE/dX) of the shower as a function of atmospheric slant depth (X), which has been already defined before as the energy deposited in the atmosphere as a function of traversed matter. An example of a longitudinal profile from an Auger event in shown in Fig. 2.9(b). The longitudinal shower profile is fitted using a Gaisser-Hillas function, which integrated with respect to X gives an estimation of the calorimetric energy E_{Cal} representing the electromagnetic component of the shower. The FD technique actually measures the calorimetric energy of the EAS, that portion of the primary cosmic ray energy visible via fluorescence light, providing an almost a measurement of the primary's energy, since the measurements are not exact due to the muons, neutrinos, etc. which carry some fraction of the energy to the ground that cannot be measured by the FD. This energy fraction is known as *invisible energy* and has been studied at Auger via simulations [128][129] and real data [130].

---

[17] R_{p}: impact parameter or distance of closest approach

A small (~ 15%) correction has to be applied to the calorimetric energy to get the total energy in order to take into account the missing energy. The location of the X_{max} can be determined directly from the fitted peak and with the energy measurements make the Fluorescence telescope a helpful constituent of the Observatory. The invisible energy can be calculated for each shower using the FD measurement of the longitudinal profile and the SD signal at 1000 m from the axis, S(1000). E_{inv} can be reliably estimated only above 3×10^{18} eV (the energy above which the SD-1500 is fully efficient) as below this energy S(1000) is biased by upward fluctuations of the shower signals. E_{inv} is parameterised with an analytical function above 3×10^{18} eV, with the function being extrapolated to 10^{17} eV. High-quality hybrid events have been used to to find a relation that bound the E_{inv} and E_{Cal}:

$$E_{\text{inv}} = \alpha_0 (E_{\text{Cal}}[\text{EeV}])^{\alpha_1} . \tag{2.2}$$

The fit of the 2-parameter exponential function to the invisible energy on hybrid events above $10^{18.3}$ eV has been performed minimising a χ^2 function that takes into account the fluctuations of both E_{Cal} and S(1000) measurements [130], yielding the parameters: $a_0 = (0.174 \pm 0.001)$ and $a_1 = (0.914 \pm 0.008)$. This contribution to the primary energy ranges between 15% at 10^{18} eV and 11% at the highest energies with total shower energies increasing by about 4%. Due to the stochastic nature of air showers, the invisible energy is also affected by shower-to-shower fluctuations. These are parameterised and an uncorrelated uncertainty of about 1.5% is introduced.

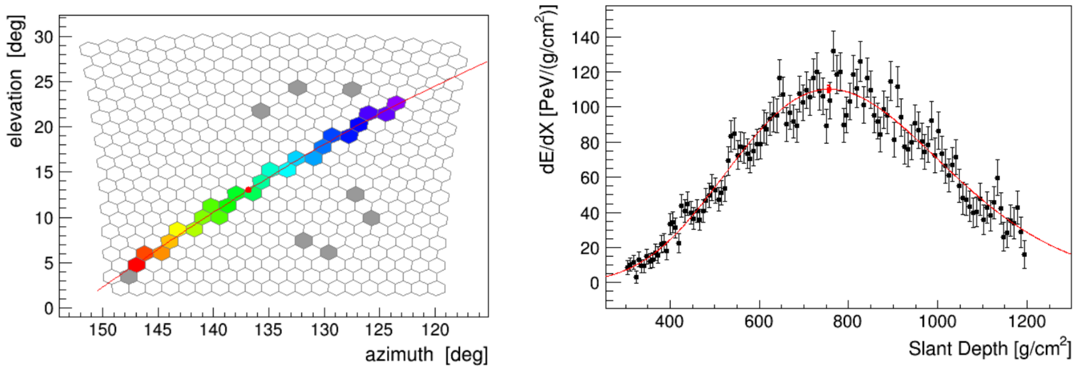

(a)

(b)

Figure 2.9: Fig. 2.9(a): shows the results of a hybrid reconstruction (in this case Loma Amarilla+Coihueco+SD) of a 7×10^{18} eV shower with a zenith angle of 51°. The air shower is seen over many pixels as it develops. The colors indicate the timing in which the pixels were triggered (earlier is purple). The red line indicates the fitted SDP with a red dot signifying the location of the shower maximum. Fig. 2.9(b): The energy deposit of the shower in the atmosphere as a function of the slant depth. The calorimetric energy of the shower is calculated by integrating the curve under the profile. Black dots depict the measurements of the signal intensity in the FD pixels of the differential energy deposit (dE/dX)). The red line is the Gaisser-Hillas function fit to the measurements. The shower maximum is indicated by the red circle at the peak directly extracted from the fit.

2.2 Surface detector

The complementary technique used at the Observatory is the SD array [131]. It consists of an array of more than 1600 stations separated by a distance of 1.5 km and arranged in a triangular grid, as mentioned before. Each detector in the array, is a Water-Cherenkov Detector (WCD): a large polyethylene tank with a base of 10 m^2 of 1.6 m height and 3.6 m diameter filled with 12000 lt of ultra purified water. The water volume is contained in a Tyvek reflective liner which provides an interface between the water volume and the light sensors. The purpose of this liner is double: as a water-tight container to seal out external light, and to isotropically reflect Cherenkov light produced within the detector by traversing particles independent of the their arrival direction, given its high reflectivity (about 98% depending on wavelength). The Cherenkov light is collected by three 20.3 cm diameter photo-multiplier tubes (PMTs) mounted at the top of the tank looking vertically downward into the detector volume. Access to the liner and the PMTs is through three hatches located on the top of the tank. An electronics box containing front-end charge amplifiers, shapers, trigger logic, signal buffers, power control, radio transmitter and receivers is located on the top roof of the tank on one of the hatch-covers and is protected by a dome. All the cables connecting the electronics and the light sensors run inside the tank and connect to the electronics via feed-troughs in the hatch covers. The power is provided locally for each station with two 53 Wp solar panels loading two 12 V batteries connected in series, and a Global Positioning System (GPS[18]) receiver is used to tag each trace with a timestamp establishing a common time among the different stations with a resolution of 7.2 ns. The GPS receptor is also used to monitor the position and altitude of each WCD with a $\sim$1 m precision. Fig. 2.10(b) shows an actual picture of an SD station and the different elements that compose an operating WCD, whilst in Fig. 2.10(a) is shown a schematic cross section of the detector with indicated components. One output is in the anode of the PMT(referred as to the low gain channel) and an amplified one in the last dynode (also called high gain channel) amplified 32 times and inverted within the PMTbase electronics. The charge gain between the two channels is used to provide a higher dynamic range in order to cover with good precision detection signal close to the shower core where the density of secondary particles increases to about $1000/\mu$s as well as those produced far away where the density is as low as $1/\mu$s. These signals from the PMTs are filtered and digitized by 40 MHz 10-bit Flash Analog Digital Converters (FADCs), with each bin covering 25 ns, and read by a Programmable Logic Device (PLD) performing trigger decisions. Finally, when requested, these data are sent to the CDAS, which combines the information from the local stations. The WCDs are calibrated locally as discussed in Sec. 2.2.1 and an extensively description of the hierarchical trigger system is given in Sec. 2.2.2. The hardware of the surface detector is explain in detail in [133, 134].

The Cherenkov radiation

It is named after Soviet physicist Pavel Alekseyevich Cherenkov, who shared the Nobel Prize in physics in 1958 with Ilya Frank and Igor Tamm for the discovery of Cherenkov radiation, made in 1934. Nothing can travel faster than the speed of light in a vacuum. However, when light travels through a transparent medium such as water, its speed is slowed down by the refractive index of the medium: the refractive index of water at room temperature is 1.33, so light in water is travelling at about 3/4 of the speed of light in a vacuum. High-energy charged particle, as a secondary particle generated in an EAS, which is travelling at nearly the speed of light in vacuum, its speed in water exceeds the speed of light in this medium ($\gg 0.75c$ in water), giving rise to Cherenkov radiation inside the tank. In a time Δt, the particle travels a distance $\beta c \Delta t$ and a photon travels a distance $c\Delta t/n$, where n is the refractive index of the medium and c/n is the speed of light in the considered medium. This means that the

---

[18] Global Positioning System

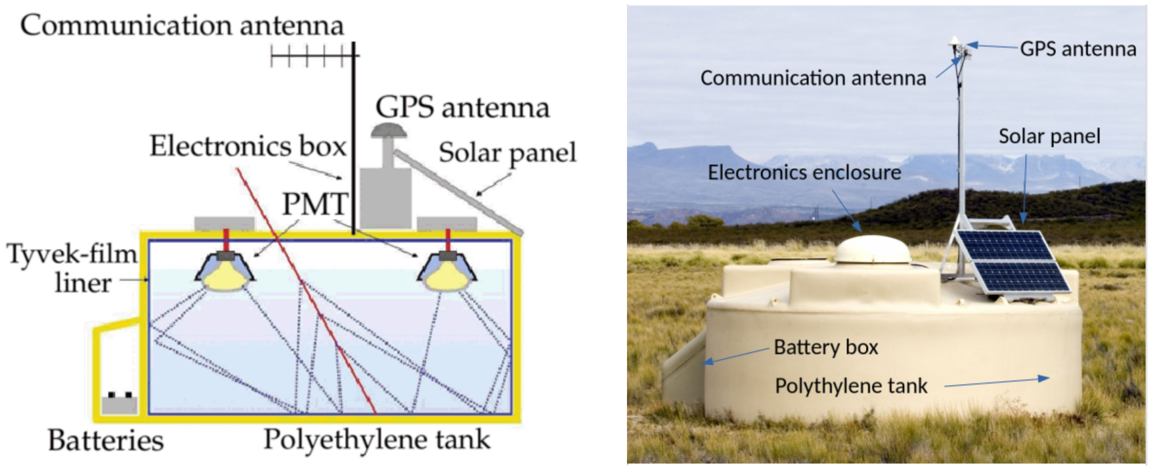

(a) (b)

Figure 2.10: Fig. 2.10(a): Schematic internal view of an SD station with its components. Image adapted from [132]. Fig. 2.10(b): a picture of a water Cherenkov detector in the field, showing its main components.

angle between the particle trajectory and the trajectory of the coherent wavefront, or in other words the Cherenkov radiation emission angle, is defined by

$$\cos\theta = \frac{c}{vn} = \frac{1}{\beta n}, \tag{2.3}$$

that becomes

$$\cos\theta \approx \frac{1}{n}, \tag{2.4}$$

when the particle is relativistic enough that $\beta \approx 1$. IN the case of water with $n = 1.33$, the limiting angle for high speed is given by

$$\theta = \cos^{-1}\frac{1}{1.33} = 41.2^\circ\,. \tag{2.5}$$

In the WCD, the Cherenkov radiation is detected as mentioned before, by PMTs, and the cone of emission reconstructed. The axis of the cone gives the direction of the particle, and the light yield gives the particle energy. The schematic of Cherenkov radiation is shown in Fig. 2.11. Only charged particles with $\beta > 1/n$ can be detected: this gives a threshold particle speed for Cherenkov radiation. According to the relativistic formula $p = \beta\gamma m_0 c$ and the condition for Cherenkov production $\beta > 1/n = 0.75(\gamma \approx 1.52)$, the minimum momentum for a particle with rest mass $m_0$to produce Cherenkov radiation is

$$p_{\mathrm{Ch}} = 1.13 m_0 c\,. \tag{2.6}$$

For an electron in water we can calculate the total energy as

$$E_{\mathrm{e}}^{\mathrm{tot}} = \gamma m_e c^2 = \frac{1}{\sqrt{1-\beta^2}} m_e c^2 = (1.52)(0.511\,\mathrm{MeV}) = 0.775\,\mathrm{MeV}\,. \tag{2.7}$$

Thus, the kinetic energy that an electron has to have for the Cherenkov radiation to occur in water is given by

$$p_{\mathrm{e}} = E_{\mathrm{e}}^{\mathrm{tot}} - m_e = 0.775\,\mathrm{MeV} - 0.511\,\mathrm{MeV} = 0.26\,\mathrm{MeV}\,. \tag{2.8}$$

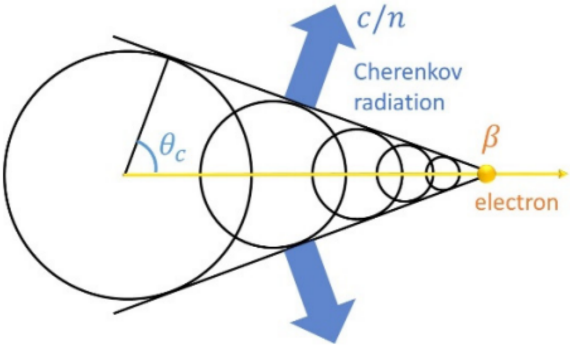

Figure 2.11: The diagram of Cherenkov radiation

In the case of other charged particles, the energy threshold is 160 MeV for muons and 1.4 GeV for protons and neutrons (somewhat higher in practice since the amount of Cherenkov radiation emitted exactly at threshold is negligible). Although only charged particles produce Cherenkov light, the WCDs are sensitive to photons since they cascade down through pair production in the water. Photons with energies $E_\gamma > 2p_\mathrm{e} \simeq 1.6$ MeV will be able to produce Cherenkov radiation. The response of the WCD to photons is determined by the probability P that a photon interaction inside the tank will result in conversion to an $e{+}e^-$ pair which is given by

$$P_{e^\pm}(E_\gamma) = 1 - e^{-\frac{x}{\lambda(E_\gamma}} \, . \tag{2.9}$$

where $\lambda = \frac{1}{\mu\rho}$, being μ the mass attenuation coefficient and ρ the density, is the photon mean free path, and $x = \frac{h}{\cos\theta_\gamma}$, being θ_γ the zenith angle of the photon, is the amount of traversed matter.

Another interesting quantity is the maximum distance,R, a particle of a given energy can penetrate through a material before all kinetic energy is lost. It is a common way to parametrize particle interactions with materials and can be obtained by integrating the total stopping power over the full penetration depth in the continuous-slowing-down approximation (CSDA[19]), which assumes that the rate of energy loss dE/dx along the track length is constant. For a given incident energy E_0 the CSDA range, $R(E_0)$, is obtained such that

$$E_0 = \int_0^{R(E_0)} \left(\frac{dE}{dx}\right) dx \, . \tag{2.10}$$

It can be seen that for electrons, the typical range inside the detector is around 10 cm, up to 80 cm for an energy of $E_e = 500$ MeV. This means that all electrons in the shower will be absorbed inside the tank. For muons, it turns out that ranges are shorter than the water depth (for vertical muons). These muons will deposit their energy and eventually will decay inside the tank, being possible the detection of the muon decay.

2.2.1 Detector Calibration

The remoteness and large number of detectors spread over a very large area and often difficult to reach require a robust, automatic self-calibration procedure in order to ensure a uniform response of the array in terms of trigger rates and performance. The total bandwidth available from each SD to the CDAS is approximately 1200 bits$/s$ which implies that

---

[19] continuous-slowing-down approximation

the calibration must be done by the local electronics. Moreover, the calibration procedure has to be systematically repeated every 60 seconds to correct for temporal changes of the total detected signal at each WCD, which depends on the station specifications like the water quality, the liner reflectivity, the coupling between PMTand water and the PMTamplification factor. Therefore, the main calibration goal is to obtain with good accuracy the value of this reference unit for each PMT, in terms of electronics units for each individual local station in order to provide a stable and uniform trigger for the detector [135]. In addition, to maintain a uniform trigger condition for the array, the station must be able to set locally a common trigger threshold in detector-independent units, which needs to be the same for all SD stations. This will allow for a tank-independent analysis of the acceptance of the array by modeling the trigger.

The WCD calibration is inferred from atmospheric muons at a rate of ≈2.5 kHz. The charge deposit of muons is proportional to their track length, as muons are not stopped in the tank. The reference signal is the one produced by a vertical and central through-going (VCT[20]) muon. Therefore, the total signal which is the amount of Cherenkov light produced by shower particles passing through the detector at ground, is measured in units of vertical equivalent muons (VEM). However, the detector cannot discriminate vertical from inclined muons passing through it. Nevertheless, the distribution of produced light by isotropic atmospheric muons also generates a peak in the charge distribution [136](see Fig. 2.12(a)). WCD have been equipped with additional scintillators serving as muon telescopes, allowing

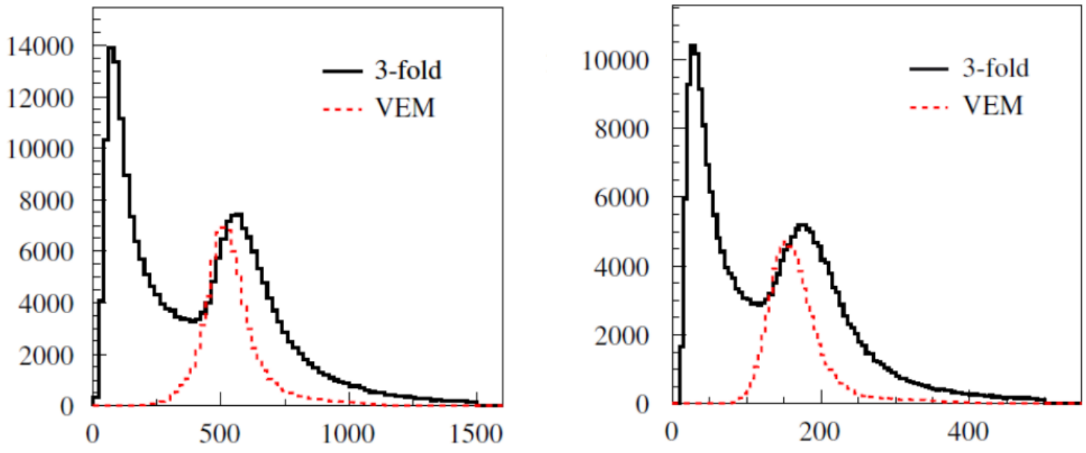

(a) Charge (Integrated ADC channels) (b) Amplitude (ADC channels)

Figure 2.12: Example of calibration histograms: charge and pulse height histograms from an SD station, triggered by a 3-fold coincidence between all 3 PMTs at a trigger level of five channels above baseline, with the signal from all 3 PMTs summed. The dashed histogram is produced by an external muon telescope providing the trigger to select only vertical and central muons. The bin containing the peak of the scintillator triggered spectrum is defined as a vertical equivalent muon. The first peak (abscissa value of 1000) in the black histogram is caused by the convolution of the trigger on a steeply falling distribution from low energy particles present in the atmosphere. The second peak is due to vertical through-going atmospheric muons.

the study of the detector response to atmospheric muons arriving with different incident angles. A muon telescope is used to provide the peak trigger in a reference tank ([137]). The charge distribution for each individual PMThas a peak at $Q_{\mathrm{VEM}}^{\mathrm{peak}} = 1.03 \pm 0.02$ VEM, which is a measure of that portion of the total signal deposited close to the PMT. For the sum of the

---

[20] vertical centered through-going

three PMTs of the WCD the peak is at $\approx 1.09 \pm 0.02$ VEM, and represents a measure of the total signal deposited in the tank. This shift is the result of the asymmetry in the distribution of the track length of muons, as well as of defects in collecting the Cherenkov light. Next to the charge, a measure of the current from the PMTs is used to set the trigger levels. Therefore, a reference unit for this current needs to be defined as well. Similarly, this unit is the pulse height of light from VCT muons, I_{VEM}. Again, atmospheric muons peak are used to supply such a reference, as they produce a peak $I_{\mathrm{VEM}}^{\mathrm{peak}}$ in the pulse-height histogram that is used as the common reference unit for threshold levels (Fig. 2.12(b)). To maintain the proper trigger level, the conversion from channels to $I_{\mathrm{VEM}}^{\mathrm{peak}}$ has to be updated constantly.

The are three main steps for the calibration to VEM[21]units in order to determine the value of 1 VEMin integrated FADC channels are:

1. The initial end-to-end gains of each of the 3 PMTs are set to have $I_{\mathrm{VEM}}^{\mathrm{peak}}$ at 50 channels. This ensures that the signals recorded from the PMTs are similar in amplitude *(gain matching)* and sets the proper dynamic range and signal size for the electronics. Therefore, the sum of the three PMTs has a peak at channel 150 above baseline. The choice of 50 ch$/I_{\mathrm{VEM}}^{\mathrm{peak}}$ results in a mean gain of approximately 3.4×10^5.

2. After setting the gain of the three PMTs, a continuous online local calibration is performed to determine $I_{\mathrm{VEM}}^{\mathrm{peak}}$ in channels to adjust the electronics-level trigger. This compensates for drifts which occur after step the previous step.

3. Determination of $Q_{\mathrm{VEM}}^{\mathrm{peak}}$ ti high accuracy using the charge histograms. After converting the peak $Q_{\mathrm{VEM}}^{\mathrm{peak}}$ to 1 VEM, it is possible to convert the integrated signal of each PMTto VEMunits.

The calibration constants $Q_{\mathrm{VEM}}^{\mathrm{peak}}$ and $I_{\mathrm{VEM}}^{\mathrm{peak}}$ are obtained with a 2% resolution and sent to the CDAS together with every triggering event.

2.2.2 Surface Detector Trigger

The 1600 SD WCDs are connected to the Central Campus via a wireless communication system which is the main limitation to the rate of recordable events. The Central Campus must serve continuously all the stations spread over 3000 km^2, each using an emitter consuming <1 W power to transmit to collectors as far as 40 km away. On the one hand the maximum sustainable rate of event per WCD is less than one per hour and on the other hand the counting rate per WCD is 3 kHz, due to the atmospheric muon flux. Thus, the SD trigger system must reduce the single station rate, without inducing loss of physics events. The data acquisition (DAQ) trigger of the Surface Detector (SD) of the Pierre Auger Observatory has been designed to reduce the single station rate without loosing events of interest, to allow data acquisition down to the lowest possible energy and discriminate between real event and background. The DAQ has a hierarchical structure which consists of different trigger levels, organized as in the diagram 2.13, which allow to reduce at each level the rate per WCD and at the same time to storage the largest possible number of candidates air-shower events. At each level the conditions to be satisfied are more strict than the previous level, in order to discriminate physical from spurious and accidental events (i.e air-shower events from single atmospheric muons).

---

[21] vertical-equivalent muon

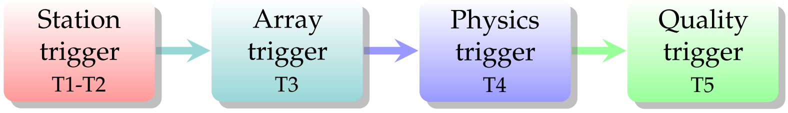

Diagram 2.13: SD trigger chain

2.2.3 Station triggers

The first two levels of triggers, called T1 and T2, are single WCD triggers performed at the detector level. Their aim is to separate possible events from background noise. The T1 trigger operate in two modes, the *threshold*(Thr) and the *time-over-threshold*(ToT) used to detect, in a complementary way, the electromagnetic and muonic components of an air shower.

- The Threshold T1 trigger (Thr1) requires a coincidence signal of the three PMTs of at least 1.75 VEMin a single time bin. The Th1 is used to select large signals that are not necessarily spread in time. It is particularly effective for the detection of very inclined showers that have traversed a large amount of atmosphere and are consequently dominantly muonic. It is used to reduce the atmospheric muon rate from 3kHz to 100Hz.

- The Time-Over-Threshold (ToT) mode needs to be satisfied a coincidence of at least two out of three PMTs recording a signal with more than 13 FADC bins ($>$ 325 ns) above 0.2 VEMwithin a sliding window of $3\mu s$ (120 bins). With a rate of $\approx$ 1.5 Hz, this condition selects small time-spread signals and for this reason it is more sensitive to the electromagnetic component of a shower. It is the relevant trigger for nearby but low energy showers or high-energetic showers with a distant core. Since the time spread of the ToT (325 ns) is larger than a single muon signal (150 ns), this trigger mode is very efficient eliminating random muons background. The ToT rate is $<$ 2 Hz.

Signals passing the ToT trigger are automatically promoted to the next level trigger T2, locally implemented in the software of the tank. The second-level T2 trigger is a stricter version of the T1 trigger, that can be described as a combination of a *threshold trigger* (Thr1) and the *time-over-threshold* trigger (T1 ToT). In order to promote a Thr1 to a Thr2 all three PMTs must exceed a signal threshold of 3.2 VEM, whereas all other ToT T1 triggers are automatically promoted. This trigger level permits to reduce to about 20 Hz the rate of events to be sent to the central WCD and it is particularly efficient for the selection of the muonic component of horizontal air showers and high energy events close to the shower core. The T2 triggered events are used to calculate the exposure of the array and to monitor the SD array performance. Only T2 signals, with their GPS timestamps are sent to the CDAS and used for the determination of the third level trigger, named T3 (see Sec. 2.2.4).

Two new trigger modes were introduced since June 2013 and stable trigger rates have been measured since January 2014.

- Time Over Threshold Deconvoluted trigger (ToTd[22]): was proposed as an optimisation of the ToT[23] trigger especially suited for lower energy events and to improve the sensitivity to photon and neutrino initiated showers [138][139]. The ToTd applies a slightly algorithm to the ToT trigger which deconvolves the digitized signal trace using the exponential tails in the Cherenkov light pulses produced by reflected light aiming at distinguish physical signals from background. Background signals appear as single peaks in the traces with an exponential tail due to the decay time of light in the tanks. The combination of many background peaks in a row may pass the ToT

---

[22] time-over-threshold deconvoluted trigger

[23] time-over-threshold trigger

criterion. For this reason, the deconvolution algorithm reduces the background signal to a single peak without tail, which would not survive the ToT condition since it is easily more distinguishable from a real signal which presents series of pulses. After this deconvolution the original ToT algorithm is applied.

- multiplicity-of-positive-steps trigger (MoPS[24]): was added in order to allow for the detection of signals below the VEMlevel in order to increase the sensitivity to small electromagnetic signals. It sums an extra constraint to the deconvoluted signal trace. The algorithm finds sequences of consecutive bins for which the FADC trace always increase with time and counts the number of subsequent positive steps that exceed a certain threshold within a 3μ window. An upper limit of 30 FADC is applied to the vertical signal time increment in order to respectively avoid statistical fluctuations and reject muon-like signals. In addition, to avoid false-positive step counts introduced by fluctuations in the tail of large signal peaks, a veto is implemented after a large step.

The two new triggers have been designed to be most sensitive to the electromagnetic part of the shower. The primary background for the signal measurement in individual stations is made of accidental muons, which are not part of the recorded shower. The new triggers are able to record smaller signals because of their insensitivity to background muons. This feature allows for measuring low energetic showers in order to extend the energy spectrum towards energies around the second knee.

2.2.4 Array triggers

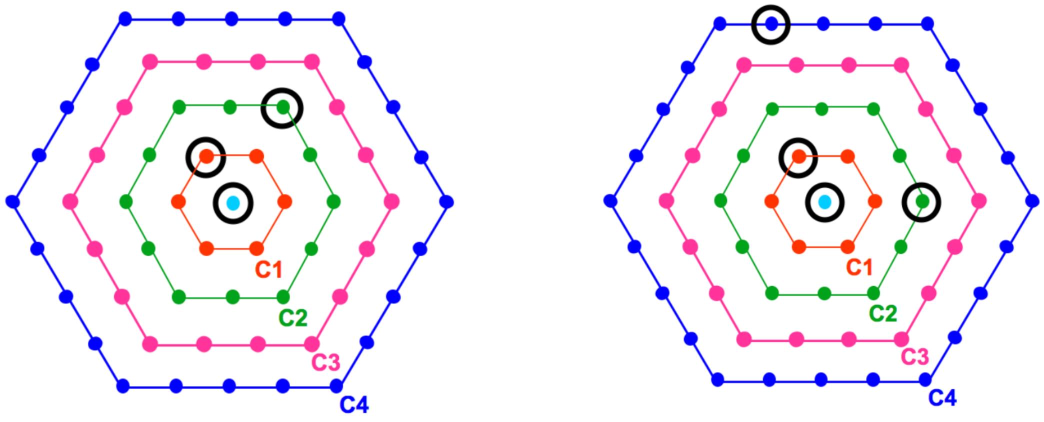

(a) 3-fold mode “ToT2C_1&3C_2” (b) 4-fold mode “2C_1&3C_2&4C_4”

Figure 2.14: Two examples of the two T3 triggering modes. For ‘the ‘ToT2C_1&3C_2” the considered detector must have one of its closest neighbours (first hexagon C_1) and one of its second closest neighbours (second hexagon C_2) triggered . For the 2C_1&3C_2&4C_4 at least one tank must be among the first set of neighbours (C_1), another one in the second set (C_2) and last one can be as far as in the fourth set (C_4).

The third-level trigger T3 is the first level trigger above the single WCD level which is formed at the CDAS. It searches for spatial and time coincidences among the saved T2 signals in different local WCDs aiming to select real air showers. Each WCD with a T2 sends

---

[24] Multiplicity of positive steps

the T2-timestamp to the CDAS that looks for one of the following patterns[25] within the whole array:

- a 3-fold condition requiring the coincidence of three neighbour stations which have passed the ToT trigger level satisfying a minimum compactness requirement, namely, selecting a central station, the two neighboring stations must be part of the first two crowns around it (C_1,C_2 [26]) (see Fig. 2.14(a)). The selected events with this so called T3-3 ToT trigger are 90% real showers, in particular showers below 60°, as the events passing the ToT condition have a very low background. The rate of T3-3 ToT with the full array in operation is around 1600 events per day, meaning that each detector participates in an event about three times per day.

- A 4-fold condition requiring the coincidence of four station fulfilling any kind of T2 (Thr2 or ToT). The 4-fold mode needs to be satisfied an additional requirement of more permissive compactness allowing the fourth station to be part of the fourth crown (C_4) around the central station instead of the second crown(see figure 2.14(b)). Due to its looser distance requirements, this condition is only relevant for horizontal showers, with zenith angles larger than 60°, with triggered detectors spread over a large ground area, as nearly all vertical showers fulfill the T3-3 ToT condition. This trigger mode selects about 1200 events per day, out of which about 10% are real showers.

Only events that pass one of the T3 criteria are sent to CDAS and stored for later analyses. The hierarchical trigger system is illustrated in Fig. 2.15.

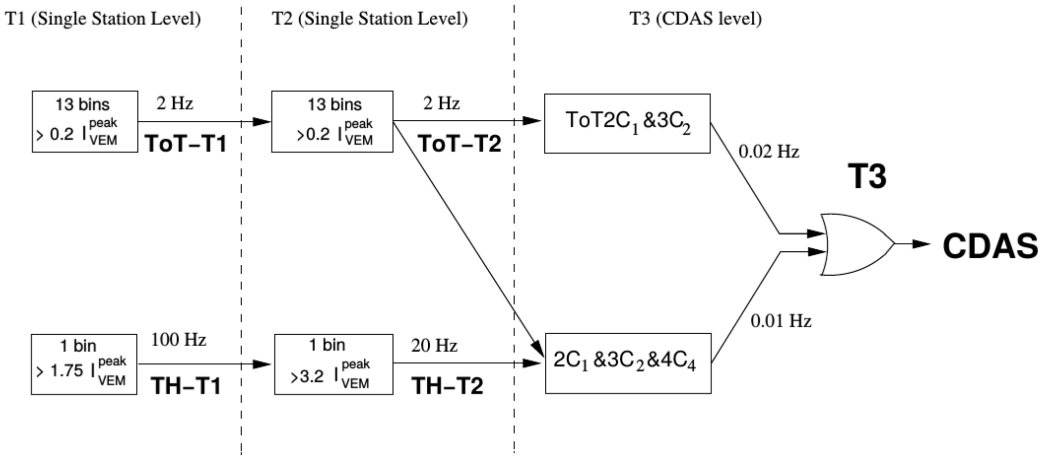

Figure 2.15: The hierarchical structure of the Surface Detector trigger of the Pierre Auger Observatory up to the third trigger level. An array trigger is obtained by the spatial and temporal combination of the local station triggers [140].

2.2.5 The Physics trigger

In order to further distinguish between real air shower events and accidental or lightning events, a stricter version of the T3 trigger, the T4 trigger algorithm, is applied on the stored T3 data. There are two different operating modes:

---

[25] In order to be sensitive to vertical ($\theta < 60^\circ$) as well as to inclined ($\theta > 60^\circ$) showers, two station patterns are allowed.

[26] referring as C_1 to the first set and as C_2 to the second set of neighbors around the reference WCD

- the compact T4-3 ToT configuration which requires at least three WCDs passing the T2-ToT in a triangular pattern (either equilateral or isosceles base triangle) configuration as depicted in Fig. 2.16(a). Due to their compactness, less than 2% of real EAS with zenith angles $\theta < 60^\circ$ are discarded by this condition. The number of accidental coincidences passing the T4-3 ToT is less that 1 per day thanks to the very low rate of the T2- ToT.

- the T4-4C1 criterion requires four non-aligned stations with any T2 trigger with the central station being surrounded by three stations lying in the first crown. Three example configurations are shown in Fig. 2.16(b).

This trigger ensures the selection of nearly-horizontal shower events, discarded by the T4-3 ToT trigger, bringing the efficiency up to almost 100% for showers below 60°. More over, to further discriminate real air showers from the background of random coincidences, an additional constraint is required: the trigger time delay among the candidates WCDs has to be compatible with the speed of light, which means that the differences in the start times between the selected WCDs has to be lower than $\frac{s}{c}$, where s is the spatial distance between two stations and c the speed of light in vacuum. In Fig. 2.17, the zenith angle and energy distributions of both trigger conditions are reported. At this trigger level two more procedures have been adopted to discard accidental stations[27]. The elementary triangle of WCDs with the highest signals, called the seed, is used to define the shower front plane of the event. A WCD will be so identified as accidental if its time delay to the front plane propagation is outside a time window of $[-2\mu; +2\mu]$. In addition, a candidate WCD with no triggered neighbours in 3 Km is considered isolated and so discarded.

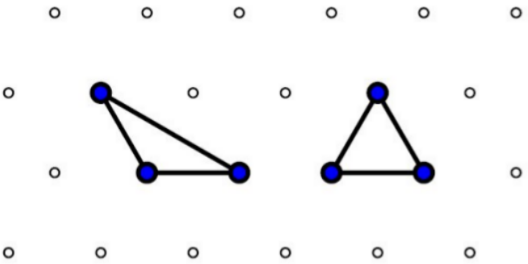

(a) The two possible compact T4-3ToT configuration

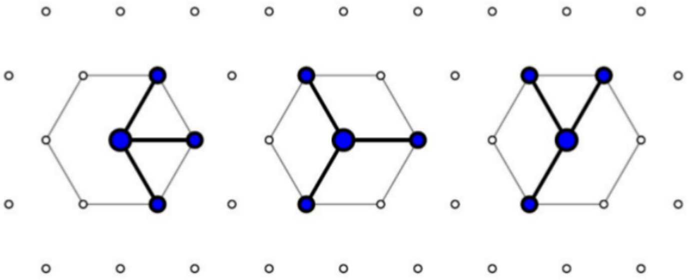

(b) Three minimal T4-4C1 configuration

Figure 2.16: Examples of some configurations of the two T4 triggering modes. All other configurations are given by symmetry transformation of the triangular grid.

---

[27] Triggered WCDs within the time window of a real atmospheric shower but originated from atmospheric muons or background radiation.

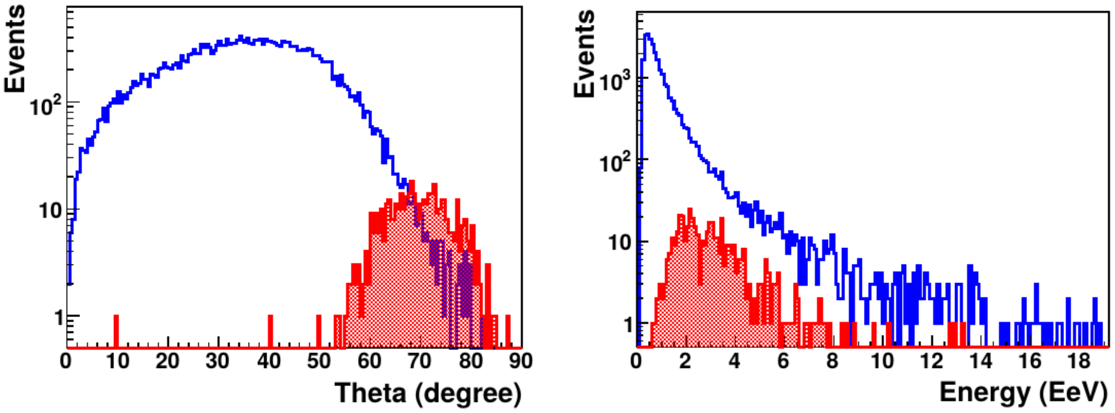

Figure 2.17: The zenith angle (left plot) and energy (right plot) distribution for event passing the T4 trigger selection. The blue unfilled histogram represent T4-3 ToT triggered events and the red filled area T4-4C1 triggered events. Those events fulfilling both T4 criteria are considered in the T4-3 ToT distribution [141].

2.2.6 The quality trigger

The quality trigger T5 is needed to select only showers fully contained in the array rejecting those events which fall too close to the border, where a part of the shower is probably missing. Such events could have wrong reconstructed core positions[28] and consequently wrong reconstructed energies. The most common T5 triggers are the 6T5 and 5T5 triggers. The 6T5 condition requires the station with the highest signal S_{max} of the event, also referred to as hottest station, to be surrounded by six active[29] stations (C1)[30]. The 5T5 is a loose version of 6T5 requiring that the hottest station has to be surrounded by five active stations. Thus, they only differ from each other for the user-defined number of required working neighbours.

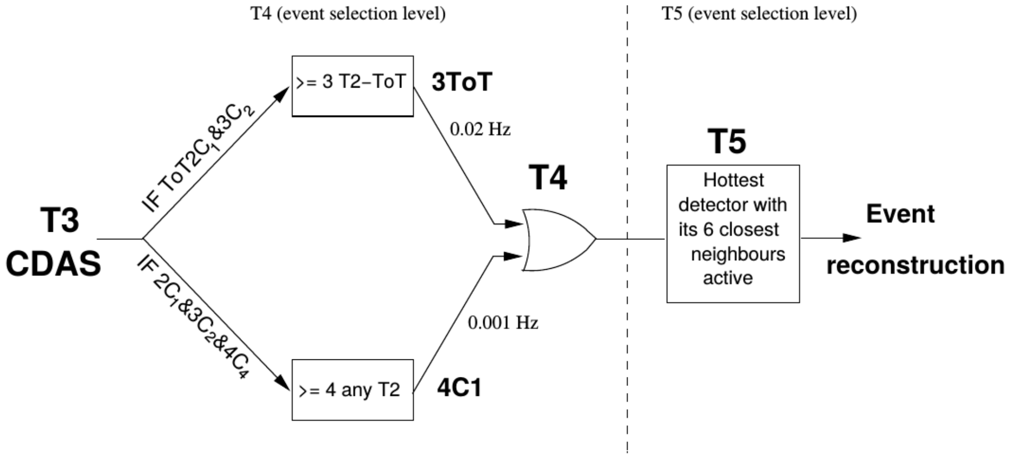

Figure 2.18: The hierarchical structure of the Surface Detector trigger of the Pierre Auger Observatory up to the fifth trigger level [140].

---

[28] Real cores outside the array are by construction reconstructed inside the array.

[29] working at the triggering time not necessarily passing any trigger condition.

[30] In reference to the first crown of neighbours

The T5 trigger ensures a good and unbiased event reconstruction by means of the selection of those events for which the shower core and energy could be properly reconstructed. More over, it allows an easier calculation of the exposure based on the determination of the geometrical aperture (available active hexagons integrated over solid angle) and observational time.

In addition, about 1% of the WCDs are expected to be not functioning at any moment even though detector maintenance is provided on a regular basis. Therefore, this criterion not only discards events that fall too close to the periphery of the array but also rejects events including a malfunctioning station around the hottest station, though contained in the array. Both event types show biases in the core reconstruction and their energy assignment as part of the signal information gets lost due to the missing or inactive stations. A side-effect of applying the quality trigger cut is the saturation of the effective detector area above a certain energy, hence becoming equal to the geometrical area. The shower footprint on ground scales with the primary energy. As a consequence, showers landing outside of the array can still trigger a sufficient amount of stations to allow for a reconstruction, leading to an increase of the detector acceptance with increasing energy without the cut. Two trigger modes have been realized in the past within the $\overline{\rm Off}\underline{\rm line}$ software.

The fifth level trigger which has been discussed until now is known as a *prior*-T5 which is calculated before the event reconstruction. A further T5 selection, called *posterior*-T5, a stricter version of *prior*-T5, takes place once the event has been reconstructed. Both T5 selections, shown in Fig. 2.19, can be enabled respectively for the *prior*-T5 by the `<EnableT5Trigger/>` and for the *posterior*-T5 by the `<EnableT5PosteriorTrigger/>` in the configuration file of the `SdEventSelectorOG`. The *posterior*-T5 condition requires that at the time of the event the station with highest signal must have at least 5 (or a user-defined number[31]) of activated WCDs (but not necessarily triggered) among its 6 closest neighbours. In addition, it requires that the reconstructed core to lie in an equilateral triangle of functioning stations and the number of active stations within the surrounding hexagon of the station with the highest signal is allowed to decrease from six to four stations. The method `SDEvent:Is6T5()` returns true if the event has a 6T5 flag before the reconstruction whereas the `SDEvent:Is5T5()` returns only true if the event is a 5T5 after reconstruction and if the shower core lies inside an equilateral triangle. In Fig. 2.18 is schematized the hierarchy of the SD trigger system up to the T5 level.

2.2.7 SD Event reconstruction

The aim of the reconstruction of air showers is the determination of the energy and the arrival direction of the primary UHECR, that can be achieved by fitting the reconstructed geometry of the shower, using the time and space information of the triggered WCDs, whereas the energy is inferred from an expected signal at a certain distance to the shower axis that serves as an estimator for the primary energy as explained in Sec. 4.6. In this section is reported the reconstruction of CR events using only the information from the SD. Once the single-station calibration procedure, mentioned in Sec. 2.2.1 to convert the signal to VEMs is performed, the air shower arrival direction can be determined using the timing of the signals.

Signal uncertainties The measurement of air showers is always object to statistical and systematic uncertainties. A precise study of these uncertainties is crucial to guarantee a valid air shower reconstruction and to assign proper uncertainties to the reconstructed quantities. As already mentioned before (see Sec 1.5.3), any particle interaction is affected by intrinsic

---

[31] The number of the required functioning stations surrounding the hottest one can be changed in the `SdEventSelector.xml`

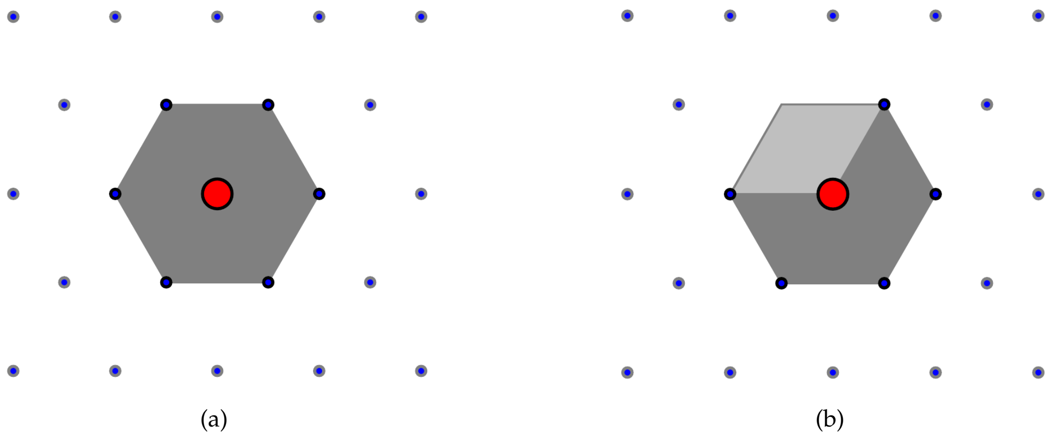

Figure 2.19: The T5 configuration, on the right the prior-to-reconstruction and on the left the posterior-to-reconstruction. In the center the station (red) with the largest signal surrounded by respectively 6 and 5 working stations (blue). In Fig. 2.19(b) the upper left corner station is missing from the array or not properly working. Only events with reconstructed cores in the grey-area will be accepted by the T5 after reconstruction criterion.

variations given by the inherent nature of particle interactions, called shower-to-shower fluctuations. Two identical primary particles with same primary quantities as energy, mass and arrival direction, and propagating through the same atmospheric conditions, will produce different showers and as a consequence signals at the ground will differ. The shower discrepancy would increase considering a non-ideal detector as the atmosphere as well as the background radiation are constantly evolving. These fluctuations have typically the size of 10% and influence all stations of the same shower in the same way. For this reason, they do not have to be considered at the event-level reconstruction. In addition, signals of the SD stations are subject to uncertainties which are driven from the statistical sampling of particles which means that measurements can only be performed up to a certain accuracy that can be estimated analyzing the signals coming from the so-called multiplet stations. The distance between the twin stations is of 11 m, which is negligible compare to the footprint of the whole shower. When a shower core falls close to a multiplet, the particle density increase when approaching the core. The different in the signals measured by the multiplets, which are considered to measure the same spot in the shower, determine the uncertainty of the signal for the whole array, which decrease as the number of particles hitting the detector and thus the signal increases. The relative uncertainty of the signals in the WCD, originating from sampling and shower-to-shower fluctuations, scales with $1/\sqrt{S}$, reflecting the Poisson-like behavior of a particle counter as shown in Fig. 2.20(a).

The Poisson-like term that describes these uncertainties, is normalized by a zenith-angle dependent factor $\propto \sec\theta$, as the signal uncertainty depends on the ratio of the electromagnetic and the muonic components. Indeed, for inclined showers the relative muonic-component contribution to the signal increases, together with the fraction of signal produced by muons in the WCD, as the electromagnetic component of the shower suffers from the attenuation in the atmosphere. The dependency of the signal with the zenith angle is shown in Fig. 2.20(b). A model for the signal uncertainty can be written as [142]

$$f_S := \frac{\sigma[S]}{\sqrt{S}}(\theta) = a \cdot (1 + b(\sec\theta - \sec 35^\circ)) = 0.865(1 + 0.593(\sec\theta - 1.22))\,. \tag{2.11}$$

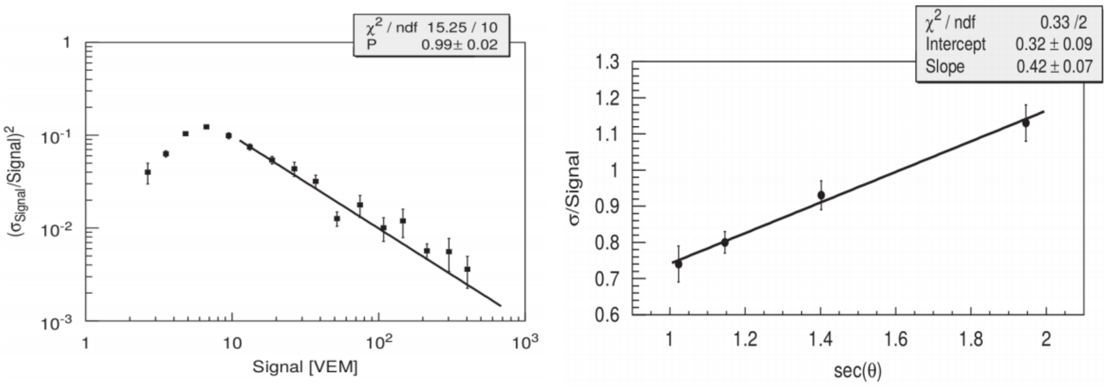

(a) (b)

Figure 2.20: Fig. 2.20(a): Surface detector signal accuracy. Values below 10 VEMare distorted by triggering efficiency. The line represents a Poissonian-like fit of the type $\sigma/\mathrm{Signal} = P/\sqrt{S}$. Fig. 2.20(b): Signal accuracy zenith angle dependence [143].

Geometry reconstruction The secondary particles arrive on the ground in a curved shower front. The shower direction can be determined by finding the zenith (θ) and azimuth (ϕ) angles for which a shower front would arrive at each station at the time of its triggering. The accuracy of the shower reconstruction improves with the number of stations included in this determination and is generally around a few degrees. The shower geometry is determined almost entirely by the start times of the signals of the triggered WCDs. The secondary particles are assumed to arrive in a shower front that is cylindrically symmetric around the shower axis. Thus, the orientation of the axis can be almost entirely determined by comparing the signal start times to the arrival time of the shower front at a particular station.

The first step of the standard reconstruction starts with the selection of a seed stations, which firstly has to fulfill either the three-fold or the four-fold mode of the T4 trigger (Sec. 2.2.5) and secondly, it has to be part of a set of stations that maximizes the sum of the individual signals. The trigger times of these chosen stations are the ones that are going to be fit to the shower front in order to determine the shower direction. The signal start times of all stations not belonging to the seed are then compared to the expected time for the shower to arrive at the individual stations. Stations with times not compatible within a certain margin are flagged as accidental and are discarded from the reconstruction.

The weighted time average is used as time origin t_0 and the weighted-signal barycenter, $\left(\vec{b}\right)$, of the stations involved in the event determines the spatial origin $\vec{x}_0$ (see Fig. 2.21(a)) as the the shower impact point on the ground (core position) .A first estimate of the CR arrival direction consists in approximating the shower-front to a plane moving at the speed of light and in identifying the direction (θ, ϕ) with the shower direction. The shower axis is then a unitary vector $\hat{a} = (u, v, w)$ at the shower impact point on the ground, perpendicular to the shower plane, and pointing towards the the primary particle. If we consider a planar shower front coming from the direction $\hat{a}$ (along the shower axis), the arrival time at a particular position $t(\vec{x})$, with respect to the baricenter $\vec{b}$, can be expressed as

$$c\,(t_0 - t(\vec{x})) = \left(\vec{x} - \vec{b}\right)\hat{a}\,. \tag{2.12}$$

Thus, the time when the shower plane passes the point $\vec{x} = (x, y, z)$ can be derived as

$$ct(\vec{x}) = ct_0 - \left(\vec{x} - \vec{b}\right)\hat{a}\,. \tag{2.13}$$

Defining the generic point $(t, \vec{x})$ as the WCD positions $\vec{x}_i \equiv (x_i, y_i, z_i)$ and the signal start times t_i, which are measured, the unknown variables in Eq. 2.13 are the three coordinates of the shower axis $\hat{a}$. Therefore, to gather the shower-axis components, a fit of the shower front can be performed by minimizing the sum of the squared time differences between the measured start times t and the expected times $t(\vec{x}_i)$, weighted by the start-time variances $\sigma_{t_i}^2$ of the start signal of the station i at the position $\vec{x}_i' \equiv \vec{x}_i - \vec{b}$ [144]:

$$\begin{aligned}\sum_{i=1}^{N_{\text{stations}}} \frac{|t_i - t(\vec{x}_i)|^2}{\sigma_{t_i}^2} &= \sum_{i=1}^{N_{\text{stations}}} \frac{|c(t_i - t_0) + \vec{x}_i' \cdot \hat{a})|^2}{c^2\sigma_{t_i}^2} \\ &= \sum_{i=1}^{N_{\text{stations}}} \frac{|c(t_i - t_0) + x_i' u + y_i' v + z_i' w|^2}{c^2\sigma_{t_i}^2} \,.\end{aligned} \tag{2.14}$$

Since the vector $\hat{a}$ is unitary, this generate a non-linear equation that can be approximately solved assuming all stations to be close enough to the tangential plane to the ground containing the barycentre. Using this approximate solution the z-component can be neglected, being $z_i \ll x_i, y_i$.

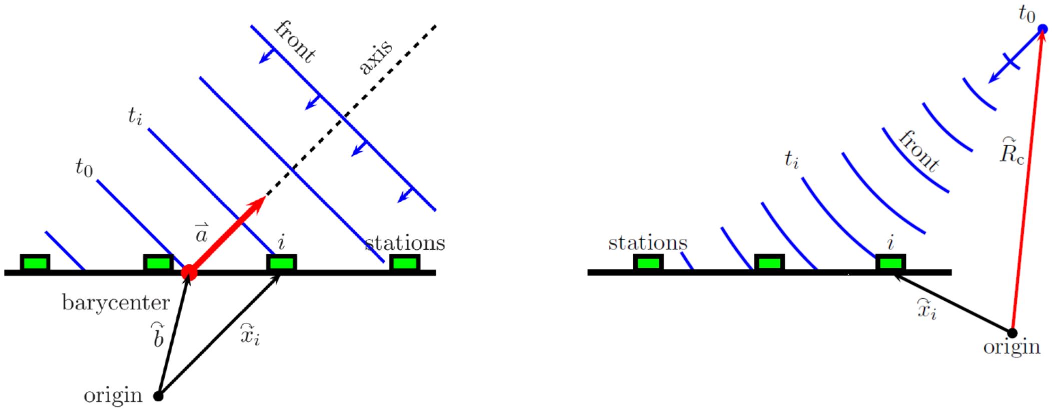

(a) Planar shower front model

(b) Spherical shower front model

Figure 2.21: Fig 2.21(a): schematic illustration of the planar-front approximation used for a first estimate of the incoming direction of the primary particle. Fig 2.21(b): schematic illustration of the spherical-front approximation used to improve the shower-direction estimate.

A more realistic approximation of a spherical shower front (depicted in Fig. 2.21(b)) is used in order to improve the estimate of the incoming direction. This more elaborate model, based on a curved front fit, is an extension of the plane fit method: the varying altitude of the stations is taken into account and a parabolic term is used to describe the curvature of the shower front near the impact point (see Fig. 2.22). Thus, considering a shower front with a spherical surface expanding at the speed of light, originating from the virtual point $\vec{R}_c$ at the time t_0, the time propagation of the shower front is described by

$$c(t_i - t_0) = |\vec{R}_c - \vec{x}_i| \,, \tag{2.15}$$

where $\vec{x}_i$ are the station positions triggered at the times t_i. As we are interested in the shower axis $\hat{a}$, the origin $\vec{R}_c$ can be parametrize as $\vec{R}_c = \vec{c} + R_c\hat{a}$, where R is the radius of curvature measured at the impact point c of the shower axis on ground, from now on denoted as shower core. The shower core has to be estimated in advance while the trigger times and the station positions serve as inputs for the fit. Because each triggered station in a T4 event

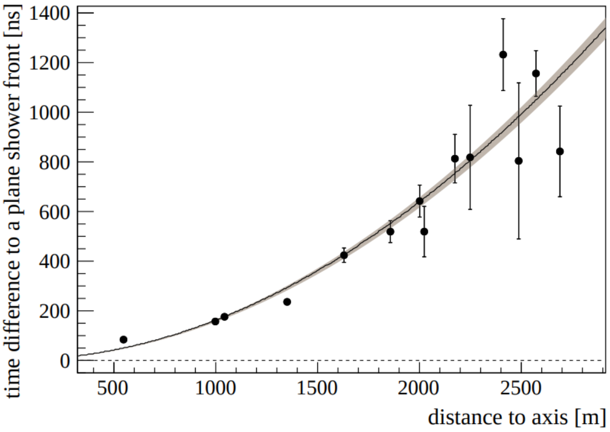

Figure 2.22: The dependence of signal start times (relative to the timing of a plane shower front) on perpendicular distance to the shower axis. The shaded line is the resulting fit of the evolution model and its uncertainty [133].

contributes one degree of freedom to the geometric fit, the four parameters can be underconstrained for small, three-station events. For events with fewer than 5 triggered stations, the shower front's curvature is ignored and the expected times are calculated from a plane front.

Therefore, the minimization of

$$\sum_{i=1}^{N_{\text{stations}}} = \frac{(|c(t_i - t_0) - |R_c\hat{a} - x'_i|)^2}{c^2\sigma_{t_i}^2}\,, \tag{2.16}$$

with $x'_i = x_i - c$ can be carried out approximately in an analytical way or with a numerical non-linear optimization, to determine the radius of curvature $\vec{R}_c$ and accurate shower-axis coordinates.

Lateral distribution function Once the shower axis vector has been estimated, it is possible to determine the lateral dependence of the measured signals. Using the geometric results coming from the previous section, the second step in the reconstruction process is the fit of the lateral distribution of the signal measured in the WCDs that can be described by

$$S(r) = S_{r_{\text{opt}}} \times f_{\text{LDF}}(r)\,, \tag{2.17}$$

where, $S(r)$ is the decreasing signal which depends on distance, r, between the station and the shower axis in the shower plane, also called axial distance. The f_{LDF} is a particular shape parametrization normalized such that $f_{\text{LDF}}(r_{\text{opt}}) = 1$. The optimal distance r_{opt} is defined as the distance on the shower plane that depends least on the functional form used for the LDF. In other words, the expected signal at this distance results in a robust estimate, as it is the point where changes in the slope (induced by shower-to-shower fluctuations and statistical fluctuations in the number of particles) have the minimum influence on the LDF. It depends on the array spacing and it was estimated to be 1000 m, 450 m, and 250 m for the SD-1500, the SD-750, and the SD-433 respectively [145–147]. Although different functional forms of the LDF have been investigated, it was found that a modified Nishimura-Kamata-Greisen (NKG[32]) function provides the best description of the data measured by Auger [148]:

$$f_{\mathrm{LDF}}(r) = \left(\frac{r}{r_{\mathrm{opt}}}\right)^{\beta} \times \left(\frac{r + r_{\mathrm{scale}}}{r_{\mathrm{opt}} + r_{\mathrm{scale}}}\right)^{\beta+\gamma} . \tag{2.18}$$

The parameters β and γ control the slope of the LDF and depend on the zenith angle. They are left fixed to a parameterization during the shower reconstruction. The shape parameter β, defines the steepness of the LDF governing the signal drop with increasing distance, while γ allows for more flexibility of the function far from the core where the lateral distribution is mainly dominated by muons. For this work, the LDF parameter γ was set to 0 and not fitted. The reason is that the beta-only LDF gives a good description of the data and, secondly, that a simultaneous fit of β and γ sets rigorous requirements on the events, especially concerning the low number of stations. The scale parameter r_{scale} plays a role only at larger distances from the shower axis, and in addition it is strongly correlated to β, hence it has been kept fixed to its hard-coded value of 700 m. If requested by the user, the slope parameter may be left as free parameter during the reconstruction procedure and estimated with a global fit. However, if the number of stations participating in the event is less than five[33][34], the slope cannot be fitted with enough precision and β is kept fixed according to the following model:

$$\beta(\log_{10} S_{r_{\mathrm{opt}}}, \theta) = a + b \log_{10} S_{r_{\mathrm{opt}}} + (c + d \log_{10} S_{r_{\mathrm{opt}}}) \sec\theta + (e + f \log_{10} S_{r_{\mathrm{opt}}}) \sec^2\theta\,, \tag{2.19}$$

where θ is the shower zenith angle, and $S_{r_{\mathrm{opt}}}$ is the signal measured at the optimal distance r_{opt}. The six parameters above depend on the array geometry, and their determination for the SD-433 array is part of this thesis work.

The maximum likelihood method is then used for estimating the LDF. The effective number of particle that induce a certain signal in the detector is unknown, since the WCD itself only provides information about photo-electrons that are induced by Cherenkov photons. This number depends on the the type of the secondary particles, their zenith angle and distance of the station from the shower core. In order to construct the likelihood, an effective conversion from signal in units of VEMto a number of particles is used. This conversion depends mainly on the zenith angle of the shower and is derived from the signal uncertainty model as described before. The effective number of particles is then given by

$$n_{\mathrm{eff}} = p(S/\mathrm{VEM})\,, \tag{2.20}$$

where p is the so-called Poisson factor depicted in Fig. 2.23(b) as a function of zenith angle and described as

$$p = t + \frac{1-t}{\sqrt{f_S}}\,, \tag{2.21}$$

where $t := 1(1+e^{z})$, $z := 40(0.98 - f_S)$ and f_S given by Eq. 2.11. For very inclined shower o larger distances from the core, the signal is dominated by the muonic component and as the signal of one VCT muon is on average 1 VEM, the Poisson factor approaches one. Thee electromagnetic shower component suffers from attenuation in the atmosphere for large zenith angles and for this reason is only important at low zenith angles, where around 20 particles are needed to produce an equivalent signal of 1 VEM.

---

[32] Nishimura-Kamata-Greisen

[33] More conditions have to be satisfied in order to properly fit β and leaving it as a free parameter. For more details see Sec. 4.5

[34] The number of candidate stations required to free the slope parameter can be changed within the $\overline{\text{Off}}\underline{\text{line}}$ reconstruction, although a minimum of four candidate stations is always required for a free β fit.

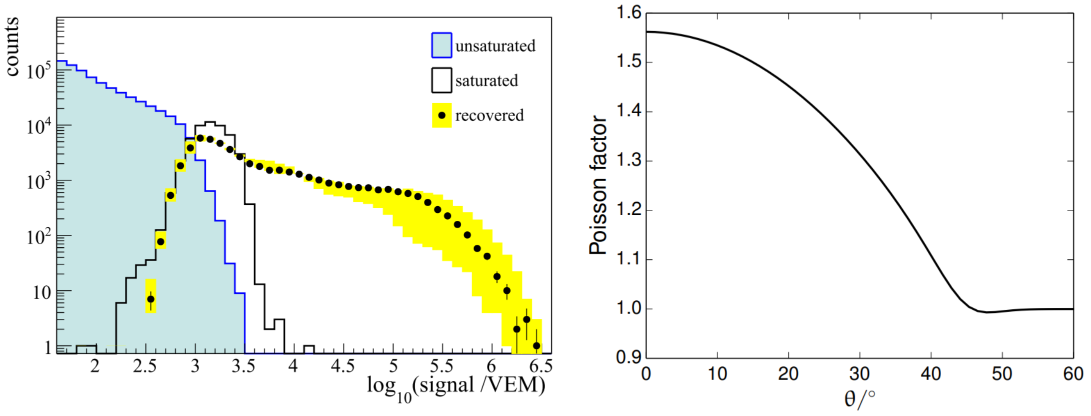

(a) (b)

Figure 2.23: The Poisson factor used to convert signals to effective particle numbers as explained in the text. The factor is shown as a function of zenith angle [146].

The factor is estimated from the signal uncertainty model as

$$p = \max\left(1, 1/f_S^2(\theta)\right) . \tag{2.22}$$

Once signals are converted to effective particle numbers, the likelihood function for the LDF fit can be constructed as follows:

$$\mathcal{L} = \prod_i f_P(n_i, \mu_i) \prod_i f_G(n_i, \mu_i) \prod_i F_{\text{sat}}(n_i, \mu_i) \prod_i F_{\text{zero}}(n_i, \mu_i) , \tag{2.23}$$

where n_i is the effective particle number for a given station and μ_i its expectation given from the LDF. The function has three contributions that cover non-saturated signals, saturated signal and non-triggered signals:

- *Small signals*: correspond to particle number less than 30 and follow a Poisson probability distribution

$$f_P(n_i, \mu_i) = \frac{\mu_i^{n_i} e^{-\mu_i}}{n_i!} . \tag{2.24}$$

- *Large signals*: with effective number of particles larger than 30 that make use of the central limit theorem that allows for the Gaussian approximation for signals with $S_i \geq S^{\text{G}} = 15$ VEM. These signals are described by the Gaussian distribution

$$f_G(n_i, \mu_i) = \frac{1}{\sqrt{s\pi\sigma_i}} \exp\left(-\frac{(n_i - \mu_i)^2}{2\sigma_i^2}\right) , \tag{2.25}$$

  where σ_i are the signal uncertainties described with the model in Eq. 2.11. Successfully recovered signals from saturated stations are used in the Gaussian approximation and the uncertainty of the saturation recovery is added to the signal uncertainty. The distribution of the recovered signals is shown in Fig. 2.23(a).

- *Saturated signals*: in the case a saturated signal can not be recovered, it is used as a lower limit in the likelihood. The probability of measuring a signal larger than the saturated one as is obtain by integrating the Gaussian distribution over all possible values larger than n_i:

$$F_{\text{sat}}(n_i, \mu_i) = \int_{n_i}^{\infty} f_G(n, \mu_i) dn = \frac{1}{2} \text{erfc}\left(\frac{n_i - \mu_i}{\sqrt{2}\sigma_i}\right) , \tag{2.26}$$

with $\mathrm{erfc}(z) = 2\sqrt{\pi}\int_z^\infty e^{-t^2}$ is the complementary error function.

- *Zero signal*: are those stations that do not exceed a certain energy threshold required from a trigger: for the standard single station triggers ToT and Thr this threshold is about 3 VEM, while for the new triggers (ToTd and MoPS) is of about 1 VEM. The non-triggered stations are also taken into account for the fit by summing up for each of the non-triggered stations that enter the likelihood, the Poissonian probabilities below the energy threshold. Therefore, the probability of obtaining an effective number of particles n_i less than the observed at the threshold, n_{th}, can be calculated by integrating the Poissonian distribution from 0 to n_{th} as follows

$$F_{\mathrm{zero}}(n_{\mathrm{th}}, \mu_i) = \sum_{n=0}^{n_{\mathrm{th}}} f_P(n, \mu_i)\,. \tag{2.27}$$

The fit of the LDF is performed maximizing the likelihood in Eq. 2.23 or, equivalently, minimizing the negative log-likelihood

$$\mathcal{L} = \sum_i \ln f_P(n_i, \mu_i) + \sum_i \ln f_G(n_i, \mu_i) + \sum_i \ln F_{\mathrm{sat}}(n_i, \mu_i) + \sum_i \ln F_{\mathrm{zero}}(n_i, \mu_i)\,. \tag{2.28}$$

The LDF in Eq. 2.18 has already three parameters: the shower size ($S_{r_{\mathrm{opt}}}$), β, and γ. Considering the core position and the arrival direction, the number of parameters that need to be fit increases to at least eight. The fit procedure implemented in the $\overline{\mathrm{Off}}\underline{\mathrm{line}}$ framework in divided into different stages in which some of the parameters are fixed to estimates[35] or to values obtained from previous parameterizations. This reduces the number of free parameters and improves the fit convergence. If there are less than five candidate stations, the parameters β and γ cannot be fitted and they are fixed to values coming from previous parameterizations. For the SD-1500 the slope parametrizations were obtained by analyzing a set of Auger events with large station multiplicities [149], while for the SD-750, the best set of parameters for β and γ were obtained from a global event fit as described in [146]. As mentioned before, for this work the parameter γ will not be considered and the set of parameters for the SD-433 is going to be presented.

Primary energy The primary energy is mainly estimated using the value of the shower size $S_{r_{\mathrm{opt}}}$. The value of $S_{r_{\mathrm{opt}}}$ decreases with increasing zenith angle because of the atmospheric attenuation of the shower particles. The amount of traversed matter (slant depth) increases approximately with $1/\cos\theta$ with the result that a shower arriving at 60° traverses about twice the amount of matter compared to a vertical shower with a zenith angle of 0°. The number of interactions increase with the zenith angle as the the amount of traversed atmosphere increases. The density of traversed atmosphere is of most relevance for the electromagnetic part of an EAS as frequent interactions are the foundation of this shower component. As the number of interactions within the atmosphere increases with zenith angle, the electromagnetic component attenuates. On the contrary, for muons is decisive their chance of decaying, which depends on the traversed distance and not on the slant depth, since muons interact more rarely compared to electrons and photons. Their chance of decaying depends on the traversed distance and not on the slant depth. Hence, the attenuation of the muonic component is negligible at least for zenith angles $< 60°$, whereas the electromagnetic component descreases with zenith angles. This leads to a dependence on the zenith angle of the shower size that need to be corrected in order to get a zenith-independent energy estimator. This

---

[35] $S_{r_{\mathrm{opt}}}$ is estimated from the signal in the station closest to the optimal distance

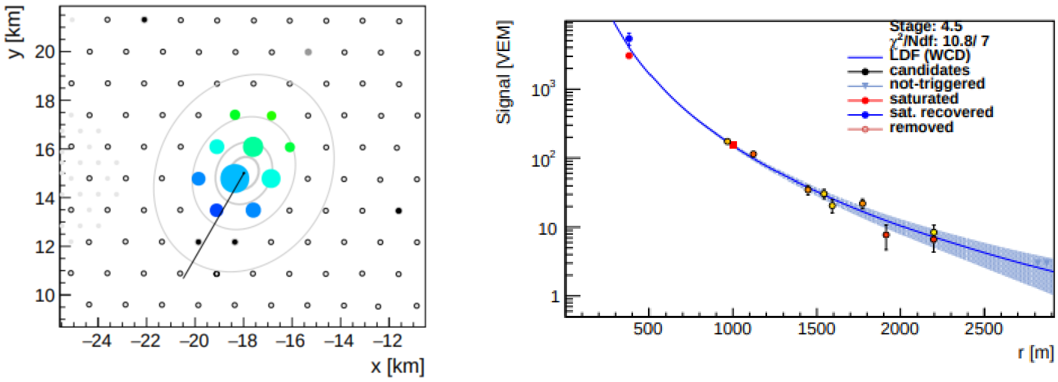

(a)

(b)

Figure 2.24: Fig. 2.24(a): Example footprint of an air shower measured by the SD. The arrival direction and the core position are indicated by the solid line. Triggered stations are indicated by colored circles with the timing ranging from blue for early trigger times to green for late ones. The size of the circle corresponds to the deposited signal in the station. The shower axis and core location are indicated by the black arrow. The x- and y-axes represent represent the eastingand northing distances, respectively. The reconstructed arrival direction is indicated by the solid black line. Fig. 2.24(b): Lateral distribution fit to the measured signals of an SD-1500 event with a reconstructed energy of 3.1210^{19} eV and a zenith angle of 32.9° (Event time: 31. May 2019, Auger ID:191508582800). The signal size at the optimal distance of 1000 m ($S_{r_{\text{opt}}} = S_{1000}$ for the SD-1500), referred to as shower size, is visualized by the square marker in red. Non-triggered stations are indicated by gray triangles and are used to estimate the position of the core. Both figures are taken from the EventBrowser of Offline.

dependency can be disentangled by means of the *Constant Intensity Cut* (CIC[36]) method [150]. Assumes an isotropic high-energy cosmic-ray flux in $\cos^2\theta$ above a certain energy threshold, $S_{r_{\text{opt}}}$ is converted into a reference signal S_{ref} solely dependent on the energy as:

$$S_{\text{ref}}(E) = \frac{S_{r_{\text{opt}}}(\theta, E)}{f_{\text{CIC}}(\theta)}\,, \tag{2.29}$$

where the attenuation function, f_{CIC}, is a third degree polynomial in the variable $x = \cos^2\theta - \cos^2(38^\circ)$ that is

$$f_{\text{CIC}} = 1 + ax + bx^2 + cx^3\,. \tag{2.30}$$

The parameters a, b, and c are obtained from the fit on the event intensities (number of events above a given threshold) at different zenith angles. The $\theta-$independent energy estimator, S_{ref}, could be interpreted as the $S_{r_{\text{opt}}}$ that a shower would have produced, had it arrived with a zenith angle of θ_{ref}, which depends on the trigger-threshold energy of the array (and thus on the array geometry) and represents the median zenith angle, so the impact of the correction factor is minimized. After the application of weather and atmospheric corrections to the S_{ref}, the energy estimate is given by

$$E_{\text{SD}} = A \cdot \left(\frac{S_{\text{ref}}}{\text{VEM}}\right)^{\text{B}} \text{EeV}\,. \tag{2.31}$$

Using the information provided by the FD, it is possible to obtain the energy corresponding to each S_{ref} almost entirely from data, except for assumptions about the missing energy. Only

---

[36] Constant Intensity Cut

data with a successful hybrid geometry reconstruction were selected to parametrize the CIC method. Therefore, with the calibration, the coefficients A and B are determined through a comparison of the estimator S_{ref} and the energy reconstructed from FD data for a set of high quality hybrid events, from which an energy estimate is obtained.

2.3 Auger Enhancements

Many enhancements have been made to the Observatory since the successful completion of the two main detectors (SD, FD) with the intent of lowering of the Pierre Auger Observatory's minimum energy threshold to improve sensitivity to showers in the knee-to-ankle region of the energy spectrum (E $\sim 10^{17}$ eV) to cover the energy range of interest for the transition from galactic to extragalactic cosmic rays. This section will discuss a number of the notable enhancements, as well as future upgrade plans for the Observatory.

The HEAT enhancement

The High Elevation Auger Telescopes (HEAT) complements the Auger FD with three additional telescopes acting as the low-energy extension of the fluorescence- detection technique [151, 152]. HEAT is located near the Coihueco FD eye, ~180 m north-east of the Coihueco building. With decreasing energy (less than 10^{18} eV), the amount of emitted fluorescence photons is reduced compared to those initiated by higher energy primaries, and the shower has to land closer to a telescope in order to be detected. Sensitivity to EAS initiated by low energy cosmic ray can be improved by extending the field of view of the FD to higher elevations. As low-energy showers reach their maximum development at higher altitudes in the atmosphere, the X_{max} is not directly accessible because it is outside the field of view of the base design of the standard FD telescopes, which is limited to 30° above the horizon. For this reason, though the optical system is the same as the standard FD, these telescopes are housed in large concrete buildings, which in turn are mounted on top of a hydraulic mechanism capable of changing the elevation of the telescope optical axis. These shelters are capable of operating in two configurations: a downward and upward tilting mode. In their upward position, the range of vertical viewing angle is extended from 30° up to 60°, which in combination with the Coihueco field of view gives an elevation coverage from 0° to 60°, allowing for the observation of lower energy showers which would otherwise be unseen by the standard FD. When operating in downward mode, the field of view of the HEAT telescopes overlap with those of Coihueco (in both azimuth and elevation), allowing for useful cross-calibration and shower reconstruction studies. A virtual FD called HeCo, is built from the combination of the three HEAT telescopes and Coihueco during the reconstruction [153]. The first measurements with a single HEAT telescope began in January 2009, and since September 2009 data acquisition started with all 3 telescopes [154].

2.3.1 The SD-750 array

The main SD array (SD-1500) has a full efficiency threshold at $10^{18.5}$ eV. In order to study the energy spectrum between the second knee and ankle, where the transition from galactic to extragalactic cosmic rays is supposed to occur, a lower energy extension of the Pierre Auger Observatory has been constructed, to extend the sensitivity of the SD array down to 3×10^{17} eV [155]. The extensions include a new surface array of 71 WCDs out of which 49 have been deployed in addition to the SD-1500 stations and the rest are shared stations

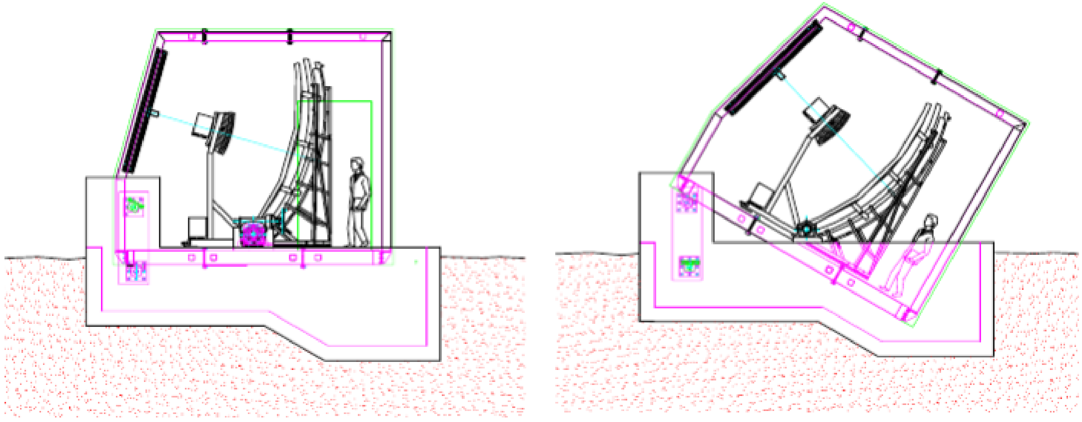

(a) Downward mode for service and calibration studies.

(b) Upward mode to improve sensitivity to lower energy showers.

Figure 2.25: The two operating configurations of the HEAT enhancement.

Figure 2.26: Photo of the HEAT telescopes in titled mode

amongst the two arrays[37], arranged in a 750 m triangular grid called Infill array or SD-750, covering an area of 27 km^2 as shown in Fig. 2.30(a). The SD-750 benefits from the preexisting infrastructure, communication systems, trigger logic, and data acquisition tools. It is located close to the FD sites Coihueco and HEAT, which both overlook the SD-750 with three telescopes having the chance to measure low energetic showers in hybrid mode. Data taking with the first hexagon started in September 2007 and the array was fully completed in September 2012. In July 2013, new station triggers were installed in all SD stations, enhancing the sensitivity of individual stations towards small signals in the 1 VEMregime. As a result or this implementation, the threshold of full efficiency for the SD-750 is lowered to about $10^{17.2}$ eV, as shown in [156]. Many experiments measuring the flux of cosmic rays in the energy region around 10^{17} eV have observed a softening near this energy which has been called the second knee that could be related to a change in the sources or the composition of the primary particles. This spectral feature has been observed for the first time at the Pierre Auger Observatory around $10^{17.22}$ eV using Cherenkov–dominated events taken by the FD [157]. Further analyses performed with the SD-750 were able to decrease its energy threshold down to 10^{17} eV giving the most precise measurement of the energy spectrum near the second knee [158]. As a result of the decreased energy threshold a change in the spectral index (from ≤ 3.1 to 3.3) near the second knee was observed for the first time. Al-

---

[37] The extra 49 WCDs needed to complete the grid have the same design as the WCDs employed in the SD-1500.

though the identified spectral feature is fairly consistent with those of other experiments that observed the second knee, it is still illustrative to compare the results from this work to other measurements, since the feature is only observed on one side by Auger and there may be a slight bias in the various values and in the fitting procedure. Because of the 750 m array's size, this is the highest precision measurement in an energy region where most other measurements begin to be dominated by statistical uncertainties. In these respects, a further extension of the SD array able to reach the second knee energy range and lower, makes possible a combined analysis with the results of the SD-750 and SD-1500 arrays with the prospect of making some of the most precise measurements of the cosmic rays in an energy range where there are theoretical motivations to expect a transition from galactic to extragalactic sources.

2.3.2 The SD-433 array

The SD-750 is 98% efficient for showers with energies greater than 10^{17} eV, restricting the angular acceptance to 40° and regardless of hadronic model or mass pointing out the need of an even denser array in order to completely cover the second knee energy range with full efficiency. The original proposal for the AMIGA enhancement included, not only a graded infill of 750 m separation, but also a denser infill with a separation of 433 m. The SD-433 was planned as the low-energy enhancement of the SD that would allow to measure low energetic showers and to extend the energy spectrum towards energies around the second knee. In November 2011 has started the deployment of the first three WCDs (Ids 97, 98, 99) placed at 433 m around the Central Station Tina Turner (TT, with Id 1764), already part of the 750 m SD array (SD-750), at the AERA site. At that moment the T2s from the new stations were not used to make an SD trigger, because the number of T3 requests for neighboring stations was too high. Indeed, such a narrow-spaced array has a very high rate and for this reason, a dedicated trigger, called AERA, was implemented in CDAS at the end of August 2012. This new trigger algorithm was designed to allow the detection of air showers by means of the 433 m array. In other words, it only requires SD-433 station to perform a trigger in order to avoid data-stream overload. In January 2013 another three WCDs (Ids 11, 12, 13) have been disposed in the field. Six more WCDs, also part of the SD-750, surround this hexagon in an incomplete second crown, as illustrated in Fig. 2.27(a) The full hexagon around TT, named AERALET, constitute the elementary cell of the SD-433 and became fully operational in May 2013. The first upgrade to the base design of the SD-433 was approved in November 2016. It consisted in the deployment of three additional WCDs (Ids 27, 28, 29) increasing the aperture from one to four hexagons. They became properly operational since January 1, 2018. For the second and final upgrade of the SD-433, three more WCDs (Ids 42, 50, 54) were arranged to reach a 7-hexagon aperture on May 11, 2019. The final and current status of the array is shown in Fig. 2.27. Between Fig. 2.27(a) and Fig. 2.27(b) a difference in the station Ids can be noticed: stations with Ids 98 and 13 have been moved (of 67 m and 33 m respectively) to a new position since they were not placed at $\sim$ 433 from their neighbors. Thus, their Ids changed from 98 to 30 and from 13 to 47[38].

In Fig. 2.28 the real asset of the SD-433 in its first deployment is displayed. Using the information provided by the T2 monitoring files (See Sec. 4.1) on one-second time base about the activity of each WCD, we are able to declare whether the station is working ("on") or not ("off"), thus if the station participate to the event or not. By taking properly into account the T2 info we can reveal that the station 98 was active until June 9, 2017, participating in the events until the GPS t_{last} =1181027481. The timestamp of the first event in which the very same WCD appears with the new id (30) is June 30, 2017 with GPS t_{first} =1181027481.

---

[38] The Ids of the SD-433 stations are always numbers < 100.

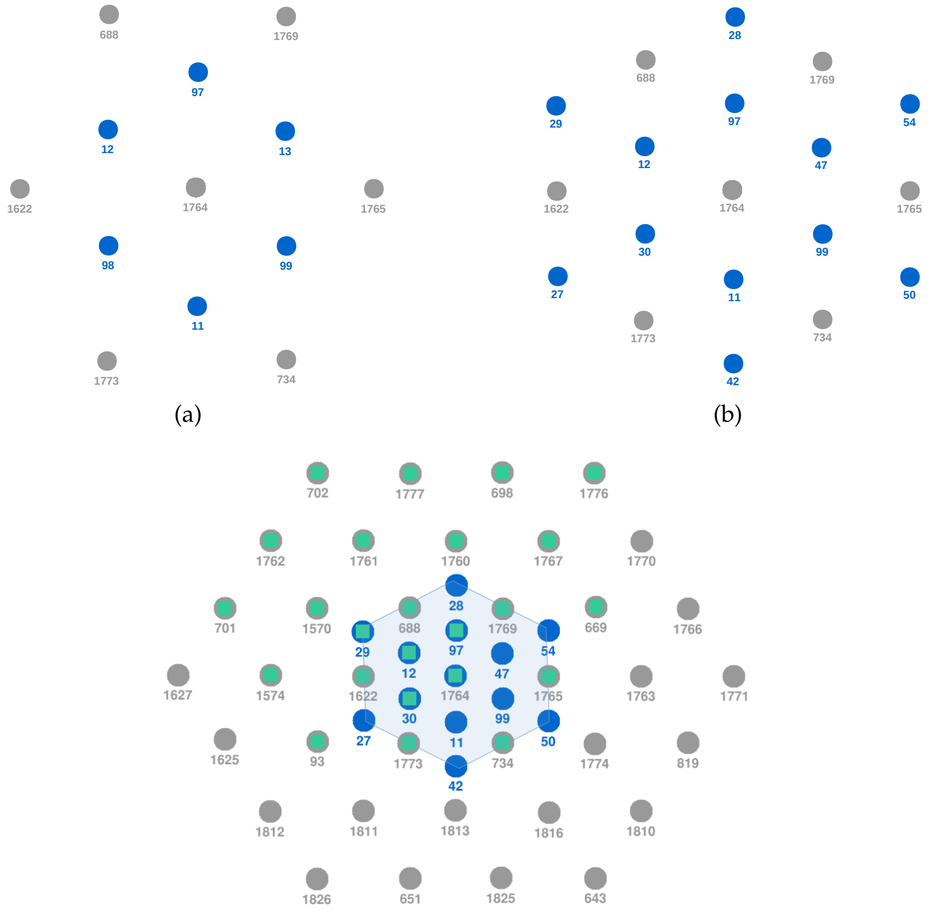

(a) (b)

(c)

Figure 2.27: The schematic map of the SD-433. Fig. 2.27(a) shows the first hexagonal cell of the SD-433 completed after the deployment of stations [97, 98, 99] and [11, 12, 13] respectively in 2011 and in 2013 around the Central one, the 1764. The SD-433 (azure markers) shares with the SD-750 (gray markers) seven WCDs. Fig. 2.27(b) displays the full array, which consists of two crowns (seven hexagons) composed of 19 WCDs (considering the ones already part of the SD-750), finished with the installation of stations [27, 28, 29] and [42, 50, 54] respectively in 2018 and 2019. In Fig. 2.27(c) are represented the whole SD-433 surrounded by the SD-750 and at the same site, the location of the Underground Muon Detector (teal markers) (see Sec. 2.4) buried close to the WCDs. The shaded area enlighten the SD-433 within the SD-750.

As follow, the same can be done for the other station, which appears for the last time in the events in October, 9, 2017 (GPS t_{last} =1191592731) with Id 13 and become active as station 47 in December,14,2017 (GPS t_{first} =1197299769). In Fig.2.29 the changes in the station Ids are visible from the rate of T2 send from each station to CDAS.

2.4 The AMIGA muon detector

The Auger Muon Detectors for the Infill Ground Array (AMIGA) enhancement was designed for the direct measurement of the muon content of air showers [159]. It a joint system which consists of a detector infill area of about 23.5 km^2 with 61 water-Cherenkov detectors on a 750 m grid (SD-750, see Sec. 2.3.1) and scintillator detectors, which are buried in a few meter distance to the SD stations and measure muons independently, as depicted in Fig. 2.30(a) and

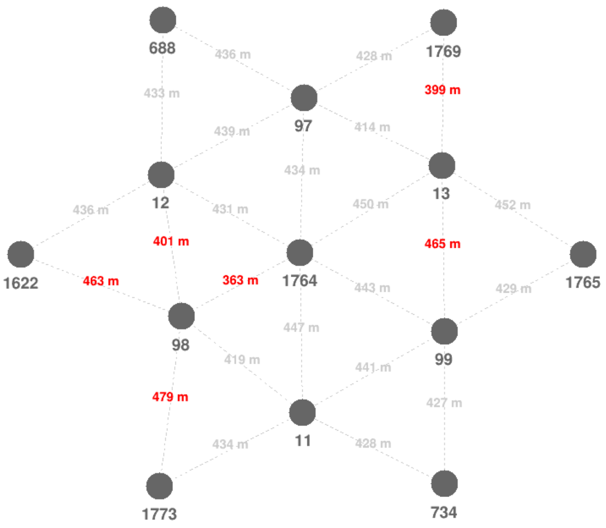

Figure 2.28: The real positions of each WCDs of the SD-433 array together with their relative distances during the first deployment fase.

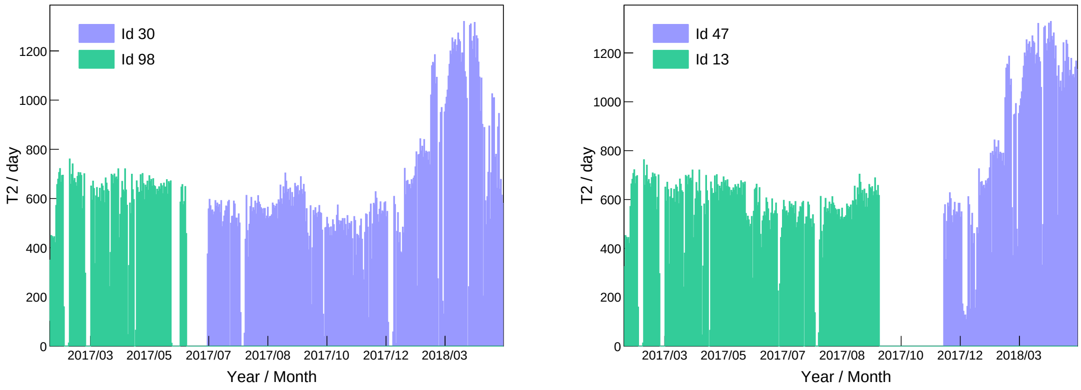

(a) (b)

Figure 2.29: Rate of T2 on a daily basis enlighten the time range when the stations 98 (2.29(a)) and 13 (2.29(b)) changed their Ids to 30 and 47 respectively considering events from 04-01-2017 to 04-01-2018 .

2.30(b). AMIGA was designed with the purpose of lowering the energy threshold of the SD, improving sensitivity to cosmic ray events with energies greater than 3×10^{17} V and for this reason the spacing of 750 m and an area of 23.5 km^2 were chosen due to the small particle footprint and high flux of low-energy showers. The collection of scintillators is referred to as *muon detector* (MD[39]). The engineering array of the MD, called Unitary Cell (UC) which consists on a hexagonal cell of seven MD stations, of scintillators was finished at the end of 2014 (Fig. 2.30(b)). Each MD module is formed by 64 scintillation bars with optical fibers lodged within a Polyvinyl Chloride (PVC) and the optic system and electronics. The MD station has a modular design in which the 30 m^2 detection area is divided in two modules with 5 m^2 and two with 10 m^2 detection area Fig. 2.30(c). Two of the UC position have twin muon detectors, which consist of two 30 m^2 MDs separated by approximately 10 m.

---

[39] Muon detector

The purpose of these detectors is to study the accuracy of the muon counting algorithm. The signal recorded in the stations is a combination of the electromagnetic and muonic components of air showers. The scintillators are buried at a depth of 2.3 m corresponding to an overburden of $\approx 540 gcm^2$ that effectively shields [40] the detectors from electromagnetic particles and imposes a cut-off in the energy spectrum for vertical muons of 1 GeV. The detector module has its own acquisition system, is paired with an SD station from which it receives the trigger condition, and provide digital counting of muons irrespective of their energies.

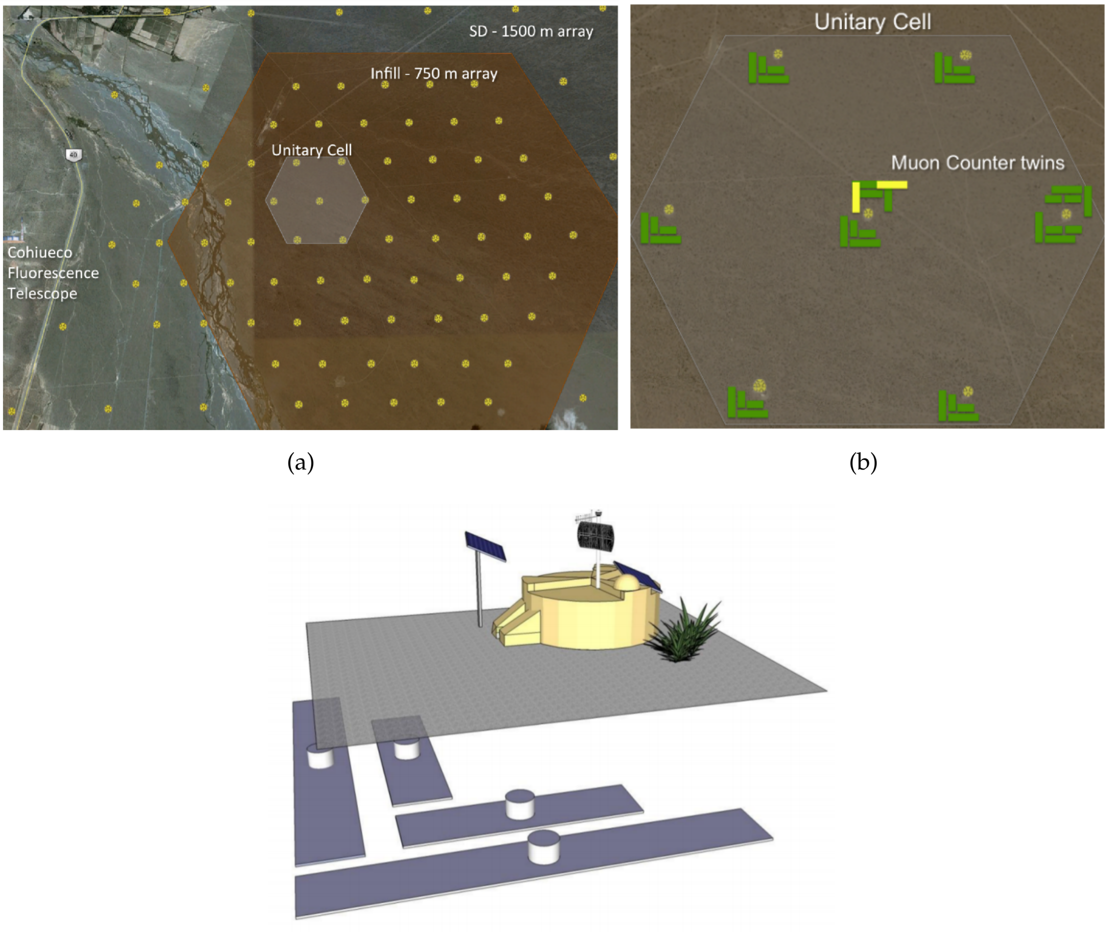

(a) (b)

(c)

Figure 2.30: Fig. 2.30(a): Map of the AMIGA array covering an area of 23.5 km^2 within the existing SD array with the Unitary Cell engineering array position (highlighted gray region). Fig. 2.30(b): layout of the Unitary Cell showing the locations of muon counters (MC) and corresponding water-Cherenkov stations. In yellow the MC buried at 1.3 m are represented, while in green the ones buried at 2.25 m.Fig. 2.30(c): Schematics of the AMIGA setup. An SD station is paired with underground muon detectors. [160].

---

[40] Or at least sufficiently reduce the electromagnetic punch-through to a negligible level at core distances of interest.

2.5 Radio detector: AERA

Cosmic ray air showers have been known for over 30 years to emit pulsed radio emission in the frequency range from a few to a few hundred MHz, an effect that offers great opportunities for the study of EAS with radio-antenna array. The radio emission of an air shower originates from two different emission processes: the geomagnetic emission [161] and the charge-excess, also known as Askaryan effect [162]. The geomagnetic emission which accounts for 80% to 90% of the emission, arises from the deflection in opposite directions of secondary electrons and positrons produced in the particle cascade by the Earth's magnetic field. This induces a drift current transverse to the shower axis that is varying in time as the number of electrons and positrons changes during the shower development. The resulting radio emission is linearly polarized along the direction of the Lorentz force, i.e. in $\vec{v} \times \vec{B}$ direction. Its amplitude is proportional to the strength of the geomagnetic field B and the $\sin\alpha$, being α the angle between the shower direction and the geomagnetic field.

The charge excess emission arises from a time-varying negative charge-excess in the shower front. During the shower development, atmospheric molecules get ionized by high-energy particles of the air shower. The knocked-out relativistic electrons propagate together with the shower front and partially annihilate with positrons in the shower. In total, the shower front accumulates a negative charge excess and a positively charged plasma is created behind the shower. Thus, the induced current, whose strength varies with the shower development, is produced along the shower axis. This yields a radio emission that is polarized radially to the shower axis. The charge-excess fraction varies with the incoming direction of the air shower and the absolute strength of the geomagnetic field. The measured radio emission on ground is given by the superposition of both emission mechanisms although the Askaryan effect is subdominant in air and accounts for about 10% to 20%.

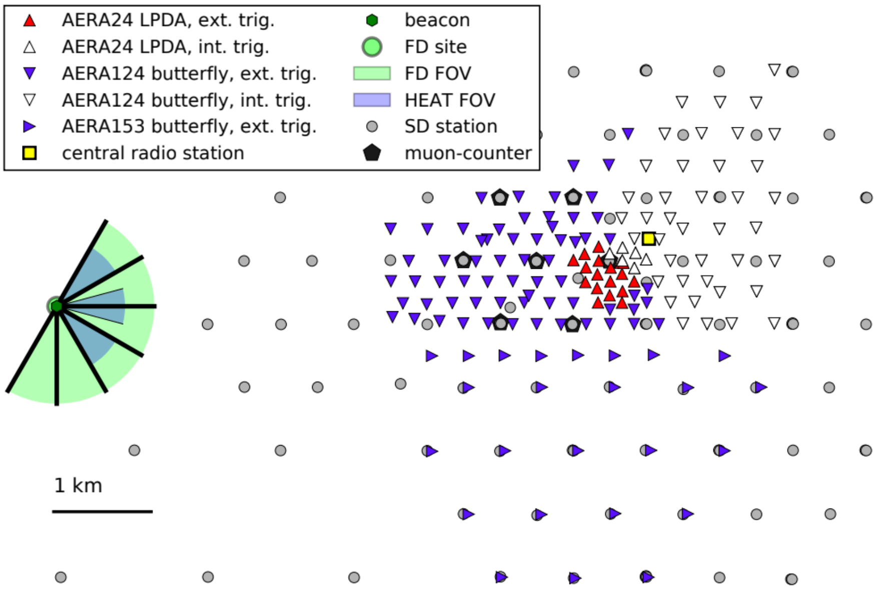

Figure 2.31: Map of AERA array The radio detector stations (triangles) equipped with different antennas and digitizing hardware are surrounded by surface detector (SD) stations (gray filled circles) and underground muon counters (black pentagons). AERA is in the field of view of the Coihueco and HEAT fluorescence telescopes [163]. The different phases of the AERA deployment are reported as AERA24(2011), AERA124(2013) and AERA153(2015).

The Auger Engineering Radio Array (AERA) is the radio extension of the Pierre Auger Observatory proposed in March 2009 by a collaboration of research groups from France, Germany and the Netherlands. AERA detects air showers with energies above 10^{17} eV which coincides with the energy threshold of the 750 m SD array and HEAT, and thus allows for a coincident detection of air showers with all three detector systems. AERA was deployed in three phases within the SD array, in the field of view of the Coihueco and HEAT FD sites. The first 24 stations (AERA24) were installed during the austral summer 2011 on a 144 m triangular grid covering a total area of 0.4 km^2. The second stage of the deployment, in May 2013, consisted in the installation of 100 additional stations (AERA124) arranged on a triangular grid with station-to-station spacing of 250 m or 375 m covering a total area of 6 km^2. With the deployment of additional 29 stations (AERA153) arranged on the SD-750 grid in March 2015, the current layout of AERA with a total instrumented area of 17 km^2 was finalized. The layout of AERA is illustrated in Fig. 2.31. In its current configuration, the array consists of 153 antennas equipped with two different operating in the frequency range of 30 to 80 MH: a *logarithmic periodic dipole antenna* for the first 24 radio stations part of AERA24 and a *butterfly antenna* which was used for all the later deployments. Fig. 2.32 shows an image of radio stations with both antenna models. Two different air shower trigger systems, a self-trigger and an external trigger, are implemented for the radio array. Self-triggers consist in a trigger performed on the radio pulse itself, based on a pulse identification algorithm in combination with a time-differences compatibility check between stations whose recorded pulse is larger than a certain threshold. The external trigger is the one radio stations receive from the SD or the FD. The detector is operated in a multi-hybrid approach with the other detectors and current results are found in [164–166]. With a duty cycle of nearly 100%, low costs and definite possibilities to reconstruct primary properties, the radio emission is a very promising candidate for the future measurement of UHECRs at the highest energies.


(a) (b)

Figure 2.32: Image of the antenna types used in AERA. Fig. 2.32(a) shows the log-periodic dipole antenna (LPDA) and Fig. 2.32(b) the butterfly antenna.

2.5.1 AugerPrime

The observatory is currently undergoing an extensive upgrade of its detectors, named *AugerPrime*, which aims to enhance the Pierre Auger Observatory's ability to clarify the mass composition of cosmic rays at the highest energies. Its main motivation to provide additional information in order to address the following questions [167]:

- elucidate the mass composition and the origin of the flux suppression at the highest energies, i.e. the differentiation between the energy loss effects due to propagation and the maximum energy of particles injected by astrophysical sources. This is a natural evolution and major step forward from the original objective of the Pierre Auger Observatory, which was motivated primarily by the question of the existence of a GZK-like flux suppression.

- the search for a flux contribution of protons up to the highest energies aiming to reach a sensitivity to a contribution as small as 10% in the flux suppression region. The measurement of the fraction of protons is the decisive ingredient for estimating the physics potential of existing and future cosmic ray, neutrino, and gamma-ray detectors, hence clarifying prospects for proton astronomy with future detectors will be clarified. As well, the flux of secondary gamma-rays and neutrinos due to proton energy loss processes will be predicted.

- the study of extensive air showers and hadronic multiparticle production. This will include the exploration of fundamental particle physics at energies beyond those accessible at man-made accelerators, and the derivation of constraints on new physics phenomena, such as Lorentz invariance violation or extra dimensions.

To accomplish these science objectives it will be of central importance to improve the composition sensitivity of the Auger Observatory and to extend it into the energy region of the flux suppression. The best option to obtain further composition-sensitive information is the discrimination between the electromagnetic and muonic components of the shower by mean of SD measurements due to the high duty cycle of almost 100%. Furthermore, additional composition-sensitive information coming from the implementation of new detectors and the enhancement of existing ones, will help to better reconstruct the properties of the primary particles at the highest energies, improve the measurements in the important energy range just above the ankle, and to reduce systematic uncertainties related to modeling hadronic showers and to limitations of reconstruction algorithms.

The proposed Auger upgrade consists of the following components:

- **Scintillator Surface Detector**: SD stations will be equipped with a plastic scintillator (*Surface Scintillator Detectors* - SSD[41]) on top of the existing WCDs providing a complementary measurement of the shower particles. Both detector subsystems, The WCD and the SSD, have different responses to electromagnetic particles and muons: while the WCDs are most sensitive to the muons in the shower, the SSD detector will be sensitive to the electromagnetic shower component. This enables the determination of the signal contributions from muons and electromagnetic particles and thus the reconstruction of the muon number. The scintillator is also insensitive to inclined air showers due to the small geometric cross-section, thus enabling mass sensitivity for vertical air showers. The design of the Surface Scintillator Detectors is simple, reliable and they can be easily deployed over the full 3000 km^2 area of the Surface Detector. The installation of the scintillators started in October 2016 and the engineering array consists of 12 upgraded stations to date. The SSD station has two modules of an area ≈ 2 m^2, each filled with 24 plastic scintillator bars which are read out by wavelength-shifting (WLS) fibers that guide the light to a PMT. The scintillator bars were produced by Fermi National Accelerator Laboratory and have dimensions of 160 cm long, 1 cm thick and 5 cm width. The bars have two holes where the fibers are positioned in a "U" configuration that maximizes light yield and allows the use of a single photomultiplier. A

---

[41] Scintillator Surface Detector

deployed SSD station is shown in Fig. 2.33(a). A layer of polystyrene-aluminum sheets is placed on top of the scintillator bars in each module to reducing any movement and damage of the inner components of the detector. In addition, the final detector enclosure is composed by a 1 mm aluminum sheet which is riveted and glued on top of the frame and a roof of waved aluminum plates placed on top to protect the detector from direct sun-light.

- **Surface Detector Electronics Upgrade:** the surface detector stations will be upgraded with new electronics that read out both WCD and SSD signals. Use of the new electronics also aims to increase the data quality (with faster sampling of ADC traces, better timing accuracy, increased dynamic range), to enhance the local trigger and processing capabilities (with a more powerful local station processor and FPGA) and to improve calibration and monitoring capabilities of the SD stations. The surface detector electronics upgrade (SDEU) can be easily deployed, and will have only minimal impact on the continuous data taking of the Surface Detector.

- **Underground Muon Detector:** the plan is to deploy the AMIGA MD stations all over SD infill area of 23.5 km^2. The the Underground Muon Detector (UMD[42]) will provide important direct measurements of the shower muon content and its time structure, while serving as verification and calibration of the methods used to extract muon information with the SSD and WCD measurements. The performance and characteristics of the AMIGA underground muon detectors, match these requirements, and thus the completed AMIGA array will serve as the UMD. The limited dynamic range of the SD electronics and PMTs for very large signals at the highest energies present an obstacle. For energies above 3×10^{19} eV, more than 40% of the events suffer from saturated signals in at least the station closest to the shower core. In light of the electronics upgrade, a fourth, new phototube with a significantly smaller cathode surface, called the *small* PMT(SPMT[43]), will be added to each WCD to extend its dynamic range (from about 600 VEMto more than 30,000 VEM). With a larger dynamic range the numbers of saturated events is expected to be less than 2% at the highest energies.

- **Extension of the uptime of the Fluorescence Detector:** in parallel with the SD upgrade, the operation mode of the FD will be changed to extend measurements into periods with higher night sky background. The current duty cycle is limited to about 19% for perfect operating conditions. Due to bad weather, power cuts or malfunctioning, and to prolong the life of the FD PMTs by limiting their exposure to periods of higher night sky background, this nominal value is reduced to 15%. In order to operate during times with higher night sky background[44], the PMTs gain must be reduced by lowering the supplied high voltage to prevent an irreversible deterioration of the PMTs sensitivity[45]. The PMTs operating at reduced gain satisfy the criteria required for the FD performance such as a linearity, stability, and lifetime. This will allow the duty cycle of the FD to be about 29%, or in other words, an increase of about 50% of the current observation period. The ongoing setup is already suited to switch between different gains, allowing the operation of the PMTs at both the nominal and the adjusted gain.

- **Radio upgrade:** each SD station will be equipped with a *short aperiodic loaded loop antenna* (SALLA) on top of the WCD and SSD as shown in Fig. 2.33(b). For inclined air

---

[42] Underground Muon Detector

[43] Small PMT

[44] Measurements made earlier in the evening, later in the morning or with a larger fraction (90%) of the moon in the sky that would result in a higher PMTs illumination

[45] PMTgain ten times lower than the nominal one

(a)

Figure 2.33: Fig. 2.33(a): An SSD module: a plastic scintillator unit mounted above a WCD station.as part of the AugerPrime upgrade. Fig. 2.33(b): an upgraded SD station comprised of the WCD, the SSD and a SALLA antenna on top.

showers the electromagnetic and hadronic components are absorbed in the atmosphere and only the muonic component can be measured by a particle detector on the ground. In contrast to that, the radio emission of an air shower originates almost solely from its electromagnetic component. With the combination of WCD and SSD the electron-to-muon (e/μ) ratio is measured for vertical showers. In a similar way the combination of water-Cerenkov detector and Radio Detector will be used to measure the (e/μ) ratio for horizontal air showers. The (e/μ) ratio will be used to derive the particle type of the incoming cosmic ray up to the highest energies, which is the main goal of the Auger upgrade. The radio upgrade increases the zenith angle in order to enhance the aperture of the observatory for mass-sensitive investigations, allowing separate measurement of the electromagnetic and muonic component of horizontal air showers [168].

The upgraded detectors will continue to operate until the end of 2024, by which time the Pierre Auger Observatory will have collected an impressive data set containing additional composition-sensitive information. Such high quality data promises to provide new and exciting results for cosmic ray astrophysics.

CHAPTER 3

Monte Carlo studies

This chapter is dedicated to the study of simulated air showers. The main focus is the estimation of the reconstruction efficiency of the SD-433[1], allowing to identify events for which the detector is not fully efficient, which is important for various analyses. Procedures to simulate the responses of the different elements of the detector to an EAS[2] with known characteristics can be studied from a full Monte Carlo approach. In this chapter, the performance of the reconstruction procedure for proton and iron primaries, is extensively described, both from the point of view of the SD-433.

3.1 Simulation of EAS

The most popular software package to simulate EAS is the COsmic Ray SImulations for KAscade (CORSIKA[3]) [169]. This software package simulates primary cosmic rays with user-chosen initial conditions (such as the primary particle type, its energy and zenith angle) and calculates all of the relevant standard model interactions to produce a list of the secondaries and their properties on the ground.

In order to have a wide variety of primary energies and zenith angles at disposal, libraries of EAS initiated by iron nuclei and protons were produced in the KIT computing center. The simulation libraries are created with the CORSIKA code to simulate air showers. The number of particles of an EAS increases with the energy of the primary cosmic ray. Therefore, to speed up the simulation time and save some disk space without losing accuracy [170, 171], the showers are thinned using an optimal thinning of level of $t = 10^{-6}$. This means that during the simulation process, particles with an energy less than some fraction of the simulated primary energy ($t \times E_0$) are combined using weights and propagate to the ground. Both the thinning level$t$ and the primary energy E_0 are included as input parameters of a CORSIKA run. For the detector simulation, the thinning has to be reverted to obtain the particles which enter the WCDs[4] and preserve as much of the unthinned shower information as possible. This process is called resampling [172–174]. Within the $\overline{\text{Off}}\underline{\text{line}}$ framework, the shower resampling is performed in the `Cached Shower Regenerator` module.

---

[1] 433 m SD infill

[2] extensive air shower

[3] Cosmic Ray Simulations for Kascade

[4] water-Cherenkov detector s

3.1.1 Continuous library produced at KIT

The simulation library used in this work is a continuous library[5] in the energy range of 10^{16} eV to 10^{20} eV with a zenith angle distribution of $\frac{dN}{d\theta} \propto \sin\theta\cos\theta$ as seen in data, up to a maximum zenith angle of 70°, that was produced at KIT. The showers were simulated for proton and iron primaries using the Quark Gluon String model with JETs(QGSJetII-04) [175] as the hadronic interaction model for the high energies regime. The simulation sample consists of 2000 for proton and 2000 for iron primaries showers for the energy range of 10^{16} eV and 10^{17} eV, resulting in 40000 total events. For the higher energies, 1000 unique CORSIKA showers are available.

The event reconstruction was performed with Offline v3r3p3 with dedicated configuration files for the SD-433. The output was stored in ADST format.

3.2 The $\overline{\text{Off}}\underline{\text{line}}$ framework

The event reconstruction is a necessary step for any high-level analysis that involves CR observables, such as the primary energy, and incoming direction. The features of the primary cosmic ray are reconstructed from the raw data gathered in CDAS[6]. It is crucial to convert these raw information at the detector level into the information concerning the primary CR, exploiting the EAS properties. This process is performed by means of the evolving C++ collaborative framework called $\overline{\text{Off}}\underline{\text{line}}$, which is the official event-reconstruction soft- ware of the Pierre Auger Observatory. Therefore, it is extremely important to validate its performance as new functionalities are added to the framework. The offline software framework of the Pierre Auger Observatory provides an infrastructure to support a variety of distinct computational tasks necessary to analyze data gathered by the observatory.

The $\overline{\text{Off}}\underline{\text{line}}$ Framework comprises three principal parts: a collection of processing *modules* which can be assembled and sequenced through instructions provided in an XML file, an *event* data model through which modules can relay data to one another and which accumulates all simulation n and reconstruction information, and a *detector description* which provides a gateway to data describing the configuration and performance of the observatory as well as atmospheric conditions as a function of time. These ingredients are depicted in Fig. 3.1 These components are complemented by a set of foundation classes and utilities for error logging, physics and mathematical manipulation, as well as a unique package supporting abstract manipulation of geometrical objects.

The *Event* data model contains all raw, calibrated, reconstructed and Monte Carlo data and acts as the principal backbone for communication between modules. The overall structure comprises a collection of classes organized following the hierarchy normally associated with the observatory instruments, with further subdivisions for accessing such information as Monte Carlo truth, reconstructed quantities, calibration information and raw data. A reduced illustration of this hierarchy is given in Fig. 3.2. User modules access the event through a reference to the top of the hierarchy which is passed to the module interface by the run controller.

3.3 Reconstruction efficiency

The particle densities and the measured signal of an extensive air shower at a fixed observation level depend on the energy and mass of the primary cosmic ray and on the atmospheric

---

[5] Depending on the specific analysis, the primary energy and/or zenith angle may be fixed or following a continuous distribution.

[6] central data acquisition system

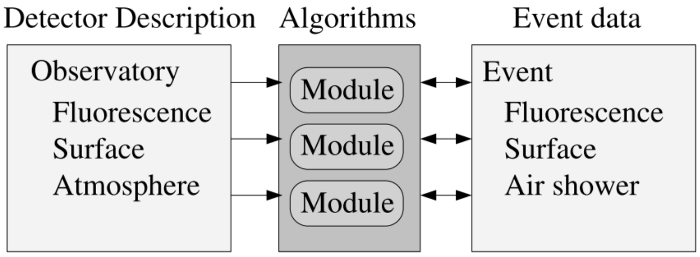

Figure 3.1: The general structure of the Offline framework. Simulation and reconstruction tasks are broken down into modules. Each module is able to read information from the detector description and/or the event, process the information, and write the results back into the event.

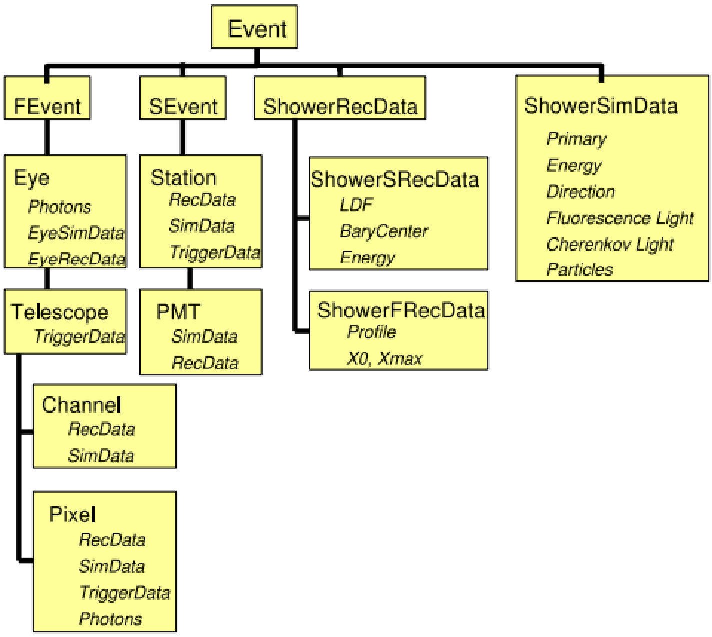

Figure 3.2: Hierarchy of the event interface. The top level Event encapsulates objects representing each detector. In this case only Fluorescence and Surface events are represented by the FEvent and SEvent respectively, as well as reconstructed and simulated shower data (ShowerRecData and ShowerSimData respectively). These components are further subdivided into objects representing simulated, reconstructed and triggering data at the level of individual telescopes, stations and photomultiplier tubes [176].

depth transversed by the shower since its first interaction with the atmospheric medium. In particular, the shower footprint size increases with the primary energy. Therefore, a denser array with detectors deployed sufficiently closed could reach a suitable number of triggered WCDs in order to perform a proper event reconstruction, even for low primary energies. However, there is a primary energy threshold below which some showers may not be reconstructed producing a decrease in the number of reconstructed events as the amount of triggered stations will not meet anymore the required number WCDs to build a T4 trigger. The reconstruction efficiency ϵ is a function of the primary energy E, the mass A and the zenith angle θ:

$$\epsilon = \epsilon(E, A, \theta). \tag{3.1}$$

The reconstruction efficiency is calculated using the library of simulated events and it is given by the ratio of the number of reconstructed events N_{rec} to available events N_{all}:

$$\epsilon = \frac{N_{\mathrm{rec}}}{N_{\mathrm{all}}}. \tag{3.2}$$

The analysis is applied for proton and iron primaries separately. For each primary, the reconstructed and available events are binned in both energy and zenith angle dimension. The efficiency is then calculated for each bin according to Eq. 3.2. We choose a conservative cut of $\epsilon_{\mathrm{cut}} = 0.97$ above which the array will be considered fully efficient.

3.3.1 Impact of the Core position

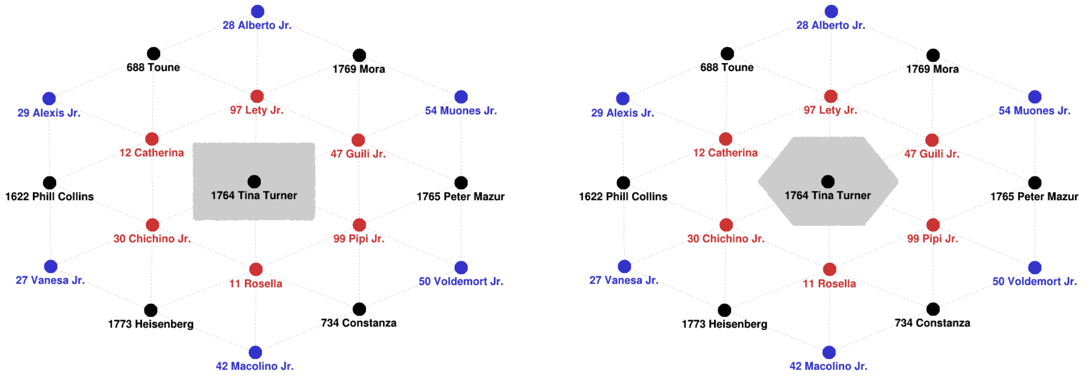

(a) (b)

Figure 3.3: Schematic view of the SD-433. The shaded region represent the area within the simulated core of the impinging particle lays respectively rectangular (Fig. 3.3(a)) and hexagonal (Fig. 3.6(a)).

Two different shower core areas have been chosen for the simulation process by means of the `EventGeneratorOG` module: rectangular and hexagonal geometry with Tina Turner as the central station while using the new triggers (Fig. 3.3).

A shower core falling very close to one station, especially for vertical showers in a low energy scenario, implies that the majority of stations is further away than for the typical event, thus affecting the quality of the reconstruction. For such events, trigger selection criteria requiring stations in triangular patterns may fail, leading to the rejection of the event itself. In order to filter out those showers which may fall too close to the central station, we required a quality cut in the simulation procedure, which is equivalent to a distance cut based on a constant minimum allowed distance between the shower core and the nearest WCD. For a new set of simulated events, we studied the impact of $r_{\mathrm{nearest}} > 100\,\mathrm{m}$, which is the inner radius cut used in the simulation procedure for each core area, asking for the shower core to be located, at least, at 100 m away from the central station, expecting to observe a decrease for the full efficiency threshold.

For the construction of hexagonal area, which parameters (Northing, Easting) can be modified in the configuration file, `EventGenerator.xml`, a dedicated function has been implemented in the module `EventGenerator.cc`[7] in order to obtain the desired area geometry.

---

[7] The rectangular is the default area for which it does not require an additional function to be created.

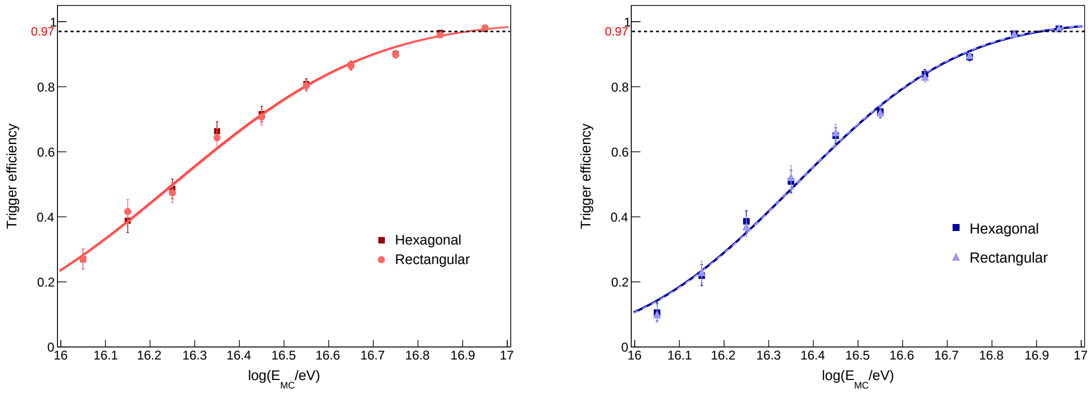

(a)

(b)

Figure 3.4: Reconstruction efficiency ϵ integrated in zenith angles between 0° and 55° for rectangular and hexagonal areas, for proton (left) and iron (right) primaries.

The reconstruction efficiency obtained for proton and iron primaries as a function of the simulated energy for the two different considered geometries is shown in Fig. 3.4 and has been modeled using the error function Erf(x), as shown in Eq. 3.3 where a and b are free parameters,

$$\epsilon(E) = \frac{1}{2} \times \left[\mathrm{Erf}\left(a \times (\log_{10}(E_{\mathrm{MC}}) - 16) + b\right) + 1\right]. \tag{3.3}$$

The fitted parameters a and b for each zenith bin are presented in Tab. 3.1.

	Core area	a	b
Proton	Hexagonal	2.02 ± 0.06	-0.51 ± 0.04
Fig. 3.4(a)	Rectangular	2.01 ± 0.06	-0.51 ± 0.04
Iron	Hexagonal	2.43 ± 0.07	-0.88 ± 0.04
Fig. 3.4(b)	Rectangular	2.45 ± 0.07	-0.88 ± 0.04

Table 3.1: The parameters a and b of Eq. 3.3 from the fit on reconstructed events generated by proton and iron primaries with energies between $E_{\mathrm{MC}} = 10^{16}$ eV and $E_{\mathrm{MC}} = 10^{17}$ eV.

According to Fig. 3.4, no significant reconstruction efficiency differences have been noticed using the two core areas, reason why only the hexagonal area plots will be further shown in this work.

The Fig. 3.5 shows the efficiency curves performed with simulated events asking for a minimum allowed distance between the central station and the shower core. There are no remarkable differences in the obtained efficiency slopes by placing a constraint of $r_{\mathrm{nearest}} >$ 100 m to the central station, respect to the case where a inner radial cut is not considered. Because the energy threshold for full efficiency is not affected by the usage of a radial cut, we will no longer use it for further analysis.

3.3.2 Dependence on the zenith angle

Very inclined extensive air showers have a smaller probability of triggering the array than more vertical showers when the energy decreases. This effect is related to the increasing

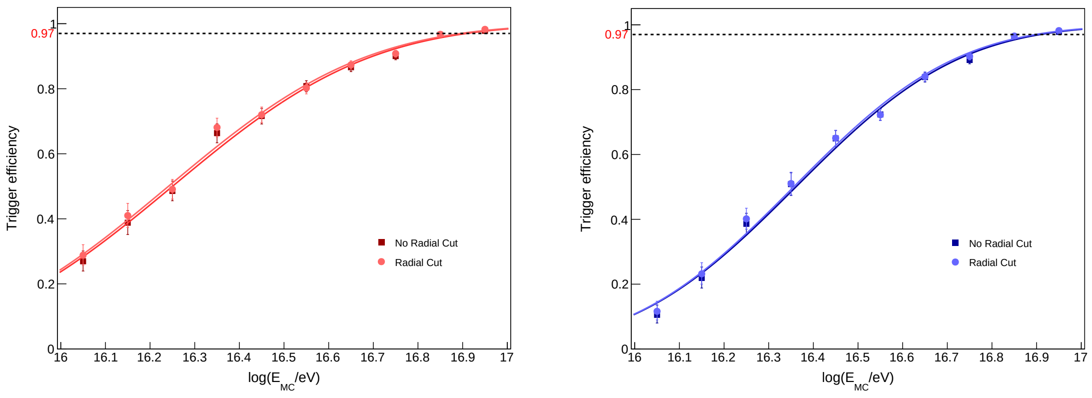

(a) (b)

Figure 3.5: The reconstruction efficiency of the SD-433 in terms of the primary energy for proton (left) and iron nuclei (right) integrated in zenith angles between 0° and 55°; the circular markers represent the reconstruction efficiency requiring $r_{\text{nearest}} > 100$ m as the inner radius cut on the area of the simulated cores around the central station.

amount of atmosphere traversed by air showers with increasing zenith angle, and it is known as atmospheric attenuation: as the amount of traversed atmosphere by the shower increases with θ, the electromagnetic component is largely absorbed and the measured particle density (and accordingly the measured signals) decreases.

In order to study the zenith-angle dependency, the reconstruction efficiency is depicted as a function of the simulated primary energy for protons and iron nuclei in Fig. 3.6, for four different zenith intervals between 0° and 55°.

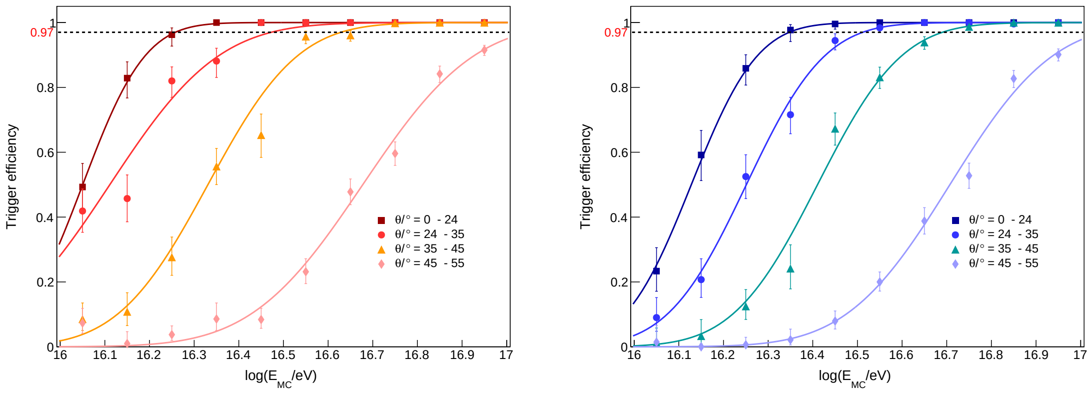

(a) (b)

Figure 3.6: The reconstruction efficiency of the SD-433 in terms of the primary proton (left) and iron (right) energy for different angle intervals. The error function $Erf(x)$ in Eq. 3.3 has been used to fit each distribution.

In Tab. 3.2 the fitted parameters a and b for each angle range from Eq. 3.3 with their associated uncertainties are displayed.

Considering a minimum value for the efficiency of 97%, an approximate trigger-threshold can be extracted from plots in Fig. 3.6. The array reaches the full efficiency threshold around

	Zenith interval (°)	a	b
Proton Fig. 3.6(a)	0 - 24	6.4 ± 1.1	-0.3 ± 0.2
	24 - 35	3.7 ± 0.6	-0.1 ± 0.1
	35 - 45	4.5 ± 0.3	-1.5 ± 0.1
	45 - 55	3.6 ± 0.2	-2.4 ± 0.1
Iron Fig. 3.6(b)	0 - 24	6.1 ± 0.8	-0.8 ± 0.2
	24 - 35	5.1 ± 0.4	-1.3 ± 0.1
	35 - 45	4.7 ± 0.3	-1.9 ± 0.2
	45 - 55	3.9 ± 0.2	-2.7 ± 0.1

Table 3.2: The parameters a and b of Eq. 3.3 from the fit on reconstructed events generated by proton and iron primaries with energies between $E_{\mathrm{MC}} = 10^{16}$ eV and $E_{\mathrm{MC}} = 10^{17}$ eV.

Zenith interval (°)		Energy threshold		Efficiency	
		Proton	Iron	Proton	Iron
0 - 24	log(E/eV)≥	16.35	16.35	$100\%^{+0}_{-2\%}$	$97.6\%^{+1\%}_{-3\%}$
24 - 35		16.45	16.55	$100\%^{+0}_{-2\%}$	$98.3\%^{+0.9\%}_{-2\%}$
35 - 45		16.75	16.75	$99.8\%^{+0.1\%}_{-0.7\%}$	$98.7\%^{+0.6\%}_{-1\%}$
45 - 55		(>)17	(>)17		

Table 3.3: The energies from which the SD-433 array reaches its full efficiency for the four different angular intervals.

$10^{16.5}$ eV for low zenith intervals $\theta < 35°$ and at $10^{16.7}$ eV for $\theta < 45°$, while for zenith angles $> 45°$ is 97% only for energies above 10^{17} eV.

In Tab. 3.3 the four energy thresholds are presented accordingly to the four zenith ranges studied. We estimated the efficiency errors using the Wilson's score interval [177] formula

$$\varepsilon_{1,2} = \frac{k + q^2/2}{n + q^2} \pm \frac{q\, n^{1/2}}{n + q^2} \left[\frac{k}{n} \left(1 - \frac{k}{n} \right) + \frac{q^2}{4n} \right]^{1/2}, \tag{3.4}$$

where k is the number of successes measured with n trials, which means in our case, $k = N_{\mathrm{rec}}$ and $n = N_{\mathrm{all}}$. For the quantile of the Gaussian distribution q we chose a value of 1.64 for a 90% confidence level. The SD-433 becomes less efficient as the zenith angle increase, and then starting from zenith angles $> 45°$ the array efficiency drops drastically and therefore we will select events with zenith angle up to 45°. This behavior can be explained considering a superposition of two effects: the geometric and the attenuation effects. Because of the projection of the WCDs distances in the shower plane, with increasing zenith angles, WCDs observe higher signals because their reduced distance to the shower core, however the traversed atmosphere increases leading to a decrease in the number of particle reaching the detector which results in lower measured signals.

3.3.3 New triggers

The *new triggers* were designed to be less sensitive to background muons and at the same time sensitive to the electromagnetic component of showers. The inclusion of ToTd[8] and MoPS[9] increases the number of triggered WCDs allowing for the detection of smaller WCD signals caused by lower energy showers. This has the effect of improving the sensitivity of the array to low energy showers and lowering the energy at which the SD-433 becomes fully efficient.

This section compares the reconstruction efficiency as a function of the simulated primary energy of events having zenith angle less than $\theta < 45°$ with and without the new triggers. The difference between the two plots in Fig. 3.7 highlights what is gained for the efficiency when turning on the new triggers. In Fig. 3.7 we observe a reduction of the energy threshold by one bin in logarithmic scale when the ToTd and MoPS algorithms are included compared to the scenario where only the old triggers are employed. The implementation of the ToTd and MoPS triggers into the reconstruction process increases the reconstruction efficiency, as expected, especially at energies below full efficiency. In Tab. 3.4 the set of reconstructed events used to calculate the efficiency thresholds reported in Fig. 3.7 is displayed.

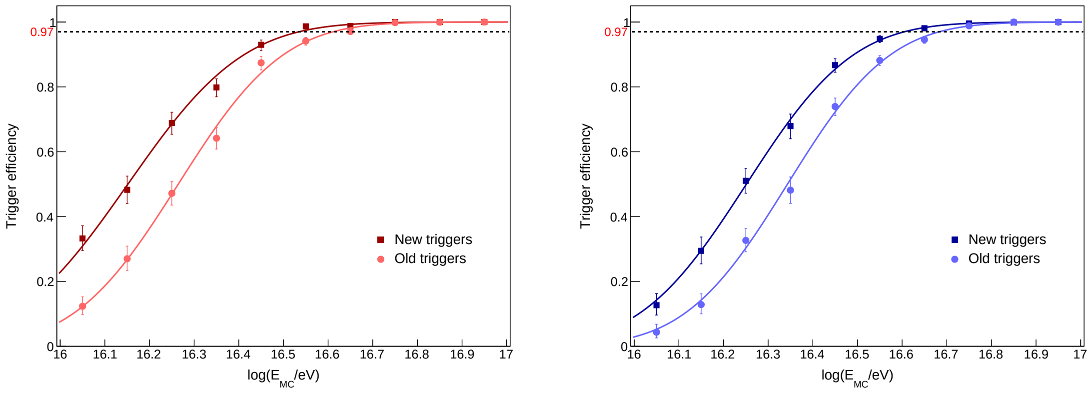

(a) (b)

Figure 3.7: The reconstruction efficiency as a function of the energy over all zenith angles up to $\theta < 45°$. It is clear the new triggers (squares) show a one bin reduction in the energy threshold for full efficiency compared to the old triggers (circles), for proton (left) and iron (right) primaries.

	Old triggers	New triggers
Proton	12069	12827
Iron	11359	12028

Table 3.4: Number of reconstructed events with $\theta < 45°$ simulated using the old and new triggers for proton and iron primaries.

3.3.4 Dependence on mass composition

The reconstruction efficiency not only has a primary energy and zenithal incidence dependence, but is affected by the mass composition of the primary particle too. Fig. 3.8 depicts

---

[8] time-over-threshold deconvoluted trigger

[9] Multiplicity of positive steps

the zenith-integrated efficiency for showers initiated by proton and iron nuclei. The energy threshold from which the array efficiency is $\geq 97\%$ is $10^{16.5}$ eV for proton and $10^{16.6}$ eV for iron primaries.

The plot in Fig. 3.8 indicates that the detector is more efficient for proton than for iron showers, which is an unexpected result if we compare it with the efficiency study made for the SD-750 [146], where it is shown that the detector reaches high efficiency for iron showers at lower energies than for proton showers.

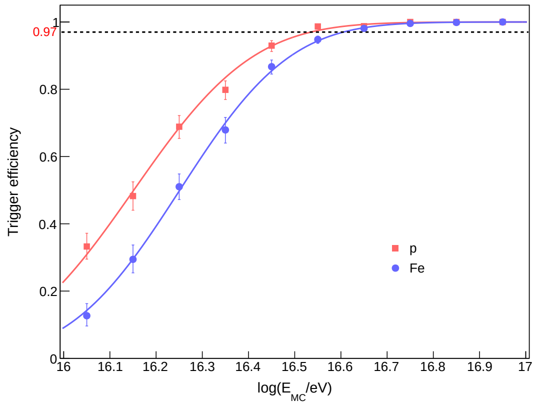

Figure 3.8: The reconstruction efficiency of the SD-433 array in terms of the simulated energy for proton (blue) and iron (red) induced showers with $\theta < 45°$.

Moreover, this effect can be seen in Fig. 3.6, where the efficiency increase faster for proton primaries for zenith angles $< 45°$ than for iron showers.

The most possible explanation is that, for inclined air showers induced by protons, the electromagnetic shower component hasn't completely vanished compensating the fewer muons compared to iron-initiated showers. Air showers generated by iron primaries have the tendency to develop at higher altitude than proton showers, which are more penetrating, reaching the ground at a more mature stage.

This effect can be studied defining the observable $\Delta X = X_{\text{obs}} - X_{\text{max}}$, where X_{obs} and X_{max} are respectively the atmospheric slant depth of the ground plane and the maximum shower development. The histograms in Fig. 3.9 present the distribution of ΔX while in Fig. 3.10 is reported the reconstruction efficiency as a function of the ΔX for showers induced by proton and iron primaries, for five selected energy values. The simulations confirm that proton shower develop deeper in the atmosphere than iron ones. As the traversed atmosphere increases, the particles densities at the ground level decrease producing lower measured signals. Proton showers, which reach the detector with a lesser degree of attenuation, tend to leave higher signals in the WCD resulting in higher efficiency compared to iron initiated showers. For the same reason there are no iron-initiated events for $\Delta X < 300$ g/cm^2 triggering the surface detector, especially at lower energies as depicted in Fig. 3.9(a), affecting the reconstruction efficiency Fig. 3.10(a). At the same time, as the energy increases, this behavior persists limited for $\Delta X < 200$ g/cm^2.

Fig. 3.10 shows that for energies above $10^{16.3}$ eV at fixed ΔX, the efficiency is higher for iron than for proton showers, which is what we expected from previous studies. The distribution of ΔX analyzed for both primaries explain the unpredicted efficiency results indicating that the detector is more efficient for proton showers than for iron showers.

The simulation setup we employed for this work is summarized in Tab. 3.5

Tab. 3.6 displays the number of available events and the action of each quality cut

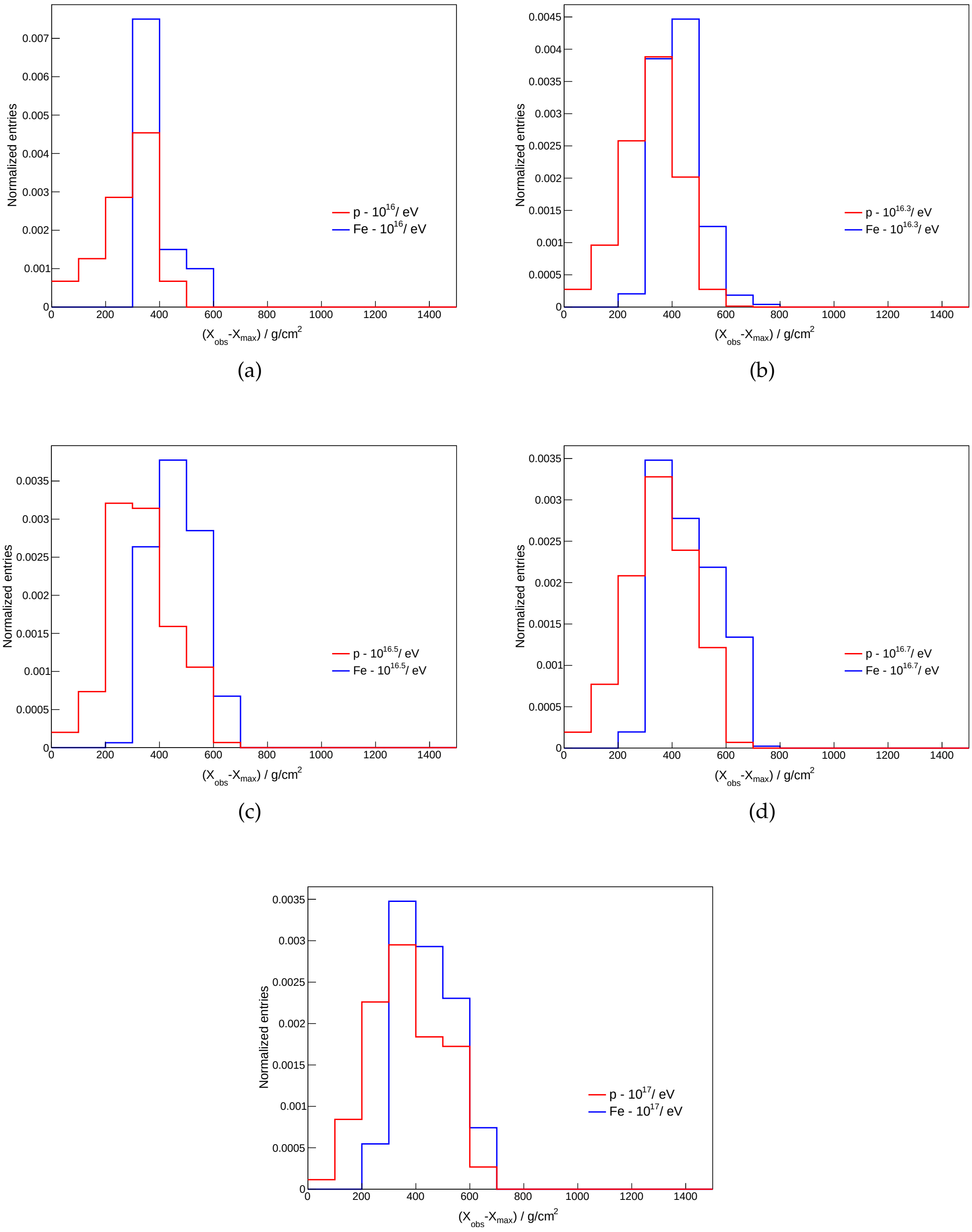

(a) (b)

(c) (d)

(e)

Figure 3.9: Distribution of the observable $\Delta X = X_{\text{obs}} - X_{\text{max}}$ for events initiated by proton and iron primaries for the five chosen energy values between $E = 10^{16}$ eV and $E = 10^{17}$ eV.

3.3.5 Impact of shower components

The development of the muonic and electromagnetic components in a cosmic-ray air shower depends on the mass of the primary particle. For this reason, in this paragraph we introduce the observable S_{mean} to exploit the difference between the electromagnetic and muonic component for the two different primaries. This observable is based on the composition-

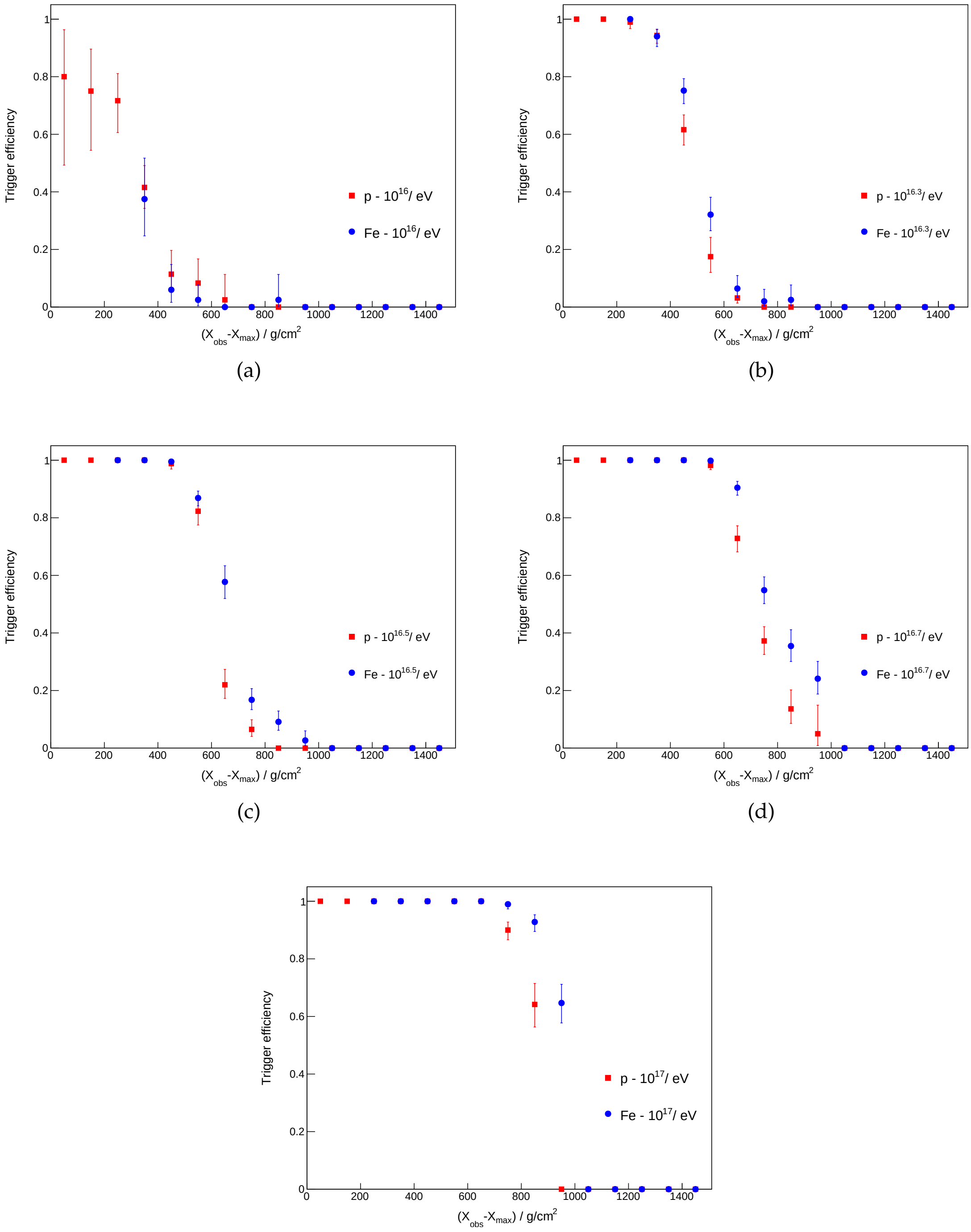

(a)

(b)

(c)

(d)

(e)

Figure 3.10: Reconstruction efficiency in terms of the $\Delta X = X_{obs} - X_{max}$ of showers originated from proton and iron primaries for events populating the five energy values between $E = 10^{16}$ eV and $E = 10^{17}$ eV.

sensitive parameter S_b used for composition studies Ref. [178] and [179], although in this analysis will not be employed for primaries discrimination purposes, but only to study the muonic and electromagnetic components of the same air shower separately.

Core area	hexagonal	✓
	rectangular	✗
WCD triggers	MoPS and ToTd	✓
Radial cut	$r_{\text{nearest}} > 100\,\text{m}$	✗

Table 3.5: SD-433 event-simulation setup.

		Events (p)	Events (Fe)
Total events		20000	20000
Cut	$\theta < 45^\circ$	15410	14970
	Fully reconstructed	12827	12028

Table 3.6: Overview of the SD-433 quality cuts used to select events for the efficiency study.

The proposed parameter is defined as:

$$S_{\text{mean}} = \sum_{i}^{N} S_i \times \left(\frac{r_i}{r_{ref}}\right)^b , \tag{3.5}$$

where S_i is the electromagnetic/muonic signal of the *i-th* WCD at a distance r_i from the shower axis, r_{ref} is the reference distance which is set to 250 m for the SD-433. The index b is a free parameter which has to be selected as to maximize the separation between primaries. In this case we chose $b = 3$. All signals and the S-parameter are measured in VEM (Vertical Equivalent Muons).

In Fig. 3.11(a) is shown the mean of the electromagnetic and muonic component, calculated all over the triggered WCDs for each event using the Eq. 3.5, for proton and iron primaries. The parameter S_{mean} for both components appears to be stronger for proton primaries (*proton-regime*) than for irons up to energies of $10^{16.5}$ eV. Above this threshold there is a change of regime and iron generated showers start to produce higher signals in the

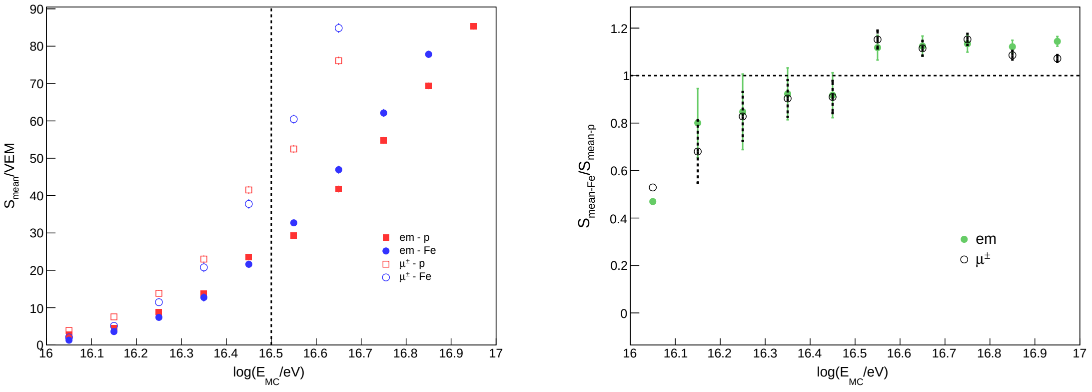

(a) (b)

Figure 3.11: Fig. 3.11(a): Mean of the electromagnetic and muonic component of the signal from each WCD weighted by its distance to the shower axis, expressed in function of the primary **MC !**[10]energy. Fig. 3.11(b): The ratio between the signals produced by proton and iron primaries for the electromagnetic and muonic component of the shower for zenith angles < 45°.

detector (*iron-regime*). This means that proton initiated showers at low energies have a more dominant electromagnetic and muonic component arriving at the ground than iron showers. This behavior can explain why the detector reaches higher efficiency for proton showers at lower energies than for iron. The dotted line shown in Fig. 3.11(a) highlights the energy where approximately the transition between the *proton-regime* to the *iron-regime* takes place. In Fig. 3.11(b) is depicted the ratio between iron and protons signals for both components covering the zenith angle range between 0° and 45° where is easy to discriminate between the proton-dominated energy range and the iron one.

We were surprised to see that the mean electromagnetic and muonic signals become larger for iron than proton at around the same energy. It's not clear to us why the muonic signal isn't dominant for iron even down to the lowest energies the SD-433 can measure.

3.3.6 Reconstruction accuracy

The reconstruction of the simulated events is performed with $\overline{\text{Off}}\underline{\text{line}}$ v3r3p3 revision 33065 with the suitable configuration files to account for the 433 m spacing [180]. Each shower core was randomly placed ten times within the unitary cell of the SD-433 around the central WCD as shown in Fig. 3.3.

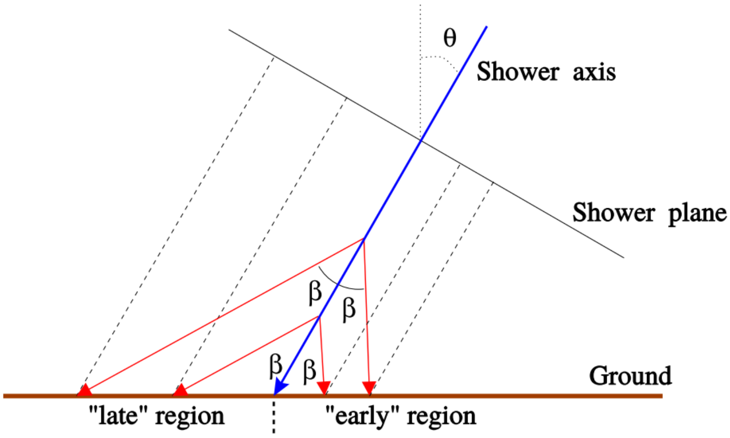

Figure 3.12: Particles going away from the shower axis with the symmetric angle β. When projecting the ground densities on the shower plane, a purely geometric asymmetry appears.

The quality of the geometrical reconstruction of an event can be checked through several aspects. The general approach is to compare the reconstructed core position r_{rec} with the simulated position r_{MC}, both measured from the origin of a local coordinate system. The detection of showers suffers from attenuation in the atmosphere as well as from geometrical projections on ground, both dependent on the zenith angle. A pure symmetric event in the shower frame, such as two particles going away from the axis with the same angle β, results in a non symmetric effect in the ground plane. When projecting the ground densities onto the shower plane, as the direction of the individual particles in not known, one has to use the shower direction. This result in what is called *geometric asymmetry* which can be seen in Fig. 3.12 that pushes the reconstructed core towards the early part of the shower as the signal density is higher for this region. The particle hitting the ground in the "early" region will be seen more vertical that the ones in the "late" region. Even with a perfect symmetry around its axis, an inclined shower will not give symmetric patterns on the ground. The bias in the core position increases with zenith angle due to the increase of traversed atmosphere and hence the increase of attenuation and as a result of the geometric asymmetry, as depicted in Fig. 3.13, where the absolute difference is presented for proton in Fig. 3.13(a) and iron

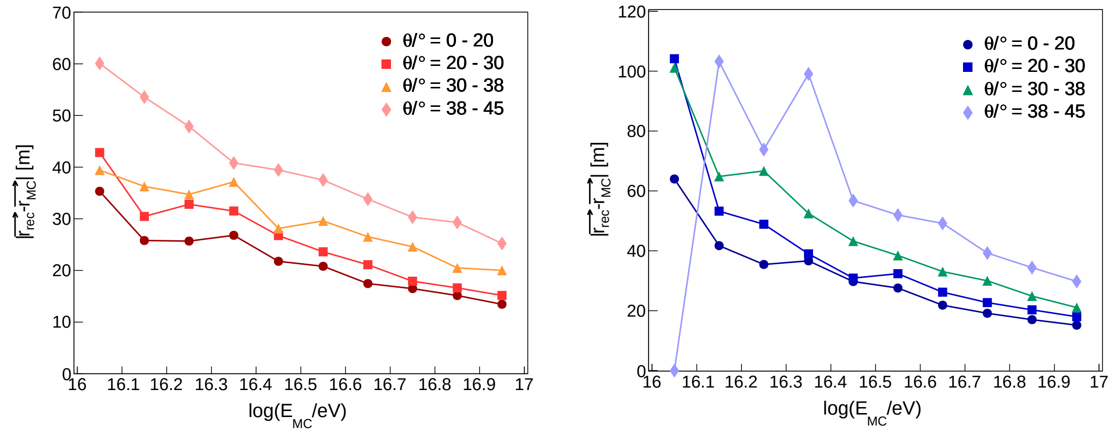

(a) (b)

Figure 3.13: The absolute difference between the reconstructed and simulated core positions in terms of the simulated energy for photon (Fig. 3.13(a)) and proton (Fig. 3.13(b)) primaries for four zenith intervals.

in Fig. 3.13(b) primaries. Below the full efficiency threshold, ($\sim 10^{16.5}$ eV, see Sec 3.3.2) the deviation of the reconstructed core position from the simulated values is below 45 m considering showers with $\theta < 38^{\circ}$ and reaches 60 m if we consider more inclined showers with $38^{\circ} < \theta < 45^{\circ}$. The accuracy of the model increases towards higher energies, above $\sim 10^{16.5}$, reaching values below ∼20 m and decreases with decreasing primary energies which is due to the diminishing number of particles in the EAS. The relative difference on the bias core position between proton and iron initiated shower is between 20 m at lower energies and 10 m above the full efficiency threshold.

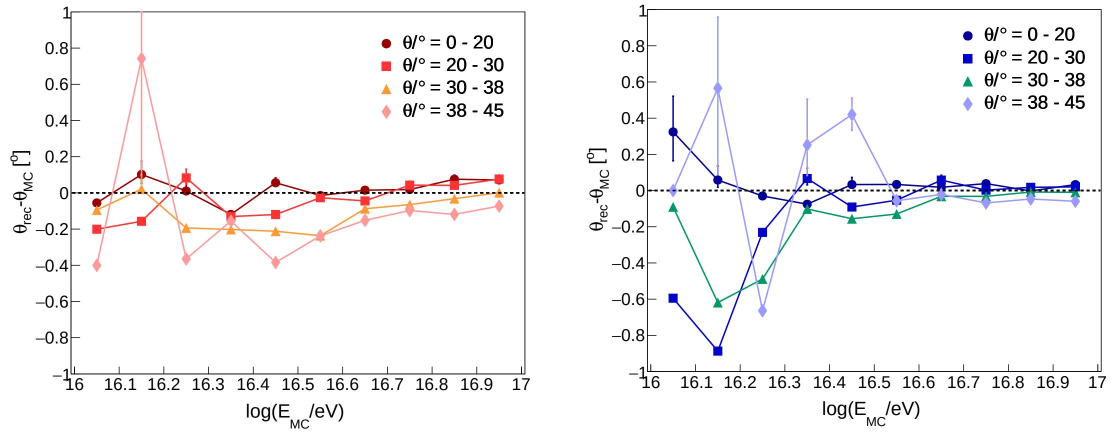

(a) (b)

Figure 3.14: The absolute difference between the reconstructed and simulated zenith angles in terms of the simulated energy for photon (Fig. 3.14(b)) and proton (Fig. 3.14(b)) primaries for four zenith intervals.

Another aspect to take into account is the precision of the angular reconstruction, in particular the zenith angle. The absolute difference between the reconstructed and simulated zenith angle, θ_{rec} and θ_{MC} respectively, is shown in Fig. 3.14. There are again larger differences for the primary energies below full efficiency, where the the reconstructed zenith angle differs the most from the simulated angle for iron initiated showers compared to proton ones. The accuracy of the reconstruction is very good for showers with an energy $> 10^{16.5}$ eV, which are described with deviations below 0.4° for proton and 0.2° for iron primaries that can be reduced to less than 0.2° and 0.1° respectively considering $\theta < 38°$, while for vertical showers ($\theta < 30°$), with energies above the full efficiency threshold, is less than 1° independently of the features of the primary particle.

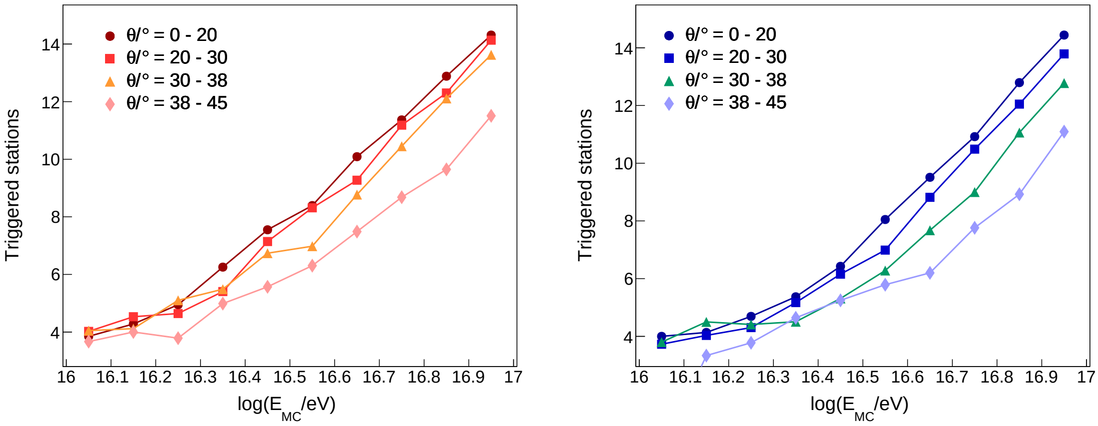

(a)

(b)

Figure 3.15: The average number of triggered stations in terms of the primary energy for different zenith intervals. The proton-produced shower are shown in Fig. 3.15(a), while the iron-produced in Fig. 3.15(b).

The number of triggered WCDs in this energy domain is tightly connected with the zenith angle, as depicted in Fig. 3.15. In particular, events with a $\theta > 38°$ have a smaller multiplicity of triggered WCDs than in the case of vertical events. Therefore, as the number of triggered stations reduces, the reconstructed zenith angle starts to depart from the simulated value. The angular reconstruction of non-vertical events shows a slight dependence on the position of the shower core at energies below 1016.9 eV. Indeed, if the shower core is close to the central WCD, the stations from the first crown are located at nearly the same distances from it. This degeneracy affects mostly the non-vertical events because of The smaller number of available triggered stations at $E_C < 1016.5$ eV affects mostly the non-vertical events for both primaries, although in the case of iron showers, it additionally influences the angular reconstruction at $20° < \theta < 30°$, resulting in a huge discrepancy between the data and the model provided θ (blue-squared markers in Fig. 3.15(b)).

In Fig. 3.15, the average number of triggered stations as a function of the primary energy is shown for proton and iron initiated showers. On the one hand, a clear dependence on the primary energy and zenith angle is appreciable, as the number of available WCDs increases for increasing energies and lower angles, for both primaries. On the other hand, the averages do not show a strong dependence on the primary particle for energies above the efficiency threshold since there are not significant differences displayed between Fig. 3.15(a) and Fig. 3.15(b). At lower energies, the average number of triggered stations between the two primaries differs of 1 as for iron showers the increment in the slope is smoother than for protons. For vertical showers, the average number of stations increases from 4 to 8 (7) for proton (iron) primaries, increasing to $\sim$ 14 in both cases for higher energies. Hence, the increase in the number of triggered WCDs starts to be noticeable at the latter energies and the systematic effect produced by the primary composition is negligible because of the reduced number of WCDs that composes the array. The study on the energy accuracy is

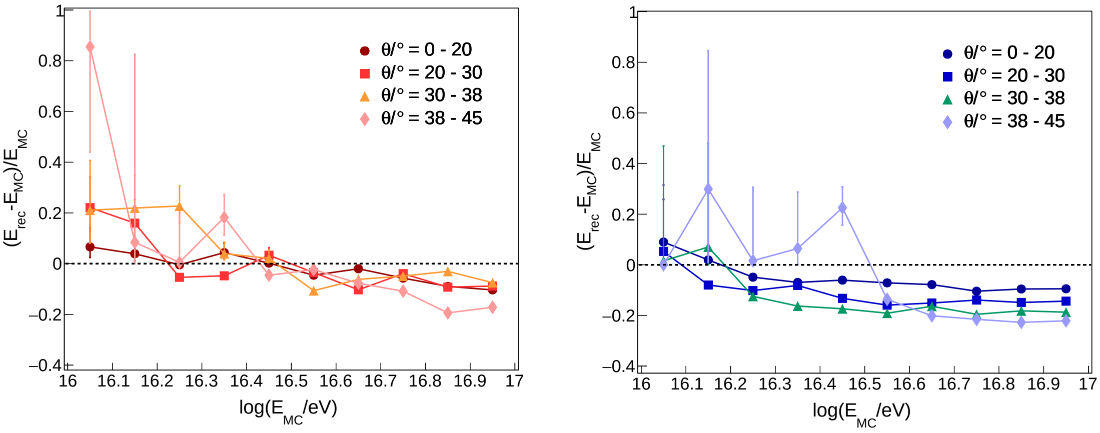

(a) (b)

Figure 3.16: The relative energy bias in terms of the simulated energy for proton (Fig. 3.16(a)) and iron (Fig. 3.16(b)) primaries with the quoted zenith angles.

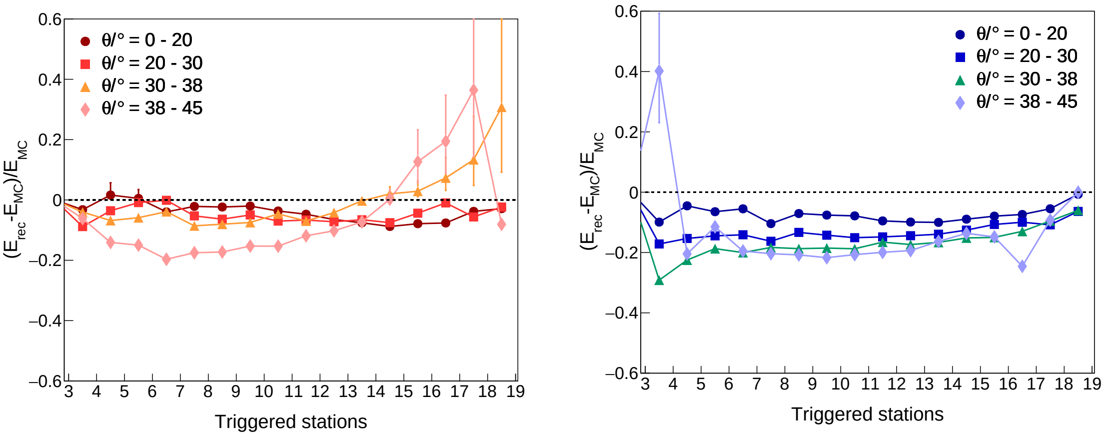

(a) (b)

Figure 3.17: The relative energy bias against the number of triggered WCDs for proton (Fig. 3.17(a)) and iron (Fig. 3.17(b)) primaries with the quoted zenith intervals.

performed by comparing the reconstructed to the simulated energy. The relative difference is shown in Fig. 3.16(a) and Fig. 3.16(b) for proton and iron induced showers, respectively. For both primaries the bias is below 20% for energies above the threshold of full efficiency and shows an increasing bias towards lower energies. This bias can be lowered to 10% if we consider only events up to 38° in the case of proton initiated showers, while for irons is 10% for $\theta < 30^\circ$ only. More over, for vertical shower ($\theta < 20^\circ$) the deviation between the reconstructed energy and the simulated one is below 10% even for lower energies for both primaries. For $\theta > 38^\circ$, the atmospheric attenuation starts to be relevant, specially for energies below full efficiency. This effect is more emphasized for iron primaries where it starts to be relevant at $E_C < 10^{16.5}$ eV and it is producing a worsening of the energy estimation with respect to the proton produced showers for which starts to be dominant for $E_C < 1016.3$ eV, where the mismatch for proton primaries is much higher than for irons. These deviations are still well contained by the SD-433 energy resolution which was calculated as $\sim 18\%$ between $E = 10^{16.6}$ eV and $E = 10^{18}$. At higher energies, the SD array is already fully efficient for non-vertical events, which compose the vast majority of the events in data because of geometrical reasons since the median of the θ distribution is $\sim 30^\circ$ as we will see in Sec. 4.6. Above $E = 10^{16.5}$ eV, all profiles stabilize for both primaries, culminating in what seems a plateau, although an increased discrepancy in the energy reconstruction is displayed for non-vertical showers. The reason has to be found in the numbers of triggered WCDs, that tends to be smaller compared to vertical events, which in turn produces an increased discrepancy in the energy reconstruction, as displayed in Fig. 3.16(a) and Fig. 3.16(b) for proton and iron showers respectively. Since the energy bias is strongly dependant on the number of triggered stations for inclined events than for vertical events, the intrinsic variance of the stations multiplicity produces larger fluctuations for $\theta_{\text{MC}} > 38^\circ$ than in the other cases.

In this section, we presented the geometrical reconstruction of proton- and iron-initiated EAS. The accuracy of the model is very good in the most relevant and intermediate energies of interest. The energy biases shown are well contained within the energy resolution of the SD-433 for the energies and zenith angles of interest. The largest deviations, between the reconstructed and model provided values, occur at lowest primary energies and for very inclined showers.

CHAPTER 4

Measurements of cosmic-ray events with the SD-433 array

The SD-433[1] array consists of 19 WCDs[2] around the Central one named "Tina Turner",already part of the 750 m SD-433 array. As in the CDAS[3] a dedicated central-trigger algorithm has been implemented for AERAlet, once the array was fully deployed, it has become possible to reconstruct cosmic-ray events detected by this denser array. For this purpose, it is crucial to adjust those parameters, used in the LDF[4]-fitting procedure that depend on the array geometry, i. e. the optimal distance r_{opt} and the slope β of the LDF (see Sec. 2.2.7). After this step, the CIC[5] method has been applied to the newly reconstructed events, to allow for an estimation of the energy-calibration parameters for SD-433.

4.1 Array monitoring: T2 files

As each SD station communicates its T2 trigger to the CDAS, which combines these to form higher-level triggers, the number of T2 triggers is stored every second in the so called T2 files. The T2 raw files store the microsecond times and flags of all T2 triggers of all the stations in all the GPS[6]-seconds, provide detailed information of all SD stations, which are received by CDAS and stored. These files are used to monitor the activity of each SD station second by second. The information coming from monitoring files is combined to estimate the uptime for each hexagonal cell, which in turn allows the calculation of the instantaneous aperture of the SD.

Each second all the Local Stations (LS[7]) are sending to the CDAS the time corresponding to each T2. This information is sent the Central Trigger application (CT) of the CDAS, to find and build the T3. The CT dumps on disk each second the number of T2 received by each LS in the following format :

---

[1] 433 m SD infill

[2] water-Cherenkov detector s

[3] central data acquisition system

[4] lateral distribution function

[5] Constant Intensity Cut

[6] Global Positioning System

[7] Local Station

`GPS_time` $\texttt{LS\_ID}_1$ `#T2` $\texttt{LS\_ID}_2$ `#T2` $\texttt{LS\_ID}_3$ `#T2` $\cdots$ $\texttt{LS\_ID}_n$ `#T2`,

where #T2 is the rate of T2s for each station of the array identified by its ID_i. Due to the huge amount of information, these files are too large to be exported, and a compression process is needed. Finally, after a compression process performed by LSStatus package of the CDAS (once per hour), one file is produced each day. It is exported and stored in the monitoring area as: /Raid/monit/Sd/year/month/t2_year_month_day.dat The information about the "apparition" (identified by a + symbol at the beginning of the line) or the "disparition"(-) of LS at the given GPS time can be retrieved from these T2 files.

For the following work we preferred to used T2Raw uncompressed files, in order to have an overview of the whole array per second. In order to obtain the information we wanted, knowing the IDs of the SD-433 LSs, we selected from the T2raw files stations of the SD-433 array only over the great amount of LS, reducing per event the T2raw information to 19 lines, each line for each SD-433 ID. From now on we will refer to those T2 files as *T2life-SD433*.

4.1.1 Silent Stations

SD events, to be successfully reconstructed are required to pass the 6T5-prior selection (Sec. 2.2.6). This necessitates that the station with the largest signal in an event is surrounded by six active and functional stations at the time of triggering. Though, not all of these stations need to have triggered. In the following, a functioning (active) station implies that the station exists in the required place of the selected grid and is working properly in the particular GPS second of the event: this status is obtained from the T2 monitoring files, and in our case from the T2life-SD433 files. We will consider a station as active if its T2 rate is not zero. Stations that are inactive, according to T2 information, at the time of the event are rejected in the reconstruction of events, while stations whose signal is below the T1 trigger threshold, are kept but are denoted as *silent stations*. This is highly relevant, because bad stations (inactive) and silent (functional but non-triggered) stations are important to distinguish, both for the reconstruction and for the calculation of the exposure. More over, the last step in the Surface Detector (SD) reconstruction algorithm is fitting the geometry (core location and shower direction) and the Lateral Distribution Function (LDF). The LDF fit, used to find the reference signal for the arrays, is done using the signal amplitudes in each triggered station vs the distance of that station to the shower axis. Silent stations, to keep data consumption low, have no trace information associated with them. Even though the signal in the stations is unknown, these stations can still be used to inform the LDF fit.

At the beginning of 2018, a first inspection of the data recorded with the SD-433 revealed a rate of 6T5 events below the expected value for the array spacing (close to 100 6T5 events per day and per hexagon). Out of a total of 1081,942 reconstructed events, only 33,530 events were classified as 6T5 (about 3%), which could be identified corresponded to a T3 trigger originated by the SD-433. These events had high multiplicity of WCDs, and higher energy than the range of interest for which the SD-433 was conceived. As already mentioned before, The CDAS central trigger receives the T2 of the whole array. The information, directly extracted from T2 files, is crucial since it is the base of the exposure calculation. Indeed, the hexagons are counted on the base of this T2 information. In theory, each time a station is flagged as active in the T2 files whether of not it is going to pass further checking of an event trigger, it should appear in the reconstructed event as a *silent* or *candidate* station. Unfortunately, since its first deployment, the SD-433 dedicated trigger (see Sec.2.3.2, due to the high rate required by this array, and its limited bandwidth available in the communications system, was storing information upon candidate stations only and did not record the activity status of the WCDs during the data acquisition process. This means that only stations with signals passing a T3 trigger, were taken into consideration during the reconstruction process, while silent stations were not included in the event. To overcome this limitation, part of the communications system was replaced. In mid-2018 the Leeds set of radios from the original SD-750[8] stations was replaced with AMIGA radios. With the increased bandwidth of the communications system, it was possible to upgrade the SD-433 dedicated trigger, now called *fast CDAS*. Therefore, at the time of the formation of a T3 trigger, with at least one participating SD-433 station, the fast CDAS requires the activity status of the 19 WCDs belonging to the SD-433 and consequently stores this information. The smaller spacing between the SD-433 WCDs compared to the other arrays and the implementation of the new MoPS and ToTD triggers, increase the rate of T3 by an order of magnitude. For this reason the fast CDAS only waits 3 seconds to receive the requested information, unlike the conventional CDAS, which waits 7 seconds to collect the response of all the stations in the SD-1500[9] and the SD-433. With these implementations in the telecommunications and the data acquisition system, the non-triggered station started to be included in the events since July 20, 2018. Fig. 4.1 shows the same event originally reconstructed without (Fig. 4.1(a)) and with (Fig. 4.1(b)) considering the information of the Silent Stations, enabling in the latter case, its promotion to a 6T5 event.

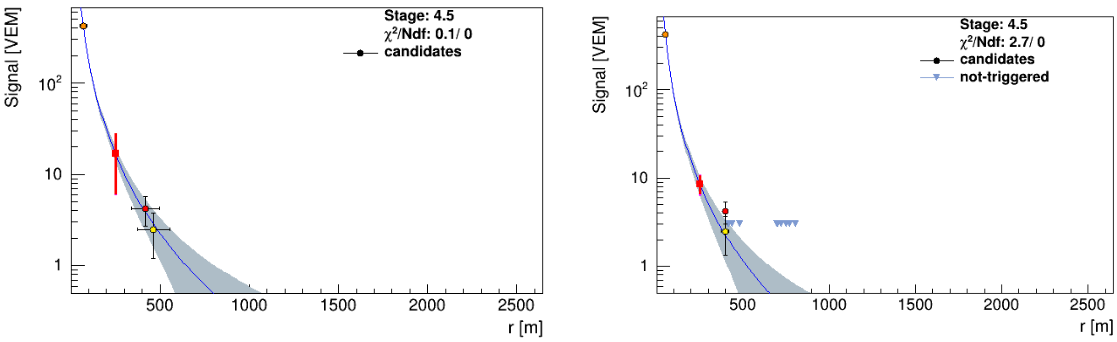

(a)

(b)

Figure 4.1: Fit of the lateral distribution function to the measured signals of an SD-433 event with reconstructed energy of 3.26×10^{16} eV and zenith angle of 13°. (Event time: 05. September 2014, Sd Id: 28962749, figure from Offline EventBrowser). In Fig. 4.1(a) the event is reconstructed without the information of the Silent Stations, while in Fig. 4.1(b) the same event is depicted incorporating the silent stations in the reconstruction. As a result of the incorporation of the non triggered stations, indicated by gray triangles, the event has been labeled as 6T5 as it satisfies the 6T5 selection criterion.

To ensure the correct determination of the shower geometry and the lateral distribution function, to perform a good LDF fit and a proper exposure calculation, it is imperative to restore the missing silent station in all events covering the data taking period since 2013 until July 2018. We developed a new Offline application dedicated to restore, during the reconstruction process, the missing silent stations in each event. This procedure is achieved by mean of a new module implemented in the module sequence, called T2Restorer, able to extract the activity status of each WCD from the T2life-SD433 (Sec. 4.1) and combining this information with the event we are reconstructing (see Appendix A.1). The module, during the reconstruction instance, simply looks for a match between the GPS of each event with the ones in the T2life-SD433 files. In the case a match between two GPSs is found, the module checks the activity status of all SD-433 WCDs in order to find discrepancies between the "alive" stations according to the T2 files and the stations in the data. Stations

---

[8] 750 m SD vertical

[9] 1500 m SD vertical

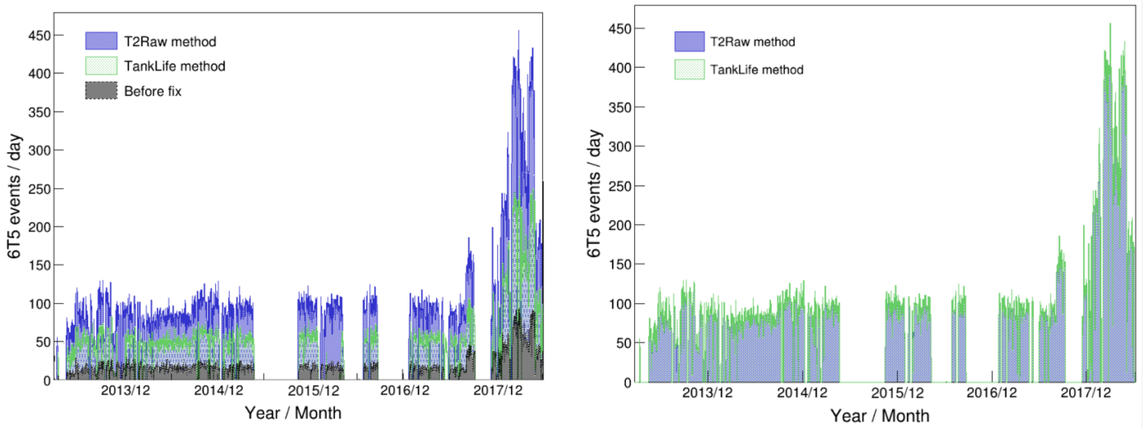

(a) (b)

Figure 4.2: Time distribution of the rate of 6T5 events. In Fig. 4.2(a) the event is reconstructed without the information of the Silent Stations, while in Fig. 4.2(b) the same event is depicted incorporating the silent stations in the reconstruction. As a result of the incorporation of the non triggered stations, indicated by gray triangles, the event has been labeled as 6T5 as it satisfies the 6T5 selection criterion.

that are declared "on" in the corresponding T2 files should be in the data. If an inconsistency is found, the active non-triggered stations are added in the event as a whole new station and labeled as *SilentT2*, in order to prevent the `SdCalibrator` to reject it during further steps of the reconstruction procedure. Once the stations have been included in the data, the reconstruction continues and the event is store in the usual ADST[10] format. The described repairing process was validated using a second method that reviews and repairs the data set prior-to-the-reconstruction, combining the production files with the tankLife monitoring files. The rate of 6T5 as a function of the time is shown in Fig. 4.2 for events obtained with the *T2Raw* and the *TankLife* methods. Initially, the rate 6T5 events reconstructed with both methods showed a discrepancy close to 40% (Fig. 4.2(a)). The methods have been validated manually crosschecking the divergences in the number of recovered 6T5 events. Every discrepancy was carefully investigated by means of the $\overline{\mathrm{Off}}\underline{\mathrm{line}}$ reconstruction outputs until converging to the same set of data (Fig. 4.2(b)) resulting in a compatibility between the two methods of 99.9% as depicted in Fig. 4.2(a). The total number reconstructed events is 1067098 and by means of the procedure described above, the number of 6T5 events increased by a factor ~ 4.5 passing from 33541 to 148139 (and from 30967 to 138897 if we consider events with $\theta < 45°$) in the time period between January 1, 2013 and July 31, 2018 as depicted in Fig. 4.3. This value is comparable with the expected event rate within the energy range covered by the SD-433 and the new set or reconstructed events, constitute a set of high quality data suitable for future studies of the energy spectrum with the SD-433.

As an example of the importance of using the silent stations when fitting the LDF, Figure. 4.4 shows the fractional change in energy that occurs when taking a fewer number of silent stations into account. It is quite apparent that the energy always decreases when a great number of silent stations is neglected. This shows the important role that the silent stations play when calculating the shower energy. The impact of the missing silents on the estimation of the reconstructed energy shows a smooth zenith dependence, at least up to $\theta < 45°$. The histograms depicted in Fig. 4.4(c) shows a shift between 4% and 6% upwards for the four considered zenith intervals. If we extend the zenith range integrating all over the

---

[10] Advanced Data Summary Tree

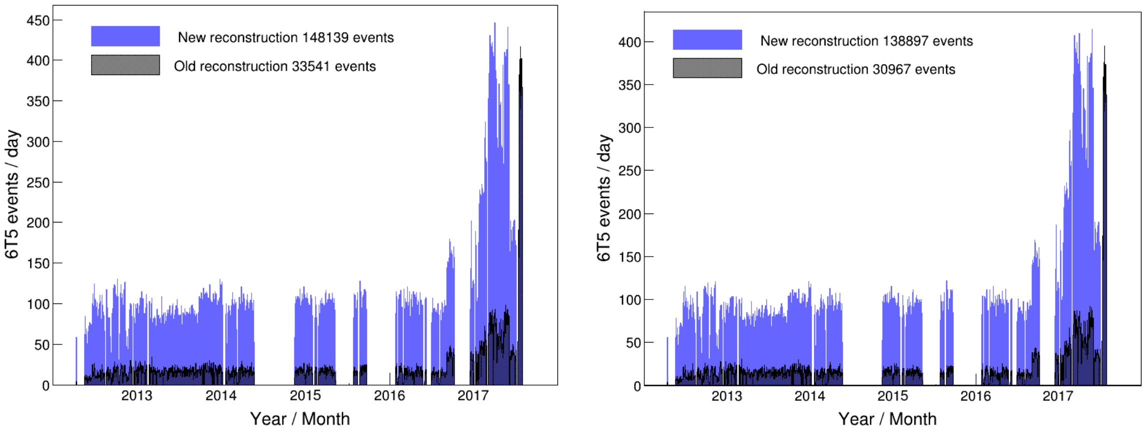

(a)

(b)

Figure 4.3: Daily distribution of events identified with the 6T5 condition and for all zenith angles (Fig. 4.3(a)) and with $\theta < 45^\circ$ (Fig. 4.3(b)), recorded with the SD-433 before (shaded region - old reconstruction) and after (blue - new reconstruction) the recovery process of the silent stations.

reconstructed angles, the energy bias decreases by a 2% as showed in Fig. 4.4. The energy bias between the old and the new reconstruction as a function of the new reconstructed energy is presented in Fig. 4.5. It reduces for energies above 10^{17} eV, as shown in Fig. 4.5(a), while it increases reaching a maximum value around the 20% for energies of 10^{16} eV. Inclined showers present larger biases for $E > 10^{16}$ eV than vertical ones as reported in Fig. 4.5(b) considering zenith angles up to 45° and within the energy range of interest. This analysis has shown that the right number of silent stations to be considered in the fit is very important to the final energy calculation. It was then shown that on average the signal is underestimated when silent stations or at least part of them are neglected during the reconstruction process.

4.2 Event selection

The SD-433 started to be operational since January 2013, although because of a persistent communication problem with station 97 the amount of data heavily reduced until April 2013. Thus, we shall consider the data taking period formally starting in April 2013 when data acquisition began more stable. The events used for the analysis presented in this chapter are of high quality to determine the flux of the cosmic rays as precisely as possible. All events have to be reconstructed successfully, meaning that the lateral distribution was fit, and they have to fulfill 6T5-prior trigger condition that requires the station with the largest signal in an event to be surrounded by six functional stations at the time of triggering, though not necessarily with signal. To ensure a proper reconstruction, we applied a zenith angle cut limiting the events to 45°, the zenith angle upper limit chose for the SD-433 in Sec. 3.3.2. Detailed information about other quality selection criteria used for the following analysis, are going to be discussed in each analysis dedicated section since different set up have been used. Here, we just report the general selection of cosmic rays events in which we are interested that has been performed in two steps further explained below. First, to reduce the computational time, at the raw level only data written by the AERA trigger algorithm are selected. Second, a selection of events with at least three SD-433 stations within the Unitary Cell is performed in Offline, by means of the `Select433Events` module, before attempting the reconstruction. This module was included in the `ModuleSequence` and whether the events does not contain the user required number of SD-433 stations, the event is discard and and it will not be con-

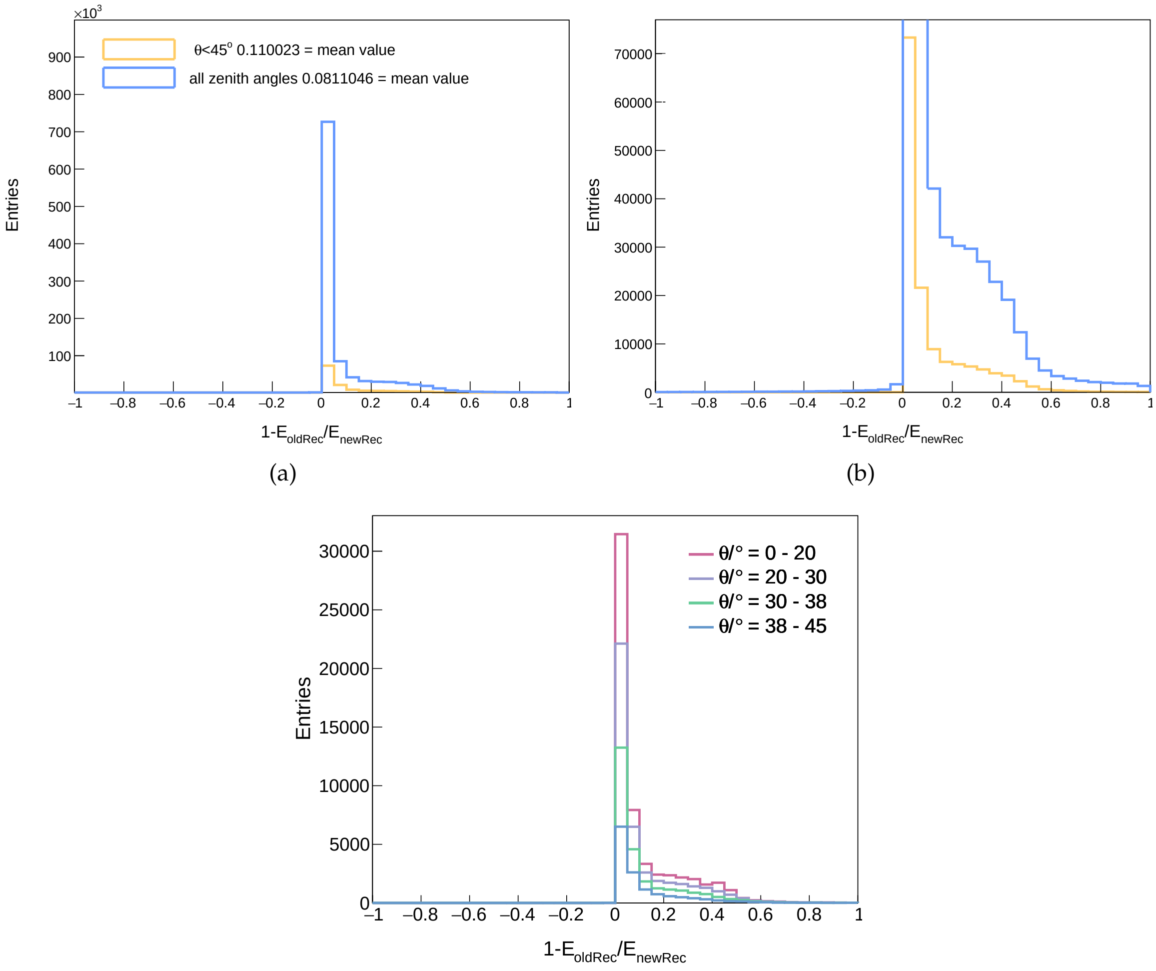

(a) (b)

(c)

Figure 4.4: The LDF fit takes into account the silent stations when performing a normal SD reconstruction. As an extreme example, this histogram shows the fractional difference in reconstructed energy for the old reconstruction, in which we have a deficit in the number of silent stations, and the new reconstruction for which the silent stations have been restored. The energy essentially always shifts upward by 8% on average considering all zenith angles ($\theta_{\text{max}} \sim 82°$), as shown with the blue histogram and by 6% for events with $\theta < 45°$ as represented by the yellow histogram. Fig. 4.4(b) is the zoomed histogram in Fig. 4.4 showing the same set of events with the same characteristics.

sidered by the subsequent modules performing the actual reconstruction. This pre-selection has been essential for the aim of reconstructing the whole data set in a reasonable amount of time, and to be able to perform the reconstruction many times (e.g. after varying a single parameter in the Offline configuration). The `ModuleSequence` used to reconstruct the data within the Offline framework is detailed in A.2. The single-station calibration procedure, described in Sec. 2.2.1, to convert the signal to VEMs is performed by the `SdCalibratorOG` module. The task of selecting physics events is committed by the `SdEventSelectorOG` module. As the Observatory includes SD arrays with different baselines (1500, 750, and 433 m), one needs to specify in the configuration file of this module, which array has to be considered. This module iterates over the candidate station list to check whether the station is part or not part of the chosen array. In the latter case the station is flagged as off-grid and it will not further continue the reconstruction process. Finally, the data set of eight years of data resulted in 2078179 CR events, which still need to undergo the quality cuts.

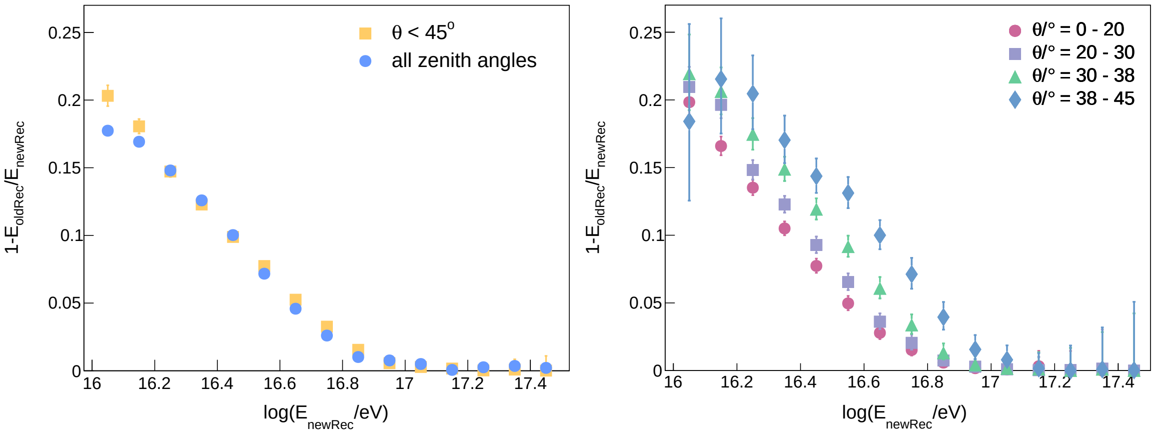

(a) (b)

Figure 4.5: The average energy bias as a function of the reconstructed energy using new reconstructed events. *Old/new reconstruction* refers to the reconstructed events before/after the recovering process of the missing silents.

4.3 Event reconstruction

The reconstruction of physical air-shower events detected by the SD-433 has been performed with the Offline trunk revision 33771. The features of the reconstructed events, such as the energy and the geometry, are addressed in this section. Each WCDs could be non-functional at any given time due to failures in the telecommunications, the batteries, the electronics, causing the rejection of events that results in a loss of statistics. However, this does not affect the discussion of the general features seen in data and it has been taken into account in the calculation of the exposure described in Sec. 4.7.1. The number of reconstructed events on a daily basis is displayed in Fig. 4.6 where no selection or quality cuts have been applied. The data-taking period is not stable during the years, in particular from January 2013 to April 2013 and between May 11 and July 2016, due to failures in the communication system of the SD-433 unitary cell.

The reconstructed energy distribution of all the events in the data-taking period between January 2013 and December 2020 is shown in Fig. 4.7(a). For $E < 10^{16.5}$ eV the number of reconstructed events after reaching its maximum decreases with the reconstructed energy. This is an expected result knowing that this energy is compatible with the full efficiency threshold found in Sec. 3.3.2. Above this energy, the SD-433 is fully efficient and the decrease of the events is explained by the steeply falling spectrum of the cosmic rays. The zenith angle distribution is depicted in Fig. 4.7(b) for the same set of events, showing a maximum at $\theta \sim 25^\circ$. As for the energy distribution, no quality cut have been applied to the events. From Fig. 4.8 it can be deduced that events with smaller reconstructed energy tend to a have a more vertical incidence. This effect is due to the atmospheric attenuation of particles reaching the ground.

The footprint of an air shower on the ground depends on the primary energy and the zenith angle. On the one side, it expands with the energy and on the other side it gets smaller as the zenith angle increases because of the smaller number of particles arriving to the ground due to the strong atmospheric attenuation if the energy is not high enough. More over, the array spacing is reduced in the coordinate system co-moving with the shower front when a primary particle impinges the atmosphere with an inclined incidence, thus promoting the proliferation of triggered stations. The number of SD-433 triggered stations is visualized in terms of the reconstructed energy for four different zenith intervals is presented

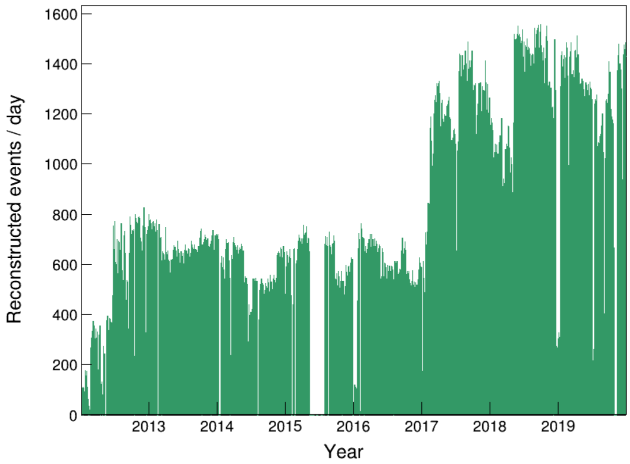

Figure 4.6: The daily rate of reconstructed events by the SD-433 since January 2013 until December 2020.

in Fig. 4.9(a). It can be seen that showers with greater energies tend to fire a larger number of stations compared to lower energies where they suffer a stronger atmospheric attenuation. The number of triggered stations reaches its maximum at $E \sim 10^{17.5}$ eV where it starts to retreat instead of keeping growing, as a consequence of the lack of selection cuts imposed in the events. For energies above $0^{17.5}$ eV, the SD-433 array is fully efficient and then data start to be acquired with this array. Although the shower core might fall outside the SD-433 area, in the case of high energetic EAS containing enough particle, it can trigger some of the peripheral stations of the SD-433 array, explaining the decreasing number of SD-433 stations seen in Fig. 4.9(a) for $E > 10^{17.5}$ eV. The decline of the number of stations is zenith dependent and appears at $E \sim 10^{17.5}$ eV for events with $\theta < 30°$ and around $10^{17.8}$ eV for more inclined showers, indicating the zenith angle dependence of the SD-433 trigger efficiency. If we consider only events fully contained in the SD-433 unitary cell, this feature vanishes and the expected dependence is completely recovered as pointed out in Fig. 4.9(b). All the 13 WCDs part of the SD-433 grid are, on average, triggered for $E > 10^{17.5}$ eV and $\theta < 45°$, and for energies above $10^{16.8}$ eV in the case of the first crown of stations. Since the quality of the reconstructed events is affected by the position of the shower core, in the next section a discrimination procedure will be described in order to exclude those showers falling at the edge of the array, which will unavoidably bias the analysis if taken into account, and to only include those events with fitted slope. In fact, in this case, as only part of the shower front will be sampled, the resulting LDF would represent only part of the actual LDF, and consequently the particle content would be underestimated and so the primary energy.

For the following analysis the applied quality cuts to the events are listed below:

1. Zenith-angle cut: $\theta < 45°$.
2. Events that fulfil the posterior 6T5 condition.
3. Events with no saturated stations.
4. Fully-reconstructed events with fitted LDF-slope β.

More over, we wish to reconstruct events with β as a free parameter to be fitted in order to obtain the model of average LDF. This is achieved by setting the `<minNumberRelaxBeta>`

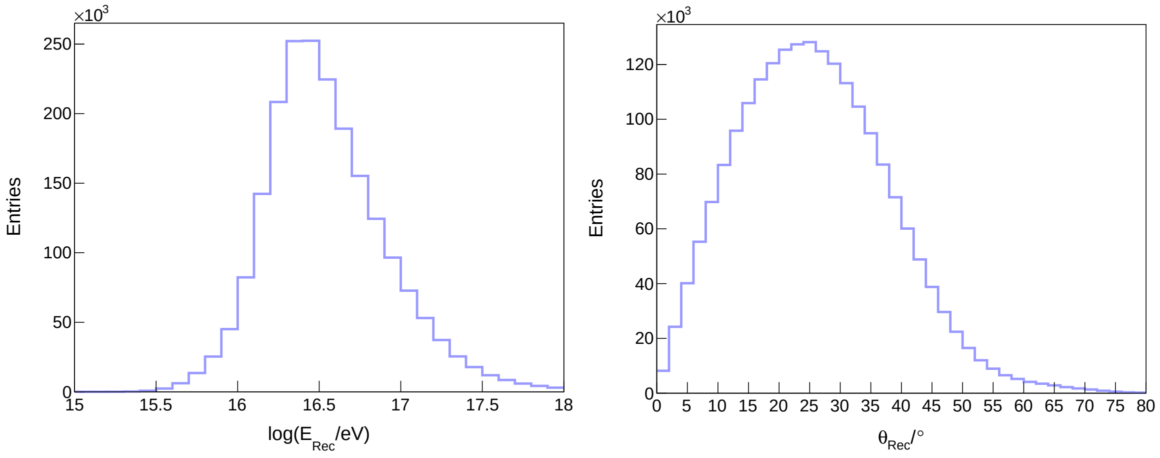

(a) (b)

Figure 4.7: The distribution of reconstructed energy (Fig. 4.7(a)) and zenith angle (Fig. 4.7(b)) for events in the selected period (2013-2020). No selection or quality cuts are applied to the events.

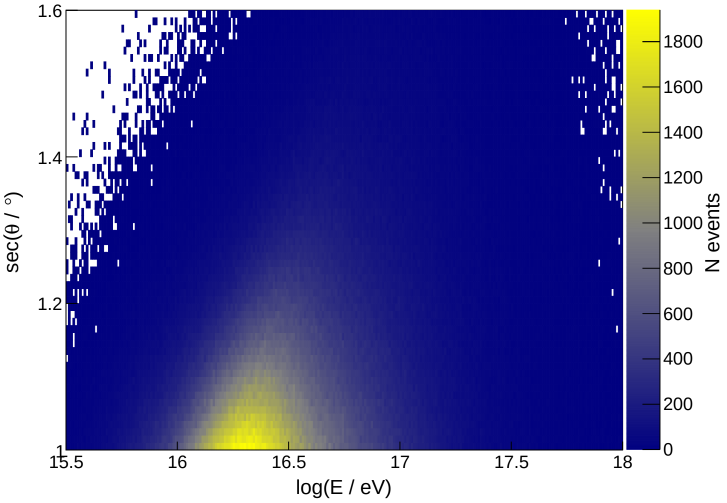

Figure 4.8: The two-dimensional distribution of the $\sec\theta$ and the reconstructed energy of the events in the selected period from begin 2013 to the end of 2020. No selection or quality cuts are applied to the events.

tag to 5 in the `LDFFinder` module. This tag indicates the minimum required number of stations the event has to have in order to attempt a reliable fit of β. The LDF parameter β is directly correlated with the slope of the LDF. Thus, on the one hand stations close to the core have a strong influence on the estimation of the parameter and are crucial to be be able to perform a successful fit. On the other hand it is important that the triggered stations are not too close to each other in order to include sufficient information about the variation of the lateral distribution. For this reason a fit of β will be performed if the stations participating in the event fulfil the following additional requirements, where again the distances have been adjusted accordingly to the array spacing:

- at least two stations within $100 - 400$ m from the shower axis with $r_{max} > 225$ m or
- at least three stations within $100 - 400$ m from the shower axis with $r_{max} > 200$ m or
- at least four stations within $100 - 400$ m from the shower axis with $r_{max} > 175$ m

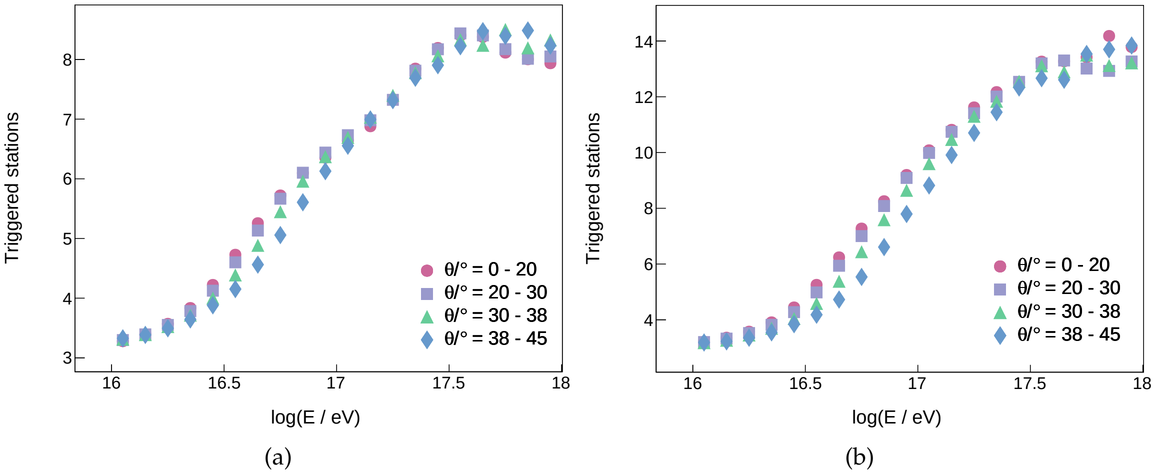

(a) (b)

Figure 4.9: The average number of triggered WCDs against the reconstructed energy when no geographic constraint is imposed to the shower cores (Fig. 4.9(a)) and when taking only events well-contained within the SD-433 unitary hexagon (Fig. 4.9(b)) presented for four different zenith intervals. The different markers represent zenith angle bins.

with r_{max} as the maximum distance between any corresponding pair of WCDs in the shower plane.

4.4 Optimal distance

The current optimal distance method starts with the fact that most of the events only trigger a handful of detectors. As consequence the detector signals have to be adjusted with a lateral distribution function (LDF) with a fixed slope (β) which is previously parametrized with the zenith angle and the shower size using events with many triggered detectors in order to be used in the fit. As the slope fluctuates event to event, there is an unavoidable mismatch between the true event slope, which is unknown, and the average value used in the fit. However varying the slope changes the reconstructed LDF and, consequently, the estimated shower size. In turn this systematic effect propagates to the energy estimated for an event. To minimise this impact an optimal distance, $r_{\rm opt}$, can be found for each event at which the value of the fitted LDF is independent of the slope. This pivotal point is found for each event by fitting the detector signals with different slopes.

The original SD-433 optimal distance proposed in [147] was 270 m which was obtained obtained using the mode of the optimal distance histogram instead of the mean as done elsewhere. The optimal distance was subsequently reduced to 250 m, the value configured currently in Offline.

As the sensitive parameter to the array geometry, $r_{\rm opt}$, enter in the functional form of the LDF, specified in Eq. 2.18, as $S_{r_{\rm opt}}$ and the slope-model parameters as well. Though the shower size $S_{r_{\rm opt}}$ is fitted event-wise by the `LDFFinderKG` module, the optimal distance needs to be specified a priori in the module configuration file through the `<ldfReferenceDistance>` tag. We will refer to the prior choice of the reference distance set in the configuration file as $D_{\rm ref}$ in order to distinguish it from the optimal distance $r_{\rm opt}$ to be determined as result of the fitting process. As mentioned before, the optimal distance $r_{\rm opt}$ is defined as the distance on the shower plane where the fluctuations of the LDF slope have the minimum influence on the average LDF. Stated otherwise, the signal provided by a model of average LDF at this distance is maximally reliable. This parameter depends on the array spacing and can

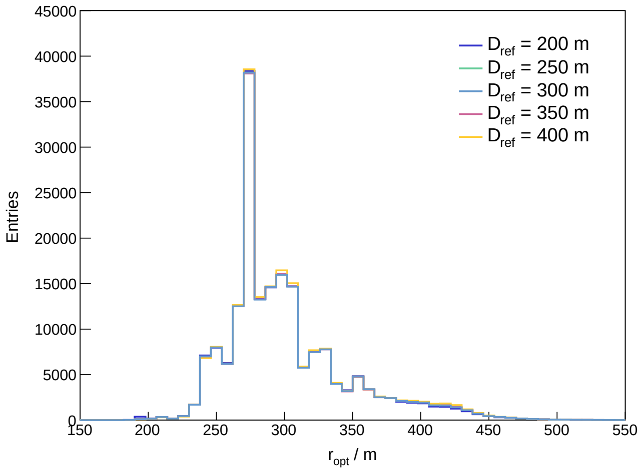

Figure 4.10: r_{opt} distribution of reconstructed events with fitted LDF-slope β for all chosen reference distances.

be estimated by varying the slope multiple times during the event reconstruction with an initial guess D_{ref}. Technically, r_{opt} is then defined as the distance corresponding to the crossing point of these resulting fitted LDFs. For this reason, a reconstruction of different data sets has been performed for five different D_{ref}, as shown in Fig. 4.10, in order to determine the suitable optimal distance analysing the reconstructed events. Although the LDFFinder configuration allows the user to set a prior D_{ref}, the module includes the possibility to calculate r_{opt} as soon as the LDF fit has been performed. To calculate the optimal distance, the slope estimate is varied within its uncertainty a number `<RoptN>` times, which has been fixed to 2, and a new LFD fit is attempted. Fig. 4.10 shows the optimal distance calculated in this way as independent from the prior D_{ref} choice. This result is related to the slope parameter that is independent from the parametrization in Eq. 2.19 and consequently is unconnected to the $S_{r_{\mathrm{opt}}}$. A peculiar feature can be observed from Fig. 4.10, as a peak at $r_{\mathrm{opt}} \sim 270$ m. In order to investigate this trait, we divided the data set of reconstructed events with $D_{\mathrm{ref}} = 250\ m$ into four samples. The shower-core positions for the four samples are shown in the two-dimensional histograms in Fig. 4.11, in particular for r_{opt} <260 in Fig. 4.11(a), 260< r_{opt} ≤280 in Fig. 4.11(b), 280< r_{opt} ≤300 in Fig. 4.11(c), and r_{opt} ≥300 in Fig. 4.11(d). As it can been noticed from Fig. 4.11(a), a high events-per-bin density is observed between the central station and the station 30, which has been installed closer to the central WCD than the other stations of the hexagon. As a consequence, in Fig. 4.11(a) an aggregate of event in visible between the station 30 and the central one, whilst in Fig. 4.11(b), Fig. 4.11(c), and Fig. 4.11(d) a lower event density is shown for events with $r_{\mathrm{opt}} > 260$ m.

The optimum core distance to measure the size of the shower can be calculated for each shower and is determined primarily by the array geometry, with no significant dependence on the shower zenith angle, energy or the assumed lateral distribution function [181]. The presence of saturated tanks has a significant impact on r_{opt}. If, by chance, a shower core lies close to one tank, the signal in that tank may be saturated. In the case of one saturated WCD, a ring of 6 stations with similar signals surrounds it with all WCDs lying at about 433 m from the core. The reconstructed values are only weakly constrained by the presence of the saturated station, and so r_{opt} is found at the point where most of the signals are measured. Therefore, the asymmetry we found in the array geometry (Fig. 4.11(b)), is more accentuated if the station 30 is the one with the second highest signal, since the optimal distance depends on the mutual distance between the WCDs and it approaches this distance as much as

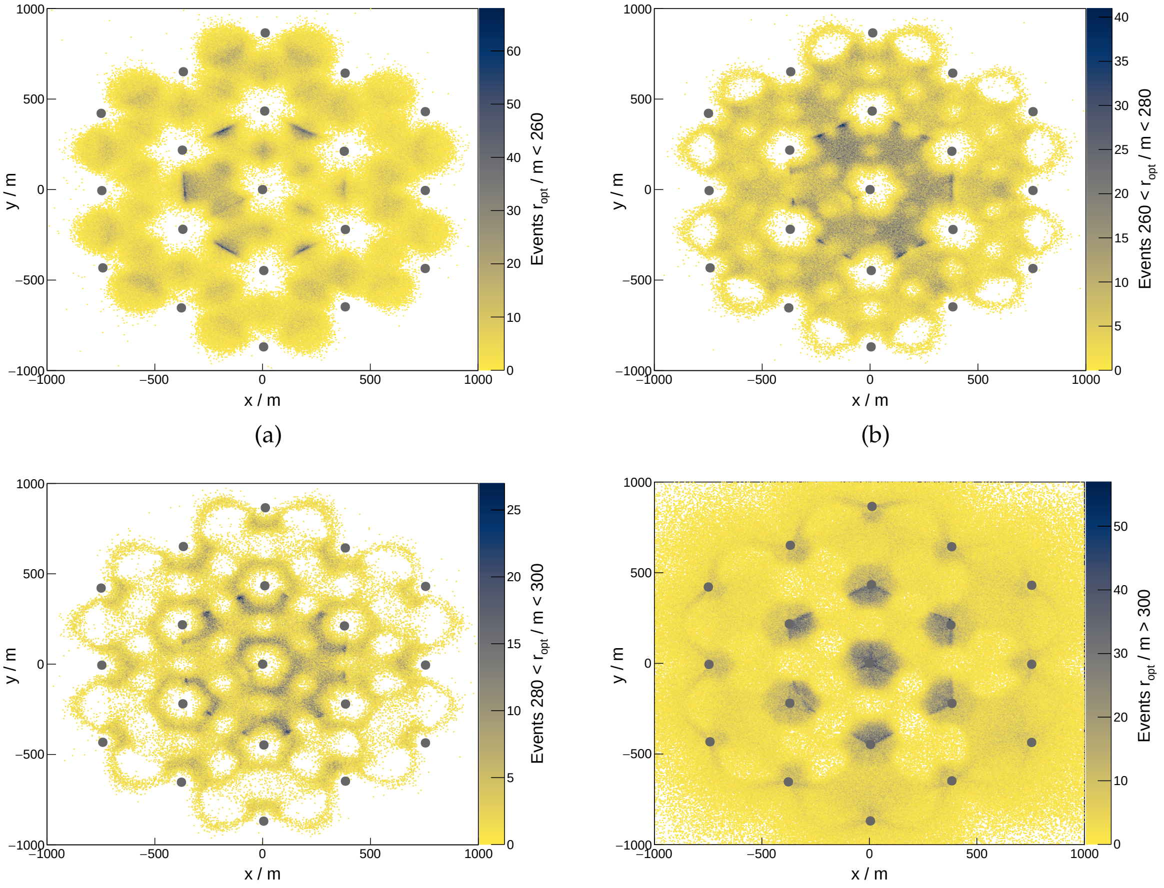

(a) (b) (c) (d)

Figure 4.11: Shower-core position distribution of the reconstructed events with fitted LDF-slope and $D_{\text{ref}} = 250$ m. The data set of reconstructed events has been split into four samples: $r_{\text{opt}} <260$ in Fig. 4.11(a), $260< r_{\text{opt}} \leq 280$ in Fig. 4.11(b), $280< r_{\text{opt}} \leq 300$ in Fig. 4.11(c), and $r_{\text{opt}} \geq 300$ in Fig. 4.11(d).

the shower core falls close to a station. Another way to look at the the optimal distance distribution is shown in Fig. 4.12, where r_{opt} is plotted as a function of the distance of the core to the station $r_{S_{\text{max}}}$ with the maximum signal in the event. The gray points represent the average r_{opt} in each $r_{S_{\text{max}}}$-bin, the error bars correspond to 1σ spread in that bin, whilst the two-dimensional histogram in the background shows the event density. Two lines are are drawn respectively at 300 m (solid) and at 270 m (dashed). It is visible how the tail of the r_{opt} distribution arises for events where the maximum-signal station is very close to the shower core, which means for $r_{S_{\text{max}}} \leq 100$ m. These events have a peculiar LDF, very steep close to the core, due to the station configuration: the highest-signal station very close, and all the other 6 neighboring stations approximately at the same distance. At the same time, the bulk of the distribution concentrates around three r_{opt} values: at ∼270 m, at ∼300 m, and at ∼340 m. Looking at the binned values, the average distance where the slope fluctuations are minimal is 270 m which is also the r_{opt}-bin where one can notice the highest congregation of events. Therefore, this result could lead to an explanation of the peak around $r_{\text{opt}} \sim 270$ m seen before in Fig. 4.10 and in the histograms that follows.

We built a histogram with normal events, i.e. events that had all detectors free of saturation, and another histogram with saturated events as shown in Fig. 4.13 leaving the slope parameter as free or fixing it to the known parametrization. The distribution has two dis-

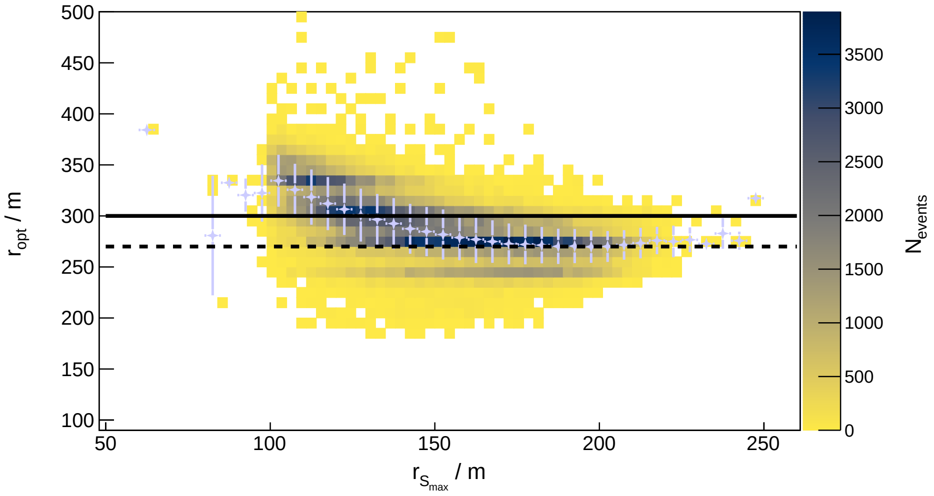

Figure 4.12: The optimal distance r_{opt} as a function of the maximum-signal-station distance $r_{S_{max}}$. The lilac circles represent the average value of r_{opt} values in that particular bin, the error bars their 1 spread around the average, and the background histogram the events-per-bin density. Finally, the lines are respectively drawn at 300 m (solid) and 270 m (dashed).

tinct populations corresponding to events with and without saturated signals. The optimal distance of saturated events is higher on average due to the fact that, for saturated events, the shower core falls very close to one stations and thus the majority of stations is further away than for the typical event. The mean value for the events without a saturated signal is 290 m in both cases and its RMS deviation is $\sim$ 30 m independently of the β constraint.

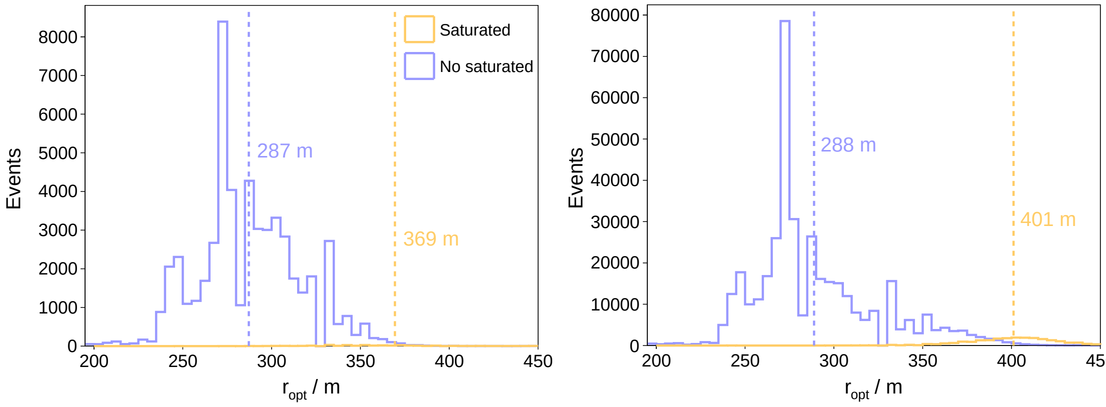

(a) (b)

Figure 4.13: Histograms of the optimal distance for normal events (without saturated events) and with saturated events for a set of data reconstructed leaving β as free parameter to be fitted (Fig.4.13(a)) and fixed (Fig.4.13(b)) to its value taken from the parametrization. Stated and depicted with the vertical lines are the mean values of the histograms.

We investigated the dependence of the optimal distance with the variance of the triggered stations multiplicity for the SD-433 (Fig. 4.14(a)) and for consistency for the SD-433 (Fig. 4.14(b)). It can be seen in Fig. 4.14 that for both arrays the distribution of the optimal distance shifts towards higher mean values as the multiplicity of station increases, although lower multiplicity events with less than 5 stations dominate the data set statistics. On the one hand, the sample with a multiplicity of triggered stations < 5 is the one that contains the majority of reconstructed events, thus, it is reasonable to think that the average value of the optimal distance of the whole data set tends to approach the mean value of the $< 5-$fold distribution, which matches the r_{opt} values reported in Fig. 4.13 as in [182, 183]. On the other hand, the set of real data was reconstructed leaving β as a free parameter to be fitted, which is possible if the event has at least five triggered stations. This is consistent with the result obtained from Fig. 4.13, where the two histograms present a similar behaviour and about the same mean value, independently of the choice of leaving β free or fixed by the parametrization in [147], since the bulk of the distribution will concentrate around the r_{opt} value dictated by events with less than 5 triggered stations and consequently with β fixed.

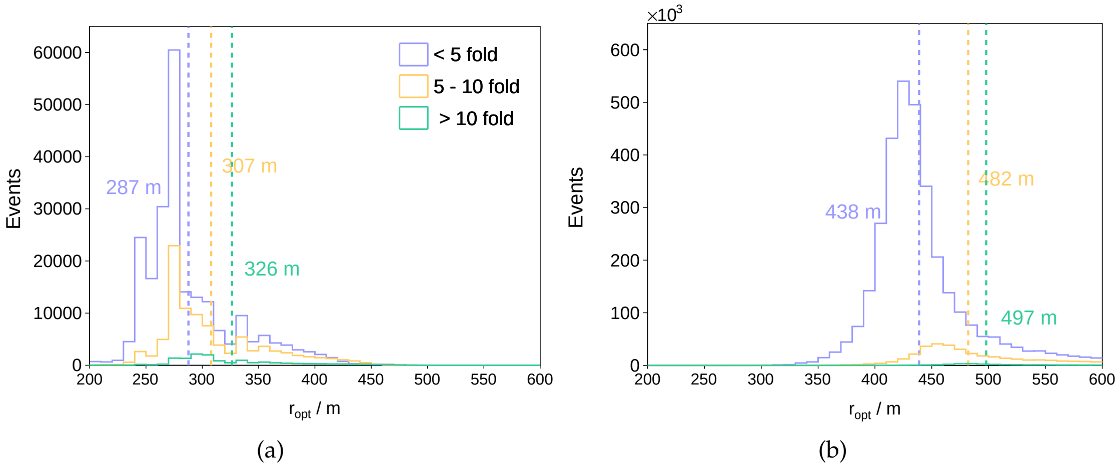

Figure 4.14: Distribution of the optimal distances obtained from events observed by the SD-433 (Fig. 4.14(a)) and the SD-750 (Fig. 4.14(a)) for three different station multiplicities.

In addition, we applied the pivot method to calculate the optimal distance from simulations and from real data as shown in Fig. 4.15. The mean r_{opt} is estimated to be about 300 m independently of the zenith angle and the measured signal at 250 m as depicted in Fig. 4.15(a). Recalling that the LDF, hence the shower footprint, is directly linked to the primary energy, it can be deduced that r_{opt} is also independent of the cosmic-ray energy. Similar distributions are obtained for simulated events with known primary composition as displayed in Fig. 4.15(b). Therefore, the optimal distance for the SD-433 is chosen as $r_{\text{opt}} = 300$ m.

4.5 Lateral distribution function

Once that r_{opt} has been fixed, the complete data set has been reconstructed again using $r_{\text{opt}} = 300$ m. The $\overline{\text{Off}}\underline{\text{line}}$ LDFFinder settings were adjusted accordingly in order to set β as free parameter. In what follows, this data set has been used to determine the parametrisation in Eq. 2.19 adopting an event-by-event fit approach.

The lateral distribution of signals measured with WCDs is customarily described by modified versions of the Nishimura-Kamata-Greisen (NKG[11]) function:

$$S(r) = S(r_{\text{opt}}) \cdot f_{\text{LDF}}(r) = S(r_{\text{opt}}) \cdot \left(\frac{r}{r_{\text{opt}}}\right)^{\beta} \left(\frac{r + r_{\text{opt}}}{r_{\text{scale}} + r_{\text{opt}}}\right)^{\beta}, \tag{4.1}$$

where by construction, the shape factor f_{LDF} is unity at the distance r_{opt}, while the parameter β governs the expected signal drop with increasing distance. The scale parameter r_{scale} plays

---

[11] Nishimura-Kamata-Greisen

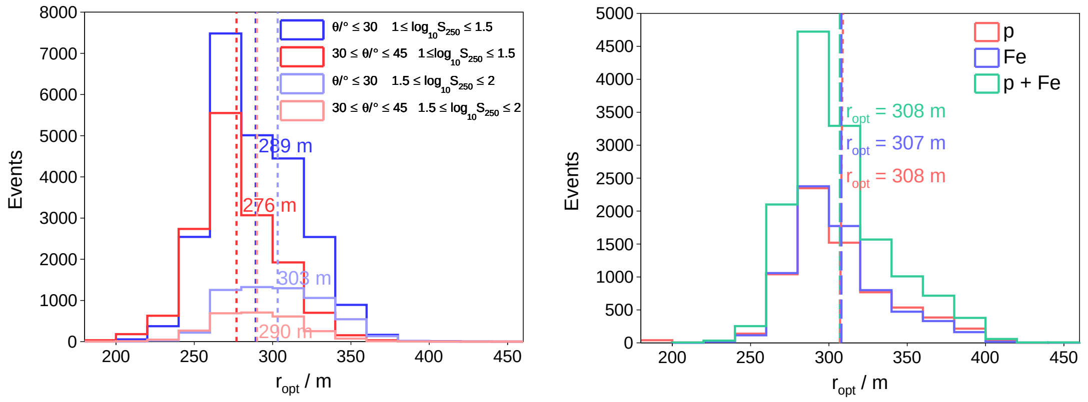

(a) (b)

Figure 4.15: Fig. 4.15(a) shows the r_{opt} distribution of reconstructed events for two different zenith angles and shower size intervals. In Fig. 4.15(b) the optimal distances is illustrated for simulated events produced produced by proton, iron and mixed composition showers. Stated and depicted with dashed vertical lines are the mean values of the histograms.

a role only at larger distances and has been kept fixed to 700 m. The normalization factor $S(r_{\mathrm{opt}})$ is the so-called shower size which is a measure of the primary energy.

The event-by-event β, as already presented in Eq. 2.19, can be described by a first degree polynomial in $\log_{10} S_{300}$. The functional form is

$$\beta(\log S_{300}, \theta) = A(\theta) + B(\theta) \times \log_{10} S_{300}\,. \tag{4.2}$$

where, in turn, the two coefficients follow a second degree polynomial in $\sec\theta$ given by

$$\begin{pmatrix} A \\ B \end{pmatrix} = \begin{pmatrix} a & c & e \\ b & d & f \end{pmatrix} \times \begin{pmatrix} 1 \\ \sec\theta \\ \sec^2\theta \end{pmatrix}\,. \tag{4.3}$$

The events were selected according to the cuts introduced before in Sec. 4.3.

The next task is to construct a suitable function to estimate the parameters. For the fit, we have used a least-squares method to determine the set of parameters (a, b, c, d, e, f) of the β model, that minimizes the objective function (summing over all n events):

$$\chi 2 = \sum_{i=1}^{n} \frac{|\beta_i - \beta(\sec\theta_i, \log_{10}(S_{300,i})|^2}{\sigma[\beta_i]^2}\,, \tag{4.4}$$

where $\sigma[\beta_i] = \sigma_i$ since instead of an uncertainty model we used the data uncertainties. An uncertainty β model is going to be described below. The minimisation is done with the MINUIT2 package and, for consistency checked with the ROOT data analysis framework. The model is fitted to data using an unbinned and a binned least squares fit. Fig. 4.16 shows the residuals between the unbinned fit, the binned fit, and the old fit [147]. In order to optimise the description of the lateral distribution of the observed events, we chose the binned fit as the residuals of this fitting procedure are closer to zero compared to the unbinned fit and the old parametrization.

The resulting parameters and their uncertainties are summarized in Tab. 4.1.

In Fig. 4.17(a) and in Fig. 4.18(a) a comparison of the event-by-event fitted slope β_i (markers) and the model prediction $\tilde{\beta}_i$ (solid lines) is shown respectively as a function of the

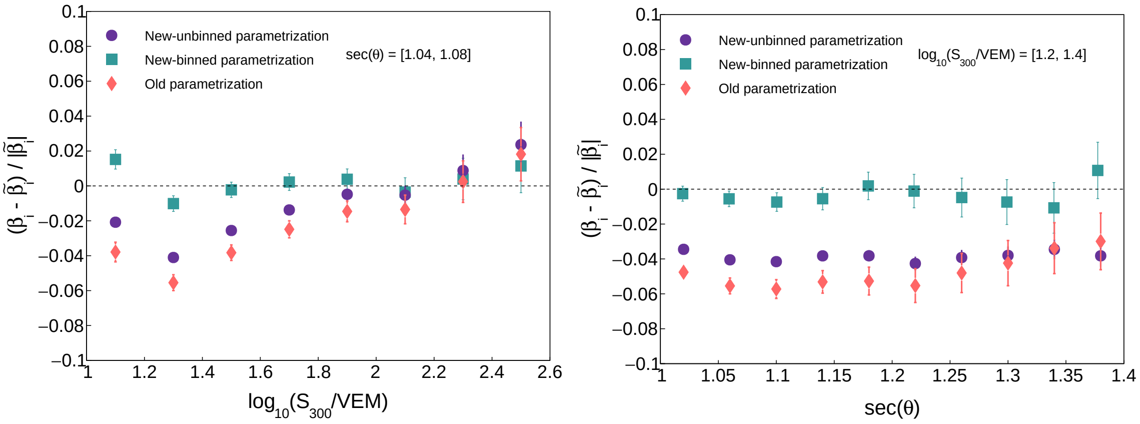

(a) (b)

Figure 4.16: A comparison of the LDF residuals between the model resulting from the unbinned fit, the binned fit and using the old parameters for one interval of $\sec\theta$ (Fig. 4.16(a)) out of the considered ten and for one interval of $\log_{10} S_{300}$(Fig. 4.16(b)) out of the considered eight. The residuals of the new model using a binned fit are closer to zero. For this reason we chose the binned fit as the best method to evaluate the new LDF parameters

Parameter	a	b	c	d	e	f
Value	-1.773	-0.400	-1.611	0.781	1.174	-0.415
Uncertainty	0.0111	0.008	0.012	0.009	0.008	0.006

Table 4.1: Parameters and uncertainties the LDF-slope model, specified in Eq. 2.19.

$\sec\theta$ and of the $\log_{10}(S_{300})$. In order to evaluate the goodness of the parametrization, it is instructive to look at the residuals in Fig. 4.17(b) and Fig. 4.18(b) calculated as follows

$$\mathrm{Res}(\beta_i) = \frac{\beta_i - \tilde{\beta}_i}{\tilde{\beta}_i}\,, \tag{4.5}$$

that are given by the differences between data points β_i and relative model predictions $\tilde{\beta}_i$.

It can be observed that the model gives an accurate description of the data with an average relative difference of the order of 2% for the considered zenith angle range. The bin points resemble the weighted averages $\bar{x}$ of the data points with a weighting $w_i = 1/\sigma_i$ according to the individual independent uncertainties. Since the average LDF slope can be fixed by the mentioned parametrization, a similar procedure can be conducted for its fluctuations. The β distribution follows a Gaussian probability density function when limited to a certain energy interval or, analogously, to a shower size interval. Thus the uncertainty can be represented as the standard deviation of the mean of the Gaussian distribution. In this sense, Fig. 4.19 shows the uncertainty of the parametrized β as a function of the shower size. The slope uncertainty model is defined by

$$\sigma_\beta = \exp\left[p_0 + p_1 \cdot \log_{10}(S_{300}/\mathrm{VEM})\right]\,, \tag{4.6}$$

with fitted parameters $p_0 = (0.01 \pm 0.02)$ and $p_1 = (1.2 \pm 0.02)$.

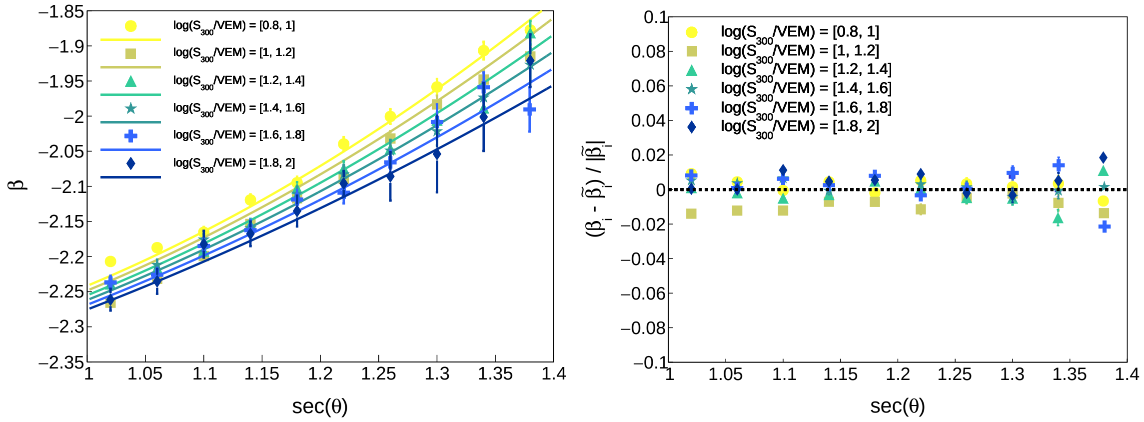

(a) (b)

Figure 4.17: Fig. 4.17(b): The event-by-event fitted β and the superimposed model predictions by means of Eq. 4.1 in terms of the $\sec\theta$ for the quoted shower size intervals. Fig. 4.17(b): the relative differences between fitted data and the model prediction of β.

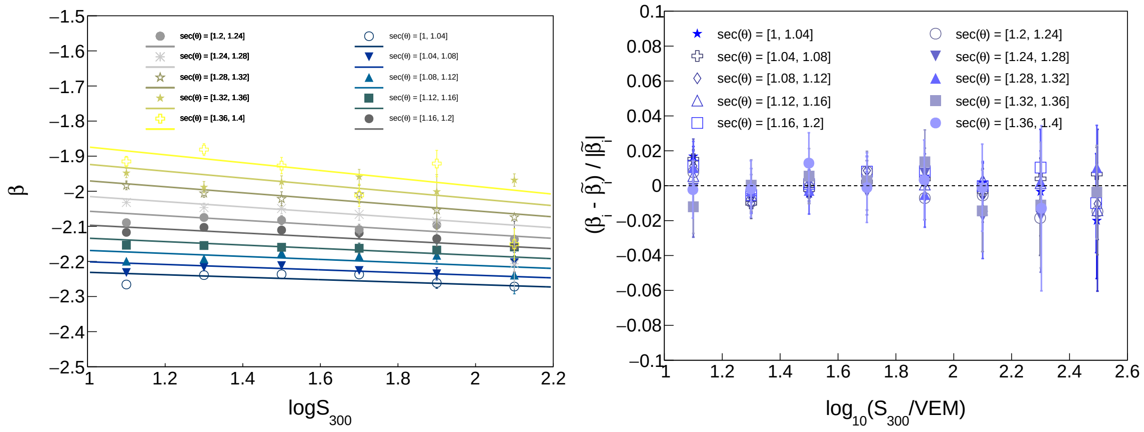

(a) (b)

Figure 4.18: Fig. 4.18(a): The event-by-event fitted β and the superimposed model predictions by means of Eq. 4.1 in terms of the $\log_{10}(S_{300})$ for the quoted $\sec\theta$ intervals. Fig. 4.18(b): the relative differences between fitted data and the model prediction of β.

4.6 Constant Intensity Cut

As mentioned in Section 2.2.7 the signal at the optimal distance S_{opt} depends on the energy E and on the zenith angle θ of the primary CR, as the attenuation changes with the amount of traversed atmosphere. The amount of traversed matter by the shower and therefore the number of interactions within the atmosphere increase with θ, the electromagnetic component is largely absorbed[12], thus the measured particle density decreases and accordingly the measured signals at ground level are attenuated depending on the different amount of atmosphere that is crossed for different arrival directions.

This effect is zenith-angle dominated while is definitely independent from the shower azimuth angle, as the amount of atmosphere does not change with it. This dependence has to be corrected for to get an energy estimator solely dependent on the energy. The

---

[12] For showers below 60°, the attenuation of the muonic component is negligible, whereas the electromagnetic component decreases with zenith angle.

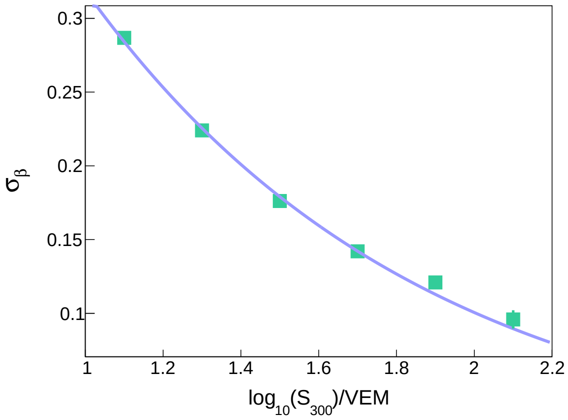

Figure 4.19: The uncertainty of the parametrized β in terms of the shower size S_{300} for events with $\theta < 45°$.

Constant Intensity Cut (CIC) method is a well established method, that eliminates the zenith angle dependence of the signal or shower size at the optimal distance $S_{r_{\mathrm{opt}}}(E, \theta)$ [150] . In this Section, we will make use of the CIC method to obtain the zenith-independent energy estimator $S_{\theta_{\mathrm{ref}}}(E)$ in order to make possible the calibration of this energy estimator with a reference energy measurement. Therefore, the Constant Intensity Cut is a vital step in the reconstruction towards a final SD-433 energy spectrum.

In general, the $S_{r_{\mathrm{opt}}}$ depends on the zenith angle for several reasons. The main reason is that, compared to an air shower with low zenith angle, once it has passed the depth of shower maximum, an air shower with higher zenith angle has to traverse more atmosphere until reaching the ground. Therefore, the particle densities and measured signals at the ground decrease with rising zenith angle. Another reason is of geometrical nature. With rising zenith angle, the station distances in the shower plane are decreasing and the projected area of a surface detector tank is increasing at first and then decreasing again. Compared to the attenuation, these are minor effects and the CIC is an empirical correction for all effects together.

4.6.1 Energy estimator

The empirical method assumes an isotropic arrival distribution for the primary particles above a certain trigger energy threshold E_{thr}, and therefore the energy and zenith-angle dependencies of $S_{r_{\mathrm{opt}}}(E, \theta)$ can be factorized. As the detector measurement is symmetric in azimuth, in mathematical terms the isotropy assumption is stated as

$$\frac{d}{d\theta} J = 0 \,. \tag{4.7}$$

The flux of cosmic rays J expressed as the number of particles dN with energy E incident on an effective-surface element dA_{eff}, within a solid angle $d\Omega$ and time dt, is given by

$$J(E) = \frac{d^4 N}{dE\, dA_{\mathrm{eff}}\, d\Omega\, dt} \,. \tag{4.8}$$

The stations are located in the detector plane, thus the effective detector area $dA_{\mathrm{eff}} = \cos\theta dA$ corresponds to the projection of the flat area A, where the stations are located, into the shower plane. With the solid angle element $d\Omega = d\cos\theta d\phi$ the condition of an isotropic flux reads

$$\frac{d}{d\theta}\left(\frac{d^4N}{dEd\cos^2\theta dAdt}\right) = 0\,, \tag{4.9}$$

where $2\cos\theta d\cos\theta = d\cos^2\theta$ has been used. Zenith angle independent variables can be neglected and the previous condition in then equivalent to

$$\frac{d}{d\theta}\left(\frac{d^2N}{dEd\cos^2}\right) = 0 \Rightarrow \frac{d^2N}{dEd\cos^2} = \text{constant}\,. \tag{4.10}$$

The Eq. 4.10 can be integrated over energy above the trigger-threshold energy E_{thr} to define the intensity I of events

$$\int_{E_{\mathrm{thr}}}^{\infty} dE\frac{d^2N}{dEd\cos^2} := \frac{dI}{d\cos^2\theta}\bigg|_{E=E_{\mathrm{thr}}} = -\frac{dI}{d\sin^2\theta} = \text{constant}\,. \tag{4.11}$$

Therefore, for $E > E_{\mathrm{thr}}$ we expect the same number of events in equally spaced $\sin^2\theta$ intervals. This condition is exploited in order to disentangle energy and zenith-angle dependencies of the signal at the optimal distance $S_{r_{\mathrm{opt}}}$. Fig. 4.20 shows the distributions in four zenith angle bins with equal $\sin^2\theta$ binning. With rising zenith angle the distributions are shifted to lower signals due to the increasing attenuation of the air showers, confirming that the zenith-angle dependency of $S_{r_{\mathrm{opt}}}$ can be factorized. The horizontal line corresponds to a constant intensity which is clearly not achieved for the same value of $S_{r_{\mathrm{opt}}}$. in the different angular bins. This cut value for the first bin corresponds to $S_{250}^{\mathrm{cut}} \approx 73$ VEM and to $S_{300}^{\mathrm{cut}} \approx 45$ VEM decreasing to 36 VEM and 23 VEM for the last bin respectively. For a zenith-independent energy estimator, an equal intensity needs to be observed at all zenith angles.

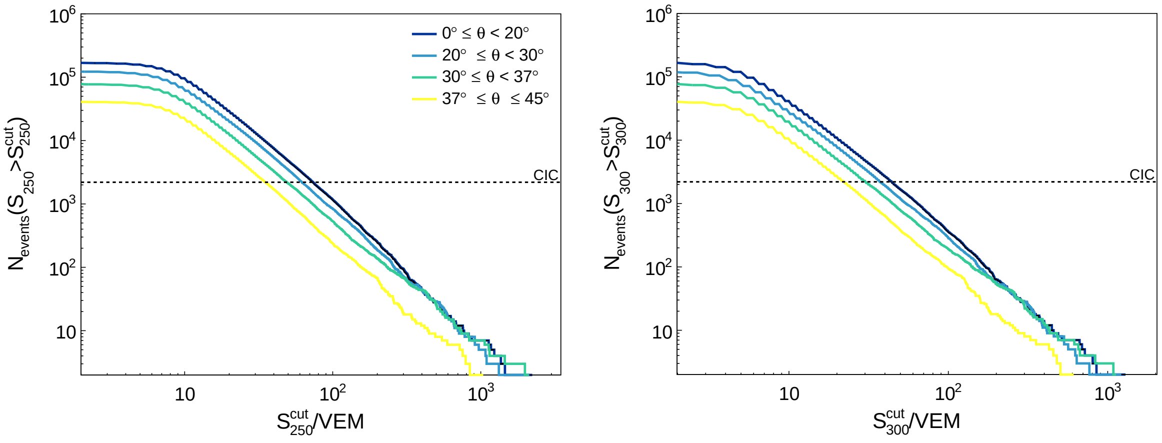

(a) (b)

Figure 4.20: Number of events with $S_{r_{\mathrm{opt}}}$ above the corresponding $S_{r_{\mathrm{opt}}}^{\mathrm{cut}}$ value on the x-axis for four angular bins of equal width in $\sin^2\theta$ for both sets of data: in Fig. 4.20(a) is presented the intensity of events of the data set reconstructed with $r_{\mathrm{opt}} = 250$ m and the old LDF parameters, while in Fig. 4.20(b) the one reconstructed with $r_{\mathrm{opt}} = 300$ m and the new LDF parameters. The horizontal dashed line corresponds to a cut intensity at 500 events, which is achieved at smaller $S_{r_{\mathrm{opt}}}^{\mathrm{cut}}$ values as the zenith angle increases. Because of the atmospheric attenuation, at the ground level, inclined showers will contain less particles than vertical ones.

It follows that a separation of the signal distribution into n bins of equal $\sin^2\theta$ size will give n $S_{r_{\rm opt}}(E,\theta)$ values that correspond to the same (still unknown) energy E. The goal is to transform each $S_{r_{\rm opt}}(E,\theta)$ into an energy estimator that does not depend on the zenith angle and it is only energy-dependent, $S_{\theta_{\rm ref}}(E)$. In the following step, the zenith angle dependence is separated from the energy dependence by factorizing $S_{r_{\rm opt}}$ into $S_{\theta_{\rm ref}}(E)$ and the mentioned angular dependence CIC(θ) as in

$$\begin{aligned} S_{r_{\rm opt}}(E,\theta) &= S_{r_{\rm opt}}(E,\theta=\theta_{\rm ref})\cdot \mathrm{CIC}(\theta) \\ &= S_{\theta_{\rm ref}}(E)\cdot \mathrm{CIC}(\theta)\,, \end{aligned} \tag{4.12}$$

where the definition $S_{r_{\rm opt}}(E,\theta=\theta_{\rm ref}) := S_{\theta_{\rm ref}}(E)$ is used. The function $\mathrm{CIC}(\theta)$ is the Constant Intensity Cut correction function which is empirically parametrised as in Eq. 4.13. For a certain intensity (cut) value, the function in $\mathrm{CIC}(\theta)$ determines the correspondence between the different zenith-dependent cut values $S^{\rm cut}_{r_{\rm opt}}$ (Fig. 4.20), and the single value of the signal at the reference angle.

For the present analysis, the same set of repaired data (silent stations included) used before has been reconstructed again using two different reconstruction configuration:

- *Dataset-1*:β fixed from the previous parametrization and $r_{\rm opt} = 250$ m [147],
- *Dataset-2*: β fixed from the parametrization obtained in Sec. 4.5 and the optimal distance of $r_{\rm opt} = 300$ m determined in Sec. 4.4.

To characterize the attenuation function, several methods have been designed [184]. The most usual approach is the so-called countdown method, which consists in binning events in $\sin^2\theta$ to ensure equal exposure, then order events in each bin by decreasing $S_{r_{\rm opt}}$, select the same number of events n at each bin (i.e. constant intensity), and finally record for each bin the $S_{r_{\rm opt}}$ at the cut. Taking some reasonable assumptions like that the cosmic ray Flux is isotropic above the trigger threshold energy $E_{\rm thr}$ and that the detector is fully efficient at the cut, the cut represents the attenuation of $S_{r_{\rm opt}}$ with zenith angle. We divided the zenith angle range between 0° and 45° in 18 $\sin^2\theta$ bins and then we registered the $S_{\rm cut}$ values at the different constant intensity $n^{\rm th}_{\rm cut}$ positions as depicted in Fig. 4.21 for the two different reconstructed sets: in Fig. 4.21(a) we considered data from *Dataset-1*, while for Fig. 4.21(b) we used the *Dataset-2*.

Given a constant intensity $n_{\rm cut}$, the associated $S^{\rm cut}_{r_{\rm opt}}$ is found by scanning the curves. Since the curves do not lie on top of each other, a value of $n_{\rm cut}$ correspond to different abscissa values in each $\sin^2\theta$ bin as exemplified in Fig. 4.21. The asymmetric uncertainty of each $S^{\rm cut}_{r_{\rm opt}}$ is calculated with an approximate method. Given the number $n_{\rm cut}$ we selected events in the positions $N_\pm = n_{\rm cut} \pm \sqrt{n_{\rm cut}}$. Thus, the uncertainty is provided by the mean of the difference between the $S^{\rm cut}_{r_{\rm opt}}$ calculated at N_- and N_+, following the poissonian nature of the countdown method [185]. The obtained $S^{\rm cut}_{r_{\rm opt}}$ uncertainty fluctuates between the 4.5% (for $n_{\rm cut} = 100$) and 1.6% (for $n_{\rm cut} = 1000$).

If no attenuation effect were in play, $S^{\rm cut}_{r_{\rm opt}}$ at a fixed $n_{\rm cut}$ would be independent of the zenith angle.Nevertheless this dependence can be modeled with a polynomial function, $\mathrm{CIC}(\theta)$, which is the Constant Intensity Cut correction function to be determined, with functional form:

$$\mathrm{CIC}(\theta) = 1 + ax(\theta) + bx^2(\theta)cx^3(\theta)\,, \tag{4.13}$$

where

$$x(\theta) := \sin^2(\theta) - \sin^2(\theta_{\rm ref})\,. \tag{4.14}$$

The choice of the reference angle $\theta_{\rm ref}$ is not crucial from a mathematical point of view, but it can be chosen cleverly. In the CIC formulation is chosen as the median of the zenith angle

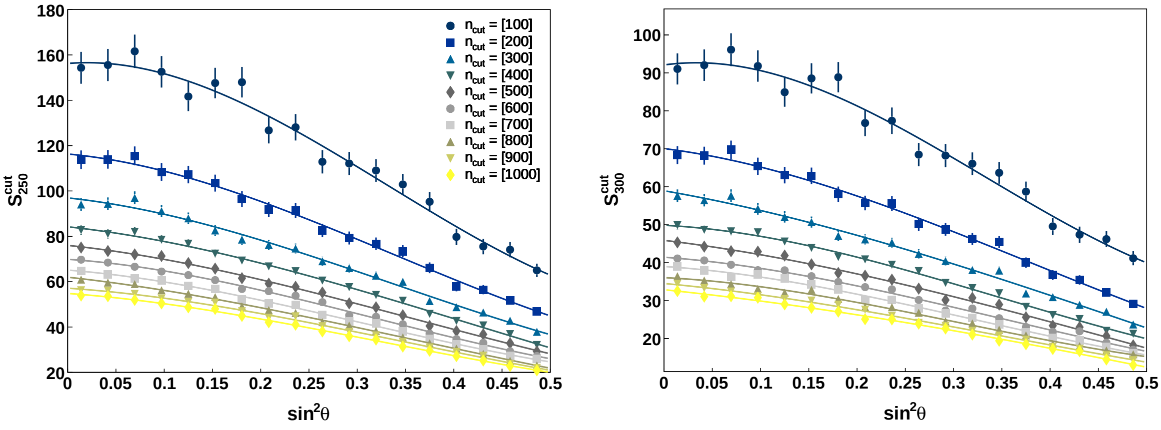

(a) (b)

Figure 4.21: The attenuation curves of the $S^{\rm cut}_{r_{\rm opt}}$ in terms of the zenith angle for the quoted intensity cuts. The $S^{\rm cut}_{r_{\rm opt}}$ values at the selected $n_{\rm cut}$ positions in each $\sin^2\theta$ bin are reported in Fig. 4.21(a) using events of the *Dataset-1*, while in Fig. 4.21(b) using events from *Dataset-2*.

distribution since in this way the impact of the CIC correction is minimized. Therefore, choosing $\theta_{\rm ref}$ in the centre of the $\sin^2\theta$ range is reasonable:

$$\begin{gathered}\sin^2\theta_{\rm ref} = \langle \sin^2\theta \rangle = \frac{1}{2}\left(\sin^2\theta_{\rm min} + \sin^2\theta_{\rm max}\right) \\ \Longrightarrow \theta_{\rm ref} = \arcsin\sqrt{\langle \sin^2\theta \rangle}\,. \end{gathered} \tag{4.15}$$

For the SD-433 array the zenith angle range of vertical events is [0°,45°] and thus $\theta_{\rm ref} = 30°$.

Several attenuation curves are shown in Fig. 4.22. The intensity cut $n_{\rm cut}$ should be chosen as to eradicate, as much as possible, the angular dispersion of the shower size. For a given value of $n_{\rm cut}$, the CIC curve is applied to each reconstructed event as to find the reference shower size $S_{\theta_{\rm ref}}(E) = S_{30}(E)$ from Eq. 4.12 and Eq. 4.13. The CIC functions showed in Fig. 4.22 were explored in order to choose the one which provides the minimum angular dispersion in $S_{30}(E)$. The uncertainty model of the CIC curve is estimated by examining the spread between the CIC curves. No substantial differences have been observed. The spread of the attenuation curves is maximum at the extremes of the allowed zenith angle range collapsing to a null value at $\theta = \theta_{\rm ref}$ by construction. The maximum difference across the range of x decreases from $\sim 10\%$ for $x < 0.15$ and increases up $\sim 4\%$ for $x < 0.3$.

The attenuation function associated with $n_{\rm cut} = 500$ is chosen as a first estimation of the CIC corrections defined by the fitted parameters shown in Tab. 4.2 and in Tab. 4.3 for both sets of reconstructed data. The $S^{\rm cut}_{r_{\rm opt}}$ uncertainty for $n_{\rm cut} = 500$ is $\sim 2.5\%$

Parameter	$S^{\rm cut}_{30}$/VEM	a	b	c
Value	55.68	-1.92	-1.03	3.25
Uncertainty	0.48	0.09	0.31	2.23

Table 4.2: The parameters resulting from the fit of the correction function of the Constant Intensity Cut at $n_{\rm cut} = 500$ for *Dataset-1*.

The fitted parameters in Tab. 4.2 and Tab. 4.3 can be seen in Fig. 4.23(a) and Fig. 4.23(b) respectively for both sets of data. The third-degree polynomial parameter fluctuate strongly,

Parameter	S_{30}^{cut}/VEM	a	b	c
Value	34.15	-1.76	-1.15	1.56
Uncertainty	0.30	0.09	0.31	2.27

Table 4.3: The parameters resulting from the fit of the correction function of the Constant Intensity Cut at $n_{\mathrm{cut}} = 500$ for *Dataset-2*.

compared to the first and second degree parameters which evolution is approximately linear with S_{30}. Seeing that the third-degree term did not add a substantial improvement to the resulting CIC functions calculated from Eq. 4.13 and presented in Fig. 4.22, it can be dropped out from the model, leaving the expression to a second degree polynomial function.

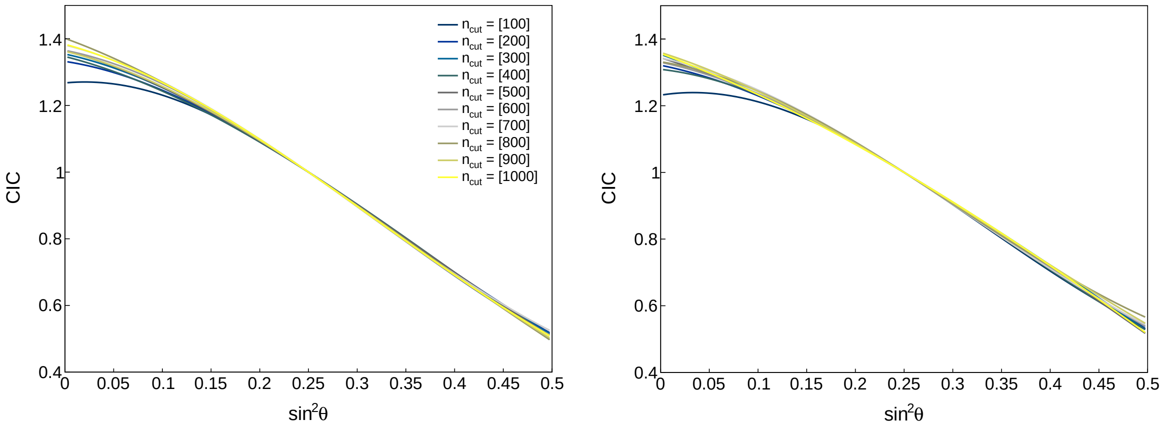

(a) (b)

Figure 4.22: The CIC function of Eq. 4.13 for several values of n_{cut} for *Dataset-1* and *Dataset-2* respectively shown in Fig. 4.22(a) and Fig. 4.22(b).

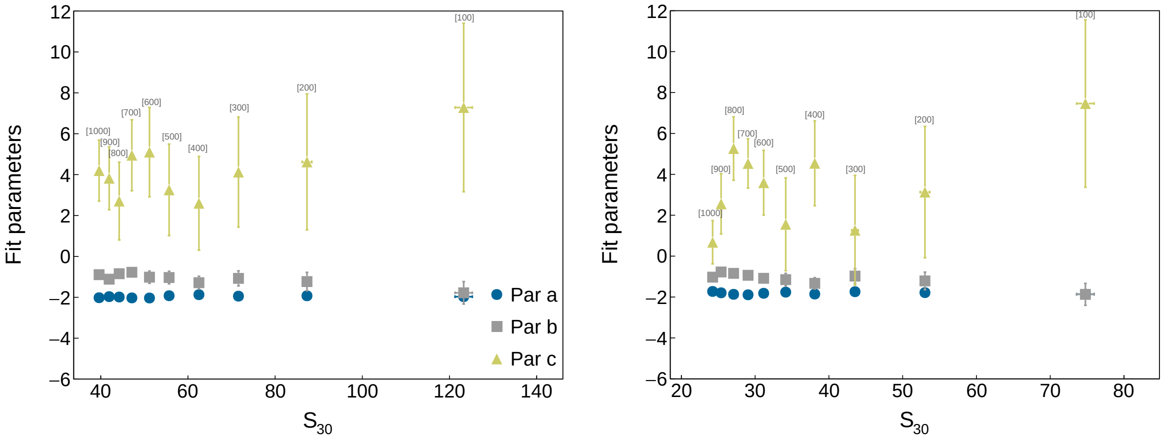

(a) (b)

Figure 4.23: Variation of the fitted parameters a, b, c from Tab. 4.2 and Tab. 4.3 depicted in Fig. 4.23(a)(*Dataset-1*) and Fig. 4.23(b)(*Dataset-2*) respectively, for the correction function in Eq. 4.13 using the selected 10 n_{cut} values.

Thereafter, assuming that the correction function in Eq. 4.13 is valid at any intensity, every measured $S_{r_{\mathrm{opt}}}$ can be converted to the corresponding S_{30} value according to Eq. 4.12.

Here, the symbol S_{30}^{cut} is introduced because for every value of the constant intensity cut one can define a value of the signal at the reference angle. As a consistency check, the input spectra from Fig. 4.20 are shown again in Fig. 4.24 after applying the CIC correction. The intensity spectra is shown in four $\sin^2\theta$ bins, for the attenuation-corrected reference signal $S_{30}(E)$, i. e. the number of events with S_{30} greater than the corresponding S_{30}^{cut} on the x-axis.

As one can see, comparing with Fig. 4.20, the intensity corresponding to the chosen Constant Intensity Cut[13] is now attained at the same reference signal $S_{30}(E)$, in each zenith-angle bin. In other words, the corrected S_{30} spectra match nicely at least in the S_{30} range above trigger effects and with reasonable statistics meaning that except for the region below the trigger-threshold, the θ and energy dependencies of the reference signal have been completely disentangled. The systematic uncertainty of the energy estimate S_{30} due to the CIC method varies between 0% and 6% depending on zenith angle.

On the one hand, the choice of the CIC seems something arbitrary, on the other hand, it is evident from the intensity spectra shown in Fig. 4.24 and from the definition in Eq. 4.11, that the detector is not efficient at the very low energies mainly because of the atmospheric attenuation. Therefore, the CIC method cannot be applied at high intensities for the reason above, and at low intensities due to the scarce event statistics. To check the choice of the $n_{\text{cut}} = 500$ events for the CIC, we have scanned the range of intensities corresponding to $n_{\text{cut}} = [10, 10000]$ events (in steps of 100). Fig. 4.25 shows the estimated parameters extracted from Eq. 4.13 for every n_{cut}, indicated as a_{CIC}, b_{CIC}, c_{CIC}, against the corresponding S_{30}^{cut} fitted value. The fitted coefficients are seen to depend on n_{cut}, hence on the energy threshold above which the hypothesis of isotropic flux is enforced. The intensity dependence and the fit uncertainty are stronger for larger values of n_{cut}, specially above $n_{\text{cut}} = 6000$ as it can be noticed from Fig. 4.26 and $S_{30}^{\text{cut}} < 20$ VEM as displayed in Fig. 4.25. The choice of an intensity cut at 500 events seems then reasonable.

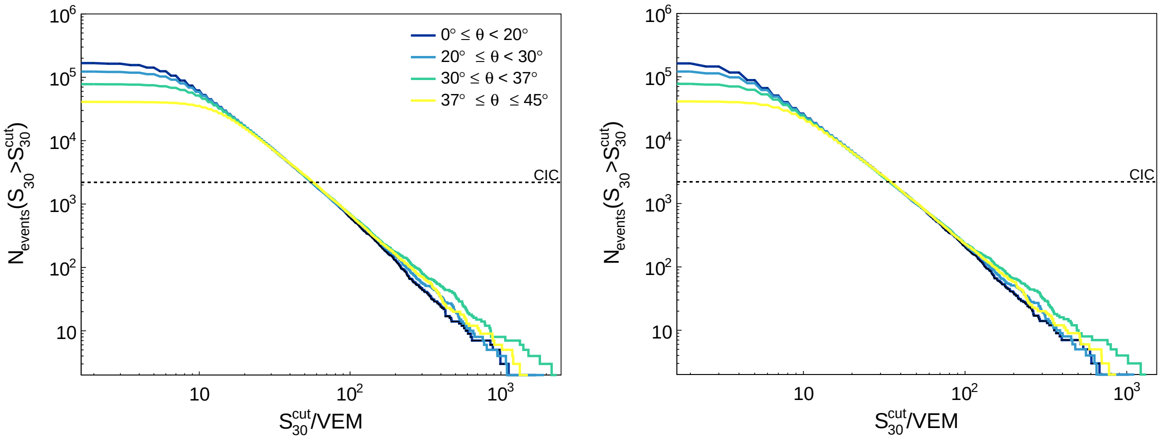

(a) (b)

Figure 4.24: Intensity of events with $S_{30} > S_{30}^{\text{cut}}$ in four angular bins of equal width in $\sin^2\theta$ for both sets of data: in Fig. 4.24(a) is presented the intensity of events of the data set reconstructed with $r_{\text{opt}} = 250$ m and the old LDF parameters, while in Fig. 4.24(b) the one reconstructed with $r_{\text{opt}} = 300$ m and the new LDF parameters.. For every S_{30}^{cut} on the x-axis, the number of events divided by the bin width is reported on the y-axis. The solid-horizontal line indicates the constant intensity at 500 events, which is achieved at small S_{30}^{cut} values as the zenith angle increases. Because of the atmospheric attenuation, at the ground level, inclined showers will contain less particles than vertical ones.

---

[13] $n_{\text{cut}} = 500$ events considering 18 equally spaced $\sin^2\theta$ bins.

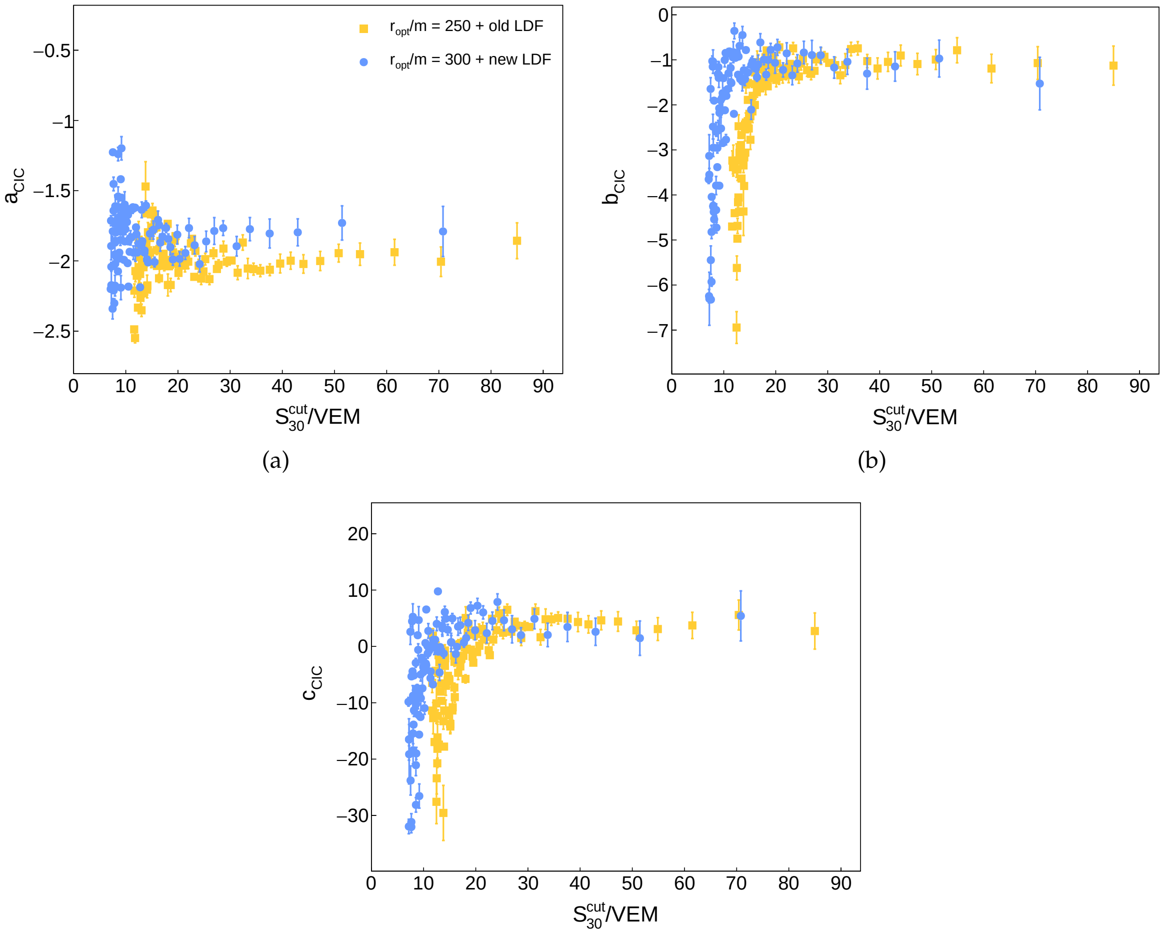

(a)

(b)

(c)

Figure 4.25: Variation of the fitted parameters a, b , and c for the correction function in Eq. 4.13, as one varies the number of events at which the CIC is performed for the two considered set of data: in yellow the *Dataset-1* and in blue the *Dataset-2* are depicted.

4.7 Low-energy extension of the energy spectrum

In this section we present the calculation of the energy spectrum for the CR events observed with the SD-433 at the Pierre Auger Observatory from January 2013 to September 2018. We performed the analysis chain consisting in the optimization of the optimal distance, LDF parametrisation and Constant Intensity Cut. The final step towards the energy spectrum would have been the assignment of an energy to SD events in the cross calibration with another detector. For this purpose, a calibration with an independent measurement needs to be carried out, if one does not want to rely solely on simulations. The FD provides a reliable measurement of the calorimetric energy of an air shower, but, thought the preferred calibration method would have been to use the calorimetric energy measurement by FD, two major problems that prevented this possibility appeared. On the one hand, we found very few events in coincidence between the SD-433 and the HEAT/Coihueco eyes, partially due to the limited duty cycle of FD and the energy range covered by the SD-433 and the FD detectors. On the other hand, those coincident events were extremely unlikely to pass the strict quality cuts for a reliable energy measurement. Cherenkov–dominated events detected by the FD and reconstructed with the Profile Constrained Geometry Fit (PCGF) [186] method were taken into account for the calibration of the SD energy estimates to the

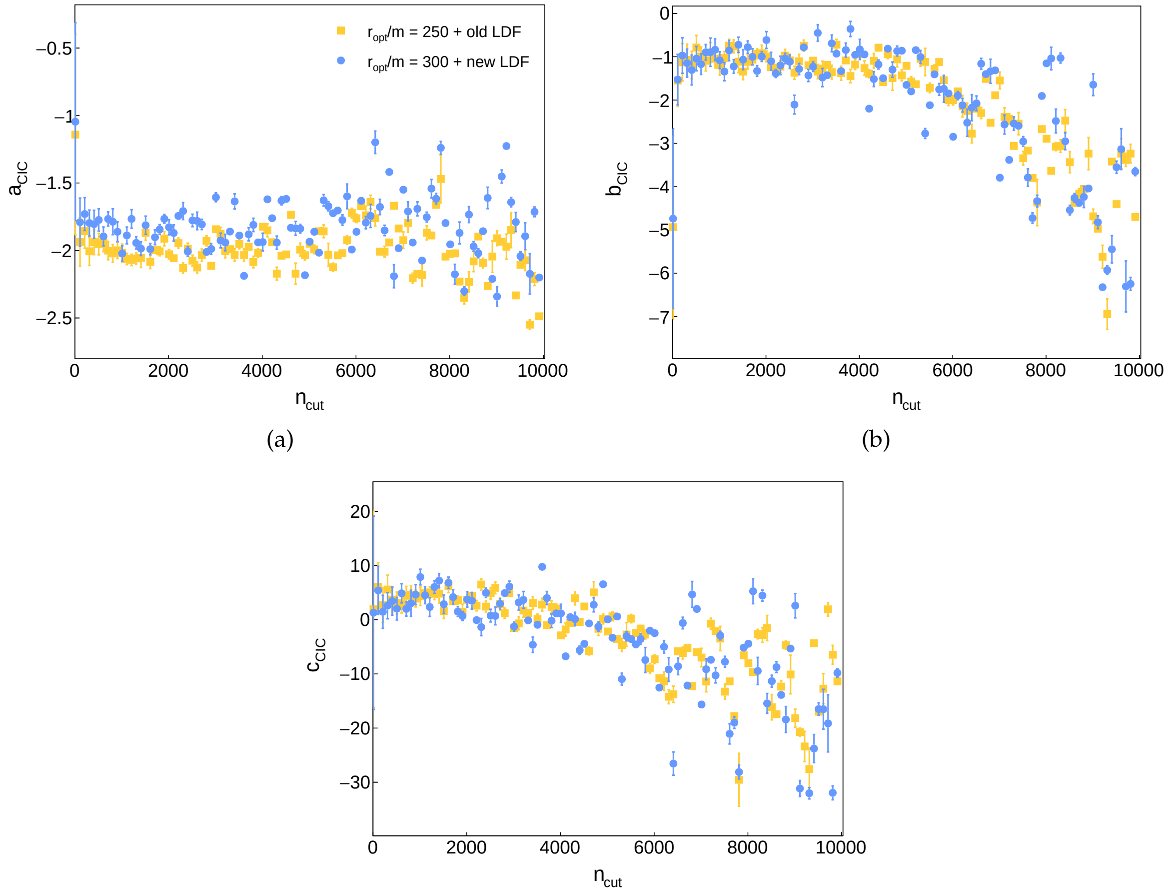

(a) (b)

(c)

Figure 4.26: The coefficients a, b , and c of the attenuation function Eq. 4.13 against the intensity cut value for the two considered set of data: in yellow the *Dataset-1* and in blue the *Dataset-2* are depicted.

energy of Cherenkov-dominated data. As it can be seen from Fig. 4.27, measurements of the Cherenkov light span more than one order of magnitude lower that FD events making this set of events the best suitable candidate to be used to calibrate the SD-433. Though, given the the scarce statistics of events that was observed from both detectors, we chose not to consider this set of data for further studies. Therefore, a set of events simultaneously observed by the SD-433 and the SD-433 arrays, is going to be used to perform the energy calibration. Tab. 4.4, shows the number of events synchronously detected by the SD-433 and the other facilities using the same detection technique as for the case of the SD-433 or a different one in the case of FD and Cherenkov events. The calibration analysis is still ongoing. For this reason, in this section we present the SD-433 energy spectrum using the new set of recovered data reconstructed with the old analysis set up [147].

The deployment of new radios in September 2018 in the infill area generated a cascade of unexpected problems in the SD data transmission because the new radios were not communicating. These problems were creating errors at the acquisition level, the so-called ”T3 errors”, that occur when the central data stations tries to form a T3 trigger but some station information get lost during the process of querying. In many cases this can result in a loss of events. The problems, of both hardware and software origins, were solved the one after the other to reach a mostly stable situation early in July 2019, however, until the end of 2019, there were still small periods with event loss.

The effect of T3 errors is clearly reflected into a deficit in the event rate between 2018 and 2019. It is thus impossible to use such data to build the spectrum since the exposure is clearly not under control during these periods. As a future step, a method to try to reconcile the exposure with the number of events and check if we can avoid throwing away the data for the full period shall be considered as it has been proposed for the SD-433 [187]. For this reason, for the spectrum analysis reported in this section the time range between September 2018 until the end of 2019 has not been further considered in order to avoid unknown exposure uncertainties.

	FD	Cherenkov	SD-433
time period	2013-2019	2013-2015	2013-2019 ICRC
SD-433	836	60	33822 (6T5)

Table 4.4: Number of events synchronously detected by the SD-433 and the FD, SD-433, and from measurements of the Cherenkov light with FD.

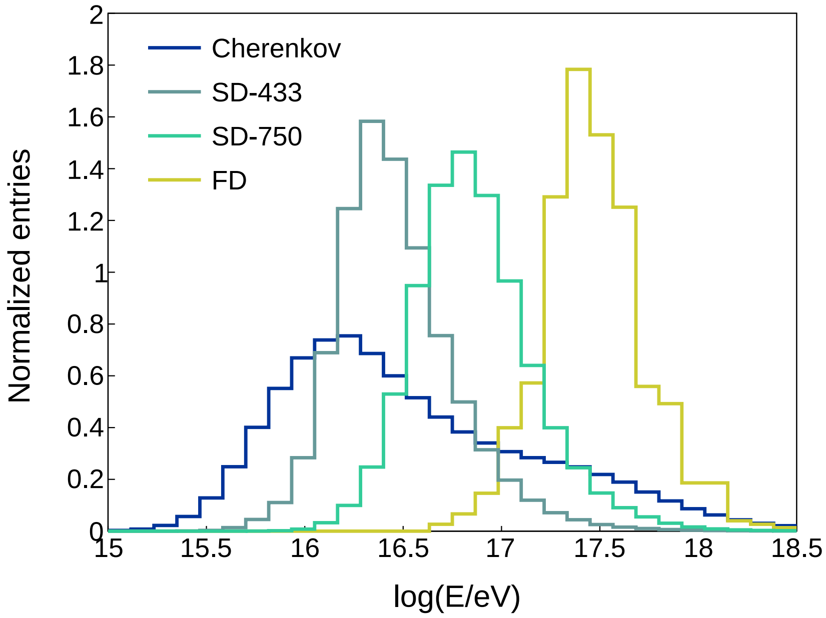

Figure 4.27: Energy distribution for the selected candidate to calibrate the SD-433 energy estimator.

For the event distribution depicted in Fig. 4.28, we selected 150065 events that survived the following quality cuts:

- zenith angle cut: $\theta \leq 45^\circ$
- 6T5 events
- “comms crisis” period rejected
- time period 2013-2018

All quality events are included in this plot. Due to the inherent power law, the event counts drop dramatically with increasing energy. There is a massive drop in the event statistics at

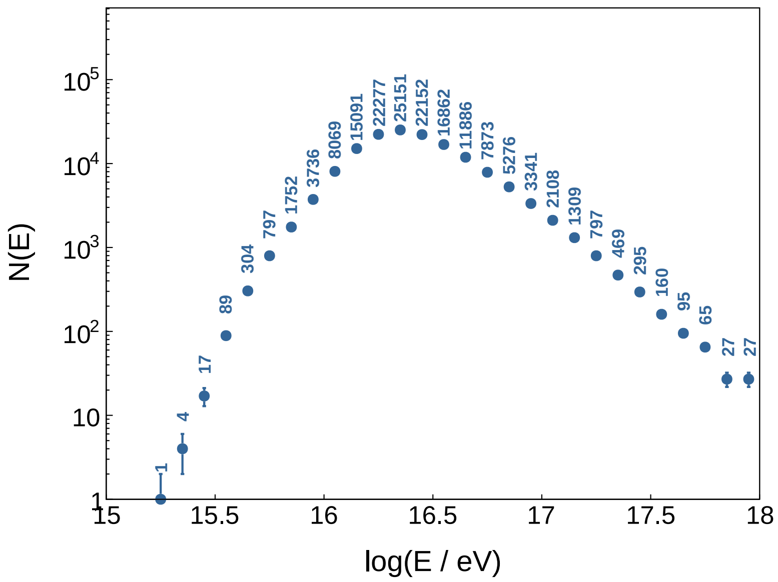

Figure 4.28: The event distribution of the SD-433 after the required quality cuts.

lower energies (log(E/eV)< 16.5), due to the vanishing trigger efficiency. For this reason for the energy spectrum analysis we will consider only events with $log(E\mathrm{eV}) > 16.5$.

The flux of cosmic rays J as a function of energy is given as in Eq. 4.8, or operationally defined as:

$$J(E) =: \frac{dN^2}{dEd\Sigma} \simeq \frac{\Delta N}{\Delta E}\frac{1}{E}\,. \tag{4.16}$$

where N is the number of events with energy between E and $E + dE$, and $d\Sigma = dA_{\mathrm{eff}} d_{\omega} dt$ is the differential exposure, in which the effective observation time and area are combined. In practice, the flux can be approximated by counting the number of events $\Delta N(E)$ in the energy bin ΔE, and dividing by the exposure Σ, which is constant only above the energy threshold. To divide by the exposure is an essential step in order to be able to directly compare the measured flux with the one obtained by other experiments.

4.7.1 Exposure Calculation

A necessary ingredient to determine the flux of UHECRs is a precise knowledge of the experimental exposure. The exposure Σ, is defined as the time integrated aperture, which is given by the effective detector area integrated over the subtended solid angle. In other words, it summarizes the observational detector capabilities combining the acceptance of the detector dA_{eff}, the solid angle $d\Omega$, and the effective time dt. The acceptance is the effective collection area for the detection of the flux of cosmic rays, which is obtained taking into account the zenith angle, by projecting the hexagonal cell area onto the shower plane $dA_{\mathrm{eff}} = A_{\mathrm{cell}} \cos\theta d\Omega$, the solid angle $d\Omega$. The hexagonal cell element A_{cell} is elementary unit of the array made up of seven active stations as depicted in Fig. 4.29, one in the middle and six neighbours. The unitary cell area is given by:

$$A_{\mathrm{cell}} = \frac{\sqrt{3}}{2} d^2 \simeq 0.162\,\mathrm{km}^2\,, \tag{4.17}$$

where $d = 0.433\mathrm{km}^2$ is the array spacing for the SD-433. In order to calculate the effective

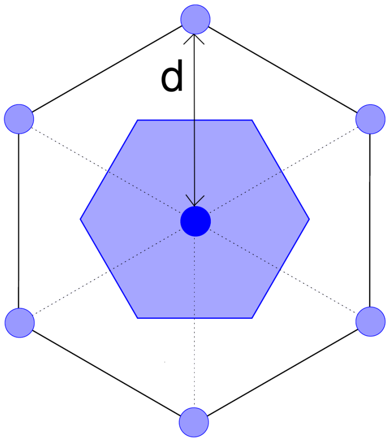

Figure 4.29: Schematic view of an hexagonal cell of WCDs separated by a mutual distance d. The shaded area around the central station defines the acceptance of the hexagon.

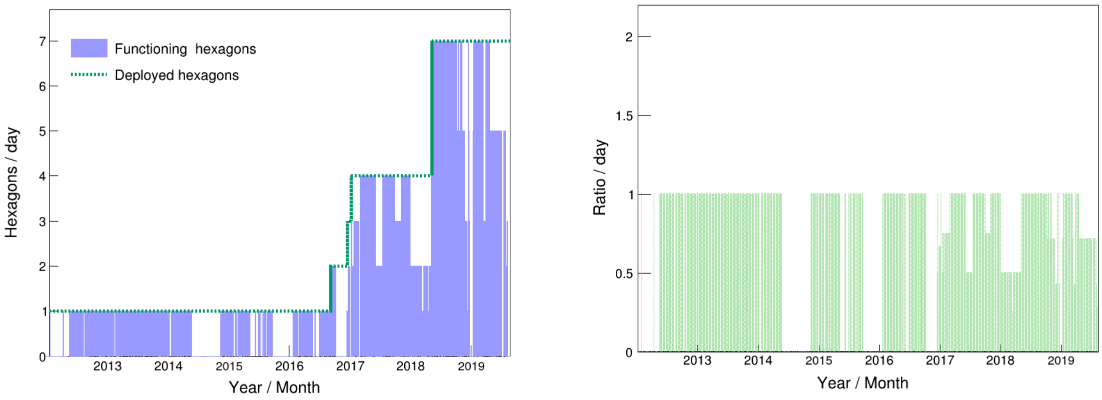

(a) (b)

Figure 4.30: T2 files are used to estimate the time intervals during which the hexagons were active. In Fig. 4.30(a) the number of hexagons is shown in a daily basis compared to the number of deployed hexagons cells. In fig. 4.30(b) the fraction derived from Fig. 4.30(a) is represented.

sensitive area A_{6T5} of a 6T5 cell, the subtended solid angle has to be taken into account since the relevant area is obtained by the projection of A_{cell} on the shower plane:

$$dA_{6T5} = A_{\text{eff}} d\Omega = A_{\text{cell}} \cos\theta d\Omega \,, \tag{4.18}$$

with the solid angle $d\Omega = \sin\theta d\theta d\phi = -d\cos\theta d\phi$, it follows

$$\begin{aligned} A_{6T5} &= A_{\text{cell}} \int_0^{2\pi} d\phi \int_{\cos_{\theta_{\min}}}^{\cos_{\theta_{\max}}} \cos\theta(-d\cos\theta) \\ &= A_{\text{cell}} \cdot \pi \cdot (\cos^2\theta_{\min} - \cos^2\theta_{\max}) \\ &= A_{\text{cell}} \cdot \pi \cdot (1 - \cos^2\theta_{\max}) \\ &= 0.25\,\text{km}^2 \cdot \text{sr} \,, \end{aligned} \tag{4.19}$$

where we used as zenith range $\theta_{\min} = 0^\circ$ and $\theta_{\max} = 45^\circ$. Therefore, one has $A_{\text{eff}}(45^\circ) \sim 0.25$ Km^2·sr. The total exposure $d\Sigma = dtdAd\Omega$ is then obtained by integrating over the active time and summing up the contributing 6T5 cells:

$$\Sigma = \int_{t_0}^{t_1} dt \sum_i A_{6T5,i} = \int_{t_0}^{t_1} dt A(t)\,, \tag{4.20}$$

where $A(t) = N(t)A_{6T5}$, with $N(t)$ the number of active hexagons in the time range $[t - dt][t + dt]$. The T2 files allows to calculate the number of active elementary hexagons at a certain second since the activity of each station is recorded at each second. Thus, the calculation of the exposure is reduced to the sum of the time intervals (in seconds) during which all seven stations of the hexagon were functioning:

$$\Sigma = \sum_i A(t_i)t_i\,. \tag{4.21}$$

For the purpose of this work, a software was developed that calculates the exposure based on the T2life-SD433 files. From the same program, we calculated the number of functioning hexagons per day as reported in Fig. 4.30(a) and the fraction of the active cells at the time of each event in term of the deployed hexagons as shown in Fig. 4.30(b). The SD-433 exposure calculation for the time range 01.01.2013 - 09.01.2018 and a zenith angle interval $0^\circ \leq \theta \leq 45^\circ$, results in $\Sigma = 1.35$ km$^2 \cdot$ yrs ·sr. In Fig. 4.31, the evolution of the exposure as a function of time for the SD-433, based on the T2life-SD433 monitoring files is shown.

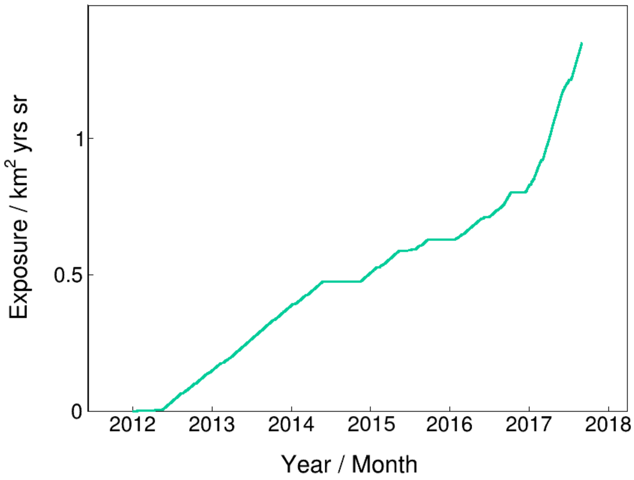

Figure 4.31: The SD-433 exposure as a function of time for the zenith angle range $0^\circ \leq \theta \leq 45^\circ$.

4.7.2 Preliminary SD-433 energy spectrum

The preliminary histogram of events reconstructed using the SD-433 array is shown in Fig. 4.32. This is a very preliminary result, although a softening is visible around 10^{17} eV where a change in the spectral index from $\gamma_1 = 3.01 \pm 0.03$ to $\gamma_2 = 3.24 \pm 0.05$ has been derived from a broken power law fit. It is worth mentioning that the observed break is compatible with the observation of the second knee already seen at the Pierre Auger Observatory with Cherenkov events at $10^{17.22}$ eV[186]. The preliminary Auger energy spectrum derived from SD-433 data is compared with other measurements from other facilities of the Pierre Auger Observatory as shown in Fig. 4.33 and with measurements of other experiments in Fig. 4.34 scaling all of them with E^3 to improve the visualization of the features.

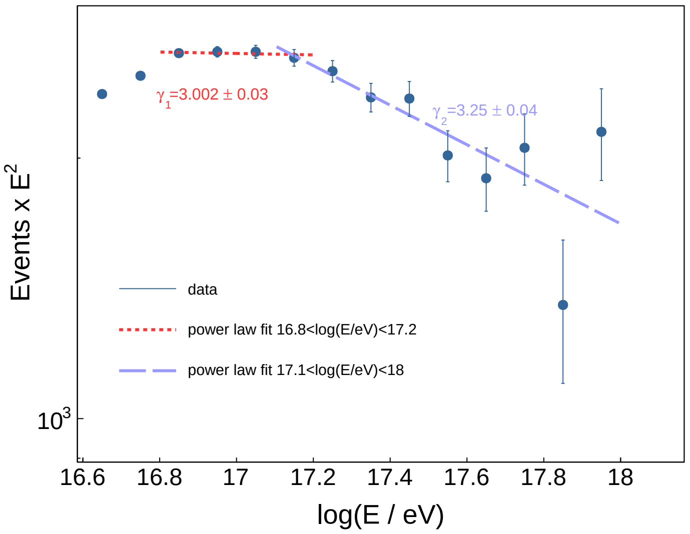

Figure 4.32: Histogram of SD-433 reconstructed events in the time range between January 2013 and August 2018, which have been scaled with E^2 and fitted with two power laws.

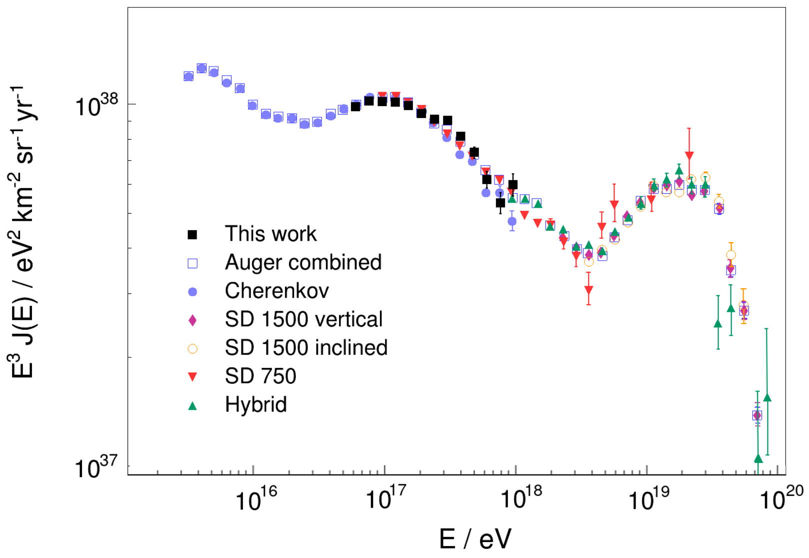

Figure 4.33: Energy spectrum combined from measurements performed at the Pierre Auger Observatory. Energy spectrum from SD-433 data is depicted by Cyan squares markers. The combined spectrum is shown by blue squares. Error bars correspond to statistical uncertainties.

Although more detailed studies and a new energy calibration using the reconstruction parameters found in this thesis work are desirable, this approach has given us the opportunity of exploiting the data below the energy threshold of the other two surface detector arrays at the Observatory. As a matter of fact, although this shall be considered as a raw energy spectrum, we found a very good agreement with the energy spectra measured by other experiments.

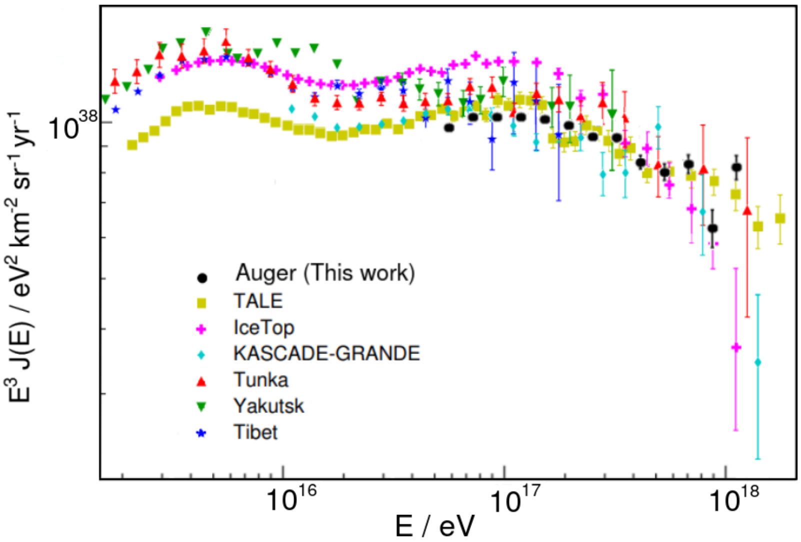

Figure 4.34: Energy spectrum of different experiments compared with the one obtained from SD-433 reconstructed data at the Pierre Auger Observatory (black). The all–particle spectra of Tibet [188], Yakutsk [189], Tunka [190], KASCADE[14]–Grande [191], IceTop [192], and TALE [193] are shown.

CHAPTER 5

Conclusion

This thesis was focused on the low-energy extension of the SD, a nested array of WCD stations with 433 m spacing, 1/4 that of the larger array, that offers the opportunity to observe cosmic rays in the energy region of $10^{16} - 10^{18}$ eV. The work presented above included three main components. The first one was the production of a high-quality data set through a recovering process for "silent detectors", which made possible all this thesis work. Without this vital step towards the creation of a suitable data set, we would have not been able to perform any of the analysis described before.

The second one is the deployment and operation of this denser facility, that was completed in 2019. The analysis required the tuning of the event-reconstruction process, which ultimately provides the primary-CR energy (among other observables). Most of the effort was put into employing the seven-year data-set to optimize the steps of the event reconstruction process. The standard approach is based on the empirical description of the overall lateral distribution of secondary particles on the ground. For each event, the distribution is fit by means of the Lateral Distribution Function (LDF). As the LDF slope and the (optimal) normalization factor depend on the mutual distance between the detectors, we have deduced the suitable coefficients for the slope parameterization, as well as the convenient distance and zenith angle needed to define a reference signal acting as an energy estimator. The size of this LDF function at an optimal distance of 300 m to the shower core is a very robust estimate of the primary energy. By means of Monte-Carlo simulations, we reported a full-efficiency threshold of $10^{16.5}$ eV for proton and $10^{16.6}$ eV for iron primaries up to $\theta = 45^\circ$, offering the possibility to fully observe the second-knee feature in the CR spectrum, reported around 10^{17} eV, with full reconstruction efficiency. The correction of the zenith angle dependencies of the primary energy estimator with a CIC method was studied and an energy estimate threshold for zenith angles up to 45° was derived. The fine-tuning of the SD-433 event reconstruction is still ongoing. The transformation from the zenith-independent shower size to the estimated primary energy requires a study of the weather-induced modulations and geomagnetic effects on the measured signals prior to the calibration of the shower size with an independent measurement of the primary energy.

The third component is the measurement of the cosmic ray spectrum. With the improved reconstruction and detector capabilities, this measurement extended into a lower energy range than what was previously possible with the surface detector at the Observatory. The spectrum derived from SD-433 data exhibits an interesting changes in the spectral slope at energies below the ankle. The all-particle energy spectrum in the low–energy region exhibits a softening from to $\gamma_1 \approx 3.01$ to $\gamma_2 \approx 3.24$ around 10^{17} eV. Additionally, the spectral feature ultimately agreed with that of previous Auger measurements from the SD-750 and from data produced using Cherenkov light measured with FD. The effects of systematic uncertainties on the energy spectrum measurement from SD-433 events has to be considered for further works as the systematic uncertainty in the energy scale may produce systematic uncertainty in the flux. While, the spectrum presented in this work is preliminary, it is the first observation of the second knee using SD-433 measurements.

The SD-433 array provides the opportunity to extend the sensitivity of the Auger surface detector to lower energies and with this analysis we set the foundations for extending the SD-oriented research lines in Auger to energies down to 10^{16} eV, opening a low-energy window on UHECR research at the Pierre Auger Observatory.

Acronyms

This is a list of acronyms used within this work sorted alphabetically according to the short version.

ADST	Advanced Data Summary Tree	102
AERA	Auger Engineering Radio Array	3
AGNs	active galactic nuclei	6
AMIGA	Auger Muon Detectors for the Infill Ground Array	43
BHs	Black holes	7
CDAS	central data acquisition system	99
CIC	Constant Intensity Cut	99
CMB	cosmic microwave background radiation	13
CSDA	continuous-slowing-down approximation	53
CORSIKA	Cosmic Ray Simulations for Kascade	81
CR	cosmic ray	2
EAS	extensive air shower	81
FD	Fluorescence detector	41
GRB	gamma-ray burst	14
GPS	Global Positioning System	99
GZK	Greisen–Zatsepin–Kuzmin	3
HEAT	High Elevation Auger Telescopes	136
KASCADE	Karlsruhe Shower Core and Array Detector	22
LDF	lateral distribution function	99
LHC	Large Hadron Collider	
LS	Local Station	99
MD	Muon detector	74
MoPS	Multiplicity of positive steps	88
NKG	Nishimura-Kamata-Greisen	112
PAO	Pierre Auger Observatory	41
PMT	photo-multiplier tube	44
SD-1500	1500 m SD vertical	101
SD-433	433 m SD infill	99
SD-750	750 m SD vertical	101
SD	Surface detector	41
SDP	Shower detector plane	48
SPMT	Small PMT	79
SSD	Scintillator Surface Detector	78
TA	Telescope Array	
SNR	supernova remnant	6
SGR	Soft Gamma-ray Repeaters	14
TA	Telescope Array	
ToT	time-over-threshold trigger	56
ToTd	time-over-threshold deconvoluted trigger	88
UHECR	ultra-high energy cosmic ray	xiii
UMD	Underground Muon Detector	79
VCT	vertical centered through-going	54
VEM	vertical-equivalent muon	55
WCD	water-Cherenkov detector	136

List of Figures

---

[1] water-Cherenkov detector

[2] High Elevation Auger Telescopes

List of Tables

APPENDIX A

Offline modules

A.1 Silent station restoring module

```
#include "T2Restorer.h"
#include <fwk/CentralConfig.h>
#include <det/VManager.h>
#include <utl/Branch.h>
#include <sevt/Header.h>
#include <evt/Event.h>
#include <sevt/SEvent.h>
#include <sevt/Station.h>
#include <sdet/SDetector.h>
#include <utl/ErrorLogger.h>

using namespace std;
using namespace fwk;
using namespace det;
using namespace utl;
using namespace evt;
using namespace sevt;


namespace T2Restorer {

  VModule::ResultFlag
  T2Restorer::Init()
  {

    Branch topBranch = CentralConfig::GetInstance()->GetTopBranch("T2Restorer");
    topBranch.GetChild("InputT2Filename").GetData(fInputT2Filename);

    return eSuccess;
  }


  VModule::ResultFlag
  T2Restorer::Run(Event& event)
  {
    INFO("Restoring T2 Life using monitoring file t2raw");
    /*Keep T2Life file open*/
    if (!fT2File.is_open()) {
      fT2File.open(fInputT2Filename.c_str());
```

```
    if (!fT2File.is_open()) {
      cout << "Error opening " << fInputT2Filename.c_str()<< " file..." << endl;
      return eFailure;
    }
  }
  /*else*/ cout << "File " << fInputT2Filename.c_str()<< "  opened." << endl;

  if (!event.HasSEvent())
    return eSuccess;

  sevt::SEvent& sEvent = event.GetSEvent();

  TimeStamp eventTime = sEvent.GetHeader().GetTime();
  unsigned long eventGPS = eventTime.GetGPSSecond();
  int column1, column2;
  int column3;
  std::string line, endS;
  size_t counter = 0;

  /*Keep file position after every loop of the while*/
  streampos curPos = fT2File.tellg();
  while (counter < 18 && std::getline(fT2File, line)) {
      std::istringstream iss(line); // put the line into a string stream
      iss >> column1;
      if(column1 == eventGPS){
        iss >> column2 >> column3 >> endS;
        int stationId =  column2;
        bool t2Flag =  column3;
        ++counter;
        if (t2Flag) { //checks if the station has T2!=0
          if (sEvent.HasStation(stationId)) {cout << "station" << stationId << " alredy
 ↪ exists" << endl;}
          else {
            sEvent.MakeStation(stationId); //the station is add to the event
            cout <<"making station id " << stationId << endl;
            Station& oStation = sEvent.GetStation(stationId);
            oStation.SetSilentT2();//the stations is create under the name SilentT2 to
 ↪ rpevent the SdCalibrator rejection
            oStation.SetT2Life(1);//restore T2Life flag in the Offline
          }

        }

      }
      else if (column1 > eventGPS) break;
      /*AS: Update file position if eventGPS is less than current read GPS*/
      else curPos = fT2File.tellg();
  }  //end while
  if (counter == 0) {
    ERROR ("----------------> No GPS match found <-----------------");
  }
  /* Go back one line in the file (no match found) or to the beginning of the event (match
 ↪  found)*/
  fT2File.seekg(curPos);

  return eSuccess;
} //end run


VModule::ResultFlag
T2Restorer::Finish()
{
```

```

    return eSuccess;
  }

}
```

A.2 Data reconstruction module sequence

```xml
<sequenceFile
  xmlns:xsi="http://www.w3.org/2001/XMLSchema-instance"
  xsi:noNamespaceSchemaLocation='/cr/data01/silli/offline_trunk_2020/install/share/auger-
    ↪ offline/config/ModuleSequence.xsd'>

  <enableTiming/>

  <moduleControl>

  <loop numTimes="unbounded" pushEventToStack="yes">

    <module> EventFileReaderOG     </module>
    <module> Select433Events             </module><!--Requires at lest 3 SD-433 stations
    ↪ withing the unitary hexagon -->
    <module> EventCheckerOG              </module>
    <module> T2Restorer                  </module><!-- Restores the missing silent stations
    ↪ -->
    <module> SdPMTQualityCheckerKG       </module>
    <module> TriggerTimeCorrection       </module>
    <module> SdCalibratorOG              </module>
    <module> SdStationPositionCorrection </module>
    <module> SdBadStationRejectorKG      </module>

    <module> FdCalibratorOG              </module>

  <!-- FD reconstruction -->
  <try>
    <module> FdEyeMergerKG               </module>
    <module> FdPulseFinderOG             </module>
    <module> FdSDPFinderOG               </module>
    <module> FdAxisFinderOG              </module>
    <module> HybridGeometryFinderOG      </module>
    <module> HybridGeometryFinderWG      </module>
    <module> FdApertureLightKG           </module>
    <module> FdEnergyDepositFinderKG     </module>
  </try>

  <!-- SD reconstruction -->
    <module> SdSignalRecoveryKLT         </module>
    <module> SdEventSelectorOG           </module>
    <module> SdPlaneFitOG                </module>
    <module> LDFFinderKG                 </module>
    <module> EnergyCalculationPG         </module>

  <!-- used to perform geomagnetic corrections-->
    <module> Risetime1000LLL             </module>
    <module> DLECorrectionGG             </module>
    <module> SdEventPosteriorSelectorOG  </module>
    <module> SdRecPlotterOG              </module>

  <!-- export the ADST -->
```

```
    <module> RecDataWriterNG              </module>


  </loop>

 </moduleControl>

</sequenceFile>
```

APPENDIX B

Acknowledgments

First and foremost I am extremely grateful to my directors, Prof. Alberto Etchegoyen and Prof. Johannes Blümer and for giving me the opportunity to take part in the Double Doctorate Degree in Astrophysics. Such a program has enriched me with many professional but also personal experiences. I would like to thank my supervisors Dr. Diego Melo, Dr. Diego Ravignani, and Dr. Markus Roth for their invaluable advice, continuous support, and patience during my PhD study. They kept me on the right track while also ensuring the project was enjoyable and productive.

Getting through my dissertation required more than academic support, and I have many, many people to thank for listening to and, at times, having to tolerate me over the past five years. I cannot begin to express my gratitude and appreciation for their friendship to all of those with whom I have had the pleasure to work during these five years, in Germany and in Argentina. I could not have completed this dissertation without the support of my collegues, who provided stimulating discussions as well as happy distractions to rest my mind outside of my research.

Nobody has been more important to me in the pursuit of this project than the members of my family. I would like to thank my parents and my partner, whose love and guidance are with me in whatever I pursue. They are the ultimate role models.

Bibliography

[1] V. Hess, Über die Beobachtungen der durchdringenden Strahlung bei sieben Freiballonflgen, Phys. Z. 8 (1912) 1084.

[2] N. Giglietto, A. D. Angelis, S. Stramaglia, Domenico Pacini, the forgotten pioneer of the discovery of cosmic rays (2010)`arXiv:1002.2888`.

[3] C. D. Anderson, The Positive Electron, Phys. Rev 43 (1933) 491–494.

[4] J. C. Street, E. C. Stevenson, New Evidence for the Existence of a Particle of Mass Intermediate Between the Proton and Electron, Phys. Rev. 52 (1937) 1003–1004. `doi:10.1103/PhysRev.52.1003`.

[5] G. P. S. Occhialini, C. F. Powell, Nuclear disintegration produced by slow charged particles of small mass, Nature 159 (1987) 186–190. `doi:10.1038/159186a0`.

[6] J. Bluemer, R. Engel, J. R. Hoerandel, Cosmic rays from the knee to the highest energies, Prog.Part.Nucl.Phys 63 (293) (2009). `arXiv:0904.0725`, `doi:10.1016/j.ppnp.2009.05.002`.

[7] P. Auger, P. Ehrenfest, R. Maze, J. Daudin, R. v. Fréon, Extensive cosmic-ray showers, Rev. Mod. Phys. 11 (1939) 288–291. `doi:10.1103/RevModPhys.11.288`.

[8] E. Fermi, On the origin of the cosmic radiation, Phys. Rev. 75 (1949) 1169–1174. `doi:10.1103/PhysRev.75.1169`.

[9] E. Fermi, Galactic magnetic fields and the origin of cosmic radiation, Astrophys. J. 119 (1-6) (1954). `doi:10.1086/145789`.

[10] G. W. Clark, J. Earl, W. L. Kraushaar, J. Linsley, B. B. Rossi, F. Scherb, D. W. Scott, Cosmic-ray air showers at sea level, Phys. Rev. 122 (1961) 637–654. `doi:10.1103/PhysRev.122.637`.

[11] J. Linsley, Evidence for a primary cosmic-ray particle with energy 10^{20} ev, Phys. Rev. Lett. 10 (1963) 146–148. `doi:10.1103/PhysRevLett.10.146`.

[12] K. Greisen, End to the cosmic-ray spectrum?, Phys. Rev. Lett. 16 (1966) 748–750. `doi:10.1103/PhysRevLett.16.748`.

[13] G. T. Zatsepin, V. A. Kuzmin, Upper limit of the spectrum of cosmic rays, JETP Lett. 4 (1966) 78–80.

[14] W. Galbraith, J. V. Jelley, Light Pulses from the Night Sky associated with Cosmic Rays, Nature 171 (4347) (1953) 349–350. `doi:10.1038/171349a0`.

[15] N. J. V. Jelley, J. H. Fruin, Radio Pulses from Extensive Cosmic-Ray Air Showers, Nature 205 .

[16] D. M. Edge, A. C. Evans, H. J. Garmston, R. J. O. Reid, A. A. Watson, J. G. Wilson, A. M. Wray, The cosmic ray spectrum at energies above 10^{17} ev, Journal of Physics A: Mathematical, Nuclear and General 6 (10) (1973) 1612–1634. `doi:10.1088/0305-4470/6/10/019`.

[17] N. Chiba, K. Hashimoto, N. Hayashida, K. Honda, M. Honda *et al.*, Akeno giant air shower array (agasa) covering 100 km^2 area, Nucl. Instrum. Meth. A 311 (1) (1992) 338–349. `doi:https://doi.org/10.1016/0168-9002(92)90882-5`.

[18] The Fly's Eye (1981-1993) (1981).
URL `http://www.cosmic-ray.org/reading/flyseye.html`

[19] J. N. Matthews, C. C. H. Jui (Fly's Eye Collab.), First results from the high resolution Fly's Eye experiment, Nucl. Phys. B Proc. Suppl. 87 (2000) 411–413. `doi:10.1016/S0920-5632(00)00706-4`.

[20] A. Horneffer *et al.* (LOPES Collab.), LOPES: Detecting radio emission from cosmic ray air showers, 2004. `arXiv:astro-ph/0409641`.

[21] D. t. Ardouin, Radiodetection of cosmic ray extensive air showers: Present status of the codalema experiment, Int. J. Mod. Phys. A20 (29) (2005) 6869–6871. `doi:10.1142/S0217751X0503034X`.

[22] D. J. Bird *et al.*, Detection of a cosmic ray with measured energy well beyond the expected spectral cutoff due to cosmic microwave radiation, Astrophys. J. (441(1)) (1995) 144–15. `arXiv:astro-ph/9410067`, `doi:10.1086/175344`.

[23] J. Abraham *et al.* (Pierre Auger Collab.), Upper limit on the cosmic-ray photon fraction at EeV energies from the Pierre Auger Observatory, Astropart. Phys. 31 (2009) 399 – 406.
URL `https://doi.org/10.1016/j.astropartphys.2009.04.003`

[24] A. Aab *et al.* (Pierre Aguer Collab.), Observation of a large-scale anisotropy in the arrival directions of cosmic rays above 8×10^{18} ev, Science 357 (6357) (2017) 1266 – 1270. `arXiv:1709.07321`, `doi:10.1126/science.aan4338`.

[25] K. Ptitsyna, V. Kseniya, S. Troitsky, Physical conditions in potential accelerators of ultra-high-energy cosmic rays: updated hillas plot and radiation-loss constraints, Phys.Usp. 53 (7) (2010) 691–701. `arXiv:0808.0367`, `doi:10.3367/ufne.0180.201007c.0723`.

[26] M. Kachelriess, Lecture notes on high energy cosmic rays (2008). `arXiv:0801.4376`.

[27] A. M. Hillas, The origin of ultra-high-energy cosmic rays, Ann. Rev. Astron. Astrophys. 22 (1) (1984) 425–444. `doi:10.1146/annurev.aa.22.090184.002233`.

[28] W. F. G. Swann, A mechanism of acquirement of cosmic-ray energies by electrons, Phys. Rev. 43 (1933) 217–220. `doi:10.1103/PhysRev.43.217`.

[29] K. S. Cheng *et al.*, Energetic radiation from rapidly spinning pulsars. II. Vela and Crab., Astrophys. J. 300 (1986) 522–539. `doi:10.1086/163829`.

[30] P. Blasi, R. I. Epstein, A. V. Olinto, Ultra–high-energy cosmic rays from young neutron star winds, Astrophys.J. 533 (2) (2000) L123–L126. `arXiv:astro-ph/9912240`, `doi:10.1086/312626`.

[31] A. Venkatesan, M. Coleman Miller, A. Olinto, Constraints on the production of ultra–high-energy cosmic rays by isolated neutron stars, Astrophys.J 484 (1) (1997) 323–328. `arXiv:astro-ph/9612210`, `doi:10.1086/304304`.

[32] A. Neronov, D. Semikoz, I. Tkachev, Ultra-high energy cosmic ray production in the polar cap regions of black hole magnetospheres, New Journal of Physics 11 (6) (2009) 065015. `arXiv:0712.1737`, `doi:10.1088/1367-2630/11/6/065015`.

[33] P. Bhattacharjee, G. Sigl, Origin and propagation of extremely high-energy cosmic rays, Phys. Rept. 327 (3-4) (2000) 109 – 247. `arXiv:astro-ph/9811011`, `doi:10.1016/s0370-1573(99)00101-5`.
URL `http://dx.doi.org/10.1016/S0370-1573(99)00101-5`

[34] E. Fermi, On the origin of the cosmic radiation, Phys. Rev. 75 (1949) 1169–174. `doi:10.1103/PhysRev.75.1169`.

[35] M. S. Longair, High Energy Astrophysics, Vol. 2, 1994.

[36] L. Anchordoqui, T. Paul, S. Reucroft, J. Swain, Ultrahigh energy cosmic rays: The state of the art before the auger observatory, Int. J. Mod. Phys. A 18 (13) (2003) 2229 – 2366. `arXiv:hep-ph/0206072`, `doi:10.1142/s0217751x03013879`.

[37] W. Axford, The acceleration of cosmic rays by shock waves, Annals of the New York Academy of Sciences 375(1) (1981) 297 – 313. `doi:https://doi.org/10.1111/j.1749-6632.1981.tb33702.x`.

[38] D. Torres *et al.*, Supernova remnants and γ-ray sources, Phys. Rept. 382 (6) (2003) 303–380. `arXiv:astro-ph/0209565`, `doi:10.1016/s0370-1573(03)00201-1`.

[39] A. M. Hillas, ORIGIN OF ULTRAHIGH-ENERGY PARTICLES, in: 19th Rencontres de Moriond: Origin of High-Energy Cosmic Rays, 1984, pp. 11–26.

[40] S. I. Ginzburg, V. L. Syrovatskii, The Origin of Cosmic Rays. (1964)`doi:https://doi.org/10.1016/C2013-0-05547-8`.

[41] B. L. Fanaroff, J. M. Riley, The Morphology of Extragalactic Radio Sources of High and Low Luminosity., Monthly Notices of the Royal Astronomical Society. 167.1 (Apr. 1974) 31–36. `doi:10.1093/mnras/167.1.31P`.
URL `https://doi.org/10.1093/mnras/167.1.31P`

[42] A. Uryson, Identification of active galactic nuclei as possible sources of uhecr, Astronomical & Astrophysical Transactions 20 (2) (2001) 347–348. `doi:10.1080/10556790108229727`.

[43] C. Megan Urry, P. Padovani, Unified schemes for radio-loud active galactic nuclei, Publications of the Astronomical Society of the Pacific 107 (1995) 803. `doi:10.1086/133630`.

[44] R. Nemiroff, J. Bonnell, image Credit: X-ray: NASA/CXC/SAO; Optical: NASA/STScI; Radio: NSF/NRAO/AUI/VLA.

[45] A. Graham, Populating the galaxy velocity dispersion: Supermassive black hole mass diagram, a catalogue of ($m_{bh,}$, σ) values, Publications of the Astronomical Society of Australia 25 (4) (2008) 167 – 175. doi:10.1071/AS08013.

[46] G. Sigl, M. Lemoine, P. Biermann, Ultra-high energy cosmic ray propagation in the local supercluster, Astropart. Phys. 10 (2-3) (1999) 141–156. arXiv:astro-ph/9806283, doi:10.1016/s0927-6505(98)00048-6.

[47] P. Kronberg, Extragalactic magnetic fields., Rep. Prog. Phys. 57(4) (1994) 325 – 382. doi:10.1088/0034-4885/57/4/001.

[48] A. Ferrari, Acceleration of ultra-high-energy cosmic rays (UHECR) in clusters of galaxies, National Radio Astronomy Observatory Workshop 16 107 (1986) 207 – 212.
URL https://ui.adsabs.harvard.edu/abs/1986NRAOW..16..207F/

[49] G. Ghisellini *et al.*, Ultra-high energy cosmic rays, spiral galaxies and magnetars, Monthly Notices of the Royal Astronomical Society: Letters 390 (1) (2008) 88–92. doi:10.1111/j.1745-3933.2008.00547.x.

[50] B. Paczynski, Gamma-ray bursters at cosmological distances, The Astrophysical Journal 308 (1986) 43 – 46. doi:10.1086/184740.

[51] M. J. Rees, P. Mészáros, Relativistic fireballs: energy conversion and time - scales, Mon. Not. Roy. Astron. Soc 258 (1) (1992) 41–43. doi:10.1093/mnras/258.1.41P.

[52] K. Kotera, A. V. Olinto, The astrophysics of ultrahigh-energy cosmic rays, Annual Review of Astronomy and Astrophysics 49 (1) (2011) 119–153. doi:10.1146/annurev-astro-081710-102620.

[53] G. Lemaître, The Primeval Atom - an Essay on Cosmogony, Van Nostrand, 1950.

[54] M. Takeda *et al.* (Pierre Auger Collab.), Extension of the cosmic-ray energy spectrum beyond the predicted greisen-zatsepin-kuz'min cutoff, Phys.Rev.Lett. 81 (6) (1998) 1163–1166. arXiv:astro-ph/9807193, doi:10.1103/physrevlett.81.1163.

[55] C. Isola, M. Lemoine, G. Sigl, Centaurus a as the source of ultrahigh-energy cosmic rays?, Phys.Rev. D 65 (2) (2001). arXiv:astro-ph/0104289, doi:10.1103/physrevd.65.023004.

[56] G. Albuquerque, M. Farrar, E. Kolb, Exotic massive hadrons and ultrahigh energy cosmic rays, Phys. Rev. D 59 (1998) 015021. arXiv:hep-ph/9805288, doi:10.1103/PhysRevD.59.015021.

[57] P. Jain, D. McKay, S. Panda, J. Ralston, Extra dimensions and strong neutrino-nucleon interactions above 10^{19} ev: breaking the gzk barrier, Phys. Lett. B 484 (3-4) (2000) 267–274. arXiv:hep-ph/0001031, doi:10.1016/s0370-2693(00)00647-x.

[58] F. Stecker, S. Scully, Lorentz invariance violation and the spectrum and source power of ultrahigh energy cosmic rays, Astropart. Phys 23 (2) (2005) 203–209. arXiv:astro-ph/0412495, doi:10.1016/j.astropartphys.2005.01.001.

[59] Z. Fodor, S. D. Katz, A. Ringwald, Z burst scenario for the highest energy cosmic rays, in: Conference on Physics Beyond the Standard Model: Beyond the Desert 02, 2002. arXiv:hep-ph/0210123.

[60] V. Berezinsky, M. Kachelrieß, A. Vilenkin, Ultrahigh energy cosmic rays without greisen-zatsepin-kuzmin cutoff, Phys. Rev. Lett. 79 (1997) 4302–4305. `doi:10.1103/PhysRevLett.79.4302`.

[61] V. A. Kuzmin, V. A. Rubakov, Ultra-High Energy Cosmic Rays: a Window to PostInflationary Reheating Epoch of the Universe?, Phys. Atom. Nucl. 61 (1998) 1028–1030. `arXiv:astro-ph/9709187`.

[62] M. Kachelriess, The rise and fall of top-down models as main uhecr sources (2008). `arXiv:0810.3017`.

[63] A. Vilenkin, E. P. S. Shellard, Cosmic Strings and Other Topological Defects, Cambridge University Press, 2000.

[64] P. Bhattacharjee, G. Sigl., Origin and propagation of extremely high-energy cosmic rays, Physics Reports 327 (3-4) (2000) 109–247. `arXiv:astro-ph/9811011`, `doi:10.1016/s0370-1573(99)00101-5`.

[65] B. Dawson, M. Fukushima, P. Sokolsky, Past, present, and future of UHECR observations, Progress of Theoretical and Experimental Physics (2017)`arXiv:1703.07897`.

[66] D. Semikoz *et al.* (Pierre Auger Collab.), Constraints on top-down models for the origin of uhecrs from the pierre auger observatory data, in: Proc. 30th Int. Cosmic Ray Conf., Vol. 4, 2007, p. 433–436. `arXiv:0706.2960`.

[67] J. Abraham *et al.* (Pierre Auger Collab.), Upper limit on the cosmic-ray photon flux above 10^{19}eV using the Surface Detector of the Pierre Auger Observatory, Astropart. Phys. 29 (4) (2008) 243 – 256. `doi:DOI:10.1016/j.astropartphys.2008.01.003`.
URL `http://www.sciencedirect.com/science/article/B6TJ1-4RT4XR9-1/2/0951f40e49569776d6edd52ee603ca50`

[68] J. P. Rachen, “Interaction processes and statistical properties of the propagation of cosmic rays in photon backgrounds, Phd thesis, Rheinische Friedrich-WilhelmsUniversität (1996).

[69] M. Nagano, A. A. Watson, Observations and implications of the ultrahigh-energy cosmic rays, Rev. Mod. Phys. 72 (2000) 689–732. `doi:10.1103/RevModPhys.72.689`.

[70] R. Aloisio, V. Berezinsky, S. Grigorieva, Analytic calculations of the spectra of ultra high energy cosmic ray nuclei. ii. the general case of background radiation, Astroparticle Physics 41 (2013) 94–107. `doi:https://doi.org/10.1016/j.astropartphys.2012.06.003`.

[71] V. S. Berezinskii, S. I. Grigor'eva, A bump in the ultra-high energy cosmic ray spectrum, Astron. Astrophys. 199 (1-2) (1988) 1–12.

[72] D. Allard, Extragalactic propagation of ultrahigh energy cosmic-rays, Astroparticle Physics 39-40 (2012) 33–43. `arXiv:1111.3290`, `doi:10.1016/j.astropartphys.2011.10.011`.

[73] R. Durrer, A. Neronov, Cosmological magnetic fields: their generation, evolution and observation, The Astronomy and Astrophysics Review 21 (1) (2013). `arXiv:1303.7121`, `doi:10.1007/s00159-013-0062-7`.

[74] K. Subramanian, The origin, evolution and signatures of primordial magnetic fields, Reports on Progress in Physics 79 (7) (2016) 076901. arXiv:1504.02311, doi:10.1088/0034-4885/79/7/076901.

[75] R. Jansson, G. R. Farrar, A new model of the galactic magnetic field, The Astrophysical Journal 757 (1) (2012) 14. arXiv:1204.3662,archivePrefix={arXiv}, primaryClass={astro-ph}, doi:10.1088/0004-637x/757/1/14.

[76] R. Adam, P. Ade, M. Alves, M. Ashdown, J. Aumont, C. Baccigalupi, A. Banday, R. Barreiro, N. Bartolo *et al.*, Planckintermediate results, Astronomy & Astrophysics 596 (2016) A103. arXiv:1601.00546, doi:10.1051/0004-6361/201528033.

[77] G. R. Farrar, M. S. Sutherland, Deflections of uhecrs in the galactic magnetic field, Journal of Cosmology and Astroparticle Physics 2019 (05) (2019) 004–004. arXiv:1711.02730, doi:10.1088/1475-7516/2019/05/004.

[78] O. Deligny, Measurements and implications of cosmic ray anisotropies from tev to trans-eev energies, Astroparticle Physics 104 (2019) 13–41. arXiv:1808.03940, doi:10.1016/j.astropartphys.2018.08.005.

[79] T. Sanuki *et al.*, Precise measurement of cosmic-ray proton and helium spectra with the bess spectrometer, The Astrophysical Journal 545 (2) (2000) 1135–1142. arXiv:astro-ph/0002481, doi:10.1086/317873.

[80] H. Ahn *et al.*, Measurements of cosmic-ray secondary nuclei at high energies with the first flight of the cream balloon-borne experiment, Astroparticle Physics 30 (3) (2008) 133–141. arXiv:0808.1718, doi:10.1016/j.astropartphys.2008.07.010.

[81] O. Adriani *et al.*, Cosmic-ray electron flux measured by the pamela experiment between 1 and 625 gev, Physical Review Letters 106 (20) (2011). arXiv:1103.2880, doi:10.1103/physrevlett.106.201101.

[82] M. A. *et al.*, The alpha magnetic spectrometer (ams) on the international space station: Part ii — results from the first seven years, Physics Reports 894 (2021) 1–116, the Alpha Magnetic Spectrometer (AMS) on the International Space Station: Part II - Results from the First Seven Years. doi:https://doi.org/10.1016/j.physrep.2020.09.003. URL https://www.sciencedirect.com/science/article/pii/S0370157320303434

[83] M. Tanabashi *et al.*, Particle Data Group, Review of Particle Physics, Phys. Rev. D 98 (3) (2018) 030001. doi:10.1103/PhysRevD.98.030001.

[84] J. J. Beatty, S. Westerhoff, The highest-energy cosmic rays, Annual Review of Nuclear and Particle Science 59 (1) (2009) 319–345. arXiv:https://doi.org/10.1146/annurev.nucl.58.110707.171154, doi:10.1146/annurev.nucl.58.110707.171154.

[85] G. V. Kulikov, G. B. Khristiansen, On the Size Spectrum of Extensive Air Showers, Sov. Phys. ETP (8) (1959) 441–444.

[86] k. H. Kampert *et al.* (KASCADE Collab.), Cosmic ray energy spectra and mass composition at the knee – recent results from kascade –, Nuclear Physics B - Proceedings Supplements 136 (2004) 273–281, cRIS 2004 Proceedings of the Cosmic Ray International Seminars: GZK and Surroundings. arXiv:astro-ph/0410559, doi:https://doi.org/10.1016/j.nuclphysbps.2004.10.035.

[87] W. D. Apel *et al.* (KASCADE Collab.), Ankle-like feature in the energy spectrum of light elements of cosmic rays observed with kascade-grande, Physical Review D 87 (8) (2013). `arXiv:1304.7114`, `doi:10.1103/physrevd.87.081101`.

[88] S. Knurenko, I. Petrov, Z. Petrov, I. Sleptsov, The spectrum of cosmic rays in the energy range $10^{16} - 10^{18}$ eV according to the Small Cherenkov Array in Yakutsk, in: Proc. 34th Int. Cosmic Ray Conf., Vol. ICRC2015, 2015, p. 252. `doi:10.22323/1.236.0252`.

[89] T. Karg (IceCube Collab.), Cosmic Ray Physics with the IceCube Observatory, in: Proc. 34th Int. Cosmic Ray Conf., Vol. ICRC2015, 2015, p. 365. `doi:10.22323/1.236.0365`.

[90] C. H. Jui (TA Collab.), Results from the telescope array experiment, Nuclear and Particle Physics Proceedings 273-275 (2016) 440–445, 37th International Conference on High Energy Physics (ICHEP). `doi:https://doi.org/10.1016/j.nuclphysbps.2015.09.064`.

[91] Y. H. C. Fedorova, HiRes Stereo Cosmic Rays Composition Measurements, in: 30th International Cosmic Ray Conference, Vol. 4, 2007, pp. 463–466.

[92] M. N. *et al.*, Energy spectrum of primary cosmic rays between $10^{14.}$ and 10^{18} ev, J.Phys. G: Nucl. Phys 10 (9) (1984) 1295–1310. `doi:10.1088/0305-4616/10/9/016`.

[93] W. D. Apel *et al.* (KASCADE-Grande Collab.), Kneelike structure in the spectrum of the heavy component of cosmic rays observed with kascade-grande, Phys. Rev. Lett. 107 (2011) 171104. `doi:10.1103/PhysRevLett.107.171104`.

[94] R. Aloisio, V. Berezinsky, P. Blasi, Ultra high energy cosmic rays: implications of auger data for source spectra and chemical composition, Journal of Cosmology and Astroparticle Physics 2014 (10) (2014) 020–020. `arXiv:1312.7459`, `doi:10.1088/1475-7516/2014/10/020`.

[95] R. Aloisio, V. Berezinsky, P. Blasi, A. Gazizov, S. Grigorieva *et al.*, A dip in the uhecr spectrum and the transition from galactic to extragalactic cosmic rays, Astroparticle Physics 27 (1) (2007) 76–91. `arXiv:astro-ph/0608219`, `doi:10.1016/j.astropartphys.2006.09.004`.

[96] D. Allard, E. Parizot, A. V. Olinto, E. Khan, S. Goriely, Uhe nuclei propagation and the interpretation of the ankle in the cosmic-ray spectrum, Astronomy & Astrophysics 443 (3) (2005) L29–L32. `arXiv:astro-ph/0505566`, `doi:10.1051/0004-6361:200500199`.

[97] D. De Marco, T. Stanev, On the shape of the ultrahigh energy cosmic ray spectrum, Physical Review D 72 (8) (2005). `arXiv:astro-ph/0506318`, `doi:10.1103/physrevd.72.081301`.

[98] M. Unger, Cosmic rays above the knee (2008). `arXiv:0812.2763`.

[99] M. Unger, G. R. Farrar, L. A. Anchordoqui, Origin of the ankle in the ultrahigh energy cosmic ray spectrum, and of the extragalactic protons below it, Physical Review D 92 (12) (2015). `arXiv:1505.02153`, `doi:10.1103/physrevd.92.123001`.

[100] R. Abbasi *et al.* (High Resolution Fly's Eye Collab), oration, First Observation of the Greisen-Zatsepin-Kuzmin Suppression, Phys. Rev. Lett. 100 (2008) 101101. `doi:10.1103/PhysRevLett.100.101101`.

[101] J. Matthews, A heitler model of extensive air showers, Astroparticle Physics 22 (5) (2005) 387–397. doi:https://doi.org/10.1016/j.astropartphys.2004.09.003.
URL https://www.sciencedirect.com/science/article/pii/S0927650504001598

[102] C. Patrignani *et al.*, Particle Data Group, Review of Particle Physics, 2016-2017, Chin. Phys. C 40 (2016) 100001. 1808 p. doi:10.1088/1674-1137/40/10/100001.
URL https://cds.cern.ch/record/2241948

[103] M. Rao, B. Sreekantan, Extensive Air Showers, World Scientific Publishing Company, 1998.
URL https://books.google.com.ar/books?id=lwXtCgAAQBAJ

[104] T. K. Gaisser, R. Engel, E. Resconi, Cosmic Rays and Particle Physics: 2nd Edition, Cambridge University Press, 2016. doi:10.1017/CBO9781139192194.

[105] A. Porcelli, Measurements of Xmax above 10^{17} eV with the fluorescence detector of the Pierre Auger Observatory, in: Proceedings of The 34th International Cosmic Ray Conference — PoS(ICRC2015), Vol. 236, 2016, p. 420. doi:10.22323/1.236.0420.

[106] M. Unger *et al.* (Telescope Array Collab. & Pierre Auger Collab.), Pierre auger observatory and telescope array: Joint contributions to the 34th international cosmic ray conference (icrc 2015) (2015). arXiv:1511.02103.

[107] M. Bahmanabadi, S. M. Moghaddam, Simulation of the time structure of extensive air showers with corsika initiated by various primary particles at alborz-i observatory level, New Astronomy 61 (2018) 5–13. doi:https://doi.org/10.1016/j.newast.2017.11.003.
URL https://www.sciencedirect.com/science/article/pii/S1384107617302919

[108] D. Heck (KASCADE Collab.), Extensive air shower simulations with corsika and the influence of high-energy hadronic interaction models, World Scientific (2001)arXiv:astro-ph/0103073.

[109] E.-J. Ahn, R. Engel, T. K. Gaisser, P. Lipari, T. Stanev, Cosmic ray interaction event generator sibyll 2.1, Phys. Rev. D 80 (2009) 094003. doi:10.1103/PhysRevD.80.094003.

[110] S. Messina, Extension to lower energies of the cosmic-ray energy window at the pierre auger observatory, Ph.D. thesis, University of Groningen (2016).
URL https://pure.rug.nl/ws/portalfiles/portal/35176805/Complete_thesis.pdf

[111] R. Engel, D. Heck, T. Pierog, Extensive air showers and hadronic interactions at high energy, Ann. Rev. Nucl. Part. Sci. 61 (2011) 467–489. doi:10.1146/annurev.nucl.012809.104544.

[112] D. Heck, J. Knapp, J. N. Capdevielle, G. Schatz, T. Thouw, CORSIKA: a Monte Carlo code to simulate extensive air showers., 1998.

[113] P. Abreu *et al.* (Pierre Auger Colab.), The Pierre Auger Collaboration, Measurement of the proton-air cross section at $\sqrt{s}$=57 TeV with the pierre auger observatory, Phys. Rev. Lett. 109 (2012) 062002. arXiv:1208.1520, doi:10.1103/PhysRevLett.109.062002.

[114] P. Abreu *et al.* (Pierre Auger Colab.), Description of atmospheric conditions at the pierre auger observatory using the global data assimilation system (gdas), Astroparticle Physics 35 (9) (2012) 591–607. `arXiv:1201.2276`, `doi:10.1016/j.astropartphys.2011.12.002`.

[115] L. Nellen *et al.* (Pierre Auger Collab.), The observation of a muon deficit in simulations from data of the Pierre Auger Observatory, J. Phys. Conf. Ser. 409 (1) (2013) 012107. `doi:10.1088/1742-6596/409/1/012107`.

[116] A. Aab *et al.* (Pierre Auger Collab.), Muons in air showers at the pierre auger observatory: Mean number in highly inclined events, Phys. Rev. D 91 (2015) 032003. `doi:10.1103/PhysRevD.91.032003`.

[117] A. Etchegoyen (Pierre Auger Collab.), Properties of the site and layout of the pierre auger observatory., in: Proc. 27th Int. Cosmic Ray Conf., Hamburg, Germany, 2001, p. 703–706.

[118] D. Veberič, Private communication about currentmap for the pierre auger observatory (Mar 2018).

[119] J. Abraham *et al.* (Pierre Auger Collab.), Properties and performance of the prototype instrument for the Pierre Auger Observatory, Nucl. Instrum. Meth. A 523 (2004) 50–95. `doi:10.1016/j.nima.2003.12.012`.

[120] M. Nagano, K. Kobayakawa, N. Sakaki, K. Ando, New measurement on photon yields from air and the application to the energy estimation of primary cosmic rays, Astroparticle Physics 22 (3-4) (2004) 235–248. `arXiv:astro-ph/0406474`, `doi:10.1016/j.astropartphys.2004.08.002`.

[121] J. Abraham *et al.* (Pierre Auger Collab.), The fluorescence detector of the pierre auger observatory, Nucl. Instrum. Meth. A 620 (2-3) (2010) 227–251. `arXiv:0907.4282`, `doi:10.1016/j.nima.2010.04.023`.
URL `http://dx.doi.org/10.1016/j.nima.2010.04.023`

[122] P. Abreu, et al., Pierre Auger Collaboration, The Rapid Atmospheric Monitoring System of the Pierre Auger Observatory, JINST 7 (2012) P09001. `arXiv:1208.1675`, `doi:10.1088/1748-0221/7/09/P09001`.

[123] P. van Bodegom, Remote sensing of clouds with longwave infrared cameras at the pierre auger observatory, Ph.D. thesis, University of Adelaide, Adelaide, Australia (2018).
URL `http://hdl.handle.net/2440/115875`

[124] B. Dawson, Amplitude Dynamic Range in Auger Fluorescence Electronics Update for the Four Eye System at Nihuil, Auger internal note GAP-00-038 (1999).
URL `https://www.auger.org/gap-notes?task=download.send&id=1752&catid=17&m=0`

[125] C. Bonifazi, The angular resolution of the pierre auger observatory, Nuclear Physics B - Proceedings Supplements 190 (2009) 20–25. `arXiv:0901.3138`, `doi:10.1016/j.nuclphysbps.2009.03.063`.
URL `http://dx.doi.org/10.1016/j.nuclphysbps.2009.03.063`

[126] M. Mostafá, Hybrid activities of the pierre auger observatory, Nuclear Physics B - Proceedings Supplements 165 (2007) 50–58. arXiv:astro-ph/0608670, doi:10.1016/j.nuclphysbps.2006.11.009.

[127] B. Dawson, H. Dai, P. Sommers, S. Yoshida, Simulations of a giant hybrid air shower detector, Astroparticle Physics 5 (3) (1996) 239–247. doi:https://doi.org/10.1016/0927-6505(96)00024-2.
URL https://www.sciencedirect.com/science/article/pii/0927650596000242

[128] H. Barbosa, F. Catalani, J. Chinellato, C. Dobrigkeit, Determination of the calorimetric energy in extensive air showers, Astroparticle Physics 22 (2) (2004) 159–166. arXiv:astro-ph/0310234, doi:10.1016/j.astropartphys.2004.06.007.
URL http://dx.doi.org/10.1016/j.astropartphys.2004.06.007

[129] M. J. Tueros, PIERRE AUGER, Estimate of the non-calorimetric energy of showers observed with the fluorescence and surface detectors of the Pierre Auger Observatory, in: 33rd International Cosmic Ray Conference, 2013, p. 0705.

[130] V. Verzi, Pierre Auger, The Energy Scale of the Pierre Auger Observatory, in: 33rd International Cosmic Ray Conference, 2013, p. 0928. arXiv:1307.5059.

[131] I. Allekotte *et al.* (Pierre Auger Collab.), The surface detector system of the pierre auger observatory, Nucl. Instrum. Meth A 586 (3) (2008) 409–420. arXiv:0712.2832, doi:10.1016/j.nima.2007.12.016.

[132] R. C. Shellard, First results from the pierre auger observatory, Brazilian Journal of Physics 36 (4a) (2006) 1184–1193. doi:10.1590/s0103-97332006000700012.

[133] A. Aab *et al.* (Pierre Auger collab.), The Pierre Auger Cosmic Ray Observatory, Nucl. Instrum. Meth. A 798 (2015) 172–213. arXiv:1502.01323, doi:10.1016/j.nima.2015.06.058.

[134] Pierre Auger Collab., The Pierre Auger Project Design Report, Fermi Laboratory, 2nd Edition (1996).

[135] Calibration of the surface array of the pierre auger observatory, Nucl. Instrum. Meth A 568 (2) . doi:https://doi.org/10.1016/j.nima.2006.07.066.

[136] P. Bauleo, A. Etchegoyen, J. Niello, A. Ferrero, A. Filevich, C. Guérard, F. Hasenbalg, M. Mostafá, D. Ravignani, J. Martino, A water tank cherenkov detector for very high-energy astroparticles, Nucl. Instrum. Meth A 406 (1) (1998) 69–77. arXiv:hep-ex/9707036, doi:https://doi.org/10.1016/S0168-9002(97)01187-X.

[137] M. Aglietta *et al.*, Response of the pierre auger observatory water cherenkov detectors to muons 29th International Cosmic Ray Conference, ICRC 2005.
URL https://cds.cern.ch/record/965299

[138] P. Billoir, Proposition to improve the local trigger of the Surface Detector for low energy showers, Auger internal note GAP-2009-179 (2009).
URL https://www.auger.org/gap-notes?task=download.send&id=751&catid=7&m=0

[139] P. Billoir, P. Ghia, D. Nitz, R. Sato, First results of the ToTd trigger in the test hexagon, Auger internal note GAP-2011-032 (2011).
URL https://www.auger.org/gap-notes?task=download.send&id=62&catid=3&m=0

[140] J. Abraham, P. Abreu, M. Aglietta, E. Ahn, D. Allard, I. Allekotte, J. Allen, J. Alvarez-Muñiz, M. Ambrosio, L. Anchordoqui, et al., Trigger and aperture of the surface detector array of the pierre auger observatory, Nucl. Instrum. Meth A 613 (1) (2010) 29–39. arXiv:1111.6764, doi:10.1016/j.nima.2009.11.018.

[141] D. Allard *et al.* (Pierre Auger Collab.), The trigger system of the pierre auger surface detector: operation, efficiency and stability, in: Proc. 29th Int. Cosmic Ray Conf., Pune, India, 2005. arXiv:astro-ph/0510320.

[142] L. M. Bueno, P. Billoir, I. C. Maris, Signal variance for the TOTd and MoPS triggers, Auger internal note GAP-2014-035 (2014).

[143] M. Ave, P. Bauleo, A. Castellina, A. Chou, J. Harton, R. Knapik, G. Navarra, The accuracy of signal measurement with the water cherenkov detectors of the pierre auger observatory, Nuclear Instruments and Methods in Physics Research Section A: Accelerators, Spectrometers, Detectors and Associated Equipment 578 (1) (2007) 180–184. arXiv:2101.06158, doi:10.1016/j.nima.2007.05.150.

[144] M. Horvat, D. Veberič, On shower-front start-time variance, Auger internal note GAP-2007-057 (2007).

[145] I. Maris, Measurement of the ultra high energy cosmic ray flux using data of the pierre auger observatory, Auger internal note GAP-2008-026 (2006).
URL https://www.auger.org/gap-notes?task=download.send&id=852&catid=8&m=0

[146] A. Schulz, Measurement of the Energy Spectrum of Cosmic Rays between 0.1 EeV and 30 EeV with the Infill Extension of the Surface Detector of the Pierre Auger Observatory, Master's thesis, Karlsruhe Institute of Technology (2012).
URL https://www.auger.org/gap-notes?task=download.send&id=418&catid=4&m=0

[147] S. Messina, Extension to lower energies of the cosmic-ray energy window at the Pierre Auger Observatory, Dissertation, University of Groningen (2016).
URL https://www.auger.org/document-centre2?task=download.send&id=4503&catid=104&m=0

[148] K. Kamata, J. Nishimura, The Lateral and the Angular Structure Functions of Electron Showers, Progress of Theoretical Physics Supplement 6 (1958) 93–155. arXiv:https://academic.oup.com/ptps/article-pdf/doi/10.1143/PTPS.6.93/5270594/6-93.pdf, doi:10.1143/PTPS.6.93.
URL https://doi.org/10.1143/PTPS.6.93

[149] T. Schmidt, I. C. Mariş, M. Roth, Fine tuning of the ldf parameterisation and the influence on s_{1000}, Auger internal note GAP-2007-106 (2007).

[150] J. Hersil, I. Escobar, D. Scott, G. Clark, S. Olbert, Observations of extensive air showers near the maximum of their longitudinal development, Phys. Rev. Lett. 6 (1961) 22–23. doi:10.1103/PhysRevLett.6.22.
URL https://link.aps.org/doi/10.1103/PhysRevLett.6.22

[151] H. O. Klages (Pierre Auger Collab.), HEAT – Enhancement Telescopes for the Pierre Auger Southern Observatory, in: 30th International Cosmic Ray Conference, Vol. 5, 2007, pp. 849–852.
URL http://particle.astro.ru.nl/pub/30ICRC5-849.pdf

[152] H. Klages (Pierre Auger Collab.), Enhancements to the Southern Pierre Auger Observatory, J. Phys. Conf. Ser. 375 (5) (2012) 052006. doi:10.1088/1742-6596/375/1/052006.
URL https://s3.cern.ch/inspire-prod-files-1/1ed1f151e341fcc5f6b3849fff688acd

[153] C. Meurer, N. Scharf (Pierre Auger Collab.), Heat – a low energy enhancement of the pierre auger observatory, Astrophysics and Space Sciences Transactions 7 (2) (2011) 183–186. arXiv:1106.1329, doi:10.5194/astra-7-183-2011.
URL http://dx.doi.org/10.5194/astra-7-183-2011

[154] T. H.-J. Mathes (Pierre Auger Collab.), The HEAT telescopes of the Pierre Auger Observatory: Status and first data, in: 32nd International Cosmic Ray Conference, Vol. 3, 2011, p. 153. doi:10.7529/ICRC2011/V03/0761.
URL http://icrc2011.ihep.ac.cn/paper/proc/v3.pdf

[155] D. Ravignani, Pierre Auger, Measurement of the energy spectrum of cosmic rays above $3{\times}10^{17}$ eV using the AMIGA infill detector of the Pierre Auger Observatory, in: 33rd International Cosmic Ray Conference, 2013, p. 0693.
URL https://inspirehep.net/files/7433fb97708f23d7243bf2254114b433

[156] D. Mockler, The first measurement of an energy spectrum at 0.1 EeV with the Surface Detector of the Pierre Auger Observatory, Master's thesis, Karlsruhe Institute of Technology, Karlsruhe (10 2014).

[157] V. Novotný, Measurement of the energy spectrum of cosmic rays using Cherenkov-dominated data at the Pierre Auger Observatory, Ph.D. thesis, Charles U. (2020).
URL https://inspirehep.net/files/2b0fcc20a1c6b85067c9fbdb32387e4b

[158] A. Coleman, Measurement of the cosmic ray flux above 100 pev at the pierre auger observatory, Dissertation, The Pennsylvania State University (2018).
URL https://www.auger.org/gap-notes?task=download.send&id=4775&catid=107&m=0

[159] F. Suarez (Pierre Auger collab.), The AMIGA muon detectors of the Pierre Auger Observatory: overview and status, in: 33rd International Cosmic Ray Conference, 2013, p. 0712.
URL https://inspirehep.net/files/e337361ea7351ccf792c901ed3390d98

[160] Prototype muon detectors for the amiga component of the pierre auger observatory, Journal of Instrumentation 11 (02) (2016) P02012–P02012. arXiv:1605.01625, doi:10.1088/1748-0221/11/02/p02012.

[161] F. Kahn, I. Lerche, Radiation from cosmic ray air showers, Proceedings of the Royal Society of London. Series A. Mathematical and Physical Sciences 289 (1966) 206 – 213. doi:https://doi.org/10.1098/rspa.1966.0007.

[162] G. A. Askar'yan, Excess negative charge of an electron-photon shower and its coherent radio emission, Zhur. Eksptl'. i Teoret. Fiz. https://www.osti.gov/biblio/4833087.
URL https://inspirehep.net/files/50aa3b9f4a1271a1476462d1635d96a7

[163] C. Glaser, Results and perspectives of the auger engineering radio array, EPJ Web of Conferences 135 (2017) 01006. arXiv:1609.01513, doi:10.1051/epjconf/201713501006.
URL http://dx.doi.org/10.1051/epjconf/201713501006

[164] A. Aab *et al.*, Measurement of the radiation energy in the radio signal of extensive air showers as a universal estimator of cosmic-ray energy, Physical Review Letters 116 (24) (2016). `arXiv:1605.02564`, `doi:10.1103/physrevlett.116.241101`.
URL `http://dx.doi.org/10.1103/PhysRevLett.116.241101`

[165] A. Aab *et al.*, Energy estimation of cosmic rays with the engineering radio array of the pierre auger observatory, Physical Review D 93 (12) (2016). `arXiv:1508.04267`, `doi:10.1103/physrevd.93.122005`.
URL `http://dx.doi.org/10.1103/PhysRevD.93.122005`

[166] A. Aab *et al.* (Pierre Auger Collab.), Probing the radio emission from air showers with polarization measurements, Phys. Rev. D 89 (5) (2014) 052002. `arXiv:1402.3677`, `doi:10.1103/PhysRevD.89.052002`.

[167] The Pierre Auger Collababoration, The pierre auger observatory upgrade - preliminary design report (2016). `arXiv:1604.03637`.

[168] The Radio Group of the Pierre Auger Observatory, The science case for the Radio Upgrade of the Pierre Auger Observatory, Auger internal note GAP-2020-004 (2020).
URL `https://www.auger.org/document-centre2?task=download.send&id=5067&catid=144&m=0`

[169] D. Heck, J. Knapp, J. N. Capdevielle, G. Schatz, T. Thouw, CORSIKA: A Monte Carlo code to simulate extensive air showers (1998).

[170] D. Heck, J. Knapp, Upgrade of the monte carlo code corsika to simulate extensive air showers with energies $> 10^{20}$ ev, Report FZKA 6097B, Karlsruhe (1998).

[171] M. Kobal, A thinning method using weight limitation for air-shower simulations, Astropart. Phys. 15 (2001) 259. `doi:10.1016/S0927-6505(00)00158-4`.

[172] P. Billoir, Reconstruction of showers with the ground array: status of the "prototype" program, Auger internal note GAP-2000-025 (2000).

[173] P. Billoir, Does the resampling procedure induce distortions in the fadc traces of the surface detector?, Auger internal note GAP-2005-109 (2005).

[174] P. Billoir, A sampling procedure to regenerate particles in a ground detector from a 'thinned' air shower simulation output, Astropart. Phys. 30 (2008) 270–285. `doi:10.1016/j.astropartphys.2008.10.002`.

[175] S. Ostapchenko, On the re-summation of enhanced pomeron diagrams, Physics Letters B 636 (1) (2006) 40–45. `arXiv:hep-ph/0602139`, `doi:10.1016/j.physletb.2006.03.026`.

[176] S. Argirò, S. Barroso, J. Gonzalez, L. Nellen, T. Paul, T. Porter, L. Prado Jr., M. Roth, R. Ulrich, D. Veberič, The offline software framework of the pierre auger observatory, Nuclear Instruments and Methods in Physics Research Section A: Accelerators, Spectrometers, Detectors and Associated Equipment 580 (3) (2007) 1485–1496. `arXiv:0707.1652`, `doi:10.1016/j.nima.2007.07.010`.

[177] L. D. Brown, T. T. Cai, A. DasGupta, Interval Estimation for a Binomial Proportion, Statistical Science 16 (2) (2001) 101 – 133. `doi:10.1214/ss/1009213286`.
URL `https://doi.org/10.1214/ss/1009213286`

[178] G. Ros, A. Supanitsky, G. Medina-Tanco, L. del Peral, M. Rodríguez-Frías, Improving photon-hadron discrimination based on cosmic ray surface detector data, Astroparticle Physics 47 (2013) 10–17. doi:10.1016/j.astropartphys.2013.05.014.
URL https://doi.org/10.1016%2Fj.astropartphys.2013.05.014

[179] G. Ros *et al.*, S_b for photon-hadron discrimination, Auger internal note GAP-2010-052 (2010).

[180] S. Messina, A. M. van den Berg, Reconstruction comparison between infill and aera array, Auger internal note GAP 2013-049 (2013).
URL https://www.auger.org/gap-notes?task=download.send&id=130&catid=5&m=0

[181] D. Newton, J. Knapp, A. A. Watson, The Optimum Distance at which to Determine the Size of a Giant Air Shower, Astropart. Phys. 26 (2007) 414–419.

[182] D. Ravignani, G. Silli, The optimal distance to measure the shower size with the 433-metre surface detector, Auger internal note GAP 2021-019 (2021).
URL https://www.auger.org/gap-notes?task=download.send&id=5290&catid=145&m=0

[183] J. Weseler, M. Roth (Pierre Auger Collab), The energy spectrum below 10^{18} eV using the infill array, Lecce Analysis Meeting (2010).

[184] D. Veberič, B. Kégl, R. Engel, M. Roth, Constant Intensity Cut: Unbinned Estimation of the Signal Attenuation Function, Auger internal note GAP-2015-065 (2015).

[185] A. Aab *et al.* (Pierre Auger Collab.), Measurement of the cosmic-ray energy spectrum above 2.5×10^{18}4ev using the pierre auger observatory, Physical Review D 102 (6) (2020). arXiv:2008.06486, doi:10.1103/physrevd.102.062005.

[186] V. Novotnÿ, Measurement of the energy spectrum of cosmic rays using Cherenkov-dominated data at the Pierre Auger Observatory , Phd thesis, Charles University (2020).
URL https://inspirehep.net/files/2b0fcc20a1c6b85067c9fbdb32387e4b

[187] I. Lhenry-Yvon, R. Sato, The 2018_ 2019 "infill comms crisis". impact on the data set and the proposal to fix it., Auger internal note GAP 2021-007 (2021).
URL https://www.auger.org/document-centre2?task=download.send&id=5275&catid=145&m=0

[188] M. Amenomori *et al.*, The all-particle spectrum of primary cosmic rays in the wide energy range from 1014to 1017ev observed with the tibet-iii air-shower array, The Astrophysical Journal 678 (2) (2008) 1165–1179. arXiv:0801.1803, doi:10.1086/529514.

[189] A. Ivanov, S. Knurenko, I. Sleptsov, Measuring extensive air showers with cherenkov light detectors of the yakutsk array: The energy spectrum of cosmic rays, New Journal of Physics 11 (2009). doi:10.1088/1367-2630/11/6/065008.

[190] V. Prosin *et al.*, Results from tunka-133 (5 years observation) and from the tunka-hiscore prototype, EPJ Web of Conferences 121 (2016) 03004. doi:10.1051/epjconf/201612103004.
URL https://inspirehep.net/files/3a1228b010097f1c0c78440404de9b0f

[191] W. Apel, J. Arteaga-Velázquez, K. Bekk, M. Bertaina, J. Blümer, H. Bozdog, I. Brancus, P. Buchholz, E. Cantoni, A. Chiavassa, *et al.*, The spectrum of high-energy cosmic rays measured with kascade-grande, Astroparticle Physics 36 (1) (2012) 183–194. `arXiv:1206.3834`, `doi:10.1016/j.astropartphys.2012.05.023`.
URL `http://dx.doi.org/10.1016/j.astropartphys.2012.05.023`

[192] M. G. Aartsen *et al.* (IceCube Collab.), Cosmic ray spectrum and composition from pev to eev using 3 years of data from icetop and icecube, Phys. Rev. D 100 (2019) 082002. `arXiv:1906.04317`, `doi:10.1103/PhysRevD.100.082002`.

[193] R. U. Abbasi *et al.* (TALE Collab.), The cosmic ray energy spectrum between 2 PeV and 2 EeV observed with the TALE detector in monocular mode, The Astrophysical Journal 865 (1) (2018) 74. `doi:10.3847/1538-4357/aada05`.
URL `https://doi.org/10.3847/1538-4357/aada05`